Disorder in the Quantum Spin-Chains Sr_2CuO_3 and $SrCuO_2$

A thesis

Submitted in partial fulfillment of the requirements

Of the degree of

Doctor of Philosophy

by:

Koushik Karmakar

Registration ID : 20103075

Indian Institute of Science Education and Research,
Pune-411008, India

November, 2016

উৎসর্গ:

আমার পরম প্রিয়জনেদের।

Certificate

Certified that the work incorporated in the thesis entitled **"Disorder in the Quantum Spin-Chains Sr_2CuO_3 and $SrCuO_2$"** Submitted by ***Koushik Karmakar*** was carried out by the candidate, under my supervision. The work presented here or any part of it has not been included in any other thesis submitted previously for the award of any degree or diploma from any other University or institution.

Pune
Date: November 9, 2016

(Dr. Surjeet Singh)
Thesis Supervisor

Declaration

I declare that this written submission represents my ideas in my own words and where others' ideas have been included, I have adequately cited and referenced the original sources. I also declare that I have adhered to all principles of academic honesty and integrity and have not misrepresented or fabricated or falsified any idea/data/fact/source in my submission. I understand that violation of the above will be cause for disciplinary action by the Institute and can also evoke penal action from the sources which have thus not been properly cited or from whom proper permission has not been taken when needed.

Pune
November 9, 2016

(Koushik Karmakar)
ID: 20103075

Acknowledgements

It is my pleasure to acknowledge the advices and support from several persons who have influenced this work. First of all, I would like to express my deepest gratitude to my supervisor *Dr. Surjeet Singh*, for his priceless and fruitful guidance, both on academic and personal level. I hereby thank him from the bottom of my heart for his congenial interaction, timeless patience, and prompt reciprocation. I would also like to thank him for pointing out the loopholes and drawbacks of my work from an introspective aspect by his scientific comments and constructive criticisms all through, and this effectively helped me improve and develop my thesis-writing skills by a substantial amount.

I am thankful to *Prof Christian Rüegg* for providing me with the opportunity to perform neutron experiments, at PSI, Switzerland and also helping me out in person in order to understand and carry out the experiments. I would like to acknowledge *Dr Markos Skoulatos*, for giving me a detailed introduction of the neutron scattering techniques and helping me perform the experiments. I thank him for the pleasant stay and joyful outings too over there in Switzerland. I would like to thank *Dr Thorsten Schmitt* as well for allowing me to perform the resonant inelastic x-ray techniques during my stay in Switzerland. *Dr Giacomo Prando* (IFW–Dresden) was really helpful for the useful communications and his μSR results which added an edge to the understanding the physics of zigzag spin system.

I would like to thank my Research Advisory Committee that consists of *Dr. Sunil Nair* and *Dr. G. V. Pavan Kumar* and *Dr. Pankaj Poddar* (NCL–Pune) for their productive and effectual guidance during the academic meetings and the valuable suggestions throughout the PhD tenure of mine.

I would like to acknowledge *Prof. Sudesh Kumar Dhar*, TIFR–Mumbai, for allowing me to use the experimental facilities in his lab during the initial days of my PhD. I

thank *Prof. Sulabha Kulkarni* for collaboration on the spin chain compound $CuSe_2O_5$. My heartfelt gratitude to all of those respected teachers who had taught me starting from the school days to my post-graduate.

I thankfully acknowledge the Department of Science and Technology (DST), India, and the Swiss State Secretariat for Education, Research and Innovation (SERI) for financial support under the Indo-Swiss Joint Research Programme (Grant number: INT/SWISS/ISJRP/PEP/P-06/ 2012), to visit PSI, Switzerland to carry out the neutron scattering experiments reported in this thesis.

I would like to thank *Prof K. N. Ganesh*, Director, IISER Pune for providing excellent support and facilities to our research group without which this work would not have been possible.

I would like to thank my lab-mates: *Rabindranath, Prachi, Giri, Rohit, Soumendra (Panja), Amartya, Sharada, Lakshmi, Giri, Priyank* and others for their support at various stages of my research life has meant a lot. I would like to acknowledge *Dr. Luminita Harnagea*, *Dr. Smita Chaturvedi* as well for their valuable support. I wish to thank *Mr Nilesh Dumbre*, *Mr. Anil Prathamshetti*, *Parveen Nasa*, and *Mr Prashant Kale* for their technical support on many occasions. I am also thankful to the office staff members including *Mr. Prabhakar Anagare*, *Mr. Kalpesh Pednekar*, *Dhanashree Sheth* and *Mr. Tushar Kurulkar* for their timely help on many different occasions. I also extend my sincere thanks to IISER administration, transport, library, security and house-keeping staffs.

I am very much lucky to have a group of friends, who actually know me inside out. *Arindam, Sunil, Sisir, Biplab, Partha, Snehal, Supratik* and many more - without these people, life at IISER would have been quite dull. Every little joy from late night parities to hiking the mighty Sahyadri or a dive in the Arabian Sea, seems incomplete if not shared with them. Every big trouble always scales down to a trivial - almost non-existent one, as soon as they start pouring out their expert comments. Every moment spent with them has rejuvenated my soul with renewed vigour and enthusiasm to face the challenges of life. etc. . . .

Finally, I would like to take this opportunity to acknowledge my family, specially

my parents, for their incessant support since day minus one and also my wife and little daughter *Pranjali* for their blissful and wonderful company.

Contents

1 Introduction **1**

1.1 The Hubbard model . . . 3

1.1.1 Half-filled Hubbard model . . . 8

1.1.2 Transition metal oxides . . . 9

1.1.3 Cuprates . . . 10

1.2 One-dimensional Heisenberg magnets . . . 15

1.2.1 Magnetic excitations: *Spinons* . . . 18

1.3 Spin 1/2 antiferromagnetic Heisenberg model . . . 19

1.3.1 Bulk magnetic susceptibility . . . 19

1.3.2 Separation of spinon, holon, and orbiton . . . 22

1.3.3 Magnetic ordering in real spin chain compounds . . . 24

2 Disorder in Quantum Spin 1/2 Chains **27**

2.1 Disorder in the spin $1/2$ Heisenberg antiferromagnetic chains . . . 27

2.2 Survey of previous studies on disordered spin chains . . . 29

2.2.1 Strong disorder quantum spin chains . . . 31

2.2.2 Dilute impurities in spin $1/2$ chains . . . 33

2.3 Physical properties of the spin $1/2$ HAF chain with dilute impurities . . . 38

2.3.1 Bulk magnetic susceptibility . . . 38

2.3.2 Thermal conductivity . . . 41

2.4 Magnetic ground state of dilutely disordered chains . . . 42

2.5 Influence of the spin states of the doped impurity . . . 43

3 Motivation and Materials **47**

3.1 Motivation . . . 47

3.2 Compounds Sr_2CuO_3 and $SrCuO_2$ 48
3.2.1 Crystal structure 49
3.2.2 Bibliographic view of the physical properties 51

4 Experimental Methods **55**
4.1 Crystal growth 55
4.2 Structural and composition characterizations 57
4.2.1 Optical microscopy 57
4.2.2 Scanning electron microscopy 58
4.2.3 Powder x-ray diffraction 60
4.2.4 Laue-diffraction 62
4.3 Bulk physical properties measurement methods 63
4.3.1 Specific heat 63
4.3.2 dc magnetization 65
4.3.3 ac susceptibility 66
4.4 Neutron scattering 68
4.4.1 Elastic neutron scattering and bulk magnetism 70
4.4.2 Inelastic neutron scattering and magnetic excitation 73
4.4.3 Neutron instruments 76
4.4.3.1 Spallation neutron source 76
4.4.3.2 Moderation of the neutrons 77
4.4.3.3 The ^{3}He detector 79
4.4.3.4 Triple-axis spectrometer 80
4.5 Muon spin rotation (μSR) 84

5 Single Crystal Growth **87**
5.1 Principles of crystal growth 88
5.1.1 Optical floating zone growth 89
5.1.1.1 Image furnace 90
5.1.1.2 Advantages of floating-zone technique 92
5.1.1.3 Disadvantages of floating-zone technique 92

5.1.1.4 Growth process and parameters 93
5.1.2 Melting behaviour of solids 94
5.1.2.1 Congruently melting behaviour 95
5.1.2.2 Incongruently melting behaviour 96
5.1.3 Principle of working of a TSFZ growth 98
5.1.4 Single crystal growth of the doped compounds 101
5.2 Single crystal growth of Sr_2CuO_3 and $SrCuO_2$ 104
5.2.1 SrO-CuO binary phase diagram 104
5.2.2 Synthesis of the feed rod 106
5.2.3 Choice of the solvent composition 108
5.2.4 Growth protocol 110
5.2.5 Results and characterization 113
5.3 Analysis of the TSFZ process 118
5.3.1 Lamp power dependence of the TSFZ process 121
5.3.2 Solid-liquid interfaces 122
5.3.3 Voids in the solidified TSFZ 125
5.3.4 TSFZ composition 125
5.3.5 Behaviour of feed in the vicinity of the TSFZ 127
5.4 Summary 128

6 Bulk Magnetic Behaviour in the Presence of Dilute Disorder 131
6.1 Bulk magnetic susceptibility of pristine chains 132
6.1.1 Fitting procedure 135
6.1.2 Susceptibility of undoped Sr_2CuO_3 137
6.1.3 Field dependence of magnetisation in Sr_2CuO_3 139
6.2 Susceptibility of the Zn-doped chain 141
6.3 Ni impurities in spin 1/2 chain 142
6.4 Magnetic excitations in the weak disorder limit 145
6.4.1 Spinon energy dispersion in pristine spin 1/2 chains 146
6.4.2 Effect of dilute disorder on the low-energy excitations 146

6.5 Summary 150

7 Magnetic Ground State of Sr_2CuO_3 with and without Dilute Doping 151

7.1 Magnetic ground state in presence of scalar disorder 152

7.1.1 Magnetic ordering in pristine Sr_2CuO_3 152

7.1.2 Finite-size effects on the ordered state 153

7.1.3 Variation of the ordering temperature under external magnetic fields 158

7.2 Co-doping in Sr_2CuO_3 163

7.2.1 Low-field magnetic behaviour 163

7.2.2 Field dependence of the bulk magnetic properties 167

7.2.3 Field dependence of the ordering temperature 169

7.3 Summary 176

8 Spin Frustration in the Spin $1/2$ Zigzag Heisenberg Chain 179

8.1 Bulk Magnetic Susceptibility of undoped $SrCuO_2$ 180

8.1.1 Analysis of the Susceptibility data 180

8.1.2 Zinc ($S = 0$) impurities in $SrCuO_2$ 184

8.2 Magnetic Ground State of the Spin 1/2 Zigzag Chain 185

8.2.1 Co-impurities in the Zigzag Chain 186

8.3 Summary 192

9 Summary and Outlook 193

Abbreviation

1D/3D	one-dimensional/three-dimensional
ACMS	ac measurement system
ARPES	angle-resolved photo-emission spectroscopy
BSE	back-scattered electrons
CW	Curie-Weiss
EDX	energy-dispersive x-ray
ENS	elastic neutron scattering
ESR	electron-spin resonance
FC	field cool
FZ	floating zone
HAF	Heisenberg antiferromagnetic
INS	inelastic neutron scattering
LRO	long-range-order
μSR	muon spin rotation
NMR	nuclear magnetic resonance
PPMS	physical properties measurement system
RIXS	resonant inelastic x-ray scattering
RS	random singlet
SEM	scanning electron microscopy
TAP	transverse staggered phase
TAS	triple-axis spectrometer
TMO	transition metal oxide
TSFZ	travelling-solvent-floating-zone
TTL	Tomonaga-Luttinger liquid
VSM	vibrating sample magnetometer
ZFC	zero-field cool

Synopsis

Quantum spin 1/2 chains are model many-body strongly correlated systems for studying fundamental physical phenomena including spin-liquids, one-dimensional Mott insulators, fractionalization of electron into separate quasi-particles (spinon-holon or spinon-orbiton), spinon mediated metal-like thermal conductivity, and spin-Peierls dimerization, to name a few.

Due to strong quantum effects, the ground state of a spin $1/2$ chain compound can easily be tuned to obtain a wide range of novel magnetic ground states. The tuning parameter in these experiments can either be impurities incorporated directly in the spin chains and/or structural disorder introduced by doping outside the chains. In the strong disorder limit, quantum spin chains are well-known to exhibit a Random Singlet ground state, independent of the specific details of the disorder. However, their behaviour in the dilute disorder limit is not that well investigated. In this thesis, our focus is on exploring the effects of dilute disorder on the magnetic properties of the spin $1/2$ Heisenberg antiferromagnetic (HAF) chain. The thesis is organised as follows:

In the introductory chapter (Chapter 1), we shall briefly discuss the basic concepts central to understanding and interpreting the physical properties of quantum spin $1/2$ chains. The topics covered include the field theoretic calculations of the bulk susceptibility of the spin $1/2$ HAF chain, and a discussion of its low-energy spin excitations known as the spinons. We shall then discuss some of the interesting and fundamental physical phenomena exclusive to the spin $1/2$ HAF chain. Since any real spin chain compound will have a finite interchain interaction, no matter howsoever small, at fairly low temperatures, the system will either undergo a dimensional crossover to a three-dimensional long-range magnetically ordered state, or to a spin dimerized state via the spin-Peierls transition, which are discussed briefly at the end.

Disorder is ubiquitous, any real system will have some degree of disorder, it is therefore important to understand how the presence of disorder vitiate the ideal chain behaviour. Chapter 2 of this thesis, therefore, deals with disorder in quantum spin chains. In this chapter we will provide a concise review of the disorder physics in one-dimensional quantum magnets. The chapter also includes a discussion of some important results that will be used in the later chapters in this thesis.

In chapter 3, we will provide the motivation and the materials used in our investigations. The closest realizations of the spin $1/2$ HAF chain are the well known cuprates: Sr_2CuO_3 and $SrCuO_2$. We will provide the structural details of these compounds, which is followed by a brief review of the previous literature specific to these two compounds.

Chapter 4 of the thesis contains details of the experimental methods, which include crystal growth, structural/compositional characterisations, bulk physical properties measurements and neutron scattering experiments.

Chapter 5 is devoted to the single crystal growth of Sr_2CuO_3 and $SrCuO_2$, and their doped variants using the travelling-solvent-floating-zone (TSFZ) technique. In this chapter we provide details of the growth parameters and their optimization process. Details of the post growth analysis of the solidified TSFZ are reported, which will throw light on the TSFZ growth mechanism.

In chapter 6, our investigations of the magnetic susceptibility and low-energy magnetic excitations of the compounds Sr_2CuO_3 and $SrCuO_2$ are reported. The susceptibility data were analysed using the field theoretical results discussed in chapter 2. Analogous analysis of the spin susceptibility of $Sr_2Cu_{0.99}Ni_{0.01}O_3$ shows that the Ni^{2+} spin is screened, which provides an indirect evidence of the Kondo-like screening in the spin $1/2$ HAF chain in agreement with the theory. A direct evidence for screening of the Ni spin was also furnished using the inelastic neutron scattering experiments.

Chapter 7 is devoted to the magnetic ground state of the dilutely disordered linear chain compound Sr_2CuO_3. The influence of doping on the long-range spin ordered state and its field dependence is reported using bulk magnetic susceptibility, specific heat and elastic neutron scattering experiments. Due to finite-size effects, the ordering temperature is found to suppress in the presence of scalar defects, which is in accordance with

the field theoretical calculations. Interestingly, the ordering temperature is found to increase under an applied magnetic field, which gives an indication of the enhancement of transverse staggered correlations in an external magnetic field.

In the second part of this chapter we present the results of dilute Co-doping in Sr_2CuO_3. As opposed to the case of a scalar impurity (e.g. Zn^{2+}), the magnetic ordering temperature upon Co-doping increases with increasing Co-concentration. Furthermore, the ordering temperature is found to show an anisotropic suppression with the external magnetic field. A phase diagram of the Co-doped chains is constructed, which shows the existence of two ordered phases, separated by a possible quantum critical point.

In Chapter 8, the spin frustration in the zigzag spin chain compound $SrCuO_2$ is investigated. The magnetic frustration plays a crucial role in determining the nature of the magnetic ground state. We show that the 1% Co-doped $SrCuO_2$ exhibits a quasi-long-range ordered state below $T = 5$ K, as opposed to a truly long-range ordered ground state in 1% Co-doped Sr_2CuO_3 below $T = 11$ K. This difference in the magnetic behaviour of the zigzag spin chains and the linear chains having a comparable intra- and interchain couplings is related to the spin frustration in the zigzag chains. Elastic neutron scattering experiments and ac magnetic susceptibility were used to characterise the quasi-long-range ordered state of Co-doped $SrCuO_2$.

In the concluding chapter (Chapter 9), we present a summary of our results. Briefly, the material presented in this thesis shows that dilute doping in spin $1/2$ chains can induce novel magnetic behaviour which shows a strong dependence on the quantum spin-state of the doped impurity. The fact that the dilute doping can significantly alter the ground state and low-energy excitations of the spin $1/2$ chain, as shown here in this thesis, should motivate further research in this area.

List of Publications

Publications included in this thesis

1. *Crystal growth of non-magnetic Zn^{2+} and magnetic Co^{2+} doped quasi one-dimensional spin chain compound $SrCuO_2$ using the travelling solvent floating zone method*, **Koushik Karmakar**, Amartya Singh, Surjeet Singh*, Amy Poole and Christian Rüegg, Crystal Growth & design **14(3)**, 1184–1192 (2014).

2. *Finite-size effects in quasi one-dimensional quantum magnets Sr_2CuO_3, $Sr_2Cu_{0.99}M_{0.01}O_3$ (M = Ni, Zn) and $SrCuO_2$*, **Koushik Karmakar** and Surjeet Singh*, Phys. Rev. B **91(22)**, 224401 (2015).

3. *Crystal Growth of Spin Chain Compound Sr_2CuO_3 Doped with Quantum Defects: Zn, Co, Ni, and Mn*, **Koushik Karmakar**, Rabindranath Bag and Surjeet Singh*, Crystal Growth & Design, **15(10)**, 4843–4853 (2015).

4. *Effects of quantum impurity spins on the magnetic properties of zigzag and linear spin chains*, **Koushik Karmakar**, Markos Skoulatos, Giacomo Prando, Bertran Roessli, Uwe Stuhr, Franziska Hammerath, Christian Rüegg and Surjeet Singh*, Phys. Rev. Lett. (in revision); preprint: arXiv:1602.03677[cond-mat.str-el].

5. *Magnetic ground state of the disorder spin $1/2$ Heisenberg antiferromagnetic chain compound Sr_2CuO_3 probed via specific heat*, **Koushik Karmakar**, Rabindranath Bag and Surjeet Singh*, to be published (2016).

6. *Field induced quantum criticality in the ordered state of Co doped Sr_2CuO_3*, **Koushik Karmakar**, Markos Skoulatos, Christian Rüegg and Surjeet Singh*, to be published (2016).

Publications not included in this thesis

1. *Structural and magnetic investigations on a wet chemically synthesized nanoscale S = 1/2 spin chain compound – $CuSe_2O_5$*, Pryank Shyam, Smita Chaturvedi, **Koushik Karmakar**, Arpan Bhattacharya, Surjeet Singh, and Sulbha Kulkarni*, J. Mater. Chem. C, 4, 611–621 (2016).

2. *Single crystal growth of Co, Ni and Zn doped spin-ladder compound $Sr_{14}Cu_{24}O_{41}$ by the travelling-solvent floating-zone method*, Rabindranath Bag, **Koushik Karmakar** and Surjeet Singh*, accepted in Journal of Crystal Growth (2016).

3. *Floating Zone growth and magnetic properties of spinel Co_2TiO_4*, **Koushik Karmakar** Rabindranath Bag, and Surjeet Singh*, to be published (2016).

Chapter 1

Introduction

Magnetism is arguably the oldest known physical phenomena, however, it was only after the discovery of quantum mechanics in the early twentieth century that it begun to be studied in a more rigorous and formal manner. That an electron possesses a spin, which combines with its orbital motion to give rise to a net magnetic moment, was probably one of the most significant revelations of that time. Among others, *J. H. van Vleck* played a significant role in establishing the foundations of the quantum theory of magnetism of solids. However, even after hundred years of research since the inception of quantum mechanics, a complete understanding of the magnetism in solids has remained a challenging prospect. This complexity is embodied in the quantum many-body nature of the magnetic phenomena. Hence, over the years, theorists have devised simplified models to address specific classes of magnetic solids. It was probably for this reason that as early as in 1930s, *Ernst Ising*, on the suggestion of his advisor, investigated the one-dimensional Ising model. Around the same time, *Hans Bethe* developed his famous *Bethe Ansatz* to calculate the ground state and low-lying excitations of the one-dimensional antiferromagnetic Heisenberg chain, which is the cornerstone of our understanding of modern magnetism.

Quoting *H. -J. Mikeska* and *A. J. Kolezhuk* from their book-chapter on one-dimensional magnetism, "theorists were attracted by the chance to find interesting exact results without having to deal with the hopelessly complicated (case of) models in three-dimensions" [1]. The fact that one-dimensional magnetism can be realized experimentally was not given enough serious considerations in those early days and hence no experimental progress could be made for almost forty years. During the decade of the

1970s, however, experimental realizations of one-dimensional magnets begun to spring up [2].

In some three-dimensional materials comprising magnetic ions, the magnetic interactions are prevalent only along a specific crystallographic direction. Such materials are called quasi-one-dimensional magnets. The fact that quasi-1D magnets can be realized in bulk three-dimensional materials catalysed the growth of experimental research. In bulk materials, the ease of performing a diverse range of experiments motivated further research to verify theoretical models, and to explore new physics arising from various residual interactions and defects present in any real system. Widespread investigations on low-dimensional spin systems, however, had to wait for the discovery of high-temperature superconductivity in the layered cuprates. The naïve idea that one-dimensional cuprates might hold a clue to high-temperature superconductivity attracted considerable attention to the Cu based spin chain compounds. Thanks to concomitant developments in techniques for synthesizing large single crystals (for example, traveling solvent floating zone method associated with an infrared image furnace), and to the advent of novel measurement techniques including resonant inelastic x-ray scattering (RIXS) and angle resolved photoemission spectroscopy (ARPES), one-dimensional magnetism today is a thriving area of research. For reviews on experimental and theoretical advances in one-dimensional quantum magnetism we refer the reader to a comprehensive book on Quantum Magnetism edited by *U. Schollwöck, J. Richter, D. J. J. Farrel* and *R. F. Bishop* [3].

This thesis deals with the study of 1D spin $1/2$ Heisenberg antiferromagnetic (HAF) compounds Sr_2CuO_3 and $SrCuO_2$. In this chapter, our aim is to put together the basic ingredients required to understand and interpret the physical properties of quantum spin 1/2 antiferromagnetic chains. Since it is going to be a long chapter, we provide here a roadmap of the material covered. Given that there is a long history of studying spin chains, dating back to the times when laws of quantum mechanics were being formulated, the associated literature on spin chains is rather vast. Therefore, we shall cover here only those landmark developments that are directly relevant to the work reported in this thesis. We will first consider the 1D Hubbard model, which describes the electronic

correlations in a many-body interacting system. We shall show that the Hubbard model for half-filling maps onto the nearest-neighbour Heisenberg antiferromagnetic model, which describes the physics of low-dimensional cuprates. We shall then touch upon the field theoretic calculations of the bulk susceptibility of the spin $1/2$ HAF chain by *Eggert* and *Affleck*, and compare their results with those obtained by *Bonner* and *Fischer* in the thermodynamic limit. Since a good part of this thesis deals with experimental investigations of the low-energy spin excitations of antiferromagnetic spin $1/2$ chains, we will provide an adequate theoretical description of these spin excitations. We shall then provide a brief description of the phenomenon of spin-charge and spin-orbital separation in the spin $1/2$ HAF chain, both of which have been experimentally confirmed; the experimental results will be discussed. In the last section, we shall discuss the ground state of real spin-chains with examples.

1.1 The Hubbard model

Among the models of interacting electrons in condensed matter physics, the Hubbard model enjoys a special status for its simplicity and yet for providing a deep insight into the physics of strongly correlated systems. The model was originally proposed by John Hubbard in the 1960s. There are several excellent books and review articles dealing with the Hubbard model and its various extensions, and very many techniques that have been employed in the past to solve the model [see, for example, [4], [5], [6]]. In their book by Essler et al. [6], which is devoted fully to the one-dimensional Hubbard model, the authors remarked that around the same time as *Hubbard* published his research in the Proceedings of the Royal Society of London [7], the model was independently introduced by *Gutzwiller* [8] and *Kanamori* [9].

Here, we shall describe the model on a one-dimensional *Bravais lattice* of N sites with one orbital per site. The orbital can accommodate two electrons of opposite spins (up and down) allowed by the laws of quantum mechanics. However, the double-occupancy is challenged by the on-site coulomb repulsion (U), which is the energy cost to be paid for double occupancy of a given site. It should be mentioned that the

repulsion is felt only when the two electrons try to sit on the same orbital. An electron in a solid moves in a screened Coulomb potential of positive ion cores, which justify the non-inclusion of repulsion elsewhere. It is the inclusion of the on-site Coulomb repulsion, not included in the *Tight Binding model*, that results in states of very interesting, physically realizable, ground states. The model was originally introduced to understand the insulating behaviour of some transition metal oxides (for example, CoO), which the band theory (without U) predicted to have a metallic behaviour. These oxides were later called Mott Insulators to distinguish them from the ordinary band insulators. It was not until the discovery of high-temperature superconductivity that the Hubbard model gained widespread attention. The discovery of high-temperature superconductivity in a Mott insulator changed this scenario and strongly correlated electron systems became one of the most talked about subject in the condensed matter physics community. A renewed interest in the research surrounding the Hubbard model came quite recently with the realization of optical lattices of trapped cold-atoms. The Hubbard model, thus, married what was traditionally quantum optics to the condensed matter physics.

In the simple framework described above, the model can be written down as consisting of two terms: the hopping term, which causes the electron to hop between the neighbouring sites (this is also called the kinetic term); and the repulsive term (or the interaction term), which prevents double occupancy of a site due to the on-site coulomb repulsion. The strength of the Coulomb repulsion U determines the relative weight of the interaction term. On the other hand, the weight of the kinetic term is determined by the extent of the overlap of the orbitals on the neighbouring sites (the overlap integral), which is designated as t. A more rigorous definition of t will follow once the model has been written down in an algebraic form.

In the absence of U, and with a finite t, the chain would be metallic because the electrons are free to hop to their neighbouring sites. In the $U = 0$ limit, the Hubbard model in fact reduces to the familiar Tight-Binding Model, which has a metallic ground state unless the number of electrons (n) equals twice the number of sites (i.e., $n = 2N$), which fills the band completely, resulting in a band insulator.

The other extreme of the Hubbard model is reached when the hopping term goes

to zero ($t = 0$), in the presence of a finite on-site repulsion. In this case the electrons are stuck to where they belong – they are immovable; and the various lattice sites are independent of one another.

Thus, it can be argued that an electron behaves as a 'wave' in the presence of kinetic term alone; and as a 'particle' when only the interaction term is present. The wave-particle dualism that would arise if both terms of the Hamiltonian are considered together implies that even though the kinetic term and the interaction term are individually solvable, the total Hamiltonian is not. On the basis of the forgoing discussion, two important points concerning the nature of Hubbard model can be laid down: (1) the analytical solution of Hubbard model may not always be possible, (2) depending on the relative strengths of the two terms and the filling factor (i.e., no. of electrons per site), the model harbours a wide range of very interesting ground states which can be magnetic, insulating, metallic and even superconducting [4].

Before making a transition to the formal mathematical formulation of the model, let us qualitatively treat three cases of interest:

Case–I: $t \gg U$

This can be treated as a perturbation over the $U = 0$ case discussed above. Since t is appreciably large, the ensuing bands will have appreciable bandwidth (W) [we did not show it here explicitly, but it comes out of the tight binding model quite straight forwardly (see, for example, reference [10])]. If $n > N$, then after having filled-up all the sites singly, an energy barrier due to the on-site Coulomb repulsion should be overcome to add the $(N + 1)^{\text{th}}$ electron. Put in other words, at $T = 0$, the chemical potential of the system (which is the energy required to add/remove a particle) will exhibit a jump of height U, which is known as the Mott gap. Therefore, once a small on-site Coulomb repulsion is turned on, the band that was previously un-split will now split by an amount U, resulting in a Lower Hubbard Band (LHB) and an Upper Hubbard Band (UHB). The system will exhibit a metallic conductivity with high electron mobility due to wide/overlapping bands. The insulating ground state will result only for $n = 2N$, when both LHB and UHB will be completely filled. As far as magnetism is concerned,

one would not expect any preferential alignment of the spins. The system should, therefore, exhibit a Pauli paramagnetic ground state.

Case–II: $t \ll U$

This situation is most commonly encountered in transition metal oxides (CoO, NiO, etc); and, in fact, it is in this case that one comes to appreciate the real power of the Hubbard model. Starting from $t = 0$ (independent lattice sites), if one turns on a small perturbation t, narrow bands (LHB and UHB) will appear (see, figure 1.1). The ground state will be metallic for, both, $n > N$ (where the UHB is partially filled) and $n < N$ (where the LHB is partially filled). The electronic spins are expected to have both up/down orientations with equal probabilities resulting in a Pauli paramagnetic ground state.

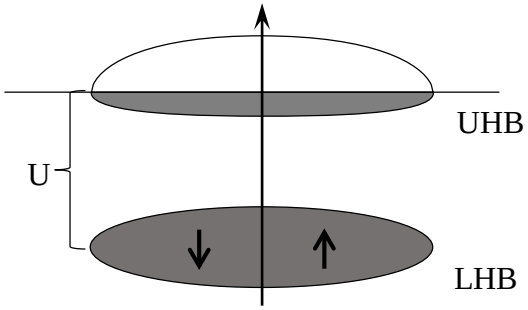

Figure 1.1: Splitting of the Hubbard band into lower and upper Hubbard bands (labelled LHB and UHB, respectively) for $t \ll U$. The shaded region is filled for n > N. The arrows indicate the orientation of the electron spin.

With this we come to the most interesting aspect of the Hubbard model that can be analysed qualitatively: the case of half-filling with $t \ll U$. What should be the ground state of the Hubbard model at half-filling? Since large U prevents double occupancy, from figure 1.1 it is straightforward to conclude that the ground state will be insulating (LHB is completely filled and UHB is completely empty with a large gap U separating the two). The electrons have no vacant states accessible to them, hence the ground state is insulating. While the question of conductivity is easily settled, the nature of magnetism will require further considerations because 't' has a non-zero value; therefore, the correct ground state cannot be decided without considering the kinetic term. In other words, had t been zero, any arbitrary orientation of the spins is as good as any

other. However, with $t \neq 0$, further considerations are necessary as discussed below. If '+' sign designates an up spin, and '−' a down spin. Then, for $t = 0$, the configurations: ... + − + + + − − + − + − + + ... or ... + + − + − − + − + + − − + ... or ..., are all degenerate in energy. On the other hand, for a non-zero t, howsoever small, it can be shown that the ground state will be antiferromagnetic [11]. That is, a state where spin orientation alternates between neighbouring sites. In our +/− notation such a state will be written as: ... + − + − + − + − + − + − + − + ... The alternating up-down configuration allows the electron to hop to their nearest neighbours intermittently which lowers the kinetic energy term. This is referred to as the virtual hopping of the electron, which lowers the energy of the alternating up/down spin configuration below any other configuration. For example, in the configuration ... − + − + − **+ + +** − + − + − +..., for the electrons in the middle '+ + +' section (shown as bold), the virtual hopping is blocked owing to the same spin orientation. Thus, a spin-flip at even one site escalates the energy over the antiferromagnetic state. Therefore, the ground state of the system has to be antiferromagnetic.

Having seen qualitatively the ground state under special cases, we will now write down the Hubbard Hamiltonian for our one-dimensional chain for a fixed number n of electrons. The Hubbard Hamiltonian can be written as:

$$\mathcal{H} = -t \sum_{\langle i,j\rangle,\sigma} \left(C^{\dagger}_{\sigma i} C_{\sigma j} + C^{\dagger}_{\sigma j} C_{\sigma i} \right) + U \sum_{i} n_{+i} n_{-i} \tag{1.1}$$

The first term, as can be easily guessed, is the kinetic energy term and the second, the interaction term. The operator $C_{\sigma j}$ annihilates an electron at the j^{th} site, which is simultaneously created at the i$^{\text{th}}$ site by the operator $C^{\dagger}_{\sigma i}$; σ is the electron spin, which can be up (+) or down (−). The symbol $\langle i, j\rangle$ in the summation is used to remind the reader that the hopping is allowed only between the nearest neighbours. The interaction term has summation index 'i' running over all the sites to add an energy U if the site is doubly occupied and zero if the site is vacant or singly occupied. In the second term 'n' is the number operator: $n_{\sigma i} = C^{\dagger}_{\sigma i} C_{\sigma i}$. Often, it is of interest to investigate the ground state for fixed values of t and U and varying n (i.e., by doping a given materials with

charge carriers). To incorporate such a possibility, a third term given by:

$$-\mu \sum_{\sigma,i} C^{\dagger}_{\sigma i} C_{\sigma i} = -\mu \sum_{i} \left(C^{\dagger}_{+i} C_{+i} + C^{\dagger}_{-i} C_{-i} \right) = -\mu \sum_{i} n_{+i} n_{-i} \tag{1.2}$$

can be included in the Hamiltonian. Typical values of t and U in various strongly correlated materials varies from $0.25 - 0.5$ eV and $2 - 10$ eV, respectively.

1.1.1 Half-filled Hubbard model

Since half-filling fixes the number of electrons to $n = N$, the chemical potential term is not required in the Hamiltonian. Further, since U is large, the states with double occupancy will be suppressed. The contribution of the interaction term to the total energy, therefore, vanishes for this case (assuming that the singly occupied sites have zero energy). As mentioned before, were it not for the kinetic term, these various spin configurations will all be degenerate. It is easy to show, using the degenerate perturbation theory (since t can be treated as a small perturbation over the degenerate large U ground state) that hopping removes the degeneracy and favours an antiferromagnetically ordered ground state over the ferromagnetic one by an energy $4t^2/U$ (see, for example, reference [11]). Therefore, it follows that the half-filled (one electron per site) system is a Mott insulator with an antiferromagnetic ground state. The antiferromagnetism is favoured because oppositely aligned alternating spin arrangement allows virtual hopping of the electron to its neighbours resulting in an energy gain $4t^2/U$. This is called the exchange energy J. Thus, the Hamiltonian of the Hubbard model at half-filling in the strong U limit can be mapped onto the Heisenberg model with $J = 4t^2/U$: i.e.,

$$\mathcal{H} = -J \sum_{\langle i,j \rangle} \boldsymbol{S}_i \cdot \boldsymbol{S}_j \tag{1.3}$$

(see, for example, reference [12]).

1.1.2 Transition metal oxides

In describing the physics of cuprates, some new concepts needs to be introduced. In fact, in any Transition Metal Oxide (TMO), the minimum model should have two transition metals ions bounded together via an intervening oxygen ion. Cuprates form a special case with d^9 electronic configuration of Cu^{2+} commonly present in the Cu based oxides; and are grouped in the category of 'late' TMOs. This distinction between 'early' and 'late' TMOs will become clear as we go further. Returning to the point, an apt description of the TMOs, therefore, require introduction of new energy scales: the charge transfer integral $\Delta = E_d - E_p$, which is the energy required to transfer an electron or a hole from the d band of transition metal (energy E_d) to the p band of ligand (energy E_p); and the transfer integral t_{pd}, which is proportional to the metal-ligand hybridization.

We shall now consider two cases corresponding to the two types of Mott insulators:

Case I: $U < \Delta$

The resulting bands are shown in figure 1.2. The p-band of the ligand is lower in energy than the LHB. In this case the p-band of the ligand is essentially passive and the oxygen p-orbital contributes only through virtual processes [12]. The nature of the ground state is, therefore, governed by the relative strength of U and W, as in the original Hubbard model. Here, W is the bandwidth, if W exceeds U, the resulting state will be metallic. On the other hand, if the on-site Coulomb interaction is stronger than the bandwidth, the resulting ground state will be insulating (as shown in the right panel of figure 1.2). This type of TMOs are known as Mott-Hubbard-type insulators. Examples include: TiO, Cr_2O_3, $LaTiO_3$, $LaCrO_3$, etc.

Case II: $U > \Delta$

In the late TMOs, such as, CuO and NiO, the p-band of the ligand is sandwiched between the UHB and LHB, resulting in $U > \Delta$. Naively speaking, the large nuclear attraction that the d-electrons experience due to the fact that d-shell in late TMOs is close to being completely filled, escalates the energy required for a d_n to d_{n-1} transition. Therefore, an added hole in the Mott insulator preferably occupies the ligand

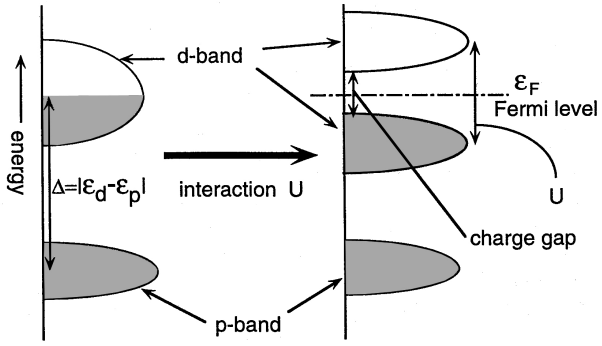

Figure 1.2: Schematic band diagram showing the characteristic bands and corresponding energies in a Mott-Hubbard type Insulator. Left ($U = 0$): The completely filled p-band of the ligand and the half-filled d-band of the transition metal, separated by a gap Δ. The ground state is metallic. Right ($U \neq 0$): Due to a non-zero U, the d-band splits into a completely filled Lower Hubbard Band (LHB) and an empty Upper Hubbard Band (UHB). The ground state is insulating. However, if $U < W$, a metallic state is possible [12].

p-band, as pointed out by Fujimori and Minami [13, 14]. The strong hybridization between the transition metal d-and oxygen p-orbitals results is strong covalancy that pushes the oxygen $2p$ orbital closer to the Fermi level (see, figure 1.3). On top of it, a large value of U causes LHB-UHB splitting to exceed Δ, giving rise to the so-called Charge-Transfer-Type Mott Insulators. Examples of this class of Mott insulators include, CuO, NiO, La_2CuO_4, Sr_2CuO_3, etc.

Based on a rigorous experimental analysis of the x-ray photoemission spectroscopy data of several TMOs, *Bocquet et al.*, [15, 16] plotted U Vs. Δ normalized by an effective one-electron mixing matrix element (T_{eff}) defined by the hybridization of the $3d$ orbitals and ligand p-orbitals. From this diagram (see, figure 1.4) one can see that most of the 'late' TMOs are *Charge-Transfer-type*, whereas the early TMOs are *Mott-Hubbard-type* and that the compounds falling close to the line $U = V$ are intermediate between these two regimes.

1.1.3 Cuprates

We shall now discuss the case of cuprates which is the main topic of this thesis. The topic is extensively covered in several excellent review articles. The contents presented

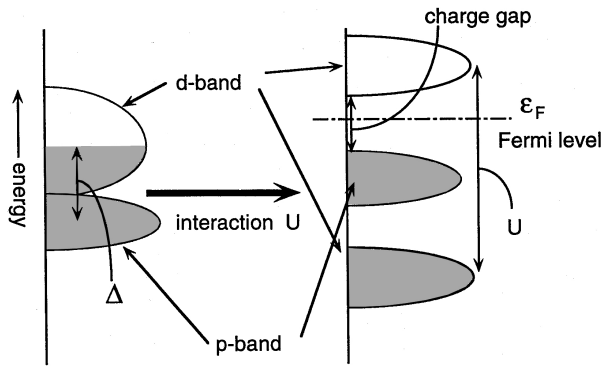

Figure 1.3: Schematic band diagram showing the characteristic bands and corresponding energies in a Charge-transfer-type Mott Insulator. Left ($U = 0$): As before, the ground state is metallic since $U = 0$. However, the crucial difference here, with respect to the left panel in figure 1.2, is that the p-band is shifted-up closer to the Fermi energy due to a strong covalancy. Right ($U \neq 0$): The splitting of the d-band is so pronounced (due to large U), that LHB sinks below the p-band. As a result, the doped holes go to the p-band in accordance with the charge gap Δ being smaller than U [12].

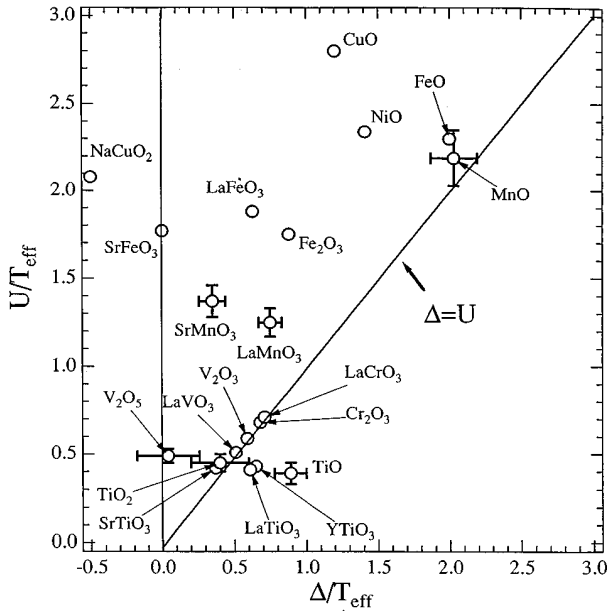

Figure 1.4: Δ Vs. U plot for several TMOs. Δ and U have been normalized by the effective hybridization strength T_{eff}. The region above the line $\Delta = U$ is the charge-transfer regime, while that below it is the Mott-Hubbard regime. Noteworthy is the example of CuO that lies deep in the Charge-Transfer regime [12].

here are taken mainly from the review article dealing with Metal-Insulator transition in TMOs by *Imada et al.* [12] and the high-temperature superconductivity in cuprates by *Lee et al.* [17]. Cuprates are compounds based on CuO. In the present day context, the term '*cuprate*' has been reserved for high-temperature superconductors and their structurally analogue relatives based on CuO. Prototypical examples of cuprates are La_2CuO_4 which is the parent compound of all the high-temperature superconductors and Sr_2CuO_3, which is derived from La_2CuO_4 by complete replacement of trivalent La by divalent Sr ion, resulting in one less oxygen per formula unit and hence a reduced magnetic dimensionality. La_2CuO_4 has the K_2NiF_4-type layered crystal structure where each Cu^{2+} is octahedrally coordinated by the oxygen ions. Since Cu^{2+}, having 9 electrons in the $3d$ orbitals is Jahn-Teller active, the oxygen octahedra tend to be apically elongated, as shown in figure 1.5. In Sr_2CuO_3, the Cu^{2+} coordination is square-planar. In the presence of the ligand crystal electric field, the degeneracy of the d-orbitals is partially removed. Figure 1.5 shows how the d-orbitals split into e_g (two-fold degenerate $x^2 - y^2$ and $3z^2 - r^2$ orbitals) and t_{2g} orbitals (three-fold degenerate xy, yz and zx orbitals) in the presence of an octahedral crystal electric field. The apical elongation of the octahedra (shown by arrows), further splits the e_g and t_{2g} orbitals. Due to the stretched octahedra along the z-axis, it is convenient to think of the structure of La_2CuO_4 as a layered structure, the layers being spread-out perpendicular to the stretched Cu-O bond, which is taken to be parallel to the z-axis in our notation.

In the xy plane, the $x^2 - y^2$ orbital has its lobes pointing directly toward the neighbouring oxygen ions. An electron in the $x^2 - y^2$ orbital, therefore, experiences the maximum electrostatic repulsion which makes it the highest lying crystal field split energy level in any symmetry lower than orthorhombic. The $x^2 - y^2$ orbital also strongly hybridizes with the p_x/p_y orbitals of the neighbouring oxygen, forming a strong covalent bond with a large hopping integral t_{pd}, which is the primary reason why the exchange integral (J) in cuprates is exceptionally large (about 1300 K in La_2CuO_4 and 2400 K in Sr_2CuO_3).

With one electron in the highest occupied $x^2 - y^2$ orbital, the system faithfully conforms to the Mott picture for one electron per site. The undoped compounds La_2CuO_4

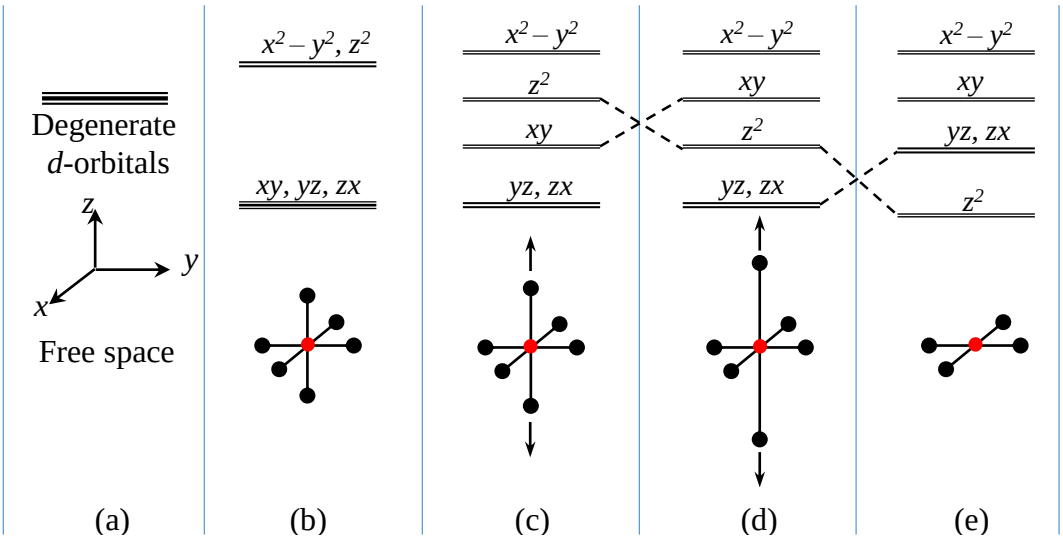

Figure 1.5: Crystal field splitting of the d-orbitals. (a) In the free space, the orbitals are five-fold degenerate. (b) Splitting into t_{2g} (lower) and e_g in the presence of an octahedral crystal electric field. From (c) to (e), the effect of lowering of the symmetry due to the octahedral elongation caused by the movement of the aplical oxygen ions. In (e), the apical oxygen ions have been completely removed resulting in a square-planar geometry characteristic of the Cu based spin chains compounds.

or Sr_2CuO_3 are, therefore, examples of half-filled Hubbard model with an antiferromagnetic ground state. As mentioned previously, the strong p-d hybridization in these compounds pushes the oxygen p-orbitals closer to the Fermi energy, which, combined with the fact that the on-site coulomb repulsion U in cuprates in rather large, makes them the *charge-transfer-type Mott insulators*.

Analogous to one-state Mott-Hubbard insulator, where the virtual hopping of electrons leads to an antiferromagnetic exchange interaction J between the neighbouring spins of strength $4t^2/U$, the spins on the neighbouring Cu sites in cuprates interact antiferromagnetically via the intervening oxygen ion. The process involves virtual hopping of electrons of the adjacent Cu ions to the intervening oxygen p-orbital. If we ignore the on-site coulomb repulsion for occupying the p-orbital, the exchange integral is roughly given by $J \approx t_{pd}^4/\Delta^3$, where we have considered an equivalent hole picture, such that, the lowest energy excitation consists of a hole hopping from d to p with amplitude $-t_{pd}(E_p > E_d)$. Such an exchange, which is mediated via a virtual hopping through the intervening anion is known as *superexchange* interaction and is the dominant exchange mechanism in most TMOs.

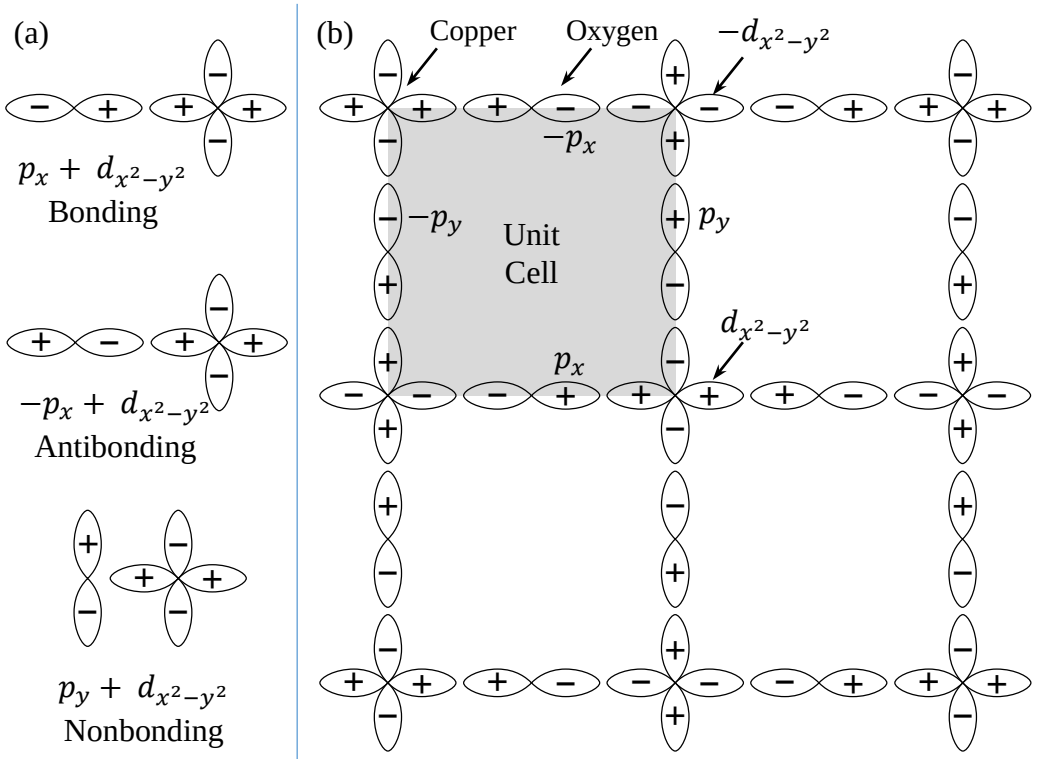

Figure 1.6: (a) Examples of bonding, antibonding and non-bonding configurations involving the $d_{x^2-y^2}$ with p_x and p_y orbitals. (b) Orbitals involved in the bonding of Cu-O plane in a low-dimensional cuprates, which includes the $d_{x^2-y^2}$ orbitals of the Cu ions and the p_x and p_y orbitals of the oxygen ions. The shaded region indicates a unit cell with contains each types of these ions and hence contains one of each type of orbitals [11].

If additional holes are doped in the Cu-O layer of La_2CuO_4 (which can be conveniently done by replacing La^{3+} by Ba^{2+}), the large on-site U prevents the additional hole from occupying the Cu site. The doped hole, therefore, resides on the oxygen p-orbitals. In fact, it resonates on the four oxygen ions surrounding the central Cu^{2+}. The spin of the doped hole combine with the spin of central Cu^{2+} ion, to form, what is known as the Zhang-Rice singlet [18]. The Zhang-Rice singlet itself can hop from one site to the other rendering the sample electrically conducting. The effective hopping integral is of the order $J = t_{pd}^2 / \left(E_p - E_d\right)$.

1.2 One-dimensional Heisenberg magnets

The 1D Heisenberg model is generally regarded as cornerstone of the quantum magnetism. Considering nearest-neighbour interactions, the Heisenberg Hamiltonian for a spin chain can be written as:

$$\mathcal{H} = J \sum_{\langle i \rangle} \boldsymbol{S}_i \cdot \boldsymbol{S}_{i+1} \tag{1.4}$$

Here, we have assumed the exchange interaction 'J' to be same all throughout the chain, i.e., the chain is assumed to be uniform, and $\boldsymbol{S}_i$ denotes the spin operator at the i$^{\text{th}}$ lattice site. In the so-called XXZ model, the Hamiltonian above can be written as;

$$\mathcal{H} = J \sum_{i} \left[\left(S_i^x S_{i+1}^x + S_i^y S_{i+1}^y \right) + \Delta S_i^z S_{i+1}^z \right] \tag{1.5}$$

Where, S^x, S^y and S^z are the Cartesian components of the spin operator $\boldsymbol{S}$, and Δ is the exchange anisotropy parameter. For $\Delta = 1$, the model becomes the isotropic Heisenberg model, while in the limit $\Delta \to \infty$ it represents the Ising model. And, for $\Delta = 0$ the spin are constrained to lie in the xy-plane and accordingly the model is called the XY model.

The magnetic behaviour of the isotropic spin-system depends on the dimensionality. While magnets with 3D arrays of interacting spins do show a magnetic ordering at $T > 0$; in the 2D and 1D cases no long-range-magnetic ordering is expected even at $T = 0$ (except for the 2D Ising case which does show an ordered state at $T = 0$)[19, 20]. The absence of magnetic ordering in these cases is attributed to the quantum spin fluctuations [20–22]. In equation 1.5, if $J < 0$, the spins tend to align in the same direction, the coupling is, therefore, ferromagnetic. If $J > 0$, the spins favour antiparallel arrangement and the exchange coupling is said to be antiferromagnetic. Here, we shall focus on the antiferromagnetic case. In most real systems the antiferromagnetic interaction is more frequently encountered than the ferromagnetic interaction. Moreover, in the antiferromagnetic case the distinction between the classical and the quantum systems is rather stark.

The absence of a long-range magnetic ordering in the 1D case can be qualitatively understood based on the following argument. Consider a 1D chain consisting of N sites,

each site of this lattice is occupied by a spin 'S'. Assume for the time being that the spins exhibit a long-range order (for definiteness, assume the order to be antiferromagnetic, i.e., $J > 0$). The spin arrangement in the ground state is as shown in the figure below:

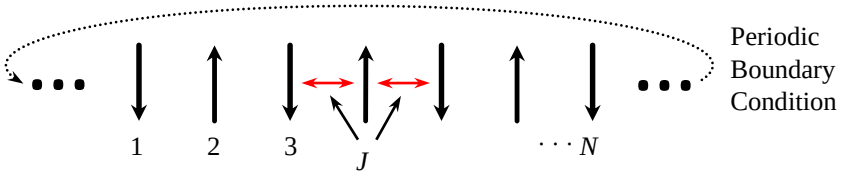

The energy cost of flipping a spin is $2JS^2$. Since the spin flip can take place at any one of the N sites, the resulting increase in the entropy of the system will be of the order of $k_B \ln N$. Therefore, the flipping of a spin increases the free energy (F) by an amount $4JS^2$, and decreases it by an amount $k_B \ln(N)$. The overall change of the free energy is, $\Delta F = 4JS^2 - k_B \ln N$. Evidently, for large enough N, ΔF is going to be negative, because the entropy term scales as $\ln N$. Since, the ground state of a thermodynamic system has the lowest free-energy, the above considerations show that the ground state of a spin-chain favours spontaneous spin-flips rather than a long-range ordering. In particular, in a spin $1/2$ chain, where the quantum fluctuations are significantly pronounced, the ground state remain disordered even at zero temperature.

In the quantum treatment of the problem, it is convenient to rewrite the isotropic Heisenberg Hamiltonian (equation 1.4 for $\Delta = 1$) in terms of the ladder operators ($\boldsymbol{S}^{\pm} = \boldsymbol{S}^x \pm i\boldsymbol{S}^y$):

$$\mathcal{H} = J \sum_i \frac{1}{2} \left(S_i^+ S_{i+1}^- + S_i^- S_{i+1}^+ \right) + S_i^z S_{i+1}^z \tag{1.6}$$

Let us consider the case of ferromagnetic and antiferromagnetic exchange separately.

Ferromagnetic case ($J < 0$):

In the ferromagnetic case the ground state will be $\psi_G = |+ + + + \cdots +\rangle$, i.e., the state where all spins point up. Now, it is easy to show that $\mathcal{H}\psi_G^{FM} = \varepsilon\psi_G^{FM}$ where $\varepsilon = JNS^2$ (N =number of spins), i.e., $|+ + + + \cdots +\rangle$ is an eigenstate of $\mathcal{H}$. For the ferromagnetic state to be stable it is necessary that the fluctuations generated by the associated *Goldstone modes* do not destroy the order. The existence of Goldstone modes can be shown

rigorously. However, here it is sufficient to note that the state $\psi_j = |+ + + \cdots - \cdots\rangle$ with a single spin flip $(-)$ at j^{th} site is not an eigenstate of the Hamiltonian $\mathcal{H}$. However, a true eigenstate of $\mathcal{H}$ can be constructed by taking a linear combination of ψ_j's:

$$\text{i.e.,}\psi = \sum_j \lambda_j \psi_j \tag{1.7}$$

where, λ_j's are coefficient given by $C_k e^{ik_j}$ and the corresponding energy eigenvalues are,

$$\varepsilon_k = -4JS^2\,(1 - \cos(qa)) \tag{1.8}$$

where 'k' is the wave vector = $2n\pi/N$.

To conclude, if J is negative the ground state is ψ_G^{FM}, where all spins point in the same direction (i.e., ferromagnetic). The elementary excitations are gapless spin waves or magnons with energy ε_k.

Antiferromagnetic ($J > 0$):

This case is more interesting because in this case the quantum fluctuations destroy the long-range ordering even at $T = 0$, which is what we shall show next. The long-range antiferromagnetic ground state can be written as: $\psi_G^{AFM} = |\cdots + - + - + - + - \cdots\rangle$. It is easy to see that the state ψ_G^{AFM} is not an eigenstate of $\mathcal{H}$. Therefore, it is not the *true* ground state. The nature of the ground state will be better grasped once the magnetic excitations are discussed. Briefly, the ground state exhibits a quasi-long range ordering consisting of antiferromagnetic domains, but with dynamical domain-walls, i.e., the antiferromagnetic domains constantly rearrange and the system exhibits non-zero spin-dynamics even at zero temperature. In this quasi-long-range ordered state, the spin-spin correlation show a power law dependence

$$\left\langle S_i^\alpha S_j^\beta \right\rangle = (-1)^r \delta^{\alpha\beta} \frac{\sqrt{\ln r}}{r} \tag{1.9}$$

where $\alpha, \beta = x, y, z$ and r in the distance between the spins at the ith and the jth site [23].

1.2.1 Magnetic excitations: *Spinons*

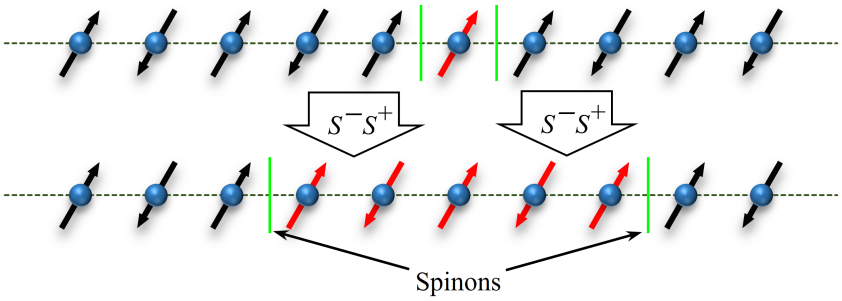

Figure 1.7: A spin excitations consist in flipping a single spin, which creates two spinons, the domain walls separating two AFM ordered domains, on the either side of the effected spin. The spinons then propagate in counter direction through spin flip operation with out costing any energy [24].

The Magnetic excitations in the 1D Heisenberg chain are as interesting as its magnetic ground state. The elementary excitations of a spin 1/2 HAF chain are associated with the domain-walls separating two ordered domains. In an inelastic neutron scattering event, the flipping of a single spin causes two domain-walls to appear on either side of the affected spin. The domain walls then move independently in the counter directions along the length of the chain without costing any energy (see figure 1.7). These domain walls are the elementary excitations of the spin 1/2 Heisenberg AFM chain and are called *spinons* [25]. In contrast with the magnons, spinons are created in pairs and are spin 1/2 fermions. Spinons are examples of fractional excitations and can be detected in an inelastic neutron scattering experiment. The dispersion relation for a single spinon is given by:

$$\omega(k) = \frac{\pi|J|}{2}\,|\sin(ka)|\,, \tag{1.10}$$

where J represents the intra-chain exchange and a is the lattice parameter. The relation 1.10 was obtained by Cloizeaux and Pearson [26], though it's correct interpretation as being the dispersion of a spinon was first described by Faddeev and Takhtajan [25].

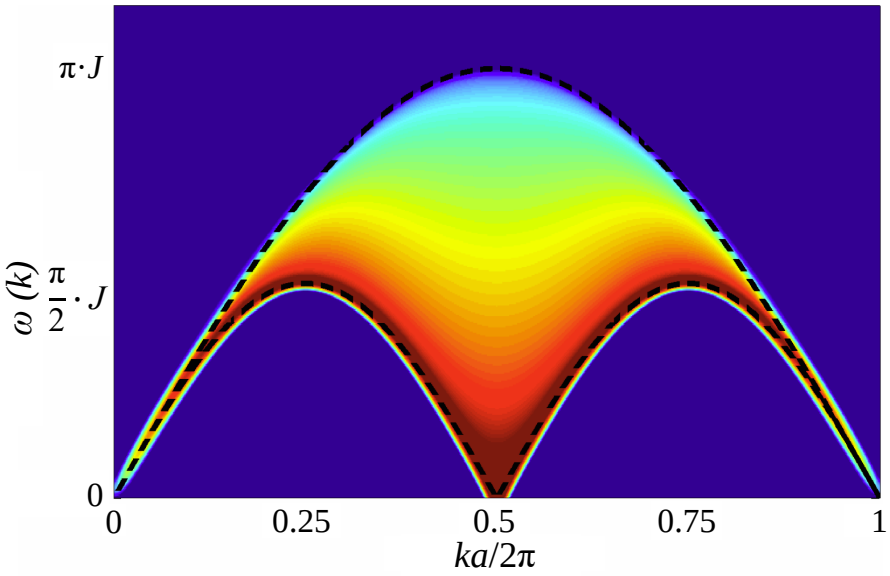

Figure 1.8: The two-spinon-continuum of the isotropic spin 1/2 HAF-chain. The lowest continuum limit corresponds to the dispersion of one spinon given by equation 1.10.

In an excitation pair of spinons, the total momentum $k = k_1 + k_2$ and energy $\hbar\omega = \hbar\omega_1(k_1) + \hbar\omega_2(k_2)$ give rise to a *two-spinon-continuum* in the dispersion diagram of $\omega(k)$ (figure 1.8).

1.3 Spin 1/2 antiferromagnetic Heisenberg model

1.3.1 Bulk magnetic susceptibility

One of most extensively used techniques to realize the magnetic behaviour of a $S = 1/2$ Heisenberg AFM chain is through bulk magnetic susceptibility $\chi(T)$. In a pioneering work done in 1964, *Bonner* and *Fisher* calculated $\chi(T)$ of the S = $\frac{1}{2}$ HAF chain [27], The numerical results for $\chi(T)$ were obtained for chains containing up to 11 spins subject to the periodic boundary condition and for temperatures $T \geq 0.4J/k_B$. A close approximation to the Bonner-Fisher numerical results had been suggested by *Estes et al.*, which can be expressed as [28];

$$\chi_{\mathrm{BF}} = \frac{Ng^2\mu_B^2}{4k_BT}\left[\frac{0.25 + 0.14995x + 0.30094x^2}{1 + 1.9862x + 0.68854x^2 + 6.0626x^3}\right] \tag{1.11}$$

where, $x = |J|/k_BT$, J is the intrachain nearest neighbour exchange and k_B is the Boltzmann constant. These results revealed a broad susceptibility maximum near $T = 0.675J/k_B$. At lower temperatures, the susceptibility decreases below the maximum value due to the gradual appearance of large antiferromagnetic domains characterised by the domain-wall-like spin $1/2$ excitations called the spinons discussed earlier. Because of the quantum fluctuations, the domain-wall dynamics persist down to zero temperature. Therefore, the ground state of the spin $1/2$ HAF chain is characterised as a spin-liquid in which the spin-correlations decay as a power law [29] and the zero-temperature susceptibility $\chi(0)$ has a finite value, which can be calculated exactly using the Bethe Ansatz [30]. The numerical result of Bonner and Fisher (BF) has been used extensively by experimentalist to fit the magnetic susceptibility of quasi 1D compounds, and in the determination of the coupling constant J. Later, the work of Bonner and Fisher was extended to longer chains and down to lower temperatures [31–35]. However, the numerical results calculated by this method are accurate only at temperatures $T/J \geq 0.4$. The $\chi(T)$ behaviour at lower temperatures, where the BF results are not accurate, was investigated separately by Eggert, Affleck and Takahashi (EAT) using the numerical Bethe Ansatz ($T \geq 0.003J/k_B$) and field-theory methods[36]. The calculated $\chi(T)$ was also compared with the $\chi(T)$ obtained using the conformal mean field theory, and the two were found to be in excellent agreement for $T/J \geq 0.003$. The magnetic susceptibility obtained by EAT was found to be roughly 10% higher than the Bonner and Fisher extrapolation of $\chi(T)$ to low-temperatures ($T/J \leq 0.25$ (see figure 1.9)). The conformal field theory calculations of EAT showed that to the leading order correction, the zero temperature limit of the susceptibility is of the form [36],

$$\chi(T) \approx \frac{1}{J\pi^2}\left(1 + \frac{1}{2\ln(T_0/T)}\right) \tag{1.12}$$

where the scaling temperature T_0 had been estimated from the log terms called the "*logarithmic corrections*". The expression 1.12 yields highly accurate results for $\chi(T)$ at low temperatures. The temperature variation of the susceptibility obtained by EAT showed a surprisingly rich behaviour with the existence of an inflection point near $T =$

$0.087 J/k_B$, below which the slope of $\chi(T)$ increases rapidly approaching infinity as T goes to zero.

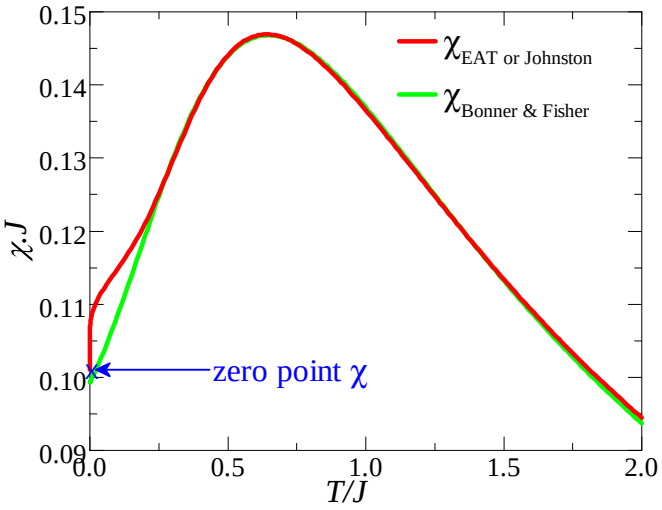

Figure 1.9: Magnetic susceptibility $\chi(T)$ of the 1D spin 1/2 Heisenberg antiferromagnetic chain. The green curve given Bonner-Fisher results calculated using equation 1.11. The red curve gives the EAT results given in equation 1.12 (see text for details).

Lukyanov extended the analytical calculation of EAT and presented an exact theory for the magnetic susceptibility at low T, which also predicts the exact value of T_0 [37]. The expression for $\chi(T)$ obtained by *Lukyanov* is given by [38]:

$$\chi(T) = \frac{1}{2J\pi^2}\left[1 + \frac{g}{2} + \frac{3g^2}{32} + \sqrt{3}\pi T^2\right] \tag{1.13}$$

where g is the running coupling constant which depends on temperature only and can be expressed as,

$$g^{-1} + \frac{1}{2}\log(g) = \log\left(\sqrt{2\pi}e^{\gamma+1/4}J/T\right)$$

where $\gamma = 0.577216...$ is the Euler constant. Highly accurate numerical results for $\chi(T)$ were obtained by *Klümper* and *Johnston* to reach an absolute accuracy ($O(1 \times 10^{-7})$) over a temperature range of $5 \times 10^{-25} \leq T/J \leq 5$ [39, 40]. *Klümper et al.* derived exact nonlinear integral equations involving just two functions describing the elementary excitations in order to calculate the exact values for the $\chi(T)$ [39]. It is often useful to employ the fit functions obtained by *Johnston et al.* by fitting the magnetic

susceptibility obtained using the *Numerical Bethe Ansatz*. The fit function that yields highly accurate values of the chain susceptibility in the temperature range $0.01J < T < 5J$ is given by [40]:

$$\chi_{\text{Johnston}} = \frac{1}{4T}\left[\frac{1+\sum_{n=1}^{q}\frac{N_n}{(T/J)^n}}{1+\sum_{n=1}^{r}\frac{D_n}{(T/J)^n}}\right] \tag{1.14}$$

Here, the values of N_n's and D_n's can be taken from reference [40]. The result of χ_{Johnston} are shown in figure 1.9, which matchs nicely with the numerically calculated values.

1.3.2 Separation of spinon, holon, and orbiton

The low-energy physics of antiferromagnetic spin $1/2$ chain is dominated by uncoupled collective modes of spin and change excitations, shown as early as 1968 by *Leib* and *Wu* [41]. One of the unique characteristics of the quantum spin $1/2$ chains is the separation of the electron's internal degrees of freedom (charge and spin). Experimentally, it was verified that the low-energy excitations are not the spin $1/2$ quasi-particle with charge e^- as in the ordinary Fermi liquid, instead they are uncoupled collective modes of spin and charge excitations called *spinons* and *holons*. The phenomena of fictionalization of electronic charge and spin into holons and spinons was realised by Kim et al. [42] in their angle resolved photo-emission spectroscopy (ARPES) experiments in the 1D spin $1/2$ Heisenberg chain compounds $SrCuO_2$ and $Sr_2CuO_2Cl_2$. The process of separation of spinon and holon is schematically shown in figure 1.10(a). The removal of an electron from the chain site by the external radiation $h\nu$ creates a hole, which has both the electronic attributes of spin $1/2$ and charge e. However, if that is the case then only a single branch is expected to be seen in the excitation spectrum. In experiments, however, one observes distinct branches corresponding to the spin and charge degrees of freedom. The transverse exchange term in the Hamiltonian 1.6, allows hopping of electron from the neighbouring site to fill up the hole, thereby creating a shift of the charge (holon) by one lattice site. Simultaneously, a domain-wall like excitation gets

created which propagates in the opposite direction under the influence of transverse exchange interaction term in 1.6. This picture has been realized through the appearance of two branches in the ARPES spectra by Kim et al. [42].

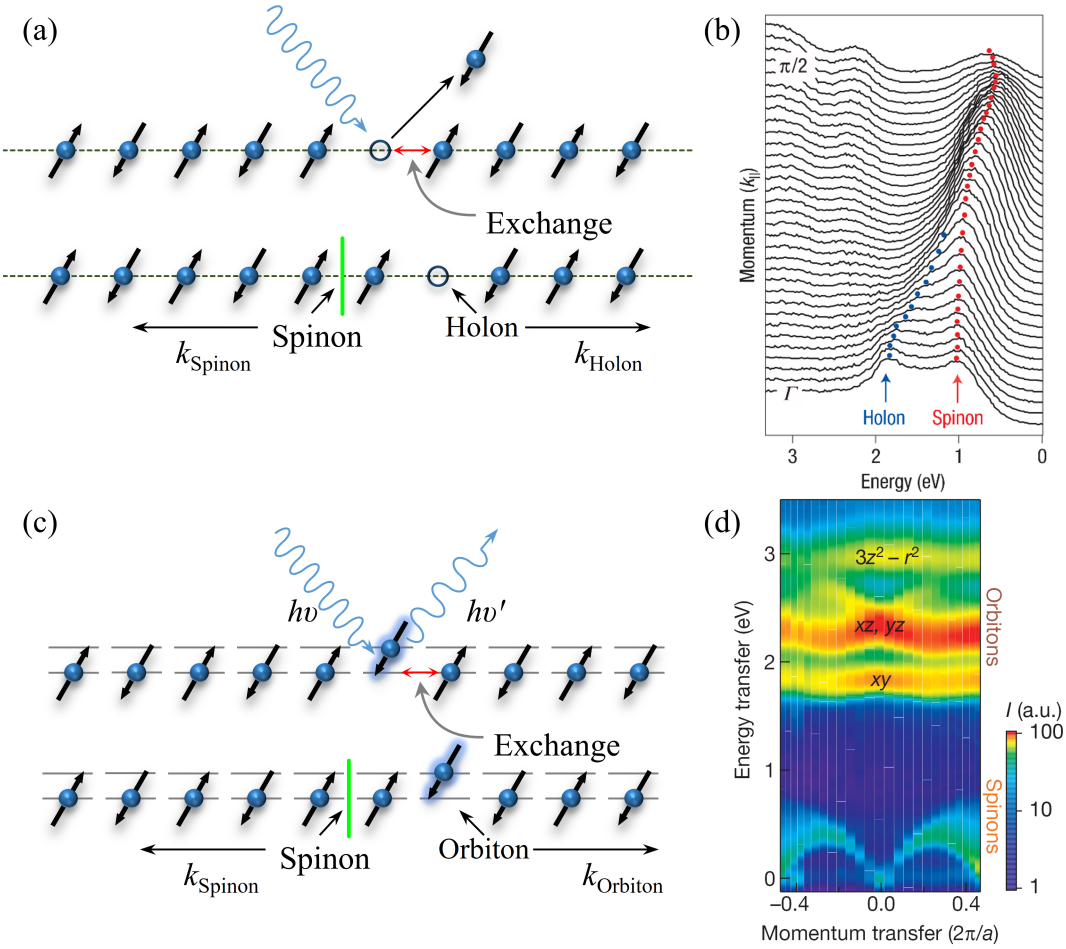

Figure 1.10: (a) Schematic diagram for an illustration of the spinon-holon separation, (b) electron photo-emission spectroscopy spectrum showing holon and spinon peaks at different energies of $SrCuO_2$ [42]. (c) The process of spinon-orbiton separation shown schematically (d) resonant-inelastic x-ray scattering experiment results showing various orbital excitations of Sr_2CuO_3 [43].

Since, in the atomic state, electron also has an additional orbital degree of freedom; recent theories and subsequent experiments show that in the antiferromagnetic Heisenberg spin 1/2 chains, spin and orbital excitation can also be separated as independent excitations [42, 44–47]. Very recently *Schlappa et al.* observed the separation electronic excitations into two quasi-particles: spinon and *orbition* (the quasi particle associated with the orbital excitation). This was done using resonant inelastic x-ray

scattering (RIXS) experiments on the single crystals of quasi 1D Heisenberg antiferromagnet, Sr_2CuO_3 [43]. A schematic diagram of the process is shown in figure 1.10(b). In contrast with the ARPES experiments, in RIXS an electron is excited from one Cu $3d$ orbital to another to create an orbiton. And, in a manner similar to that of the spinon-holon separation, the orbiton creation is accompanied by a spinon, both of which separate out by propagating in the opposite directions along the chain length, hopping from one lattice site to the next. The experimental results showing distinct orbiton and spinon dispersion branches is shown in the panel (d) of figure 1.10.

1.3.3 Magnetic ordering in real spin chain compounds

From the Mermin-Wagner theorem [19] we know that the isotropic spin chains do not favour a state with broken time reversal symmetry. However, in real 1D compounds, a finite inter-chain coupling ($J_\perp$), howsoever weak, is always present (see table 1.1). In the presence of a finite $J_\perp$, the system enters a long-range ordered state when cooled to sufficiently low-temperatures ($T \sim J_\perp/k_B$). This dimensional cross-over is commonly observed in almost all the spin-chain compounds. At low-temperatures, but well above $J_\perp/k_B$, the system exhibits a good one-dimensionality and as the temperature is lowered close $J_\perp/k_B$, the one-dimensional characteristics gradually disappear giving way to 3D spin-spin correlations. These handwaving considerations can be made rigorous by treating the interchain coupling within the mean-field approximation [48, 49]. Using this mean-field approach, *Schulz* gave a coherent description of the ordered state and derived an expression for the 3D transition temperature (T_N) for weakly coupled chains[50], given by;

$$|J_\perp| = \frac{T_N}{4A \ln^{1/2}(\Lambda J/T_N)} \tag{1.15}$$

Where the parameters A and Λ were calculated numerically [51]; $A \approx 0.32$ and $\Lambda \approx 5.8$. The results show a reasonably good agreement with the experiments. This has been demonstrated in the case of 1D compound $KCuF_3$ in references [52] and [53].

Table 1.1: Some examples of 1D $S = 1/2$ Heisenberg antiferromagnets.

Compound	$J_{\parallel}$ (K)	$J_{\perp}$ (K)	T_N (K)	Refs.
Sr_2CuO_3	2200	9	5	[54–56]
$SrCuO_2$	2100	9	< 2	[54–57]
Ca_2CuO_3	1850	42	9	[58]
$CuGeO_3$	127	12.7	4.5	[59–61]
$Sr_2Cu(PO_4)_2$	187	3	0.085	[62, 63]
$K_2CuP_2O_7$	196	0.25	< 2	[64]
$CuSe_2O_5$	165	20	17	[65]
Bi_2CuO_4	10	6	42	[66, 67]

The real spin systems are also sensitive to *Peierls* instability, which causes the spin chains to open up a gap in the excitation energy. The Peierls instability occurs due to strong coupling between the electronic spin and lattice vibrations, which leads to a modulation of the magnetic exchange coupling due to a periodic alteration of the bond length as shown in figure 1.11. The distortion in the lattice structure is favoured because the magnetic energy gained upon dimerization overwhelms the elastic energy cost due to distortion. The name spin-Peierls reflects the similarity with the Peierls distortion, associated with 1D spinless electron gas[24, 68, 69].

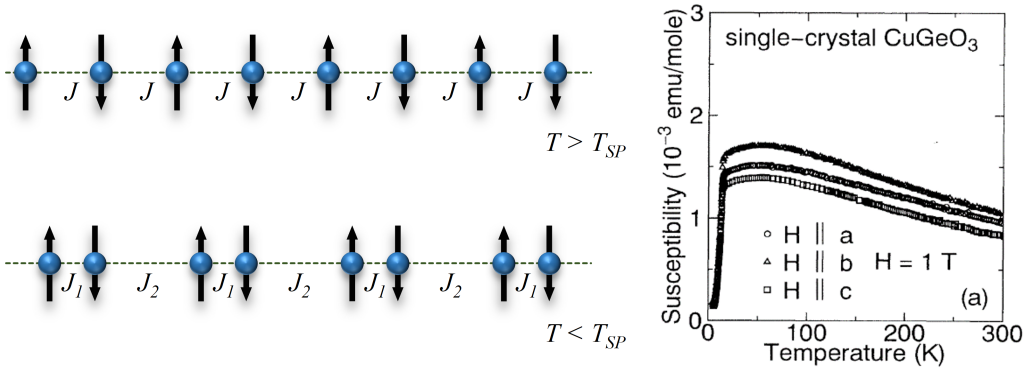

Figure 1.11: (Left) Schematic representation of the spin-Peierls transition (adapted from Stephen Blundell [69]. Above T_{SP} the spin system possesses an uniform AFM exchange (J). Below T_{SP} an alternating modulation of magnetic exchange J_1 and J_2 ($J_1 > J_2$), leads to the formation of spin singlets. The magnetic susceptibility shows an exponential decrease due to opening of a gap in the spin excitations (right panel).[70]

As schematically shown in the left panel of figure 1.11 above the spin-Peierls transition temperature, the spin 1/2 chain possesses a uniform antiferromagnetic exchange

coupling (J) and for $T < T_{SP}$ the elastic distortion, favoured by a gain in the magnetic energy, introduces an alternating uneven exchange coupling J_1 and J_2 ($J_1 > J_2$). The uneven J's leads to the formation of a spin-singlet ground state through dimerization causing the spin-excitations to become gapped. Due to the formation of the spin-singlets, magnetic susceptibility in the spin-Peierls phase decrease exponentially below $T = T_{SP}$ (see, right panel of figure 1.11). This behaviour has been observed in very for compounds due to large elastic energy cost involved. The inorganic spin chain compound, therefore, prefer a long-range ordered state at low-temperature, which forbids the Peierls instability to set in. Examples of compounds showing spin-Peierls transition are $CuGeO_3$ [70] and TTF-$CuS_4C_4(CF_3)_4$ (TTF is tetrathiafulvalene) [71], where the spin-phonon coupling dominates over the spin-spin coupling and allow spin-Peierls transition (T_{SP} = 14 K and 10 K, respectively) to set in.

Chapter 2

Disorder in Quantum Spin 1/2 Chains

Due to the one-dimensional nature of the magnetic correlations, even the slightest of disorder in the 1D spin-systems can have profound effects on their physical properties. The magnetic excitations in a 1D chain cannot avoid or bypass a defect-site. Consequently, defected chains, even for small defect concentrations, are expected to have considerable influence on the magnetic excitations. In real spin chains, at temperatures below $J_\perp/k_B$, the long-range Néel ordering temperature also exhibits a strong sensitivity to the presence of defects in a spin chain. The current chapter is intended to provide a brief review of some important results on disordered spin chains. Some of the results presented will be used in the later chapters (chapter 6, 7, and 8) for data analysis.

2.1 Disorder in the spin $1/2$ Heisenberg antiferromagnetic chains

Disorder in quantum spin chains is of significant interest for several reasons:

(1) disorder site in the spin chain cannot be bypassed by the elementary excitations -consequently, any kind of disorder in the spin chain is manifested strongly in the physical properties. For example, thermal conductivity parallel to the doped spin chains is hugely suppressed because the spinons are now scattered by the impurity potential,

(2) any real system will have some degree of disorder, therefore, understanding how exactly disorder vitiate the ground state of an ideal quantum spin chains is of considerable importance,

(3) unexpected and novel magnetic ground states can be induced by incorporating a controlled level of disorder in spin chains,

(4) the spin excitations -as briefly alluded to above- can change dramatically in the presence of disorder. For instance, the spin excitations of the spin chain compound $SrCuO_2$ exhibit the expected gapless two-spinon-continuum. However, upon doping within the chains in $SrCuO_2$ with as small as 1 % of Ni impurities open-up a sizeable gap ($\sim$ 8 meV) in the spin excitation spectrum [72].

Here we shall review some of the landmark results pertaining to disorder physics in quantum spin chains. However, before we proceed further let us discuss the various ways in which disorder can be induced in the spin chains:

Disorder induced by doping outside the chain

In a quenched disorder of this type the bond-strength varies randomly along the length of the chain. An example of such a disorder is Ca^{2+} doping in $SrCuO_2$ [73] and in Sr_2CuO_3 [74]. Since the ionic radius of Ca^{2+} is smaller than that of Sr^{2+}, the random site substitution of Sr by Ca will change the -Cu-O-Cu- bond angles locally; therefore, changing the exchange coupling J between the spins randomly. Other examples of this kind of disorder include the spin chain compounds $BaCu_2(Si_{1-x}Ge_x)O_7$ [75, 76] and $Cu(py)_2(Cl_{1-x}Br_x)_2$ [77].

Disorder induced due to a missing spin in the chain

Absence of a Cu^{2+} from its regular site in $SrCuO_2$ or Sr_2CuO_3 due to small oxygen off-stoichiometry, or probably due to dislocation of the Cu^{2+} ion to an interstitial site (*Frenkel defect*) will give rise to this kind of disorder. Such a disorder will cause the chain to break into finite-size segments. The average length of the segments will be

inversely proportional to the concentration of the missing sites. The extent of disorder either due to off-stoichiometry or dislocation is expected to be modest. However, by doping a non-magnetic ion of comparable radii one can enhance the chain-break effect. For example, by doping Zn^{2+} or Mg^{2+} for Cu^{2+} in the spin chain compounds based of copper oxide ($SrCuO_2$, Sr_2CuO_3, etc).

Disorder induced by doping in the chain

Analogous to the non-magnetic doping mentioned above, it is also possible to create disorder in a spin chain by doping it with magnetic ions of comparable ionic radii. An example of this kind of induced disorder has been studied in the compound Sr_3CuPtO_6 [78]. In Sr_3CuPtO_6, the chains consist of alternating Cu (spin $1/2$) and Pt ions (spin 0): $\cdots$-O-Cu-O-Pt-O-Cu-O-$\cdots$, which show the characteristics of the antiferromagnetic spin $1/2$ Heisenberg chain. However, it has been shown that the Pt ions in the chain can be substituted by Ir either partially or fully, thereby, allowing one to control the extent of disorder [79]. It is interesting to note that Ir^{4+}, which has an effective spin $1/2$, couples ferromagnetically with the neighbouring Cu^{2+} spins. Therefore, under partial substitution of Pt by Ir, one has a disordered state with mixed ferro- antiferromagnetic interactions.

2.2 Survey of previous studies on disordered spin chains

We present here a summary of theoretical and experimental progress made in the area of disordered quantum spin chains. The investigations on disordered quantum spin chains can be broadly classified under two categories:

(1) disordered quantum spin chains with some probability distribution associated with the exchange couplings, and

(2) dilutely disordered quantum spin chains.

Under (2) are included those cases where majority of the bonds in the chain are uniform, i.e., only a small fraction of the bonds are altered. The obvious route to dilute disorder is

through dilute doping in the spin chain with magnetic or non-magnetic impurities. For example, by substituting 1 % or even less of Co, Ni, Zn or Mg impurities at the Cu^{2+} site in the spin chain compound Sr_2CuO_3, the dilute impurity scenario can be realized.

The systems under category (1), on the contrary, are those where majority of the bonds in the chain are altered. In this class we can further classify the systems based on the strength of the disorder: Strong disorder Vs Weak disorder. Strong disorder refers to the case where the bond strength variation is considerable and weak disorder pertains to a marginal variation of the exchange couplings. The distinction between 'weak' and 'dilute' is somewhat subtle and is best explained by *Giamarchi* in his book (page 275 of reference [24]).

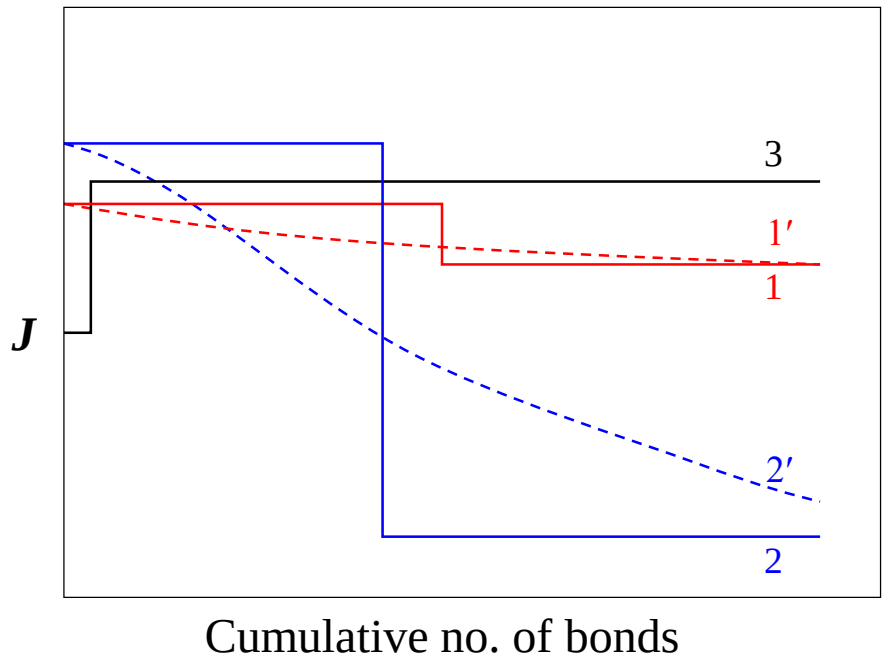

Figure 2.1: Schematic plot to illustrate the distinction between (1, 1') Weak, (2, 2') Strong and, (3) dilute disorder

In general, if the distribution of the impurities is uniform throughout the chain we can assume it to be Poissonian. The impurities are characterised by their density n_i and the strength of their potential V_i^l at the impurity site l. In the weak disorder case, the impurities are dense but the corresponding potentials V_i's are shallow. Therefore,

the impurities can only act collectively since the length scales over which the physical quantities vary is much larger than the separation between the impurities. On the other hand, dilute disorder corresponds to the dilute concentration of impurities but not necessarily a weak impurity potential. In such cases, as pointed out by *Giamarchi*, each impurity has a "strong effect in its immediate vicinity and one can essentially forget about the collective effects". The distinction between the strong, weak and dilute disorder is illustrated in figure 2.1.

This thesis deals with the case of disorder induced by dilute doping in the spin $1/2$ Heisenberg antiferromagnetic chains.There are numerous studies on disordered quantum spin chains. While most of these investigations are mainly of theoretical interest. However, some of the early theories were motivated by the experimental data available at that time on random Heisenberg spins chains, which we shall discuss next.

2.2.1 Strong disorder quantum spin chains

We shall first briefly review the progress made in strongly disordered spin chains over the last 4 decades or so. To get a glimpse of the main theoretical results one should probably look at the following references: [78, 80–87]. This list is by no means exhaustive, however, we direct the interested reader to a comprehensive review by *Igloi* and *Monthus* for progress made in disordered quantum spin chains till the year 2005 [88].

Motivated by the experimental results on some organic quasi-1D spin chain compounds (e.g., tetracyanoquinodimethanide (TCNQ) which show a Curie-like behaviour $\chi \sim T^{-\alpha}$ with $\alpha < 1$) in their magnetic susceptibility at low-temperatures, *Hirsch* and *José* investigated disorder in the Heisenberg spin $1/2$ chains using the renormalisation group (RG) methods based on *Kadanoff block decimation scheme* [80]. Around the same time *Ma, Dasgupta* and *Hu* proposed the real-space Renormalisation Group (RG) technique for studying random Heisenberg spin chains, i.e., chains with a broad continuous probability distribution $P(J_i)$ of the exchanges couplings [81] [82]. This

development can probably be marked as the beginning of a remarkable phase in statistical physics which have had ramifications beyond the realm of disordered quantum spin chains. In this technique, the strongest exchange (Ω_0) in the chain is identified and decimated away, yielding a new effective coupling (Ω_{eff}) between what were the third nearest neighbours, which are now paired-up as spin singlets. In the subsequent steps, the decimation procedure is applied iteratively resulting in a ground state where spins form singlet pairs at arbitrarily large separations, as shown in the figure 2.2. This is known as the random singlet (RS) ground state. The decimation procedure proceeds by integrating out the strongest left over bond of the chain in every step; consequently, the resulting singlets do not intercept or overlap (as shown in the figure 2.2), and their binding energy scales with inverse separation between the two spins.

Figure 2.2: Random singlet ground state of the random Heisenberg chain showing non-intercepting spin-singlets formed at arbitrarily large separations [83].

Later, *Doty* and *Fisher* [84] and Fisher [83], showed that the RS ground state is independent of the details of the disorder; and that it persists over wider regions of the phase diagram of the XXZ antiferromagnetic spin 1/2 Heisenberg model. For these reasons the RS phase is often referred to as the 'infinite randomness' fixed point [85], to which the RG flows to regardless of the details of the disorder present. The strong-disorder RG is currently used in variety of other contexts including the disordered-boson systems and the superfluid-insulator transition in one dimension. Some of these applications of strong disorder RG along with attempts to extend the theory to higher dimensions have been recently reviewed by *Refael* and *Altman* [85]. Extension of these theoretical concepts to higher dimensions was reviewed by *Vojta* [86]. Physics of random antiferromagnetic spin 1 chains was studied by *Monthus et al.* [89] in analogy with the real-space RG theory for the spin 1/2 chains. In HAF spin 1/2 chains, the experimental signature of RS phase is a Curie-like divergence of the bulk susceptibility at low-temperatures: $\chi \sim T^{-\alpha}$ with $\alpha < 1$. Examples of real systems where RS phase has been confirmed experimentally include Quinolinium $(TCNQ)_2$ consisting of

chains of stacked double benzene rings, with each pair having one excess spin-$1/2$ [85] and $BaCu_2Si_{1-x}Ge_xO_7$ [75, 76]. In many real spin chain compounds, the spin ordering at low-temperatures may impede with the expected Curie-like behaviour; in such a scenario, how the singular behaviour of the RS phase physics will reflect itself in the ordered phase has recently drawn attention. To address this point, *Kokalj et al.* [87] studied the magnetic ordering in random antiferromagnetic spin $1/2$ chains with finite interchain coupling ($J_\perp$) by treating $J_\perp$ within the mean-field approximation. The one dimensional quantum Heisenberg model with random ferro- and antiferromagnetic couplings ($\pm J$) was investigated by *Furusaki et al.* [78] in the context of the spin chain compound Sr_3CuPtO_6 doped with Ir at the Pt site.

2.2.2 Dilute impurities in spin $1/2$ chains

In this thesis, we are concerned with the behaviour of quantum spin chains with isolated impurities and boundaries giving rise to finite-size effects. This can be realized experimentally by doping a spin chain with very dilute level of magnetic/non-magnetic impurities. The main interest in this field was stimulated as an aftermath of the discovery of high-temperature superconductivity in layered cuprates. Doping experiments revealed a very strange fact about these superconductors. It was found that their superconducting transition temperatures exhibit a sharp suppression upon doping in the CuO plane. Even a tiniest amount of nonmagnetic Zn impurities in the CuO plane were found to be detrimental to the superconductivity. This led to an upsurge of research activities devoted to impurities in low-dimensional magnetic systems. These developments were comprehensively reviewed by *Alloul* in the year 2009 [90]. Quantum spin chains, owing to their simplicity, became the favourite playground for theorists to investigate dilute disorder. The last two decades have witnessed a steady growth of papers dealing with impurities in quantum spin chains. However, the experimental activities in this area remained relatively lull until very recently. Here, we shall provide a brief outline of the milestone developments in the physics of dilute impurities in quantum spin chains.

There are several different impurity configurations that have been studied in the past:

(1) the impurity spin is embedded in an interstitial site of the lattice, such that, it interacts closely with one or two nearest neighbouring spins of the chain. Experimentally this configuration can be achieved through ion implantation in the structure or even by muon implantation in μSR experiments [91–97],

(2) the impurity spin is coupled only to a boundary spin [98];

(3) the impurity spin is included within the chain. This is typically easier to achieve experimentally (for example, by substituting for a small percentage of host spins by foreign spins) [91];

(4) the chains with one altered link, which corresponds to the tunnelling problem in one-dimensional wires [91, 95, 99];

(5) chains with two altered links, which can be realized as in (2) through very dilute doping within the chains [91, 100]. The problem is also relevant to the resonant tunnelling in one-dimensional wires.

The main results of these studies are summarized as under. When the impurity spin ($S_{\rm imp} = 1/2$) is coupled to one spin ($S_i = 1/2$) at the i^{th} site, it forms a spin-singlet with the host spin (S_i), which is equivalent to an open chain with the spin at i^{th} site removed [91–97]. The two-site coupling was considered by *Clarke, Giamarchi* and *Shraiman* in reference [101]. The authors argued that the problem is equivalent to the *two-channel Kondo model*. The spin $1/2$ impurity forms a collective state with the spinons, resulting in an over screened impurity spin with a logarithmically divergent impurity susceptibility $\chi \sim T^{-1}\ln(T^*/T)$, where the energy T^* scales as $Je^{-constant.J/J'}$ where J is the intrachain coupling and J' the coupling of the impurity spin to its nearest neighbours. The problem of two-site coupling was also addressed by *Zhang, Igarashi* and *Fulde* using the density-matrix renormalisation-group methods and they also compared it with the results for the one-site coupling problem [94]. While the results for the one-site coupling problem agreed with the Kondo-screened pictured discussed above leading to an open chain, the two-site coupling yielded results in contradiction with the analytical

two-channel Kondo results due to *Clarke et al.* [101]. Briefly, the numerical analysis of *Zhang, Igarashi* and *Fulde* found partial decoupling of the impurity spin from the spins in the chain leading to a Curie-like divergence of the spin susceptibility at low-temperatures. This controversy concerning the ground state of two-site coupling problem was eventually resolved by *Eggert, Gustafsson* and *Rommer* using the field theory arguments and numerical calculations [102]. Doing so, they could classify all the fixed points and the RG flows across the phase diagram. Their model consisted of a uniform spin $1/2$ chain with an impurity coupled to the two ends of the chain as shown in the figure below.

They found the existence of four possible fixed points that are labelled as: (i) P_{N+1}, (ii) $O_N \otimes 1/2$, (iii) $P_N \otimes 1/2$, (iv) $O_{N-2} \otimes 1/2$, in figure 2.3. The fixed point P_{N+1} is stable in all directions, i.e., small perturbation on J_1 and J_2 are irrelevant here. $O_N \otimes 1/2$ is stable only for $J_1 \leq 0$. In this case, $J_1 > 0$ (antiferromagnetic) results in a flow towards the fixed point P_{N+1}, which corresponds to the "*healing*" of the chain. It is in this region of the phase diagram that one expects a behaviour analogous to the two channel Kondo effect with logarithmic divergence of the low-temperature susceptibility, recovering the results of *Clarke et al.* [101]. The fixed point $O_{N-2} \otimes 1/2$, which corresponds to the singlet formation in the limit of J_2 being very large, is argued to be stable in all directions. The only unstable fixed point in the phase diagram was found to be $P_N \otimes 1/2$ which presents a periodic chain having N sites with a decoupled impurity spin. The flow away from this point and towards one of the three stable fixed points is indicated in the phase diagram of figure 2.3. In this case a small coupling J_1 of either sign is going to be frustrating due the triangular configuration of the spins arrangement. The dotted line in the phase diagram is parabolic whose details can be found in reference [102].

A particularly detailed investigation of an impurity embedded in the HAF spin $1/2$ chain, which is also most relevant to the work presented in the later chapters of this thesis, was carried out by *Eggert* and *Affleck* using the numerical and conformal field theory techniques [91]. They showed that depending on the kind of impurity present, the low-energy behaviour either corresponds to the "healing" of the defect (as was described above in the RG from the fixed point $O_N \otimes 1/2$ to P_{N+1} for $J_1 > 0$) or else to

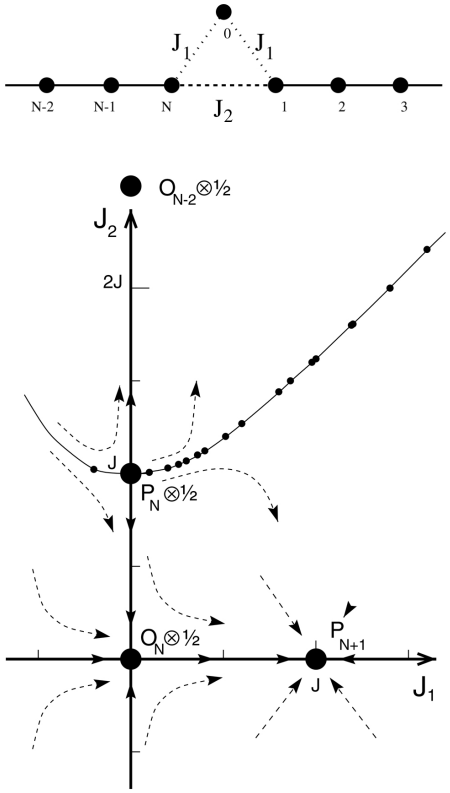

Figure 2.3: The two-site coupling impurity model of *Eggert, Gustafsson* and *Rommer*. The spin $1/2$ chain consists of N sites. The exchange coupling between the spins of the chain is antiferromagnetic, denoted by $J(>0)$. The impurity spin at the 0^{th} site couples to its nearest neighbours at the sites 1 and N by an exchange coupling J_1. The coupling between the 1_{st} and the N^{th} site spins is designated by J_2. The possible fixed points of the system are shown in the lower panel: (i) $J_1 = J$ and $J_2 = 0$ which corresponds to a periodic chain with $N + 1$ sites and no impurity spin (P_{N+1}), (ii) $J_1 = J_2 = 0$: an open chain with N site and a decoupled impurity spin $1/2$ ($O_N \otimes 1/2$). (iii) $J_1 = 0, J_2 = J$: a periodic chain with N sites and a decoupled impurity spin $1/2$ ($P_N \otimes 1/2$). (iv) $J_1 = 0$ and $J_2 = \infty$: an open chain with $N - 2$ sites, with two end sites (1 and N) paired up as singlet and the decoupled impurity spin $1/2$ ($O_{N-2} \otimes 1/2$) [102].

a "*severing*" of the chain at the impurity site. However, in both the cases, the impurity spin is integrated out through singlet formation with the neighbouring host spins. The singlet formation is akin to the Kondo screening of the impurity spin by the conduction electron spins in the metallic systems (for example, Fe-Au or Mn-Cu). In the spin $1/2$ chain, it is the separation of the spin and the charge that allows the host spins to screen the spin of the extrinsic impurity. In the low-energy limit, this amounts to breaking of the chain at the impurity site into two semi-infinite segments.

Furusaki and *Hikihahr* extended the consideration of Kondo effect in Heisenberg spin $1/2$ chain to a more general XXZ model ($-1 < \Delta \leq 1$) [96]. They considered the coupling of an impurity spins $1/2$ in the XXZ chain and showed that in the antiferromagnetic side (i.e., $0 < \Delta \leq 1$), the low-energy properties remains same as for the isotropic spin $1/2$ model: that is, the chain gets cut into two semi-infinite segments due to Kondo screening of the impurity spin. On the other hand, in the ferromagnetic region, $-1 < \Delta \leq 0$, the host XXZ chain remains as a single uncut chain through the "healing" process discussed above.

While the consistency of these theories dealing with the isolated impurities has been checked using numerical techniques, the progress in verifying these results experimentally is rather slow and scarce, and has started to gain momentum only recently. *Simutis et al.* investigated the low-energy excitations of a Heisenberg spin $1/2$ chain compound $SrCuO_2$ doped with 1 % of spin Ni impurities [72]. In the limit of 1% or less of doping, one can consider of these impurities as essentially isolated. They found that the low-energy spin excitation spectrum of the doped chain exhibit a spin pseudogap of roughly 8 meV, absent in the pristine chain (see figure 2.4). They also confirmed that this behaviour is not related to any structural phase transition. What then could be the origin of the spin gap in such a lightly doped chain? They explained this behaviour on the basis of the theoretical predictions in reference [91, 102] for an isolated spin 1 impurity in the HAF spin $1/2$ chain. The impurity spin will be Kondo screened by the antiferromagnetically coupled neighbouring host spins, magnetically breaking the chain at the impurity site. They showed that the low-energy spin dynamics can be explained by the effective fragmentation of the spin chain by the Kondo screened spin 1 defects. The

situation, at a naïve level, is analogous to that of a particle confined in a potential well; here the particles are the spinons and the potential seen by them is manifested through the magnetic isolation of the fragmented chain sections, which confine the spinons to finite length segments of the chain.

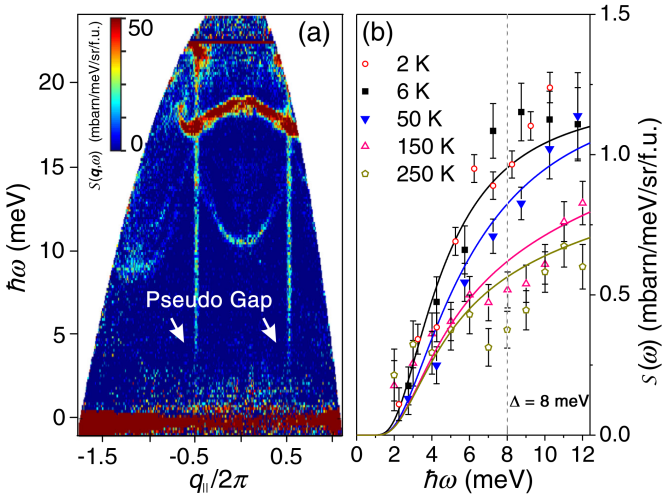

Figure 2.4: Time-of- flight neutron spectrum measured in $SrCu_{0.99}Ni_{0.01}O_2$, as a function of momentum transfer along the spin chains and energy transfer. (b) Momentum-integrated dynamic structure factor measured in $SrCu_{0.99}Ni_{0.01}O_2$ at several temperatures, using TOF (solid symbols) and three-axis (open symbols) spectroscopy. The lines are simulated structure factor, which indicates a average spin gap of $\sim$ 8 meV. [72]

2.3 Physical properties of the spin 1/2 HAF chain with dilute impurities

2.3.1 Bulk magnetic susceptibility

A scalar or non-magnetic defect in a spin-chain can be realized by replacing the magnetic ion of the chain by a non-magnetic ion, which breaks the chain into finite length segments (L). Being non-magnetic, the scalar defect at first sight may appear to have no significant contribution to the bulk magnetisation of the spin chains. However, the boundaries of the chain-segments, created by the scalar defects, exhibit a *Curie*- like behaviour in the bulk magnetic susceptibility ($\chi \propto 1/T$) at the low-temperatures. If we

replace 1% of Cu^{2+} by Zn^{2+}; the chain will break into finite length segments of length $L = 100$ sites on an average. At $T/J \ll 1/L$ a segment with even number of spin sites will have a diminishing contribution to the magnetisation due to mutual cancellation of antiferromagnetically aligned spins. On the other hand, the odd length segments will have one uncompensated spin which will lock into a doublet ground state yielding a $1/T$ contribution to the susceptibility [27, 91, 103, 104]. However, the behaviour of the boundaries at higher temperatures is much more complex. Therefore, an attempt to fit the susceptibility data using the Curie law at low-temperatures results in a serious underestimations of the defect concentration by as much as a factor of 10 [105]. As an asset, since the temperature dependence of the susceptibility due to staggered magnetisation at the chain boundaries is very different from that of the paramagnetic defects, the disorder induced by scalar defects can provide useful structural information.

If we consider a scalar defect concentration p with a Poissonian distribution, i.e., the defect sites are uncorrelated and each defect effectively removes one spin, then the average length of the chain segment would be $\bar{L} = 1/p - 1$. The average susceptibility of the chain is given by [106]

$$\chi_p = p^2 \sum_L (1-p)^L \, \chi(L) \tag{2.1}$$

The important thing to note here is that the magnetic susceptibility $\chi(L)$ of the segmented chain has different behaviour over different temperature ranges. At low-temperatures ($T/J \ll 1/L$), the segments with odd-length practically contribute as an effective $S = 1/2$. On the other hand, the even-length segments have a contribution that goes exponentially to zero as $T \to 0$ (see figure 2.5). At high temperatures ($T/J \gg 1/L$), however, the susceptibility can be written as $\chi(L) = L.\chi_{\text{bulk}} + \chi_B$, where χ_{bulk} is the contribution from the bulk of the chain segment which can be described by equation 1.14 and χ_B denotes the boundary susceptibility. In reference [107], χ_B is shown to exhibit a logarithmic correction ($\approx 1/12T \ln(2.9J/T)$). If we consider a crossover between these two temperature ranges at some length $L_c = \gamma J/T$, The total susceptibility from equation 2.1 can be written as [38]:

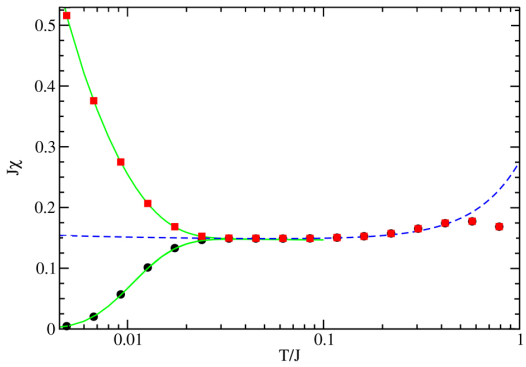

Figure 2.5: Quantum Monte Carlo calculations of the magnetic susceptibility for $\Delta = 3/4$ and $L = 99$ (red squares), $L = 100$ (black dots) compared to the field-theory result (green solid lines). The blue dashed line denotes $\chi = \chi_{\text{bulk}} + \chi_B/L$.

$$\chi_p \approx \frac{p^2}{4T} \sum_{L\text{odd}}^{L_c} (1-p)^L + p^2 \sum_{L_c}^{\infty} (L\chi_{\text{bulk}} + \chi_B)(1-p)^L \tag{2.2a}$$

$$= \frac{p}{4T}\frac{1-p}{2-p}\left(1-(1-p)^{\gamma J/T}\right) + (1-p)^{\gamma J/T}\left[\left(1-p+\frac{p\gamma J}{T}\right)\chi_{\text{bulk}} + p\chi_B\right] \tag{2.2b}$$

Here γ is the crossover parameter, which is expected to be of the order of 1, and can therefore be dropped. If we replace χ_{Bulk} by the chain susceptibility discussed in section 1.3.1, the total susceptibility for the segmented chain can be expressed as:

$$\chi_p = \frac{p}{4T}\frac{1-p}{2-p}\left(1-(1-p)^{J/T}\right) + (1-p)^{J/T}\left[\left(1-p+\frac{pJ}{T}\right)\chi_{\text{chain}} + p\chi_B\right] \tag{2.3}$$

The factor $(1-p)^{J/T}$ in this equation facilitates the crossover between high- and low-temperature limits, such that, for a given value of p and J, χ_p tends to a value $\frac{p(1-p)}{4T(2-p)}$ for $\frac{T}{J} \ll p$; i.e., at very low temperatures. In this limit, χ_p varies as 1/T with an effective paramagnetic Curie constant $\frac{p(1-p)}{4(2-p)} \approx \frac{p}{8}$ which amounts to an effective spin $\frac{1}{2}$ paramagnetic concentration $N_S = \frac{p}{2}$. This is the same old result obtained naively by considering only the odd-length segments contributing to the Curie-tail. At the other extreme, i.e., $\frac{T}{J} \gg p$ (which is easily reached at temperatures well below J for small

p), the first term diminishes quickly to zero, however the Curie behaviour persists due to the presence of term $p\chi_B = p/[12T\ln(2.9J/T)]$ which corresponds to the boundary susceptibility [107]. In this case N_S has a logarithmic temperature dependence given by $p/[3T\ln(2.9J/T)]$. At any intermediate temperature the effective paramagnetic concentration can be expressed as [38];

$$N_S/4T = \chi_p - (1-p)\chi_{\text{chain}} \tag{2.4}$$

It should be noted that the factor $\frac{N_A g^2 \mu_B^2}{k_B}$ (here N_A is the Avogadro's constant, g represents the Landé-g factor, μ_B is the Bohr magneton and k_B the Boltzmann constant) is not explicitly shown in the equations above for χ_p and N_S. This single parameter

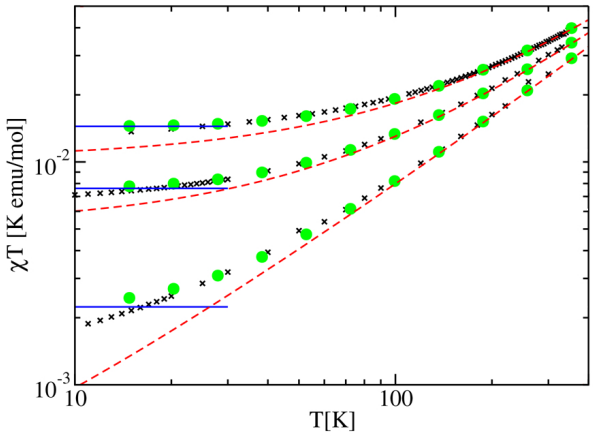

Figure 2.6: Measured susceptibility $T(\chi - \chi_0)$ for $Sr_2Cu_{1-x}Pd_xO_3$, with $x = 0.5\%, 1\%, 3\%$ (crosses from bottom to top). The green dots represent the best theoretical fit with equation 2.3. Subsequent curves are shifted by 3×10^{-3}. The blue solid lines represent $(p/4)\frac{1-p}{2-p}$ and the red dashed lines $T\chi_{bulk} + p/12 \cdot \ln(2.9J/T)$. Taken from reference [105]

equation has been shown to work satisfactorily for the linear chain compound Sr_2CuO_3 when doped with dilute amount of non-magnetic Pd, and yields a reasonably accurate estimation of the defect concentration (see figure 2.6).

2.3.2 Thermal conductivity

Thermal conductivity of the spin 1/2 HAF chains exhibit an unprecedently large magnetic contribution along the chain direction [108–112]. The $S = 1/2$ HAF chains are

particularly interesting because the fundamental conservation laws predict ballistic heat transport in these systems [113, 114]. So, an infinite heat conductivity is expected along the chain length. However, in real systems, the heat conduction is dissipative due to scattering of spinons by phonons and defects. At very low-temperatures the spinon-phonon scattering cross-section should become very small, and the spinon-defect scattering dominates, which prevents the verification of integrability mentioned above. In some very recent experiments, *Nikolai et al.* carried out thermal conductivity measurements on the crystals of the spin 1/2 HAF chain compound Sr_2CuO_3. They prepared high-quality single crystals of this compounds with progressively increasing purity of the starting precursors on which the thermal conductivity measurements were reported. In there paper, they reported measurements on three different crystals with purity of the starting precursors as 99%, 99.9% and 99.99%. As expected, with increasing purity the thermal conductivity measured parallel to the chain also increased. However, what is very interesting is that, not only this increase was non-linear – becoming more pronounced with increasing purity – but it also confirmed the ballistic nature of spinon mediated thermal conductivity, since the mean free-path of spinons in their experiments on the crystals with highest purity extended up to 1200 unit cell dimensions [112, 115] (see figure 2.7). Similar experiments, also by *Nikolai et al.*, on another spin-chain compound $SrCuO_2$ further corroborated the Ballistic nature of the spinon thermal conductivity.

2.4 Magnetic ground state of dilutely disordered chains

In low-dimensional quantum magnets, impurities can have unexpected effect on the magnetic ground state. In some cases, the presence of defects can give rise to a Néel-ordered state, as in the case of the spin-Peierls compound $CuGeO_3$ [70, 116] and two leg spin-ladder compound $SrCu_2O_3$ [117]. These results suggest that the Néel-ordered state emerges as a competitive phase to the original spin-dimerized state. On the other hand, scalar defects are shown to suppress the Néel-ordering in the Heisenberg spin 1/2 chains [91]. Experiments on Sr_2CuO_3 support these theoretical calculation. For example, it was shown that Pd ($S = 0$) [118] and Zn doping ($S = 0$) doping in Sr_2CuO_3 suppresses

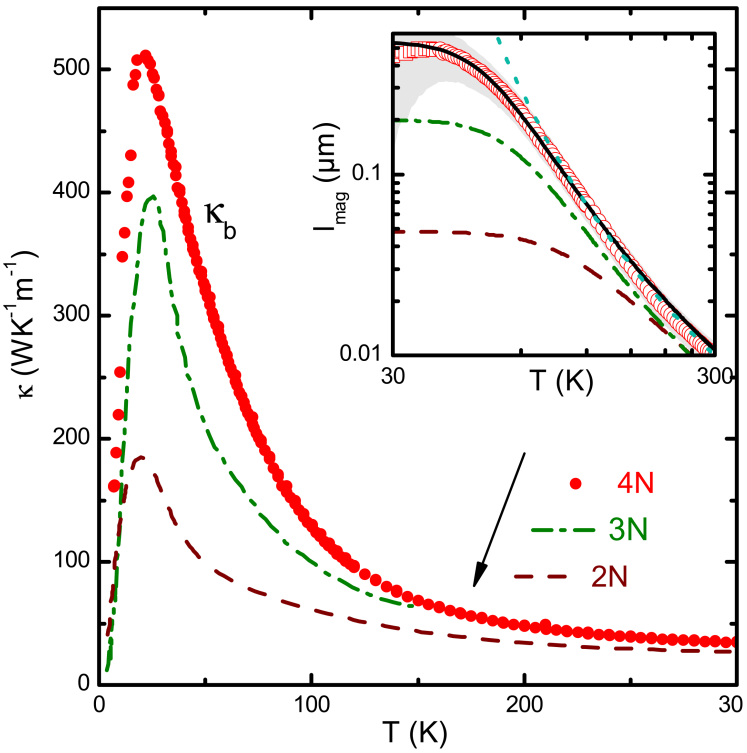

Figure 2.7: Thermal conductivity (κ_b) of Sr_2CuO_3 parallel to the spin chains (along b-axis) for 4N (circles), 3N (dash-dotted line) purity purities and 2N (dashed line). Inset: Derived mean free paths of the spinon excitations. Taken from reference [112].

T_N. A recent study on Ni doped $SrCuO_2$ using μSR also support this result [119]. The staggered moment around the defect locations cause significant disruption to the local antiferromagnetic correlations and thereby result in suppression of the Néel-ordered state. However, the effect of impurity on the ground state, and the spin excitations of a spin 1/2 chain, appears to be highly sensitive to the spin state of the impurity as discussed in the following section.

2.5 Influence of the spin states of the doped impurity

In figure 2.8, the thermal conductivity of a $SrCuO_2$ single crystal is shown in its pristine form and also after doping it with two different types of magnetic defects, namely, Ni^{2+} having spin 1 and Co^{2+} having an effective spin 1/2. In the left panel, results parallel to the chains are shown (i.e., κ_c Vs T), and in the right panel results for perpendicular direction (i.e., κ_a Vs T) are shown. A strong and counter intuitive dependence of

the thermal conductivity, and thus the magnetic excitations, on spin states of the disorder induced by the magnetic defects has been observed in these experiments. While the thermal conductivity along the chains ($\kappa_{\parallel}$) for both Ni and Co defects shows suppression due to scattering of the spinons; interestingly, these defects induce a counter-intuitive effect on the thermal conductivity in the perpendicular direction $\kappa_{\perp}$. In the Co doped crystal $\kappa_{\perp}$ exhibits the expected decrease, but in the Ni doped crystal, thermal conductivity of the doped crystals is higher than that of the pristine crystal. It has been argued that, the spinons, which mediate the heat conduction along the chain direction, also takes part in scattering of phononic waves. When the spinons are suppressed due to gapping of the excitation spectrum, the consequent suppression of the phonon-spinon scattering results in an enhancement of the phonon mediated thermal conductivity ($\kappa_{\perp}$). In the Co doped samples, no detectable spin-gap was found, therefore, Co defects exhibit the usual suppression of the thermal conductivity perpendicular to the chains.

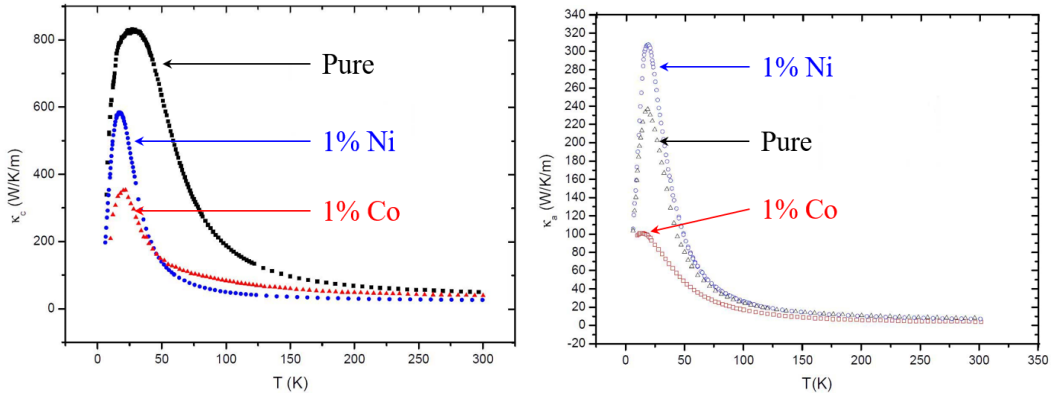

Figure 2.8: Thermal conductivity of pure, 1% Ni and 1% Co doped $SrCuO_2$, parallel to the spin chains(left panel) and in the perpendicular direction (right panel).

In the theoretical models discussed previously, there are indications that the quantum state of the impurity determines whether the spin chain will be "severed" at the impurity site (i.e., cut it into two segments) as in the case of Ni^{2+} impurity or will it be "healed" leaving the chain uncut [91].

These results emphasize on the importance of studying dilute impurities in the quantum spin chains as probes to get experimental access to fundamental scattering processes. The magnetic ground state and spin excitations of the spin 1/2 HAF chain in

the presence of dilute impurities is turning out to be an emerging field of research. Impressive progress in the crystal growth techniques over the last two decades or so has enabled researchers to dope spin chains with controlled level of various impurity types. Improvement in the measurement techniques such as inelastic neutron scattering and angle resolved photo-emission spectroscopy and resonant inelastic x-ray scattering, has added huge impetus to exploring the physics of quantum spin chains with dilute disorder.

Chapter 3

Motivation and Materials

3.1 Motivation

In the introductory chapters we emphasized that the physical properties of quantum spin chains are highly sensitive to the presence of disorder. Since any real system will have a degree of disorder, it is important to understand how disorder vitiates the intrinsic physical properties of the quantum spin chains. Advancements in low-energy field theories and numerical techniques over the last few decades have led theorists to investigate the behaviour of disordered quantum spin chains in details. Among several interesting theoretical predictions, the ones that have had a significant impact on the current research in condensed matter and statistical physics include the discovery of the random-singlet (RS) phase in the strongly disordered spin chain, and the Kondo-like screening of an isolated impurity in a spin chain. The infinite randomness RS phase and the Kondo screening of isolated impurity constitute the opposite extremes of the disorder physics spectrum in 1D. While there are a few experimental verifications of the RS phase, the physics of isolated impurities in spin chains (or in the Luttinger liquid realm, in general) has remained largely unexplored.

Very recently, *Simutis et al.* [72] confirmed one of the theoretical conjectures pertaining to the "severing" of a chain at the impurity site proposed by *Eggert at al.* [91]. However, there are several other predictions, including the "healing" of the chain at the impurity site in the XXX and XXZ Heisenberg models that remain to be investigated experimentally. Also, equally pertinent is the question of universality in the case of

isolated impurities. Put in other words, it is important to examine experimentally if the ground state in the presence of isolated impurities is also universal as the RS phase, which we know does not depend on the details of the disorder. Though not investigated here, the role of impurities as probes for understanding various scattering processes in the quantum spin chains provides strong motivation to synthesize and study dilutely disordered quantum spin chains.

The main objective of my thesis are: (i) to verify theoretical models of quantum spin chains with isolated impurities, (ii) to explore new physical phenomena that may emerge due to dilute disorder in spin $1/2$ chains, and (iii) to understand the role of magnetic frustration in spin $1/2$ chains with a zigzag topology.

3.2 Compounds Sr_2CuO_3 and $SrCuO_2$

To realize the physics of disorder in the Heisenberg spin $1/2$ chains, one must first of all select a system that is known to exhibit an excellent one-dimensionality over a broad temperature range and with large intrachain coupling (J), such that, the low-energy physics is accessible at temperatures easily accessible in a low-temperature lab. As discussed in subsection 1.3.3, the ratio of the intra-chain (J) to inter-chain ($J_\perp$) exchange couplings determine the goodness of the one-dimensionality of a given low-dimensional system (see table 1.1). In this regard, the compounds Sr_2CuO_3 and $SrCuO_2$, listed in table 1.1 appears to be excellent one-dimensional systems. Both these compounds are characterised by a high values of the intrachain exchange ($\approx$ 2000 K) [56], while the interchain exchange, for both, is much smaller: $J_\perp \approx 10$ K [120]. Since Cu^{2+} in these compounds is in a square-planar coordination, it has only one unpaired electron in the $d_{x^2-y^2}$ orbital resulting in a spin $1/2$ at each Cu site. These characteristics make these compounds the best known one-dimensional systems to explore the disorder physics. In the compound Sr_2CuO_3 the chains are linear, and in $SrCuO_2$ they have a zigzag geometry. The zigzag chain compound is a useful system to investigate the magnetic ground state of the frustrated chains.

In order to understand the magnetic one-dimensionality of these compounds, it is useful to examine their crystal structure, which is discussed next.

3.2.1 Crystal structure

The unit cell of Sr_2CuO_3 can be thought of as derived from that of the compound La_2CuO_4. The main structural feature of La_2CuO_4 is its layered morphology comprising alternating stacks of Cu-O and La-O layers perpendicular to the crystallographic c-axis. In the Cu-O planes, the Cu^{2+} ions form a square planar array where each Cu^{2+} ion is surrounded by four O^{2-} ions and each O^{2-} ion by two Cu^{2+} ions (see panel (a) of Figure 3.1). If one replaces La^{3+} completely by Sr^{2+}, then the charge neutrality of the formula unit would require removal of exactly one oxygen atom per formula unit. Thus, in the Sr_2CuO_3 structure, the corresponding Cu-O layer will appear as shown in panel (b) of figure 3.1, consisting of -Cu-O-Cu- chains parallel to the crystallographic *b*-axis. The full unit cell of Sr_2CuO_3 is shown in panel (c) of figure 3.1. The unit cell is orthorhombic with space group *Immm*. The linear -Cu-O-Cu- bonds along the chain allow for a strong antiferromagnetic superexchange between the neighbouring Cu^{2+} spins ($J \approx 2000$ K) [56]. On the other hand, due to the absence of intervening O^{2-} ion between any two adjacent Cu^{2+} ions along the c axis, the adjacent chains remain very weakly coupled. Similarly, in the direction perpendicular to the Cu-O planes, extended exchange paths, due to the presence of intervening Sr-O layer, allows the Cu^{2+} spins to have very weak interaction. The interchain interaction $J_\perp$ is estimated to be ≈ 9 K [120]. As a consequence of a non-zero $J_\perp$, the system enters a long-range spin ordered state upon cooling below $T = 5.4$ K.

The compound $SrCuO_2$ possess a similar unit cell structure as that of the compound Sr_2CuO_3 (see figure. 3.1(d)). The Cu-O layers in $SrCuO_2$ are also consists of -Cu-O-Cu- spin chains (with $J \approx 2000$ K) parallel to the crystallographic $c-$axis. However, instead of a linear spin chain, the chain in compound $SrCuO_2$ has a zigzag geometry (see figure 3.1(e)). The zigzag chain can be though as of two parallel chains coupled through 90° Cu-O-Cu ferromagnetic superexchange (J'), with exchange coupling about

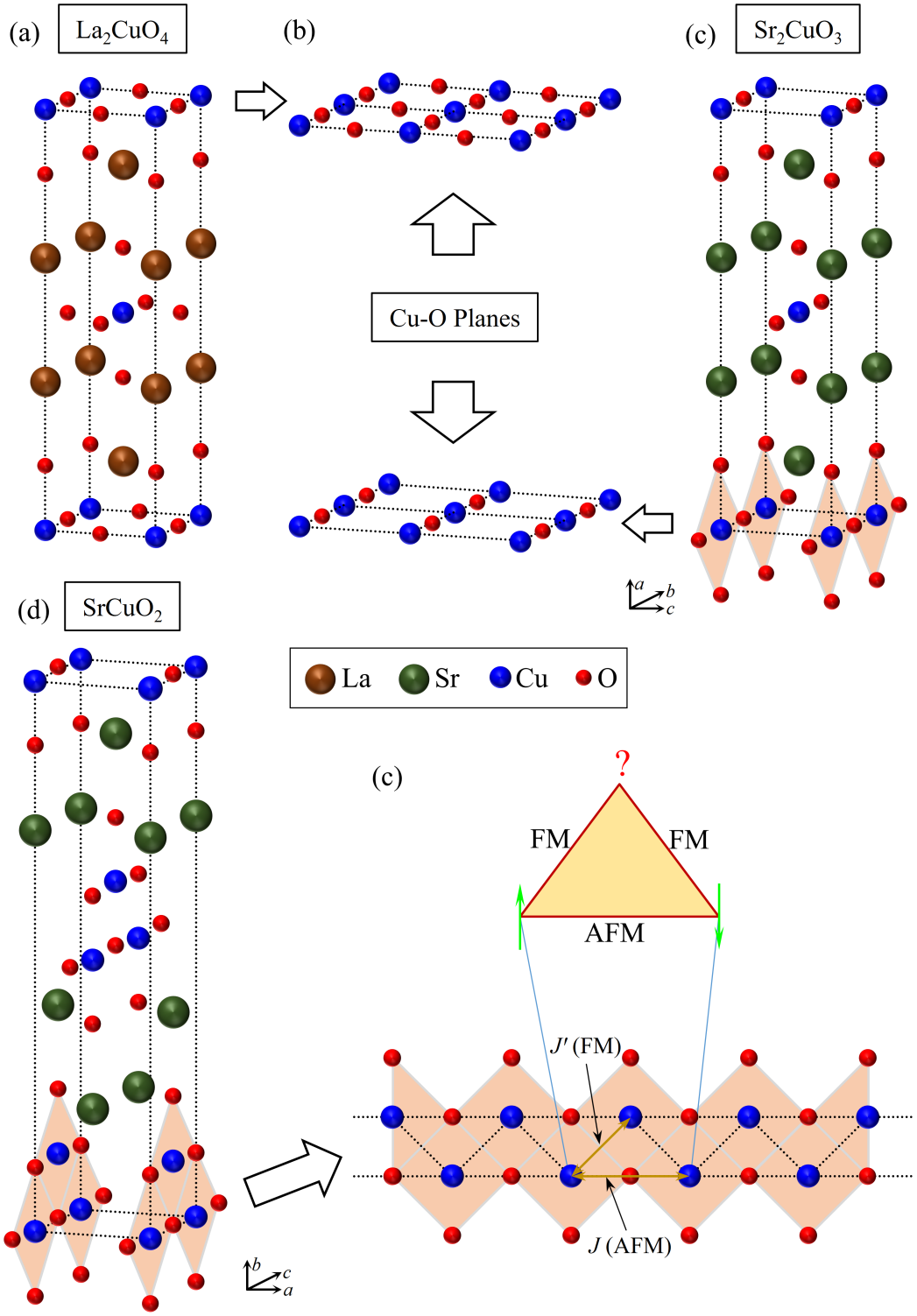

Figure 3.1: Unit cell structure of (a) La_2CuO_4, (c) Sr_2CuO_3 and (d) $SrCuO_2$. Panel (b) shows howthe Cu-O planes in La_2CuO_4 transformed to linear chains in Sr_2CuO_3. Panel (e) the zigzag morphology of spin Cu-O chains in $SrCuO_2$ leads to triangular spin geometry.

an order of magnitude less than the linear Cu-O-Cu exchange ($J'/J \approx 0.1$ [121]). Due to triangular arrangement with one AFM exchange and two ferromagnetic exchanges, the spins in the zigzag chains are frustrated. Due to spin-frustration, spin chains in $SrCuO_2$ do not show any static ordering below to $T = 2$ K, they rather freeze into a stripe-like short-range ordered state with anisotropic magnetic correlation lengths [122].

3.2.2 Bibliographic view of the physical properties

Here, we will present a summary of the landmark results from the vast literature on quantum spin chains where these two compounds have played a key role in advancing the frontier of quantum condensed matter physics. This section also serves to provide a synoptic view of the progress in the physics of low-dimensional quantum magnets.

- Using the quantum field theory and numerical Bathe Ansatz results *Eggert, Affleck* and *Takahasi* (EAT) showed that the susceptibility of the Heisenberg spin 1/2 chain exhibit an inflection point near 0.087 J/k_B, below which the slope of $\chi(T)$ increases rapidly approaching infinity as $T \rightarrow 0$ [123]. *Motoyama et al.* examined bulk magnetic susceptibility of high-quality single crystals of Sr_2CuO_3 and $SrCuO_2$ over a wide temperature range between 5 and 800 K and showed that the experimental susceptibility matches with the EAT results [56]. They also estimated the exchange interaction energy J/k_B to be 2200 ± 200 and 2100 ± 200 K, for Sr_2CuO_3 and $SrCuO_2$, respectively.

- *Cloizeaux* and *Pearson* showed that the magnetic excitations in the spin 1/2 Heisenberg chain should have the gapless two-spinon continuum form. This was experimentally verified using inelastic neutron scattering (INS) on the single crystals of $SrCuO_2$ and explained using the “Müller ansatz" by Zaliznyak el al. [124]. From the lower boundary of the continuum, intrachain exchange constant was estimated to be $J = 226 \pm 12$ meV, in good agreement with the value obtained by *Motoyama et al.* using the susceptibility analysis.

- The intensity of scattered neutrons due to the spinons in Sr_2CuO_3 vary significantly, and found to be much lower than that calculated theoretically from the

fundamental 'sum' rule [124]. This discrepancy has been attributed to the strong 2p-3d hybridization of Cu and O states. Hence, the ionic nature of magnetism appears to fail significantly in these low-dimensional cuprates [125].

- The compounds Sr_2CuO_3 and $SrCuO_2$ are excellent systems to probe the separation of spin, charge and orbital degrees of freedom of an electron. The experimental realization of the spinon-holon separation was accomplished through electron photo-emission spectroscopy [42, 44, 45] on high quality single crystals of $SrCuO_2$. The separation of the spin and the orbital degrees of freedom were experimentally observed using the resonant-inelastic x-ray scattering experiments on single crystals of Sr_2CuO_3[43].

- Although ideal spin-chains do not show long-range magnetic ordering at any temperature, the real systems do order magnetically due to a finite inter-chain coupling. The compound Sr_2CuO_3 undergoes transition to weak 3D magnetic ordering at $T = 5.4$ K with ordered moment of $\approx 0.06\mu_B$/Cu, experimentally verified using μSR and neutron scattering experiment[126]. The 3D magnetic ordering can be attributed to the weak interchain coupling of about 9 K, estimated from neutron scattering data[126].

- In the zigzag chain compound $SrCuO_2$ which has comparable values of intra- and inter-chain couplings as in the linear chains compound, a static magnetic ordering sets in only below below $T = 2$ K [127]. Zalizynak et al. further characterises the unusual magnetic phase in $SrCuO_2$ using quasi-elastic neutron scattering [122]. They reported an anisotopic spin frozen ground state (with time scale $\delta t > 2.10^{-10}$s) in in the zigzag chains of $SrCuO_2$ with correlation lengths $\xi_c \approx 200c$, $\xi_a \approx 60(25)a$ and $\xi_b \approx 2.2(3)b$.

- The antiferromagnetic ordering temperature in real spin $1/2$ chains in the presence of non-magnetic or scalar defects was investigated using quantum mechanical calculations by *Eggert et al.*[106]. It was deduced that non-magnetic doping

in Heisenberg spin $1/2$ chains should lower the T_N. This was confirmed by Pd-doping in Sr_2CuO_3, where the ordering temperature was found to suppress in accordance with the calculation [118].

- It was predicted theoretically using the quantum field theory by *Eggert et al.*, that a spin-1 impurity in the spin $1/2$ chain should be completely screened by the spins of the neighbouring ions in a manner analogous to the *single-ion Kondo effect* in metals [91]. This has been recently confirmed in $SrCuO_2$ using INS experiments [72] and in Sr_2CuO_3 using NMR experiments [128].

- Segmentation of the chains into finite-size by the defects is found to introduce a *pseudogap* in the magnetic excitation spectrum. This has been experimentally observed using the inelastic neutron scattering experiments on the Ni-doped chains of $SrCuO_2$ by *Simutis et al.*, where they found a sizeable gap of $\sim$ 8 meV in 1% Ni-doped chains[72]. A similar spin-gap has also been observed in the case of Ni-doped linear chains of Sr_2CuO_3 in the NMR experiments [128].

Clearly, these two compounds have played a phenomenal role in advancing the field of quantum condensed matter because of their excellent one-dimensionality and exceptionally large J. However, there is a lot more that remained to be done. Experimental results on spin-chain compounds in the presence of dilute disorder are scarce. Few results that are available are mainly on 90° Cu-O-Cu chains of $CuGeO_3$ which undergo a spin-Peierls transition at low-temperatures. The details of the bulk magnetic properties are scarcely reported. Furthermore, the defects with different spin values and anisotropies are yet to be explored, which will be interesting particularly in the context of the quantum field theoretical work. In the presence of magnetic defects, antiferromagnetic spin $1/2$ chains may exhibit a variety of interesting magnetic behaviours (which may depend upon the characteristics of the defects); for instance, the healing of the segmented chains in presence of the spin $1/2$ impurities [91]. These are the various factors that motivated us to undertake a detailed experimental investigation of the bulk magnetic properties and the magnetic excitations in presence of the defects with different spin values: 0 (Zn^2+), 1/2 (anisotropic, Co^{2+}), 1 (N^{2+}) and 5/2 (Mn^{2+}).

Chapter 4

Experimental Methods

Experimental investigations of the anisotropic properties of spin 1/2 chains mandates access to high quality crystals that can be employed to accurately measure their ground state properties and the spin excitations. Accurate measurements of the physical properties are crucial for the advancement of science. They provide much needed input to the theorists and are equally important in verifying the validity of theoretical models. This brings us to the "*experimental methods*" chapter of this thesis that deals with the crystal growth technique employed to obtain high-quality crystals of the spin $1/2$ cuprates, and the various experimental techniques used for their rigorous structural and compositional characterisations. The measurement techniques employed here include dc & ac magnetisation, specific heat and neutron scattering experiments. In this chapter we will focus on the working principle of these experiment techniques.

4.1 Crystal growth

Single crystals were grown using the *travelling-solvent-floating-zone* (TSFZ) method in a four-mirror optical-floating-zone furnace (Crystal System Corporation, Japan). Crystal growth of all the compounds used in this thesis will be dealt with in details in a separate chapter, here I shall provide a brief introduction to the *floating-zone* (FZ) technique. Images of the optical floating zone furnace employed in this thesis are shown in panels (a) and (b), and a schematic drawing of the vertical section of the furnace shown is in panel (c) of figure 4.1. The furnace consists of four halogen lamps, each placed at the focus of an ellipsoidal shape reflector. The second foci of these reflectors coincides

at a common point on the vertical axis of the furnace, inside the growth chamber. The energy flux of the lamps, after reflection from the walls of the reflectors, converges at the common foci where a molten zone between the polycrystalline feed and the seed rods is formed. The feed rod is suspended from the upper shaft of the furnace using a nickel wire and the seed rod is clamped to the lower shaft using an alumina holder. As the furnace shafts are pulled down, the floating zone between the rod moves up. This allows a slow directional melting of the polycrystalline feed and a subsequent crystallization on the seed, transforming the polycrystalline feed into a single crystal. The specifications of the image furnace used in the present work are given in table 4.1.

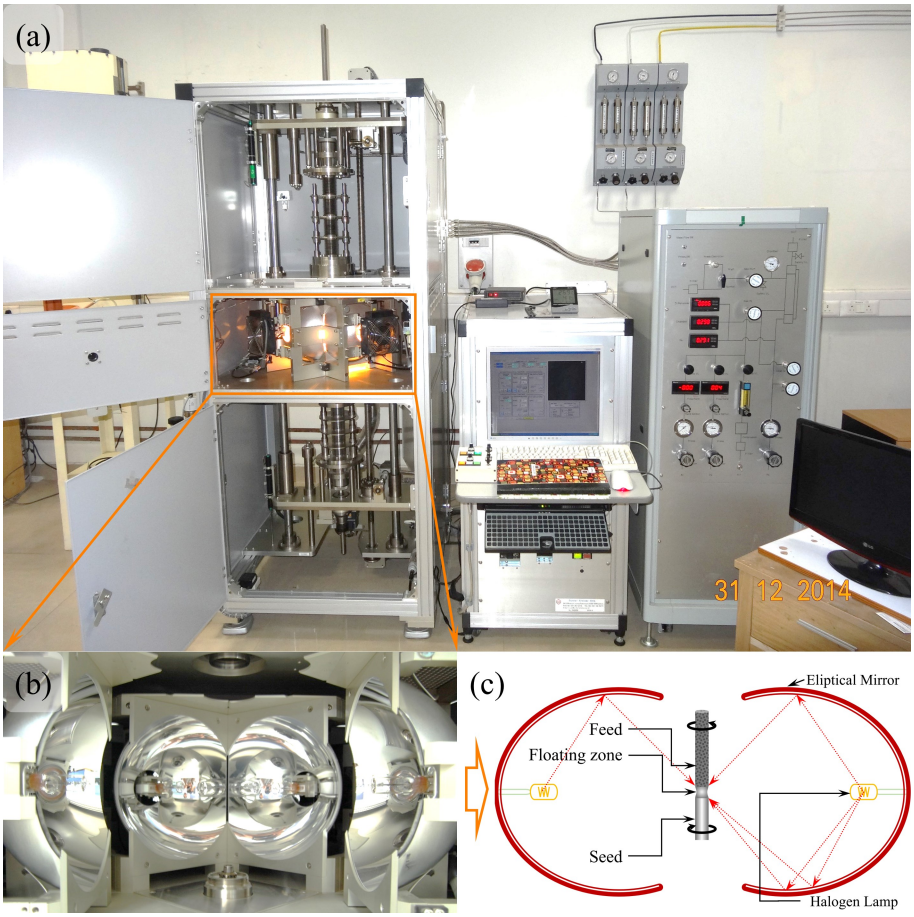

Figure 4.1: (a) Photograph of the optical image furnace used in the growth experiments. (b) Close-up image of the mirror section. (c) Schematic drawing of the vertical section of the furnace is the shown to illustrate the principle of working.

Table 4.1: Details of the image furnace used in growth of single crystals.

Parameter	Details
Model	FZ-T-10000-H-HR-I-VPM-PC
Input voltage : current	200 V (3-phase) : 40 A
Power-rating of the lamps	150, 300, 500, 1 k, 1.5 kW
Number of lamps	4
Number of mirrors	4
Max. operating temperature	$\sim$ 2200°C
Maximum growth length	150 mm
Growth speed	0.1 $\sim$ 300 mm/h
Rotation speed	3 $\sim$ 100 rpm
Maximum chamber pressure	0.95 MPa
Minimum chamber pressure	5×10^{-5} torr
Liquid magnetic seal kits are used under high pressure conditions	

4.2 Structural and composition characterizations

To ensure high quality rigorous structural and composition characterisations were carried out on all the grown crystals. For this purpose small crystal pieces were cut from different parts of the grown crystal boule and examined using optical microscopy, scanning electron microscopy (SEM), energy-dispersive x-ray (EDX) analysis, powder x-ray diffraction and single-crystal neutron diffraction techniques. The details of these characterisation methods are given in the next section.

4.2.1 Optical microscopy

Optical microscopy under polarized light on a polished crystal surface provides a quick and reliable method to identify the presence of differently oriented structural domains. For this purpose thin sections were sliced out from different parts of the grown single crystal boule using a low-speed diamond saw (Buehler, USA). The sliced crystal pieces were dry polished using SiC polishing paper with progressively increasing grit sizes. Coolants were avoided since all the crystals investigated here are known to be highly sensitive to decomposition upon coming in contact with moisture. Since coolants are generally water based or, if not water based, may contain a trace amount of moisture, enough to decompose the crystal. The final polishing in each case was done using the

grit size 1200 (i.e., granule size 15 μm). On these mirror finished crystal surfaces, segregation of secondary phases can be detected as demonstrated in panel (a) of figure 4.2. Depending upon the crystallographic orientation of the illuminated surface, the polarization axis of the outgoing light varies and thus differently oriented domains can also be easily recognised using this technique. An example of this is shown in panel (b) of figure 4.2.

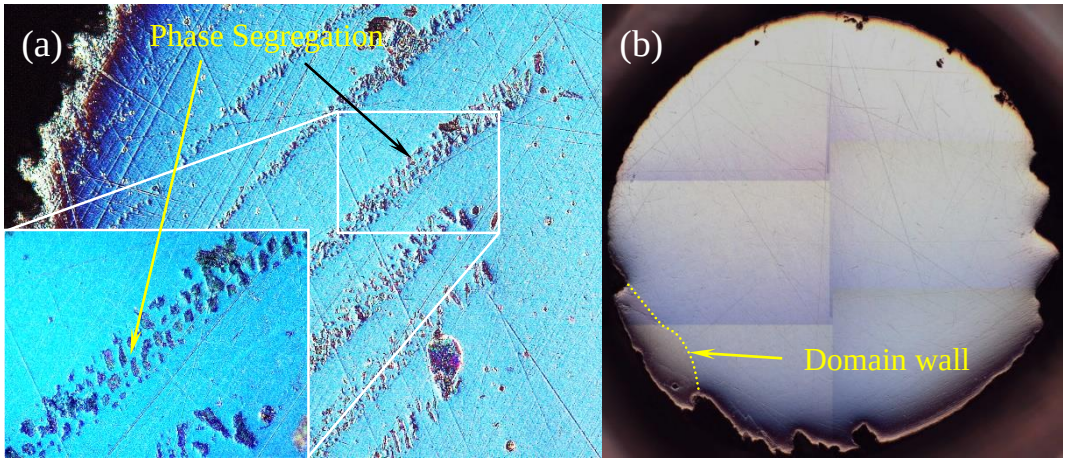

Figure 4.2: Optical images under polarised light of polished cross-sections at different lengths of the grown crystal ($SrCu_{0.99}Co_{0.01}O_2$). (a) Dark patches indicate secondary phase (confirmed using EDX), (b) differently coloured region indicates differently oriented crystallographic domains.

4.2.2 Scanning electron microscopy

The structural and compositional homogeneity of the grown crystals were further characterised using scanning electron microscopy (SEM, Zeiss Ultra Plus, Germany), equipped with a Energy-dispersive x-ray analysis probe (Oxford, UK). In this method, the cleaved or polished surfaces from different parts of a grown crystal were examined using a field emission electron beam.

In a scanning electron microscope a high-energy ($\sim$ keV) focussed electron beam is incident on the sample of interest. The incident electron beam interacts with the sample in different ways, resulting in emissions of different electrons and photons as shown in figure 5.13.

The energy released in stopping the high-energy electrons beam may energies some of the outer shell electrons of the sample and thus liberating them from it. However, the energy of electrons liberated in this process is lower and the electrons from deep inside the sample can not escape. Thus, these secondary electrons carry only the information of the surface. These electrons are very useful in determination of the surface topography of a given sample.

Some of the electrons from the incident beam are bounced back from the atomic electron cloud of the sample. The scattering cross-section of these electrons are dependent on the atom mass density. Thus, these back scattered electrons (BSE) not only provide high resolution surface topography of the sample but also carry useful information about the structural and composition variations. In our work we have used these BSE micrographs to determine the formation of crystallographic phase or segregation of secondary phases in the grown crystals, if any.

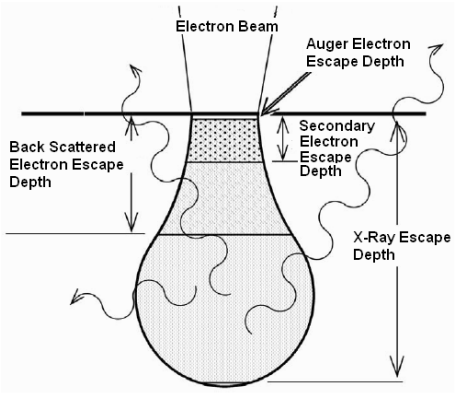

Figure 4.3: Schematic of different emissions due to the incidence of high-energy electron on a sample under high vacuum in a scanning electron microscope (taken from [129]).

With emission of secondary electrons from inner shells, the empty shell are filled up with the outer shell electrons. The energy gained in the process is released in the form of x-rays photons. The energy of an emitted x-ray photon is equal to the energy difference between shells involved in the transition that are, in turn, characteristic of the atom. Thus, by analysing the energy of the radiated x-rays, the elemental composition of the sample surface can be determined. Since x-rays have high energies, and are not

charged, they have very small scattering cross-section with the sample atoms so even signal from deep inside the sample can be detected.

The energy of the incident electron beam plays a crucial role in this process. While the lower-energies, due to its low-penetration (5 − 10 keV), are desirable for the determination of the surface topography, for BSE and EDX analysis higher energies are preferred. The optimum value depends on the elements present in the system. An empirical rule is to select the excitation voltage at least twice the corresponding excitation energy of the elements present. In the present work, among the elements present in the grown crystal, Sr possesses highest excitation energy of $14keV$ ($K_{\alpha 1}$). Therefore, to determine the molar ratio of elements present in the grown crystals an excitation voltage of 25 − 28 kV has been used for all the samples.

4.2.3 Powder x-ray diffraction

Power x-ray diffraction is a very useful tool in the compositional and structural analysis. The principle of the diffraction process and its analysis for the crystallographic structure determination (also referred to as the Bragg formulation of x-ray diffraction) was first proposed by William Lawrence Bragg and and his father William Henry Bragg in 1913[130], for which they received Nobel prize in Physics in 1915.

Table 4.2: Specification of the powder x-ray diffractometer used

Parameters	Details
Model	Bruker D8 Advance powder X-ray diffractometer, Germany
Geometry	Bragg-Brentano parafocusing geometry
Source	Cu−K_α (λ = 0.15418 nm; $P = 2.2k$W)
Detector	Solid state linear detector – Lynxeye
Primary optics	2.5° vertical soller slits + motorized divergence slit
Secondary optics	Motorized anti-scatter slit system + 2.5° vertical soller slits

In the present context, the powder x-ray diffraction has been used to confirm the composition purity of the grown crystals. For this purpose, $\theta - 2\theta$ x-ray diffraction, using Bragg-Brentano geometry, were carried out on the powders obtained by crushing

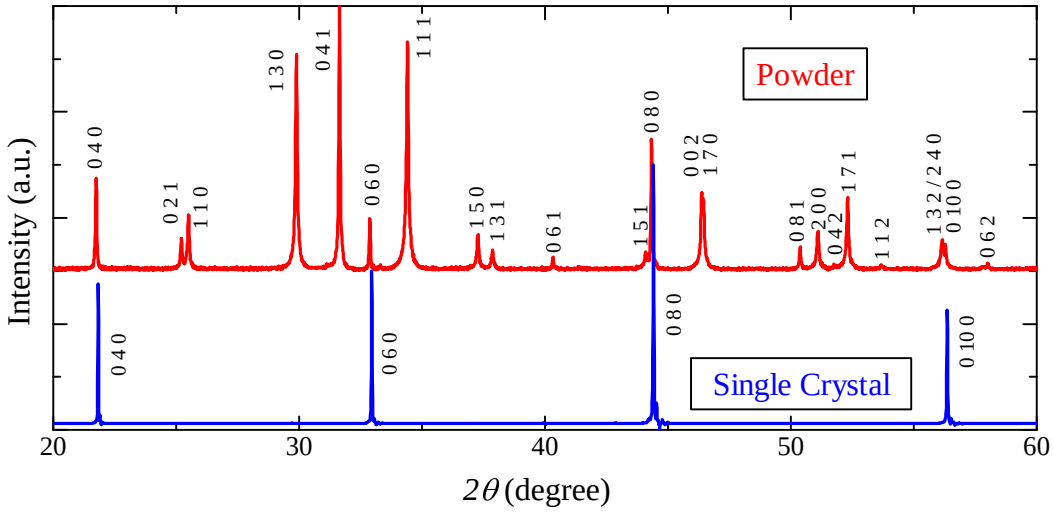

Figure 4.4: A representative powder x-ray diffraction pattern measured on (a) the crushed powder and (b) cleaved surface (crystallographic $ac-$plane) of small crystal pieces from the same crystal boule of pristine $SrCuO_2$ as in (a) obtained using the Bragg-Brentano geometry. The indices on the powder patter represents the corresponding *miller hkl* indices for the x-ray lines.

small crystal pieces cut from the grown crystal boule. The measured x-ray pattern was matched with the standard data available in the ICDD PDF-2 diffraction data base. Details of the diffractometer has been given in table 5.14. Lattice parameters for each grown crystal is determined by using the UNITCELL software. For this purpose the powder x-ray pattern is matched with the ICDD database to assign the *hkl* indices to each peak in the pattern. The mean positions of the peaks were determined by *Gaussian fit*. 9-10 strongest peaks are then considered in determination of the Lattice parameter.

We also performed x-ray diffraction, in Bragg-Brentano geometry, on the cleaved crystal sections. For this purpose very thin cleaved crystals were placed parallel to the diffraction plane the diffractometer. Depending upon the orientation of the cleaved surface, only those diffraction peaks that are characteristic of its crystallographic orientation are expected. Presence of any additional diffraction peak indicates that the surface has segregated minor secondary phases or more than one, but related, crystallographic orientation. Figure 4.4, shows examples of x-ray powder diffraction on (a) crashed crystals and (b) from a cleaved section of the same. The pattern for the cleaved surfaced are right shifted depending the sample height mismatch due to the thickness

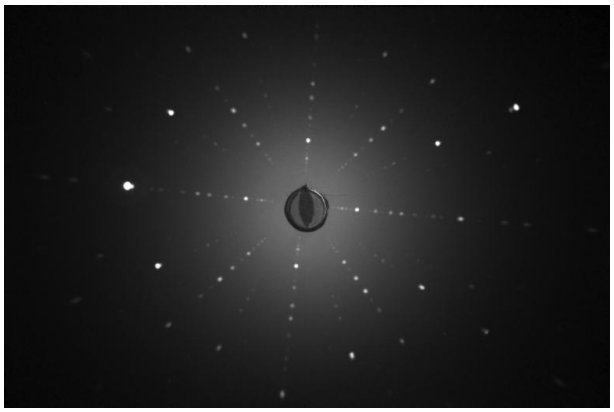

Figure 4.5: A representative Laue diffraction pattern from the crystallographic *bc*-plane of a Sr_2CuO_3 crystal.

of the sample crystal.

4.2.4 Laue-diffraction

Laue Diffraction was used for determining the orientations of the crystallographic axes in a given crystalline sample. In this method a focussed 'white' x-ray beam (conventionally obtained from the bremsstrahlung radiation off the target) is incident on a crystalline sample and the diffracted x-rays from specific set of parallel crystallographic planes are recorded as a symmetric pattern of Laue spots on a 2D detector (see figure 4.5). Use of 'white' x-ray ensures that the Bragg condition for different set of crystal planes is satisfied. By analysing the symmetry of the Laue spots the crystallographic orientation of the crystal can be obtained. From the knowledge of the crystal symmetry one can calculate the rotation matrix elements to reorient the crystal along a desired orientation. The specifications of the used Laue diffractometer are given in table 4.3.

The symmetry of the Laue spots can be conveniently analysed using the program ORIENT EXPRESS, which is freely available on the internet. The program not only determines the present orientation of the crystal with respect to the direction of the incident x-ray beam but it also calculates the rotation matrix elements to go from the present orientation to a desired orientation.

Table 4.3: Specification of the Laue x-ray diffractometer used

Parameters	Details
Model	Photonic Science Laue diffractometer, UK and France
Target	Tungsten (Model)
X-ray λ	0.35 Å– 2.5 Å(Power = 15 W)
Collimator	Microfocal brush collimator (spot size = 0.5, 1, 1.5 mm)
Detector	GdOS (Gadolinium oxysulphate) scintillator flim followed by digital optical camera
Measurement distance	4.5 cm
Measurement time	120 s

4.3 Bulk physical properties measurement methods

The Bulk properties of the grown and well-aligned crystals were measured in a *physical properties measurement system* (PPMS) from Quantum Design,Model 6000, USA. The instrument is equipped with a Ever-cool-II liquid He refrigerator which provides access to measurement temperatures ranging from 1.9 K to 300 K. Inside the sample chamber the magnetic field can be varied between ±90 kOe using a superconducting magnet submerged in the liquid He bath. For each bulk property e.g., specific heat, ac and dc magnetisation separate probes were used in the cryostat. The details of these probes are as follows.

4.3.1 Specific heat

We used specific heat probe to identify the magnetic phase transitions and try to interpret the low-temperature specific heat due to the spinons. The specific heat measurements were carried out in a calorimeter probe attachment to the PPMS. A schematic diagram of the calorimeter is shown in figure 4.6. The calorimeter consists of a sample platform which includes an inbuilt temperature sensor and a heater. The sample platform is suspended by 8 connecting wires (Au-Pd alloy) which not only provide electrical connectivity to the sensor and the heater but also allow a controlled thermal coupling between the platform and the puck, which is in thermal equilibrium with the sample chamber. Apart from these wires, any other source of thermal leak with the

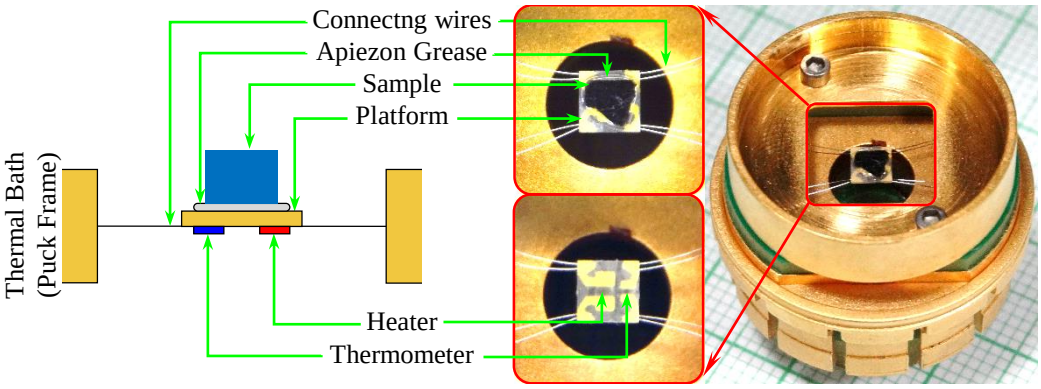

Figure 4.6: (left) Schematic diagram of the the sample platform hanging from calorimeter puck by the connecting wires. (right) Representative image of the calorimeter puck and the sample platform with a sample crystal stuck using *Apiezon* grease

sample environment is minimized by maintaining a high vacuum in the sample chamber. The sample is mounted on the sample platform using the *Apiezon* grease. For low-temperature measurement ($T < 200$ K) Apiezon 'N' grease is used, whereas, for higher temperature measurements Apiezon 'H' grease is used, which ensures good thermal contact between the sample and the platform. Limited by the platform size, a sample of maximum size 3×3 mm^2 can be used, whereas the sample mass can range from 2 mg to 200 mg [131].

During the specific heat measurement, the temperature relaxation during and after a heat pulse is given to the sample and the platform together, are recorded[131, 132]. Thus, the recoded data contains the background contributions from the grease used and the sample platform. The precise estimation of the background is obtained by carrying out the specific heat measurement of the sample platform and the grease before each measurements in the same temperature range. The advantage of this method is that no previously recorded (possibly inaccurate) data are necessary, as well as no knowledge of the quantity of apiezon used is necessary. Although, the contribution due to the platform remains constant for the zero magnetic field, it can show considerable changes for higher magnetic fields and low-temperatures. Therefore, for specific heat measurement under magnetic field and at low temperatures ($T < 10$ K), background measurement for each magnetic field has to be conducted separately in order to achieve higher accuracy

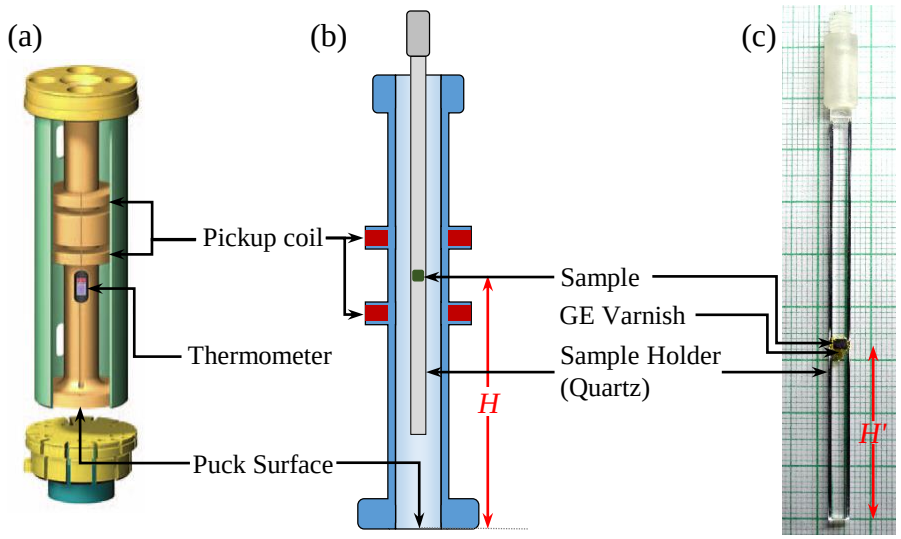

Figure 4.7: (a) Schematic diagram of pickup coil-set of the VSM probe (designed by Quantum Design, USA) and (b) its longitudinal section with the quartz sample holder along the vertical axis. (c) An image of the quartz holder with sample crystal glued using GE varnish on it.

of the measurement. This is exactly the protocol that we followed for the measurement of specific heat data reported in this thesis.

4.3.2 dc magnetization

Measurement of the dc magnetisation were carried out using a *vibrating sample magnetometer* (VSM) probe inside the PPMS cryostat. Measurements in a VSM involves vibrating/oscillating the sample near a detection (pickup) coil and synchronously detecting the voltage induced. Since the induced voltage is proportional to the magnetisation of the sample, a standard calibration is used to convert induced voltage from an unknown sample in equivalent electromagnet units. The compact *gradiometer* pickup coil configuration in the VSM coil set (see figure 4.7) enables one to use large oscillation amplitude (1 − 3 mm peak) at a frequency of 40 Hz, which provides a resolution of about 10^{-6} emu at a recording rate of 1 Hz, which is good enough for most samples investigated here.

The basic VSM probe consist of three major components. A linear motor to vibrate the sample inside the pickup coil-set, the first-order gradiometer coil-set consisting of

a pair of secondary coils wound around in opposite directions to each other, and the voltmeter to detect the signal from the pickup coil. The pickup coil-set is schematically shown in figure 4.7. The sample is placed at the center of the coil set, mounted on a quartz sample holder using a non-magnetic *GE varnish*. The superconducting magnet in the PPMS cryostat is used to generate a uniform dc magnetic field around the sample. As the linear motor vibrates the sample between the coil-set, the magnetic flux due to induced magnetisation on the sample by the dc field varies with the same frequency and thus induces a voltage in the pickup coil. The time-dependent induced voltage is given by the following equation:

$$V_{coil} = \frac{d\Phi}{dt} = \left(\frac{d\Phi}{dz}\right)\left(\frac{dz}{dt}\right) \tag{4.1}$$

Where Φ represents the magnetic flux through the coils, z is the vertical position of the sample with respect to the coil, and t is the time. For a sinusoidal oscillation of the sample between the coil-set the induced voltage can be written as:

$$V_{coil} = 2\pi f.C.m.A\sin(2\pi ft) \tag{4.2}$$

where C is a coupling constant, m is the dc magnetic moment of the sample, A is the amplitude of oscillation, and f is the frequency of oscillation.

The data acquisition for the sample magnetisation involves real time recording of the in-phase signal from the pickup coils which is converted to the sample moment using the simple algorithm as described by equation 4.2. Though the VSM technique does not have the resolution as good as a *superconducting-quantum-interference-device* magnetometer, however, the quick measurement time and ability to record data for high magnetic fields makes it very useful for measurement of dc magnetisation.

4.3.3 ac susceptibility

The measurement of the ac susceptibility provides an insight into the spin dynamics and relaxation processes in a magnetic sample. During the measurement, an ac magnetic field is applied to the sample and the voltage signal induced across a pickup coil is

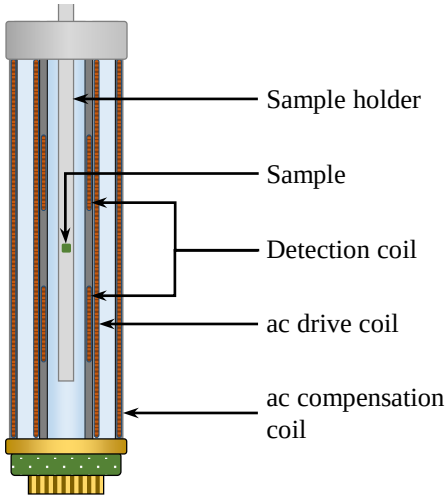

Figure 4.8: A Schematic longitudinal section of the ACMS coil set.

analysed to determine the real and imaginary part of each harmonics with respect to the phase of the driving ac field.

For the measurement of ac susceptibility we used the ac measurement system (ACMS) probe of the PPMS. The basic components of the ACMS consists of an ac drive coil set, detection gradiometer pickup coils, and an ac compensation coil set. The ac driven coil-set applies an alternating excitation field on the sample, while the detection coil-set captures combined inductive response of the sample as well as the excitation field. The ac compensation coil-set helps to get rid of the effects of the drive excitation. All the coil-sets are situated within the ACMS insert, concentric with the superconducting DC magnet of the PPMS cryostat.

A schematic diagram of the ACMS coil-sets is shown in figure 4.8. The drive coil is wound longitudinally around the detection coil-set. The drive coil can generate alternating fields of up to 10 Oe in the frequency range of 10 Hz to 10 kHz. However, the drive frequency and applied field are inter-dependent. At low-temperatures, a large drive amplitude with higher frequency may cause a large source of heat to the sample chamber due to Eddy current flow, which limits the amplitude to be used at high frequencies.

Just under the drive coil set a pair of detection coils (for first-order gradiometer configuration) are situated. The coils are wound in the counter directions to each other and are connected in series to help isolate the sample's signal from uniform background

sources. During dc measurements, as in the VSM, a constant field is applied along the axis of the coil-sets and the sample is moved quickly through both sets of coils, inducing a signal according to the *Faraday's Law*. This measurement method is commonly called the extraction method.

A compensation coil is situated outside the AC drive coil in order to minimize the instrumental interference. The compensation coil is wound in the reverse direction to that of the drive coil and connected to it in series. In this configuration both the coils receive the same excitation signal. It effectively confines the excitation fields to the volume of the coil set. Outside the coil-set the net field cancels each other and, therefore, reduces the instrument interaction with conductive materials outside the coil, such as, the walls of the sample chamber, the superconducting magnet, etc., to a great extent. Individually calibrated ACMS systems ensure that the drive coil and compensation coil produce the desirable net excitation signal at the sample.

Each detection coil also contains a low-inductance calibration coil. These two single-turn calibration coils are connected in series and are situated at the centre of each detection coil, where the sample measurements occur. During AC measurements, the accuracy of the phase and amplitude calibration is increased by placing the sample between the two detection coils and switching the calibration coils into the detection coil circuit with both possible polarities.

4.4 Neutron scattering

Neutrons are subatomic particles with rest mass 1839 times that of electrons (1.675 $\times 10^{-24}$ g). Elastic and inelastic neutron scattering techniques have been extensively used in this work to determine the magnetic ground state and the energy dispersion of the magnetic excitations in the pristine and the doped spin chains. While the bulk magnetic probes are useful to determine the magnetic ground state of the crystals, elastic neutron scattering gives a clear view of the type and size of the ordered state (if there is any). The elastic neutron scattering is also useful to determine the magnetic correlations

in different directions. On the other hand, inelastic neutron scattering experiments are used to probe the dynamics, and the energy dispersion of the magnetic excitations.

All the neutron experiments were conducted at Paul Scherrer Institute, Switzerland in collaboration with Prof. Dr. Christian Rüegg, Head, Laboratory for Neutron Scattering and Imaging, PSI. This section is intended to give a brief description of the neutron techniques and the apparatuses involved.

In a neutron scattering experiment the measured quantity is the probability that incident neutron with wavevector $\boldsymbol{k}$, is scattered by the sample to a state with wavevector $\boldsymbol{k'}$. Thus, the intensity of the collected neutron by the detectors are plotted in term of the momentum transfer,

$$\hbar\boldsymbol{Q} = \hbar(\boldsymbol{k} - \boldsymbol{k'}) \tag{4.3}$$

where $\boldsymbol{Q}$ is known as the scattering vector and the corresponding energy transfer will be given by,

$$\hbar\omega = \frac{\hbar^2}{2m}(k^2 - k'^2) \tag{4.4}$$

Eqs. 4.3 and 4.4 are the conservation of the momentum and energy of an neutron scattering experiment, respectively. The Momentum conservation is schematically sketched in Fig. 4.9. For an elastic neutron scattering process $k = k'$, and so the energy transfer $\hbar\omega = 0$. For some specific values of k and k' the momentum transfer $\boldsymbol{Q}$ is equal to the reciprocal lattice vector as shown in panel (a) of Fig.4.9.

$$\boldsymbol{Q} = \boldsymbol{k} - \boldsymbol{k'} = \boldsymbol{\tau} \tag{4.5}$$

where $\boldsymbol{\tau}$ is a reciprocal lattice vector. In a coherent elastic scattering described by equation 4.5, which is known as the Bragg's law, $\boldsymbol{\tau}$ is equal to that of the momentum transfer $\boldsymbol{Q}$. In inelastic neutron scattering $\boldsymbol{Q}$ does not coincide with a reciprocal lattice vector $\boldsymbol{\tau}$. As shown in panel (b) of figure 4.9 in inelastic neutron scattering, the scattering vector $\boldsymbol{Q}$ can be decomposed into τ and q, where $\boldsymbol{q}$ is the wavevector of an

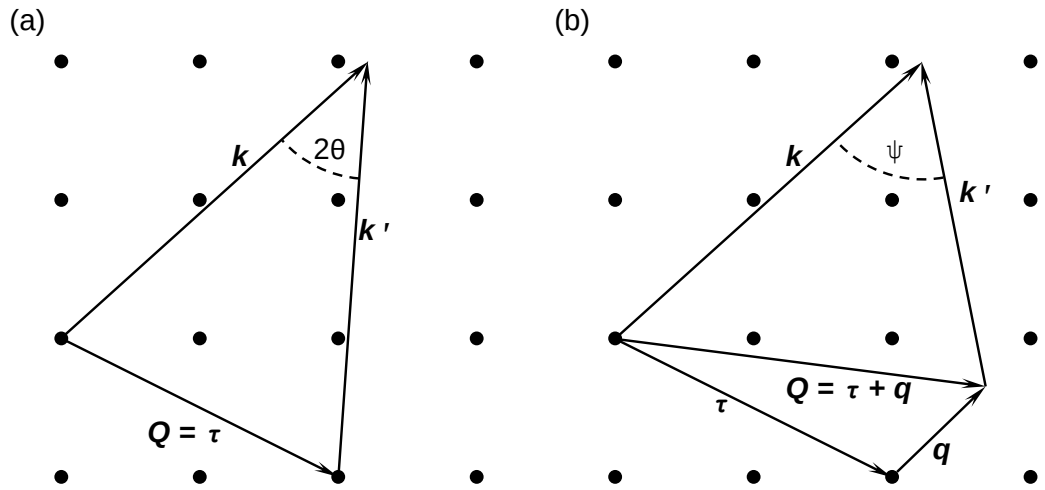

Figure 4.9: Schematic of the elastic and inelastic scattering processes in the reciprocal lattice space.

elementary excitation to be specified. Neutron scattering turns out to be the most precise experimental technique which is able to measure the dispersion relation $\hbar\omega(\boldsymbol{q})$ at any predetermined point in the reciprocal space as discussed in the subsequent sections.

4.4.1 Elastic neutron scattering and bulk magnetism

In an elastic neutron scattering experiment, elastically scattered neutrons produce strong Bragg reflections whenever the scattering vector is equal to the reciprocal lattice vector. These reflections can be studied in samples by a number of experimental methods, including (i) rotating a crystal and measuring the scattering from a monochromatic beam, looking for strong reflections, (ii) using a range of incident wavelengths (the Laue method) (iii) measuring the diffraction of monochromatic neutrons from a powder sample.

The nuclear scattering of neutrons results from interaction with the nucleus rather than with the electron cloud, and so the scattering power of an atom is not strongly influenced by its atomic number. This is in sharp contrast with the cases of both X-rays and electron scattering. This has some advantages: it is easier to sense lighter atoms, such as hydrogen, in the presence of heavier ones, and neighbouring elements in the

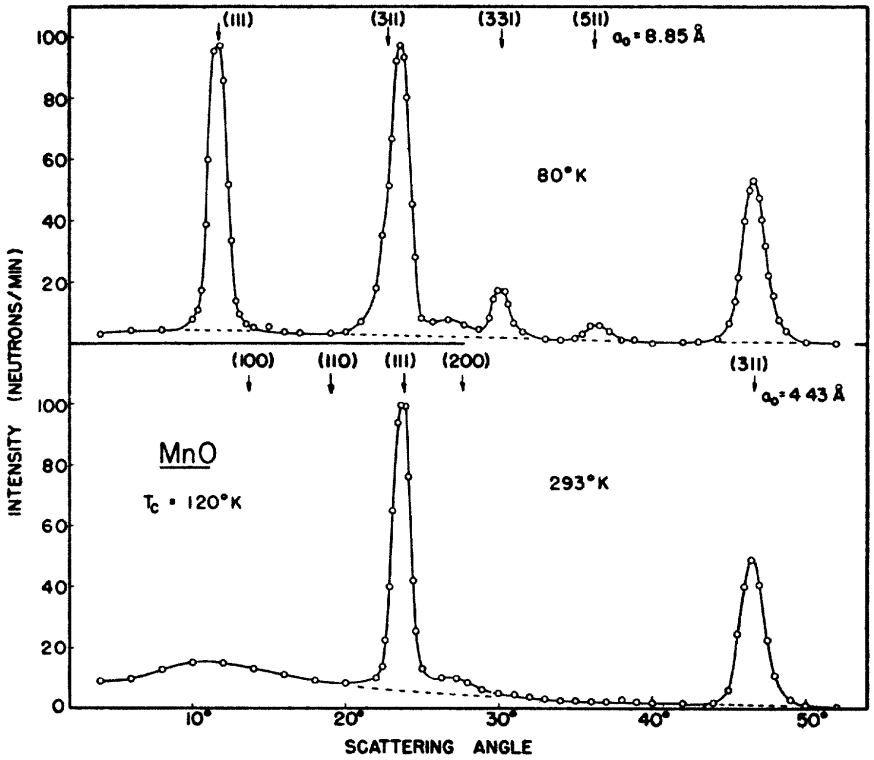

Figure 4.10: Neutron diffraction pattern for MnO below and above T_N taken from [133]

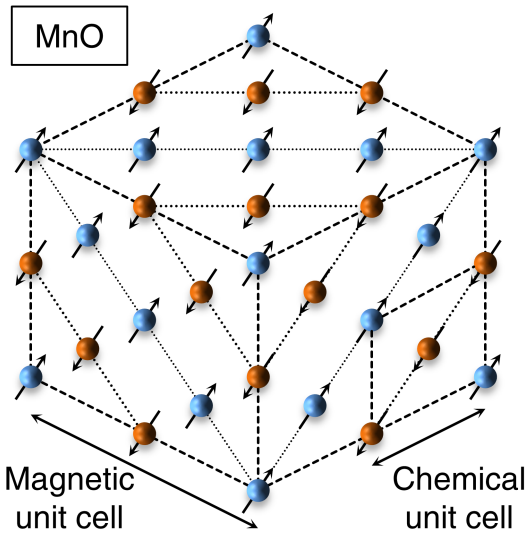

Figure 4.11: The magnetic cell structure of MnO, where Mn ions are located on a face-centered cubic lattice. The O^{2-} ions are not shown here, for clarity.

periodic table generally have substantially different scattering cross sections and can be distinguished. The nuclear dependence of scattering allows isotopes of the same element to have substantially different scattering lengths for neutrons, so that isotopic substitution can be employed. Neutrons are a highly penetrating probe, allowing for a non-destructive investigation of the interior of a material, rather than just the surface layers probed by techniques such as X-ray scattering, electron microscopy or optical methods.

Neutrons have no charge, which is why the electron clouds are invisible to them. However, if an ion has a net magnetic moment, the neutron's magnetic moment will interact with it. As a result, the spin-up and spin-down electronic moment 'look' different to the neutrons. Hence, when a sample is magnetically ordered, new peaks in addition to the nuclear peaks, can appear in the neutron diffraction pattern. For example a neutron diffraction pattern of antiferromagnetic MnO powder is shown in Fig. 4.10 taken from ref. [133]. Above $T_N = 116$ K there are neutron diffraction peaks resulting from the face-centred cubic (fcc) lattice of Mn ions. Below T_N, the magnetic structure is as shown in Fig. 4.11 with spins all being parallel within each (111) plane, But the moments in the any two adjucent (111) planes are antiparallel. The magnetic unit cell is thus double the size of the chemical unit cell, therefore, new peaks suddenly appear in the neutron diffraction pattern below T_N. The amplitude of the magnetic Bragg peaks can be used as a measure of the strength of the magnetic order, and hence the development of magnetic order in a sample can be followed as a function of temperature.

The amplitude of the scattering from a magnetic moment depends on the direction of alignment of the moment. Hence neutron diffraction can be used to determine the arrangement of the atomic magnetic moments in a magnetically ordered crystal.

In a periodic system, sharp Bragg reflections occur when the scattering vector $\boldsymbol{Q}$ equals a reciprocal lattice vector $\boldsymbol{\tau}$. In a helimagnet, there is an additional periodicity in the system because of the helix which can be described by the wave vector of the helix $\boldsymbol{h}$. The helix, hence, has its axis along the vector $\boldsymbol{h}$ and the pitch of the helix is equal to $2\pi/h$. Bragg reflections are then observed also at $\boldsymbol{\tau} \pm \boldsymbol{h}$. Since the helix pitch is larger than the lattice spacing, $h < \tau$ so that these Bragg peaks observed above

the magnetic transition temperature are still observed but together with smaller satellite peaks on either side of each Bragg peak below the transition temperature.

Neutron scattering is the most direct method available for determining the details of the magnetic state of a sample. Neutrons are however expensive and because neutrons interact relatively weakly with matter, large sample quantity is needed.

4.4.2 Inelastic neutron scattering and magnetic excitation

Inelastic neutron scattering is one of most powerful techniques for the measurement of the energy dispersion of elementary excitations in the energy range of $1 \sim 10^3$ meV. The excitations that one generally deals within condensed matter systems include, phonons, magnons or spinons. In a neutron scattering event both the conservation laws of momentum and energy (given in equations 4.3 and 4.4) have to be obeyed. This makes scattering by a single crystalline sample inevitable. The scattering experiments are most easily realized with the help of a triple-axis spectrometer, introduced in the subsection 4.4.3.4. In an experiment using a triple-axis spectrometer, there always exists the possibility of keeping one variable $\boldsymbol{Q} = \boldsymbol{q} + \boldsymbol{\tau}$ (or $\boldsymbol{q}$) or ω constant (see figure 4.4.2 for a description of $\boldsymbol{Q}$, $\boldsymbol{q}$, and $\boldsymbol{\tau}$. ω is the frequency of the incident neutron). Therefore, an experiment can be precisely performed at any point in reciprocal space. In figure 4.12 we have shown both constant-q and constant-ω scans for the dispersion ($\omega_s(\boldsymbol{q})$, s is the mode of vibration) of a given excitation. For a constant-q (or constant-ω) scans, the momentum (or energy) transfer $\boldsymbol{q}$ is kept fixed and the intensity of the scattered neutrons is maximum for $\omega = \omega_s(\boldsymbol{q})$.

Let us consider an scattering event with incident neutron flux of energy E_i and momentum $\boldsymbol{k}$ scattered from the sample crystal with energy E_f and momentum $\boldsymbol{k'}$. The differential scattering cross-section is defined as the fraction of neutrons from an incident flux scattered by the sample into a given solid angle $d\Omega$ with a final energy between E_f and $E_f + dE$, given by $\frac{d^2\sigma}{d\Omega dE}$. Here, the neutron introduces a very weak perturbation to the scattering system. Thus, the differential scattering cross-section in

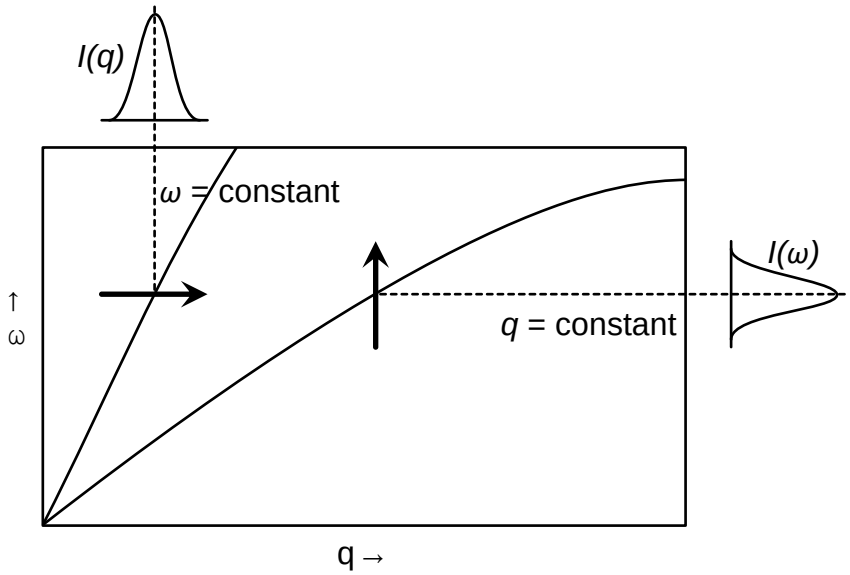

Figure 4.12: Constant-ω and constant-q scans: depending on the slope of the phonon branch one of the two scan modes is typically used.

this case as derived by *Shirane et al.* using the Fermi's Golden Rule and the Born approximation for the interaction, is given by [134],

$$\frac{d^2\sigma}{d\Omega dE} = N\frac{k'}{k}S(\boldsymbol{Q}, E) \tag{4.6}$$

where N represents the number of scattering centers in the sample, and $S(\boldsymbol{Q}, E)$ is the scattering function. In a neutron scattering experiment the measured quatity is $S(\boldsymbol{Q}, E)$, which helps in determination of the microscopic properties of system under study. For example, in an elastic neutron scattering experiment on a single-crystal, the scattering function $S(\boldsymbol{Q}, E)$, helps in determining the potential of interaction between the neutron and the atomic nuclei in the sample crystal. On the other hand, in an inelastic neutron scattering event due to the phonon, a neutron is scattered by creating (or destroying) a single phonon, the scattering function $S_{ph}(\boldsymbol{Q}, E)$ determines the response (frequencies and damping) of phononic modes in the scattering system. In the later case, the scattering function is proportional to the squared dynamic structure factor as expressed by,

$$S_{ph,s}S_{ph}(\boldsymbol{Q}, E) \propto \left|\Sigma_j b_j(\boldsymbol{Q}\cdot\boldsymbol{\varepsilon_{j,s}})e^{i\boldsymbol{Q},\boldsymbol{R}_j}e^{-W_j}\right|^2 \tag{4.7}$$

where b_j, $\boldsymbol{R}_j$, and $\boldsymbol{\varepsilon}_{j,s}$ represents the scattering length, the atomic position, and the polarization vector of the vibration mode s at the jth-site. e^{-W_j} represents the Debye-Waller factor, defines the thermal average of the atomic displacements. In the case of scattering from polycrystalline samples, the resulting scattering function, averaged over all the possible directions of $\boldsymbol{Q}$, is proportional to the total scattering cross section, including both coherent and incoherent scattering. In the case of a cubic crystal, on the other hand, the scattering function is proportional to the squared modulus of the momentum transfer, given by [134]:

$$\boldsymbol{S}_{ph}(\boldsymbol{Q}, E) \propto \left(\frac{1}{1 - e^{-E/k_B T}}\right) e^{-2W} \frac{\langle(\boldsymbol{Q} \cdot \boldsymbol{\epsilon})\rangle}{E} G(E) \propto Q^2 \tag{4.8}$$

The first term in the brackets defines the thermal population of excitations, and is also known as the thermal factor or Bose factor, can be expressed as $(n(E) + 1)$, $G(E)$ represents the phononic density, and $(\boldsymbol{Q} \cdot \boldsymbol{\varepsilon})^2$ is the average taken over all modes with energy E.

In the case of magnetic scattering, the differential scattering cross-section for an isotropic paramagnet is given by [135];

$$\frac{d^2\sigma}{d\Omega dE} = \frac{k'}{k}(\gamma r_e)^2 S_{magn}(\boldsymbol{Q}, E) \tag{4.9}$$

Where $(\gamma r_e)^2$ represents a coupling constant with neutron magnetic moment γ and classical radius r_e of the electron. $S_{magn}(\boldsymbol{Q}, E)$ defines the magnetic scattering function, which is the Fourier transform of the spin-spin correlation function in time and space. A neutron scattering event applies a small perturbation to the spin system, thus its response is proportional to the spectrum of spontaneous fluctuations (fluctuation-dissipation theorem). Therefore, the magnetic scattering is just the dissipative part of the dynamic susceptibility $\chi''(\boldsymbol{Q}, E)$.

$$S_{magn}(\boldsymbol{Q}, E) = \frac{1}{\pi}\left(\frac{1}{1 - e^{-E/k_B T}}\right) \chi''(\boldsymbol{Q}, E) \tag{4.10}$$

The imaginary and real parts of the dynamic susceptibility are related by the Kramers-Kronig relations, and χ" can be rewritten as

$$\chi''(\boldsymbol{Q}, E) = f^2(Q)\chi'(Q)EP(\boldsymbol{Q}, E) \tag{4.11}$$

where $f^2(Q)$ is the magnetic form factor, which is the Fourier transform of the magnetisation spatial density around the atom, and $P(E)$ is a power spectrum which for paramagnetic scattering and in the case of excitations with a finite lifetime[134] has a Lorentzian lineshape:

$$P(\boldsymbol{Q}, E) = \frac{\Gamma_Q}{2\pi}\left[\frac{1}{(E - E_0(\boldsymbol{Q}))^2 + \Gamma_Q^2} + \frac{1}{(E + E_0(\boldsymbol{Q}))^2 + \Gamma_Q^2}\right] \tag{4.12}$$

Here, Γ_Q is the linewidth, that is, the half width at half maximum of the peak and E_0 is its centroid. The first term in the bracket corresponds to the creation of the excitation (the Stokes term) and the second one, called the anti-Stokes term, the annihilation of it.

4.4.3 Neutron instruments

4.4.3.1 Spallation neutron source

The term “spallation" implies the chain of events that take place in a process. In this process the target (Pb at PSI) is bombarded with high energy nuclides ($\sim$ GeV) with a de Broglie wavelength $\lambda = h/\sqrt{2mE}$ shorter than the dimension of the target nucleus. The energy is then transferred to the other nuclides in the nucleus which evenly distributes the energy in the individual nucleus (intra-nuclear cascade). The highly energized nucleus then disintegrate to more nuclides (more neutron and less protons as shown in Fig. 4.13). Some of the nuclides escape the target and some of them excites the nuclides in the other nuclei of the target (inter-nuclear cascade), triggering further chain of the reaction and evaporates more neutrons from the target.

At PSI the neutrons are produced by bombarding a the spallation target (lead rods, enclosed in zircaloy tubes and cooled flowing heavy water) by protons of energy 590 MeV and current up to 2.3 mA. The protons are produces by ionizing the H atoms and then accelerate to 870 keV by a Cockcroft-Walton generator. The proton beam is then

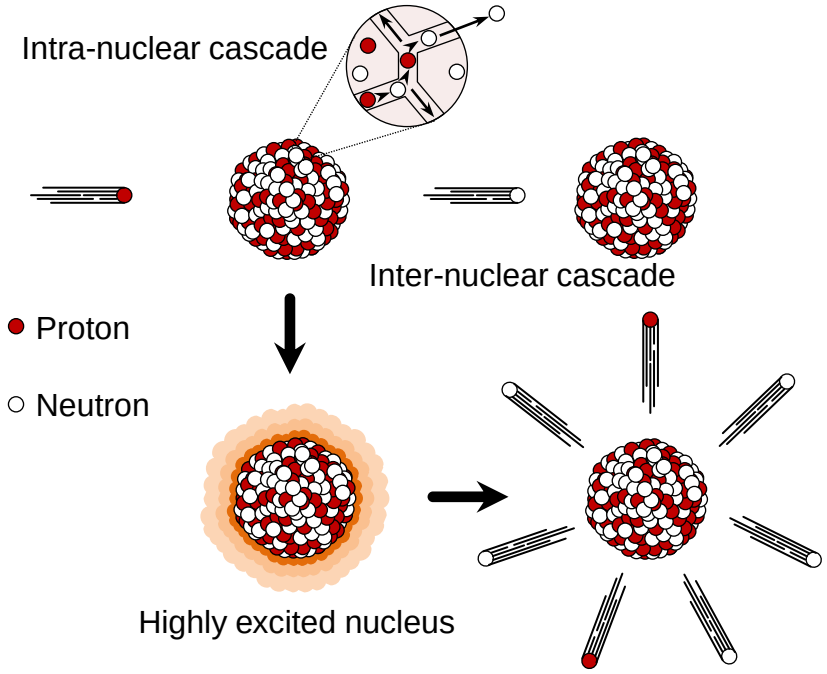

Figure 4.13: Schematic representation of spallation process (adapted from [136]).

injected to a 4-sector injector cyclotron to accelerate it to 72 MeV. The final acceleration to 590 MeV takes place in a 8-sector mainring cyclotron before hitting the target.

4.4.3.2 Moderation of the neutrons

Though the amount of low-energy electron yield in this case are comparable to that of from fission reaction. The energies of the neutrons produced in this process also extends to ranges to the that of the incident particle, due to the intra-nuclear cascading. Thus produced neutrons in a spallation source ranges in MeV in energy, whereas, in condensed matter research the required neutrons of energy few hundreds of meV. So, to achieve highest flux of neutrons with energy in this range the generated neutrons need to be slowed down. This can be done by collision with the moderator made of light atoms such as D_2O or H_2O. The slowing down process of the neutron takes place in about 10^{-6} s after which the neutrons are in thermal equilibrium with the moderator kept at constant temperature T according to the Maxwellian Distribution ,

$$\Phi(\lambda) \propto \exp\left(-\frac{h}{2k_B T m \lambda^2}\right) \tag{4.13}$$

where λ and m represents the wavelength and mass of the neutron, respectively. In this case the moderators are kept at room temperature, these neutrons are called thermal neutrons, with a maximum peak flux around the neutron wavelength $\lambda \approx 1$ Å, shown in figure 4.14.

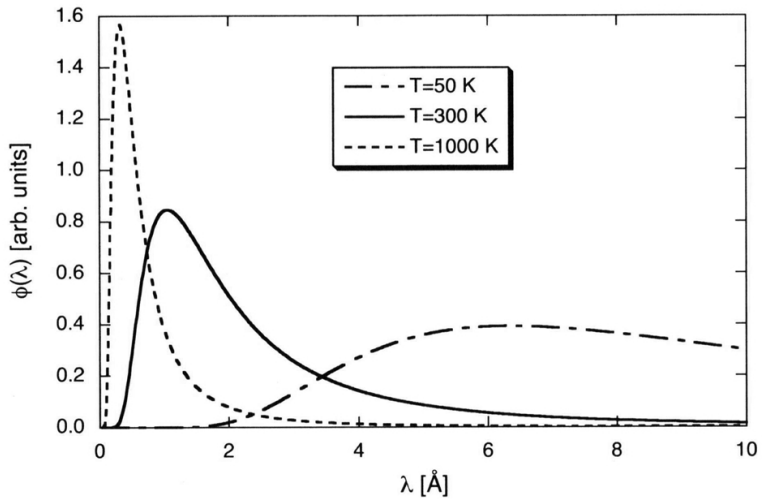

Figure 4.14: Wavelength distribution of neutrons from cold (50 K), thermal (300 K), and hot (1000 K) moderators[137].

However, use of these thermal neutrons in a scattering experiments where cold or hot neutrons are required will experience reduction of neutron flux. For these experiments, in order to obtain neutrons with desired energy, the moderated neutrons are then passed through a cold or a hot source. Maxwellian energy distribution of thermal neutron can be red-shifted by passing them through a cold source (a vessel containing D_2 at $T \geq 20$ K), or can be blue-shifted a hot source (a graphite bloc heated up to $T \leq 2000$ K). Typical spectral shift for cold and hot neutrons are shown in figure 4.14. In an neutron experiment the flux of final beam can be optimized by suitably choosing the desirable neutron spectrum.

4.4.3.3 The ^{3}He detector

Neutrons are electrically neutral, thus they can only be detected indirectly through nuclear reactions. Typically, the detection of neutron is done through a nuclear reaction between the incoming neutron and the detection element present in the detector. The reaction emit ionizing radiation and/or ionizing particle which can then be detected by the electrical circuits. The nuclear reactions involved in neutron detection process are:

$$
\begin{aligned}
&{}^1_0\mathrm{n} + {}^3_2\mathrm{He} \rightarrow {}^3_1\mathrm{H} + {}^1_1\mathrm{H} + 0.77\mathrm{MeV} \\
&{}^1_0\mathrm{n} + {}^6_3\mathrm{Li} \rightarrow {}^3_1\mathrm{H} + {}^4_2\mathrm{He} + 4.77\mathrm{MeV} \\
&{}^1_0\mathrm{n} + {}^{10}_5\mathrm{B} \rightarrow \begin{cases} {}^4_2\mathrm{He} + {}^7_3\mathrm{Li} + \gamma(0.77\mathrm{MeV}) + 2.3\mathrm{MeV} & (93\%) \\ {}^4_2\mathrm{He} + {}^7_3\mathrm{Li} + 2.79\mathrm{MeV} & (7\%) \end{cases}
\end{aligned}
$$

Where, ^{3}He and $^{10}BF_3$ are used in their gaseous form filled in detector tube, ^{6}Li is used as a film in the scintillator detectors. The detectors, used in the neutron experiments presented here, are based on He-tubes.

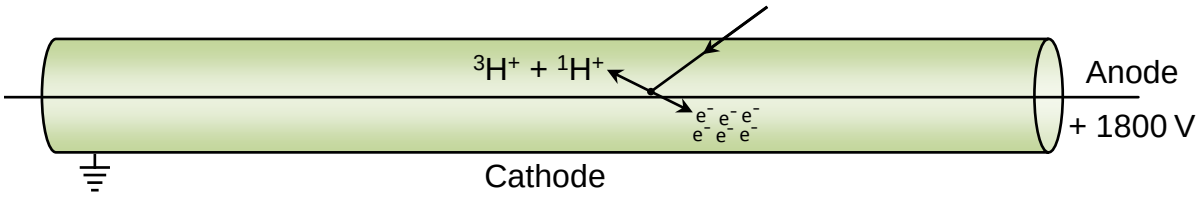

Figure 4.15: Schematic sketch of a ^{3}He gas tube (adapted from reference [137]).

In figure 4.15 we have shown the schematic working of a He-tube. Typically these tube are made of steel, which constitutes the cathode. The tube are filled with ^{3}He at pressure 5 $\sim$ 10 bar. The anode is a Cu-wire spanned through the axis of the tube, which is maintained at a high voltage ($\sim$ 1800 V). The electron produced by a nuclear reaction are then accelerated towards the anode by the potential gradient induced by the anode voltage. The collision between these accelerated electron and the gas molecules further ionize it and cause an avalanche effect. This amplifies the ionization by up to 10^5 times their initial value. This type of gas tube is called a proportional counter; it is

also known as a Geiger counter. The high gain achieved in this process enables a single neutron to be detected easily. These tubes are insensitive to magnetic field and the γ-rays generated in the nuclear reaction can easily be discriminated. However, the He-tube detectors have rather slow response time, which makes them not suitable for detection of neutrons with high-count rate. For high-count rate experiments, scintillator detector with ^{6}Li are very useful (Count rate several MHz). However, they are sensitivity to gamma rays and magnetic field and proper shielding is required.

A position sensitive detection is also possible though the Geiger counter. For this a position sensitive detector possesses a resistive wire as the anode placed across the tube. The position of the detection event is determined by ratio of the charge measured at the ends of the wire. By this process a spatial resolution of 10 mm can be achieved. In order to achieve better resolution, the anode and cathode can be replaced with a large number of thin wires assembled in a plane and mounted between two plates which are composed of separate cathode strips. A spatial resolution of 1 mm can be achieved by this technique.

All neutron instruments need beam monitors to measure the incident flux. Since the incident flux must not be attenuated, monitors are necessarily insensitive. Monitors can be either a scintillator or a low pressure ^{3}He tube.

4.4.3.4 Triple-axis spectrometer

In detection of inelastic neutrons the *triple-axis spectrometers* (TAS) are the most versatile instruments. These instruments are one of very few instrument that provide the finest resolution and allow a controlled access to the variables $\boldsymbol{Q}$ and ω of the scattering function $S(\boldsymbol{Q}, \omega)$. In figure 4.16 the working of a TAS has been shown schematically. As the name suggest the TAS possesses three axes of scattering: the monochromator, the sample crystal and the analyser. The monochromator selects a neutron beam with a well defined wave vector $\boldsymbol{k}$ from white spectrum of the neutron source. The monochromatic beam is then scattered from the sample. The scattered beam with wavevector $\boldsymbol{k'}$ is then reflected by the analyser crystal and directed onto the neutron detector, thereby, defining the energy transfer $\hbar\omega$ as well.

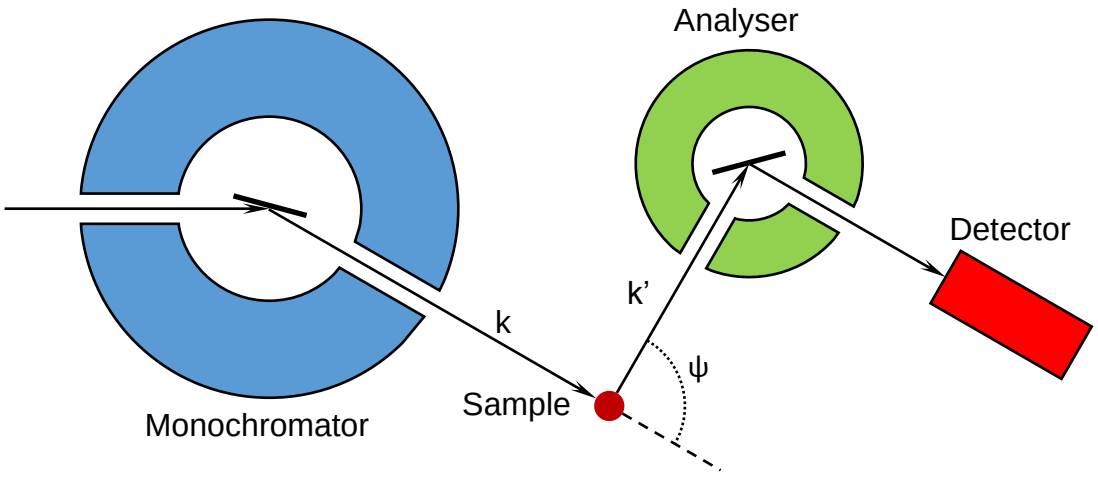

Figure 4.16: Basic layout of a triple-axis spectrometer (adapted from reference [137]).

The three axes of the spectrometer provide an outstanding control over the energy and momentum of the incident and scattered neutron been to be detected. This enables one to collect data for any predetermined point in the reciprocal space (constant-$\boldsymbol{Q}$ scan) or a fixed energy transfer $\hbar\omega$ (constant-E scan) along a particular line in the reciprocal space. Therefore, the determination of the dispersion relation in any given sample-crystal can be controlled easily (See preceding subsection). Of course, general scans in $\boldsymbol{Q}$ and ω can also be done. In a neutron scattering experiment in TAS all quantities $(\boldsymbol{k}, \boldsymbol{k'}, \psi)$ defining the momentum and energy transfer are variable, neutron data can be collected at any point in $\boldsymbol{Q}$,ω space. Typically a scan with $\boldsymbol{k'}$ fixed is performed. This involved minimum calculation to obtain cross-section from the neutron counts.

The resolution of a TAS is determined by the phase space volume transmitted by the monochromator and analyser-crystal in the scattering plane as well as on the slope of the dispersion of the measured excitation. The TAS allows different configurations of the neutron path in terms of either clockwise or anticlockwise turn angles at each axis in order to achieve optimal resolution characteristics. The general features of the resolution function including analytical expressions and guides for its determination were given by Cooper and Nathans [138] and Dorner [139]. Schematic diagrams and specifications of two triple-axis spectrometer used in this work have been shown in Figs. 4.17 and 4.18.

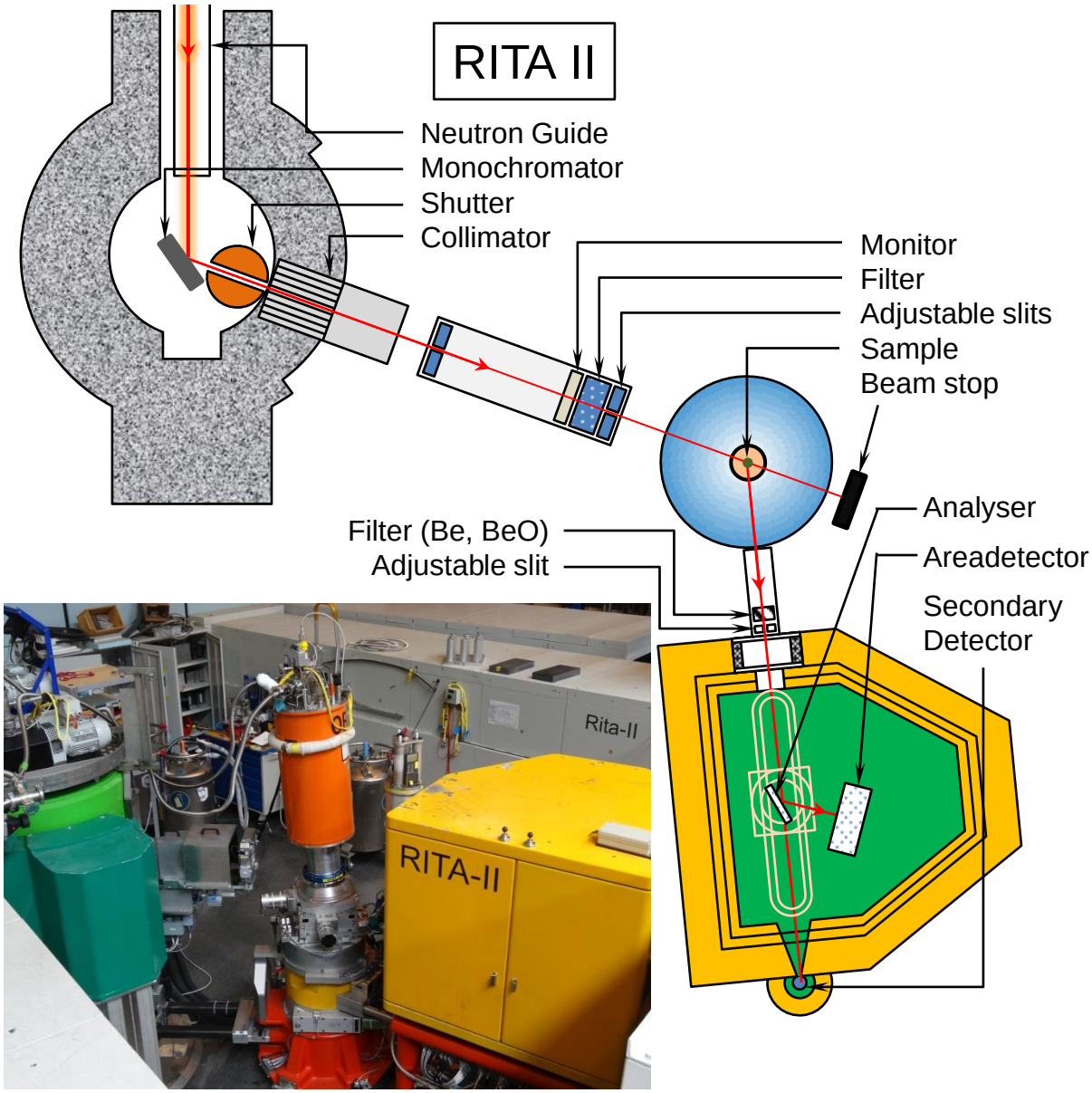

Parameters	Values
Distance cold source	RITA-II 42 m
Monochromator scattering angle	31° M
Neutron energy (PG 002)	2.5 meV M 5.7 Å> λ > 2.0 Å1.1 ÅM^{-1}
Sample Scattering Angle	$2\theta_S$
Sample environment maximum load	500 kg
External collimation	20', 40', 80', open
Detector	Position Sensitive He Detector
Typical spectrometer resolution (FWHM) (for open-40'-40'-40')	Δ E = 40 μeV (E = 2.5 meV) ΔE = 0.9 meV (E = 14.7 meV)
Filters	cooled Be, BeO, pyrolytic graphite

Figure 4.17: The Schematic of RITA II spectrometer and its photograph

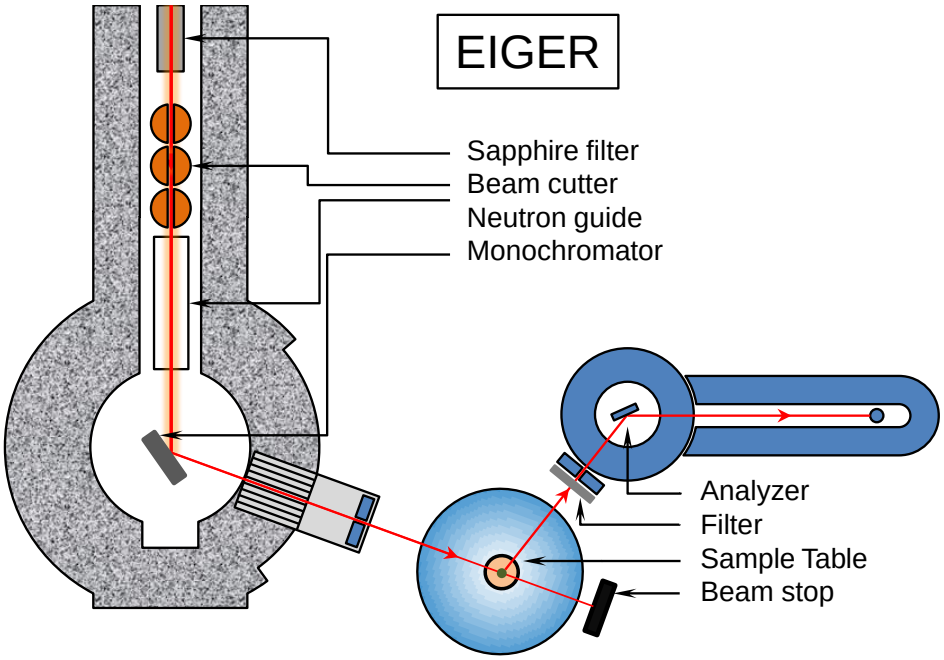

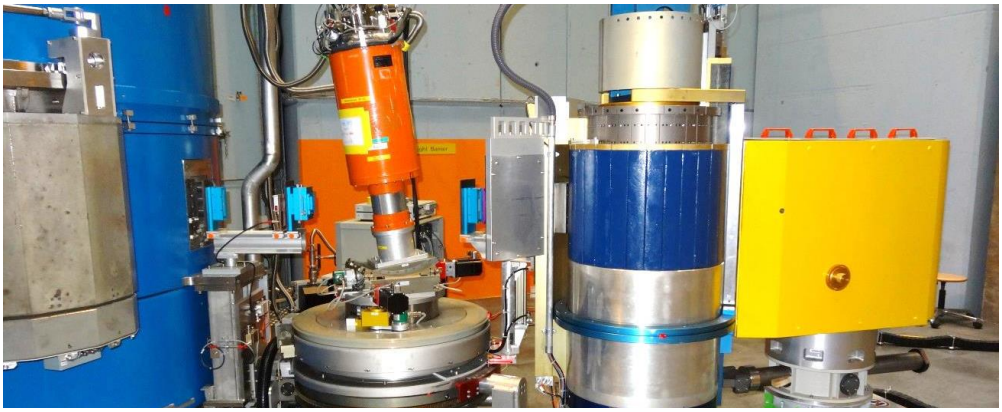

Component	Properties	Value
Monochromator	double focusing 15 x 9 pieces PG 20 x 20 mm each alignment	30' mosaicity
Virtual source	10mm	
Shielding	non-magnetic	
Beam size at sample	double focusing condition	40 x 40 mm
Filter	PG (37 or 70mm)	
Analyzer	PG horizontal focusing	
Detector	He-tube	
Collimation	20',40' or 80' available	
Elastic resolution	at k = 2.66 Å	0.66 meV
Energy transfers	at k = 2.66 Å	-11 meV $\leq E_N \leq$ 60 meV (accessible) -10 meV $\leq E_N \leq$ 45 meV (recommended)

Figure 4.18: The Schematic of EIGER spectrometer, its photograph and its various

4.5 Muon spin rotation (μSR)

μSR is a very useful technique in experimental condensed matter to investigate the magnetic properties of antiferromagnets, spin-gap systems, spin glasses as well as on ferromagnets by measuring the internal magnetic fields inside matter by means of the spin precession of implanted polarized muons. It also provides information about magnetic fluctuations and spin dynamics, even above the magnetic transition temperature. In the present study we have used μSR technique to find the spin dynamics of the magnetic ground state.

Muons are spin 1/2 unstable, subatomic, quasi particles with a lifetime of 2.2 μs. Muons are produced by high energy protons bombarding onto solid targets. It is a two-step process. In the first step, the protons above certain threshold energy collides with low atomic number nuclei, typically of Carbon or Beryllium. In this step Pions are produced. In the second step, the Pions further decay into Muons. To conserve the total number of lepton a antiparticle is produced in this process.

$$\begin{aligned}
&\text{Step1 }: p^+ + p, n \rightarrow n + p, n + \pi^+ \\
&\text{Step2 }: \pi^+ \rightarrow \bar{\mu}^+ + \nu_\mu, \\
&\qquad\quad \pi^- \rightarrow \mu^- + \bar{\nu}_\mu
\end{aligned}$$

In a typical μSR experiment polarised Muons are incident on the sample crystal, and almost instantaneously muons gets implanted at the interstitial sites and stay there until they decay into positrons.

$$\bar{\mu}^+ \rightarrow \bar{e}^+ + \nu_e + \bar{\mu}_\mu \tag{4.16}$$

The decayed products are then detected by the detectors, which carries the information about the internal field of sample at time of decay.

In the present study the muon-spin spectroscopy (μ+SR) were performed at SμS (PSI) on the GPS spectrometer (πM3.2 beamline) in the temperature region 1.6 K $< T <$ 20 K, in conditions of zero-magnetic field (ZF$-\mu^+$SR). At SμS Muons are

generated using 590 MeV proton beam (10^{16} s^{-1}) accelerated using a synchrotron and directed onto a 5 mm pyrolythic carbon target (M). Only a fraction of protons is used to keep the frequency of the muons at 50 kHz. This ensures a continuous muon beam, only one muon is present in the sample at any given time. The produced Muons are then goes through a moderator consists of two components, (1) the separator, which, at moderate field, kicks out the positrons and pions and deflectes outside the beamline from the muons and (2) the spin-rotator, where a large magnetic field is used to rotate the spin of the Muons from antiparallel to momentum, towards a direction perpendicular to momentum before implanted onto sample crystal.

The recoiled positrons form the Muon decay process are then captured by the detector arrangement consisting of a muon detector (M), 6 positron detectors (Forward, Backward, Up, Down, Right Left, with respect to the direction of the incident beam) and a Backward veto detector, which helps to get rid of the muons passed through the sample and their decayed positrons, by collimating them to a blank spot.

Chapter 5

Single Crystal Growth

As discussed in chapter two, the physical properties of quantum spin chains are highly sensitive to the presence of defects/disorder in the crystal. Upon lightly doping, novel magnetic ground states can be induced in a spin chain. Recent experimental investigations have indicated that the spin excitation spectrum of the Heisenberg spin $1/2$ chain is also very sensitive to doping within or outside the chains [72–74]. One way to understand and explore the role of defects in quantum spin chain compounds is by deliberately introducing controlled level of defects of various kinds during the crystal growth process through chemical doping. However, for such a plan to succeed we must ensure that the doped crystals are of sufficiently high-quality and are free from undesirable defects that may have been introduced during the crystal growth process.

The present chapter deals with the crystal growth of lightly doped quantum spin chains. An attempt has been made to incorporate defects of various kinds (i.e., different spin quantum number) in a controlled amount in the spin $1/2$ chains of canonical spin chain compounds Sr_2CuO_3 and $SrCuO_2$. Here, will give details of the single crystal growth of these compounds and their doped variants using the so-called travelling-solvent-floating-zone (TSFZ) method associated with an optical image furnace. We will first argue why TSFZ would be the most appropriate technique to accomplish this task. Thereafter, starting from the basic principle of the TSFZ growth process in the first section, we will give the details of the crystal growth parameters, and structural characterisations in the second section. Finally, in the third section we will analyse our growth experiments to understand the importance of several decisive factors including process parameters, lamp power dependence of the floating zone stability and floating

zone composition of all the grown crystals.

5.1 Principles of crystal growth

The single crystal of a material can desirably be obtained by transforming its polycrystalline compact under high-pressure/temperature conditions. However, such solid-solid transformation may not always be feasible. A rare example is that of tungsten (W). The single crystals of tungsten can be obtained by plastic deformation followed by an annealing at high-temperatures, which enables formation of large single crystalline grains sizing up to 20 mm in length [140, 141]. More widely used methods of single crystal growth include melt-growth and chemical-transport-method. Between these two, melt-growth is almost always favoured in view of the relatively larger size of the grown crystals. Chemical transport method is more effective when one or more components in the growth process possesses a high-vapour pressure. When a crystal is in dynamic equilibrium with its surroundings the free energy is at its minimum and no growth can occur. This equilibrium has to be disturbed suitably for the growth to occur. This may be done by an appropriate change in the conditions. The driving force for crystallization comes from the supersaturation or the supercooling of the liquid or the gas phases with respect to the target component whose growth is required.

One of the examples of melt growth is the high-temperature solution or flux-growth method. Here the crystal growth is initiated by making a supersaturated solution of the target phase in an appropriate flux at suitably high-temperature followed by a controlled cooling of the solution. During the slow-cooling process the crystals of the solute appear over the available nucleation points and grow in size as the time progresses.

Single crystals of some compounds can also be grown directly from their corresponding stoichiometric melts using the Bridgman [142] or the Czochralski methods [143]. In the Bridgman method, the melt, which is held in a crucible, is solidified by passing it through a region of constant temperature gradient. This results in a directional solidification of the melt. In this process, the crystal nucleates at the tip of the crucible, which grows in size as the crucible is made to slowly traverse through the temperature

gradient. In the Czochralski method, large single crystals are grown by pulling a single crystalline seed out of the stoichiometric melt. However, one of the drawback of these growth methods is that they cannot be employed to grow single crystals of compounds that exhibits a non-congruent (or incongruent) melting behaviour. On the other hand, the flux method, which can be applied to incongruently melting solids, does not produce large single crystals due to the presence of many nucleation sites.

The growth process which can be successfully employed to grow large crystals of both congruently and the incongruently melting solids is based on the optical floating zone method. In table 5.1 we have presented a comparison between the different melt growth techniques, which provide a general guideline for choosing the correct growth technique and the quality expected of the grown crystal.

Table 5.1: A comprehensive comparison between the single-crystal growth techniques

Growth techniques	Flux growth	Bridgman growth	Czochralski growth	Floating-zone growth
Crucible	✓	✓	✓	×
Solvent/flux	✓	×	×	×
Grown crystal size	10 ~ 50 mm^3	~ cm^3	> cm^3	~ cm^3
Growth of non-congruent melting solids	✓	×	×	✓

From the above comparison it is evident that optical floating-zone method has a high crystal growth yield when it comes to single-crystal growth of incongruently melting solids. Moreover, being a crucible-free method, contaminations of the grown crystal by the crucible material or from the flux used can be completely avoided, which is specially crucial if one is specifically interested in investigating the effect of dilute impurities on the physical properties.

5.1.1 Optical floating zone growth

The zone melting process was first introduced in 1951 by *W. G. Pfann*, a metallurgist at Bell Laboratories [144], who used this method to refine metals and called it a zone-refining technique. In 1952 *Theurer*, also at Bell Laboratories, realized the floating zone

process, which was later awarded a US patent [145]. Later on, *Keck* and *Golay* of the US Army Signal Corps developed a similar technique independently, by using incandescent heating with a short cylindrical tantalum heater rather than an optical system and published their results in 1952 [146]. However, the optical floating zone technique received far more attention because by using infrared lamps of suitable power and filament geometry the volume of the molten-zone and the temperature gradients can be controlled suitably to grow crystals of a wide range of solids.

5.1.1.1 Image furnace

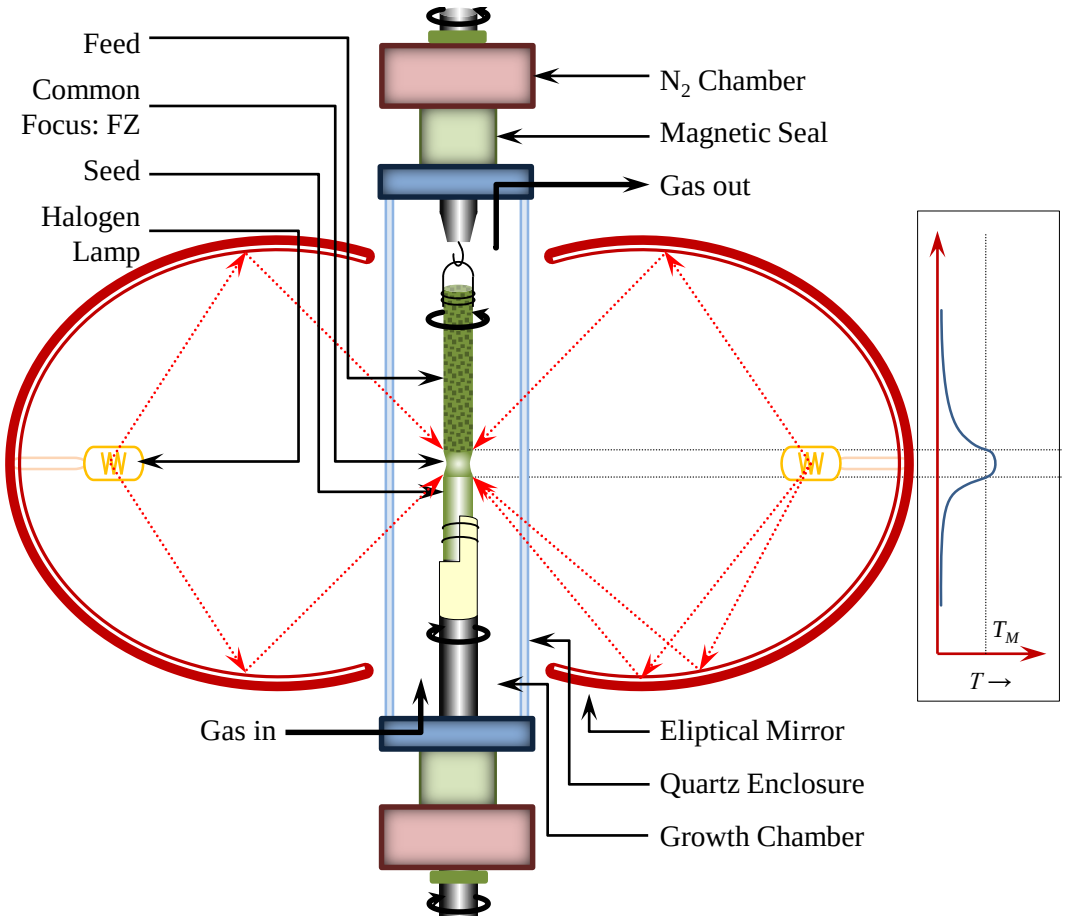

Figure 5.1: General schematic of the vertical section of the optical furnace used in the present work. Inset: the temperature gradient across the vertical axis of the furnace.

In an image furnace optical radiations are used to form and suspend a molten zone between two solid rods. Halogen or xenon lamps are typically used as the source of

radiations. These radiations are made to converge using ellipsoidal shaped mirrors to form the liquid zone. The number of mirrors and the type of radiation source can vary from furnace to furnace. We used a four-mirror optical-floating-zone Furnace (Model: FZ–T–10000–H–HR–I–VPM–PC, Crystal System Corporation, Japan). A schematic drawing of the vertical section of the furnace is shown in figure 5.1. The furnace consists of four halogen lamps, each placed at one of the foci of each of four ellipsoidal reflector. The second focus of these four reflectors coincide at a point on the vertical axis of the furnace inside the growth chamber. The energy flux of the lamps, after reflections from the walls of the reflectors, converges at their common foci where a steep vertical temperature gradient is created. A tentative temperature profile along the vertical axis of the furnace is shown in the inset of figure 5.1. In a typical crystal growth experiment, a molten zone is formed between the polycrystalline feed and the seed. The feed rod is a polycrystalline rod made by densifying the powder of the specimen to be grown as a single crystal. The densification is achieved by sealing the pre-synthesized powder of a given material in a rubber tube, which is pressed iso-statically in a water bath under a pressure of about 70 MPa. The rod is the removed from the tube and annealed at temperatures slightly below ($\sim$ 90%) of the melting temperature. The feed rod is suspended from the upper shaft of the furnace and the seed rod is clamped to the lower shaft using an alumina holder. For fixing the feed and seed nickel wire is used, since it has low vapour pressure and it remains non-reactive upto very-high temperatures. The seed is either a single crystal cut from a previously grown crystal boule; or, if the growth is being carried out for the first time, a portion cut from the polycrystalline feed rods itself is used as a seed. The growth process takes place in a closed chamber (made of high quality quartz to remain transparent to near-infrared and visible radiations). The upper and lower shafts are sealed into the chamber through magnetic fluid seal to ensure high-purity of the chamber atmosphere and at the same time to allow free rotation of the shafts. One of the features of this type of magnetic fluid sealing is that it cannot sustain high differential pressures ($>$ 0.1 MPa). So, to obtain higher pressure in the growth chamber an equal pressure of N_2 is applied outside the magnetic seal.

5.1.1.2 Advantages of floating-zone technique

- It is a crucible free technique which helps in achieving higher crystal purity.
- The method of zone-melting, as was originally envisaged by *W. G. Pfann*, helps eliminate the impurities that may have accumulated during the initial process of preparing the feed rod.
- Growth parameters, including the growth atmosphere, growth speed, rotation speed of the shafts, can be easily controlled.
- Large single crystals of incongruently melting compounds can also be grown using the so-called travelling-solvent-floating-zone technique.
- The furnace allows for real-time monitoring of the growth process, which helps in optimization of the growth parameters.
- Temperature profile can be varied by choosing lamps of suitable power and by choosing suitable geometry of the lamp filaments.
- Magnetic fluid seal enables high vacuum as well as high pressure up to 10 bar in the growth chamber and hence provide outstanding control on the growth atmosphere.

5.1.1.3 Disadvantages of floating-zone technique

- Maximum pressure in the growth chamber is limited to 1 MPa. However, in a vertical image furnace a pressure upto 20 MPa can be applied [147, 148].
- As crystal growth process takes place at high temperatures, materials with highly volatile components cannot be grown using this method.
- Temperature of the floating-zone cannot be measured directly. In a vertical image-furnace, however, it can be measured by using a Shutter-pyrometer arrangement [147, 148].

- Use of four mirrors results in non-uniformity of the temperature gradient in the horizontal plane. This, however, can be avoided using a vertical furnace consisting of two-ellipsoidal mirror, where the major-axis of the mirrors coincides with the vertical furnace axis [147, 148].

5.1.1.4 Growth process and parameters

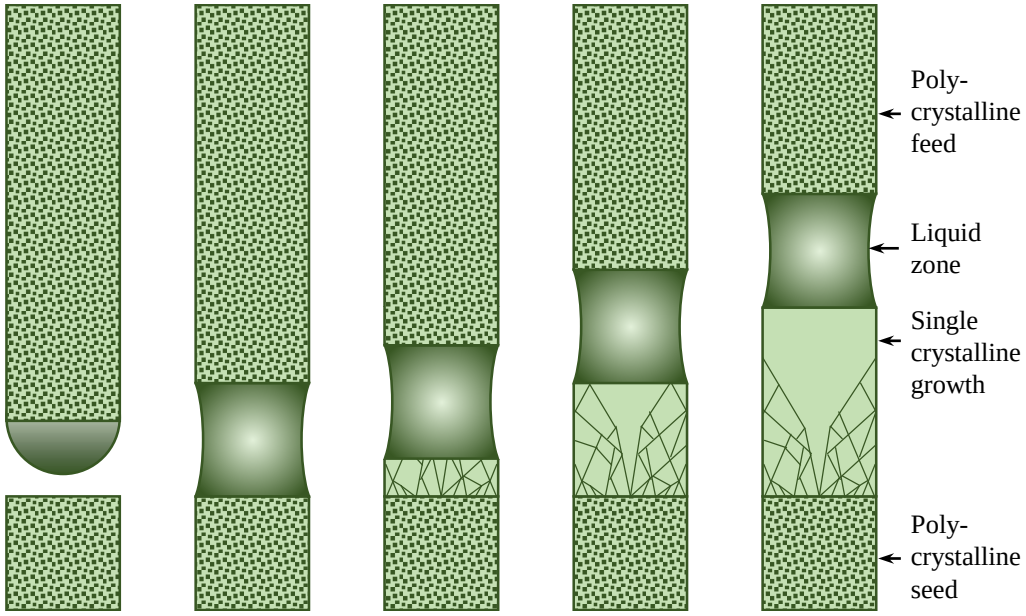

Figure 5.2: Cartoon showing various stages in a typical floating zone growth experiment (see text for details).

A floating-zone crystal growth process is carried out by gradual melting of the polycrystalline feed into the molten zone; and simultaneous crystallization of the melt from the zone on the seed. The process continues by moving the molten zone upwards (either by moving the seed and the feed rods down or by moving the mirrors-stage up). When this process is carried out at a sufficiently slow speed, the polycrystalline feed can be transformed into a single crystal. The seed is either a previously grown single crystal or a polycrystalline rod of the same compound or a compound with similar crystal structure and melting temperature. In the case of a single crystalline seed, the crystallization of zone liquid leads to an epitaxial growth of the single crystal right from the beginning. Whereas, in the case of a polycrystalline seed, large number of crystallites are first encountered. However, as the growth continues, preferably oriented domains grow

faster at the expense of others and eventually one of the domains wins, spreading out to occupy the whole growth cross-section. From here on, the single crystalline growth continues as in the case for single crystalline seed. See figure 5.2 for illustration.

The stability of a float-zone growth process is achieved by careful optimization of growth parameters. First of these is the temperature, which is directly controlled by adjusting the lamp power. The molten zone is held between the solid rods mainly due to the forces of surface tension and the force of gravity. The crystallization rate or the crystal growth speed is controlled by the travelling speed of the shafts. The growth rate is highly material specific, which ranges from very slow, ~ 0.05 mm/h (e.g. $Ba_2Sr_2Ca_2Cu_3O_{10+\delta}$[149]) to as fast as 240 mm/h (e.g. GaAs [150]), and needs to be optimized during the growth to sustain an uninterrupted growth of the crystal. Due to the use of four point sources, the temperature in horizontal plane around the molten-zone is not uniform. Therefore, to allow uniform melting of the feed and to enhance the chemical homogeneity of the floating zone, the upper and lower shafts are typically rotated in counter directions. The required rotational speeds of the rods are also material specific and can vary anywhere between $3 \sim 60$ rpm. The convection current created by the counter rotation of these rods helps in achieving temperature and composition homogeneity throughout the molten-zone, which is crucial to sustain a stable growth. For a review of growth conditions employed in the growth of various complex oxides, one may refer to the review article by Koohpayeh et al.[151].

5.1.2 Melting behaviour of solids

In single crystal growth, knowledge of the melting behaviour of the compound whose crystal is to be grown is considerably important. The melting behaviour of a compound can be obtained from the associated phase diagram. A phase diagram or a thermal-equilibrium diagram is a graphical representation of the relationship between composition, temperature and structure of various distinct phases of a system. The two types of phase diagrams that we shall deal with are shown schematically in figures 5.3 and

5.5. These are binary phase diagrams consisting of end members A and B and various phases or compounds that can be obtained through a chemical reaction between A and B under a given pressure.Typically the end members A and B are either elemental solid (for instance, lead and Tin), or oxides (for instance, SrO and CuO). As shown in these diagrams while A and B solidify at fixed temperatures (at their respective freezing points), the intermediate compositions do so over a range of temperatures; and the microstructure of the solified melt also varies across the phase diagram.

Depending upon their melting behaviour, the solids can be broadly classified into two main categories, namely; (i) congruently melting and (ii) incongruently melting solids.

5.1.2.1 Congruently melting behaviour

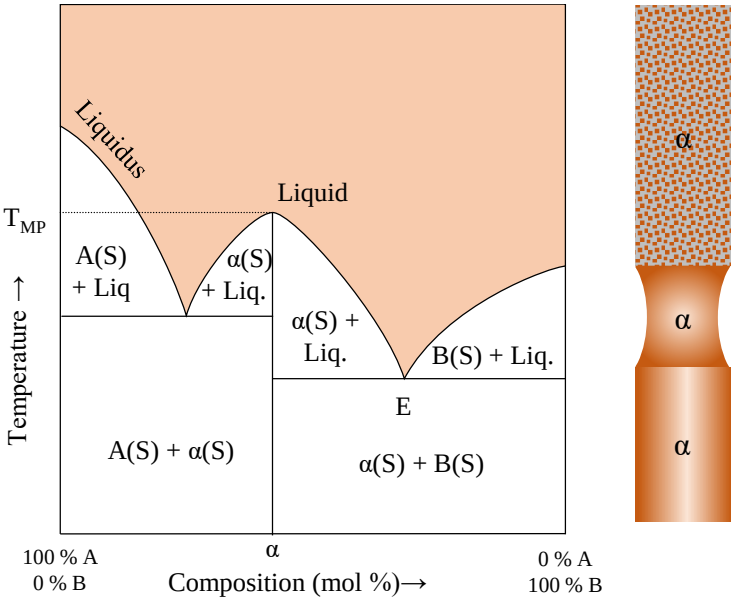

Figure 5.3: Left: Schematic of a binary phase diagram of components A and B. Right: Steady state growth condition and composition during floating zone growth of congruently melting phase α. The $x-$axis shows the composition varying between 100 % of the component A on the left of the phase diagram to 100 % of B at the opposite side.

A solid is said to be congruently melting, when it is characterised by a common equilibrium point, called the melting point (T_M),where the solid and a melt of the same

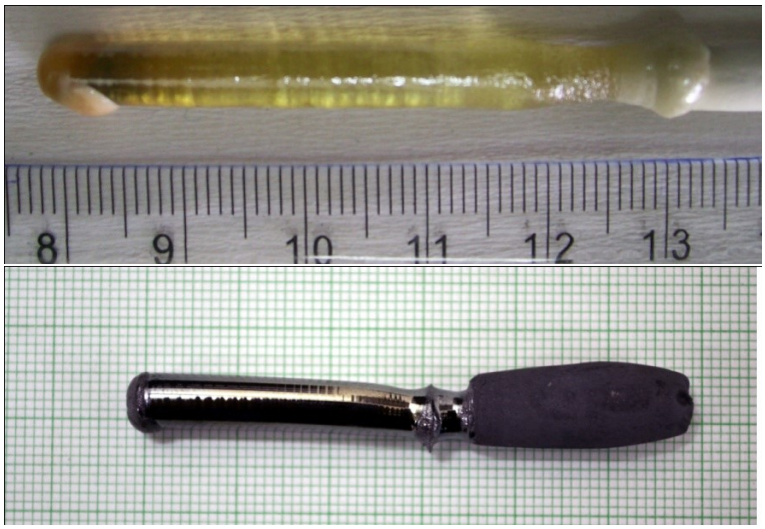

Figure 5.4: Representative images of floating zone grown crystals of congruently melting oxides $Dy_2Ti_2O_7$ (left) and Co_2TiO_4 grown during this thesis.

stoichiometry as the solid, co-exist in equilibrium. For example, in the schematic binary phase-diagram of figure 5.3, the intermediate compound α exhibits a congruently melting behaviour. As temperature increases, it remains solid till $T = T_M$. At this temperature it is transformed completely into a liquid of the same composition (i.e., α). A congruently melting solid can be grown using the floating-zone method in an image furnace as described in the previous section. During the course of this thesis, we grew several congruently melting compounds. As examples, in figure 5.4, we show the images of as-grown single crystals of Co_2TiO_4, which crystallizes with the spinel structure, and $Dy_2Ti_2O_7$, which is the well-known spin ice compound crystallizing with the pyrochlore structure. Since these compounds are not directly related to the main topic of my thesis, we will skip the details of their growth process and move directly to the crystal growth of the incongruently melting compounds, which is more complex and is still in its exploratory phase - far from being fully understood.

5.1.2.2 Incongruently melting behaviour

Many complex oxides, including most of the cuprates, do not melt congruently, but rather exhibit a peritectic decomposition upon heating. As shown schematically in the

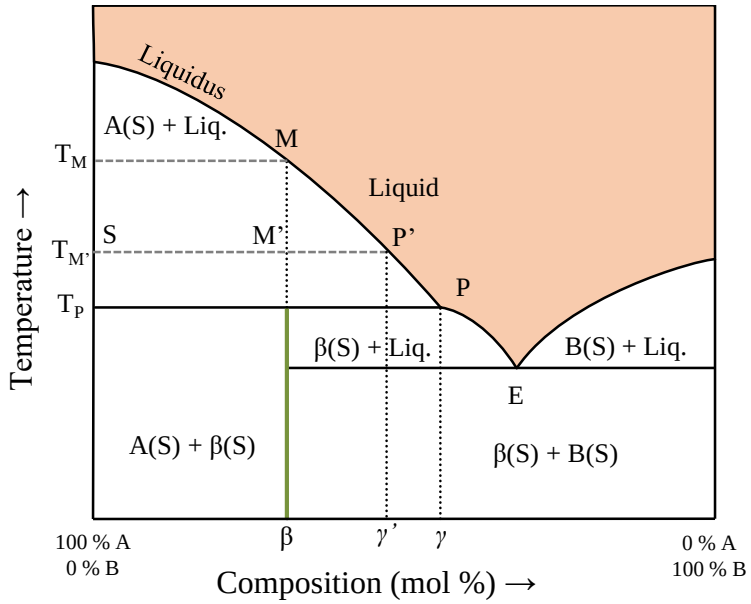

Figure 5.5: Schematic of a binary phase diagram of components A and B with incongruently melting intermediate phase $\beta = A_xB_y$.

binary phase diagram of figure 5.5, the intermediate compound β cannot be in equilibrium with its own melt of the stoichiometry β. The compound β, therefore, has the so-called *incongruent* melting behaviour, wherein it decomposes upon heating into the solid A and a melt of composition γ. The temperature at which the decomposition takes place is known as the peritectic point. The proportion of the solid and liquid phases at any temperature above T_P is governed by the so-called *Lever rule*. At temperature $T_{M'}$, for instance, if a 'temperature horizontal' (or a tie-line) is drawn through M', the $x-$coordinate of the point where it cuts the liquidus, will give the composition γ' of the liquid. On the other side, the tie line cuts directly the y-axis through A, which corresponds to the composition of the solid. Note that for simplicity we have not considered here the region of homogeneity around A; i.e., the range of the composition around A, where B can be incorporated in the lattice of A without exsolution. At temperature $T_{M'}$, therefore, both the liquid (composition γ') and the solid (composition A) will exist in equilibrium. The *Lever rule* says that.

$$\frac{\text{amount of liquid (mol \%)}}{\text{amout of solid (mol \%)}} = \frac{\text{SM'}}{\text{M'P'}} \tag{5.1}$$

Due to the non-availability of a point of equilibrium between the solid and a liquid of corresponding stoichiometry, most of the conventional crystal growth techniques can not be employed in the crystal growth of solids with incongruent melting behaviour. In particular, the Bridgeman and the Czochralski methods, that are typically used for obtaining large single crystals cannot employed here. The flux growth method can be employed to grow incongruently melting solids. However, this process is not very useful in view of the size of the grown single crystals. Moreover, the grown crystal may incorporate traces of the solvent or of the crucible material, which would be highly undesirable, particularly if the aim is to study the effects of specific impurities on the physical properties. With this view in mind, a special technique, called the travelling-solvent-floating- zone (TSFZ) technique associated with an optical image furnace can be successfully used for in obtaining large and high-quality single crystals of incongruently melting compounds. TSFZ process is an adaptation of the self-flux growth process to an image furnace, where the FZ composition differs from that of the target compound; and the FZ essentially acts as a solvent in which the feed gradually dissolves at a very slow rate as the zone moves up along the length of the feed. And, at exactly the same rate, the crystallization of the solute takes place on the seed. For this reason, the method gets its name travelling-solvent-floating-zone (TSFZ) growth technique [152, 153].

5.1.3 Principle of working of a TSFZ growth

In order to understand the working of a TSFZ process, let us refer to the binary phase diagram of figure 5.5. Here the compound β, whose crystal has to be grown, exhibits a peritectic-type decomposition at temperature (T_p) to a solid A and a liquid of composition γ (corresponding to point P on the phase diagram). As temperature increases, following the said *Lever rule*, the proporsion of liquid increases and that of the solid decreases. Accordingly, composition of the liquid shifts towards M in order to maintain the overall stoichiometry. At the temperature corresponding to point M (T_M), complete

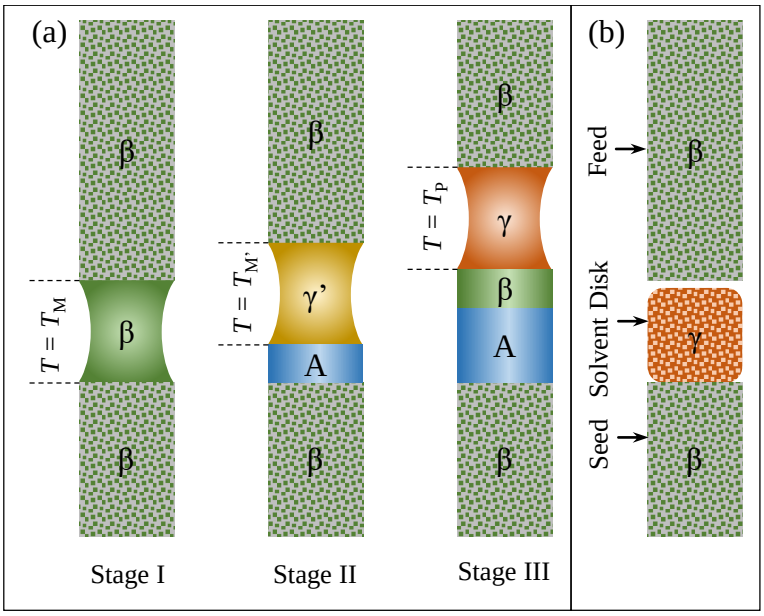

Figure 5.6: (a) Cartoon showing stages involved in the TSFZ process before reaching the steady state (see the text for details). (b) In a real TSFZ experiment, Stage III in (a) can be reached directly by melting a sintered solvent disk of composition γ. Symbols A, α, β, γ, T_M and $T_{M'}$ are same as in figure 5.5

melting takes place to form a liquid of the composition β. Imagine a hypothetical [$*$] crystal growth experiment, where a totally molten zone of composition β is formed between the feed (β) and the seed rods (β). As the rods are made to travel downwards (which amounts to moving the FZ upwards keeping the rods fixed), the phase to be first crystallized on the seed from the melt will have the composition of solid A, which is very different from that of the liquid in the zone. Subsequently, as the growth progresses, the composition of FZ will tend to enrich itself with B continuously. This would require the crystal grower to continuously adjust (decrease) the floating-zone temperature, so as to always remain in equilibrium while traversing from the point M to the point P following the liquidus line. As the temperature and the composition of the FZ reaches that of the point P ($T = T_P$), no further change in temperature is required; a steady state has been reached. In the steady state, the feed decomposes to solid A and the liquid γ at the upper interface of the zone; and simultaneously, the reverse reaction takes place at the lower interface, where the solid A and liquid γ combine to crystallize

$*$In real growth experiments this cannot sustain as the temperature of the feed and the seed near the zone will be above T_P, which will decompose a large portion of them

the solid β.

$$\beta(\text{Solid}) \underset{\text{Lower Interface}}{\overset{\text{Upper Interface}}{\rightleftharpoons}} \text{A (Solid)} + \gamma(\text{liquid}) \tag{5.2}$$

Thus, the first portion of the grown crystal will have the composition A. The rest of the growth will consists of crystal of composition β and a floating-zone of composition γ. However, the optimization process to reach the steady state is extremely complex, which involves a careful guidance of the zone composition from point M to point P by adjusting the power of the lamps. It can easily take a day or more depending on how far apart the points M and P are on a given phase diagram.

The steady-state conditions can, however, be obtained quickly from the very beginning of a growth experiment by using a solvent disk, which has the composition corresponding to the peritectic point P in the phase diagram. The solvent disk is prepared separately, using the solid state reaction route by taking the starting precursors in an appropriate ratio so as to match the composition of the associated peritectic point. To initiate the growth, the sintered solvent disk is sandwiched between the feed and the seed rods and melted completely to form the molten-zone. The weight of the sintered solvent disk is taken to match the weight of the steady state molten zone. Often its takes several trial experiments to optimize the weight of the solvent disk required for an uninterrupted growth. As the growth progresses, the solvent (molten zone) travels through the length of the feed in order to allow for the decomposition to happen at the upper interface, and simultaneous recombination reaction at the lower interface leading to crystallization of the phase β on the seed.

One of the first attempts on the single crystal growth of non-congruently melting oxides was that of Yttrium-Iron-Garnet ($Y_3Fe_5O_{12}$), pioneered by *Kitamura et al.* [154]. The method has also been used, in association with laser heating, to pull at very high growth rates single-crystalline fibers [155] in particular in the Bi-Sr-Ca-Cu-O system [156]. For a brief review on the single crystal growth of incongruently melting cuprates using TSFZ, see references [152, 153].

5.1.4 Single crystal growth of the doped compounds

In both the schematic phase diagrams shown in figures 5.3 and 5.5, the corresponding compounds α and β have been shown as line compounds to make a simple understanding to their melting behaviours. However, in reality most of the compounds have a small but finite homogeneity range with either of its components, and also possibly with some extrinsic phases. But this range can be very different in the solid and the liquid phases of a given compound. At the crystallization front, there exists an equilibrium between the solute concentration of the crystal and the liquid solution. The ratio of concentration of the solute in the solid (C_S) to that in the liquid (C_L) is known as distribution coefficient, given by:

$$k = \frac{C_S}{C_L} \tag{5.3}$$

In many cases the distribution coefficient is less than 1, which, implies that the solute concentration in the solid is less than that in the liquid. Therefore, as the crystallization front advances, a progressive enrichment of the solute in the remaining liquid takes place. If we consider directional solidification, where the crystallization front advances progressively, due to cooling of the melt under a temperature gradient, the change of solute concentration in the melt can be expressed as [157, 158]:

$$C_L(g) = C_0(1-g)^{k_0-1} \tag{5.4}$$

In deriving this equation it is assumed that the distribution coefficient remains constant throughout the process and we denote this constant value by k_0. Quantity g, here, represents the quotient of the solidified volume V_S and the total volume V_{total}, i.e. $g = V_S/V_{total}$ and C_0 the initial concentration of the liquid phase. The solute concentration in the growing crystal is $C_S = k_0 \cdot C_L$. In case of growth with uniform cross-section, the ratio of volumes is same as the ratio of lengths x/L, where x and L represents the growth length, and the total length, respectively (see figure 5.7). In figure 5.8 the solute concentration of the growing crystal has been shown for $k_0 < 1$, which shows a continuous increment of the solute concentration as the growth progresses. This, of course, is undesirable. A possible way out could be to use a large amount of

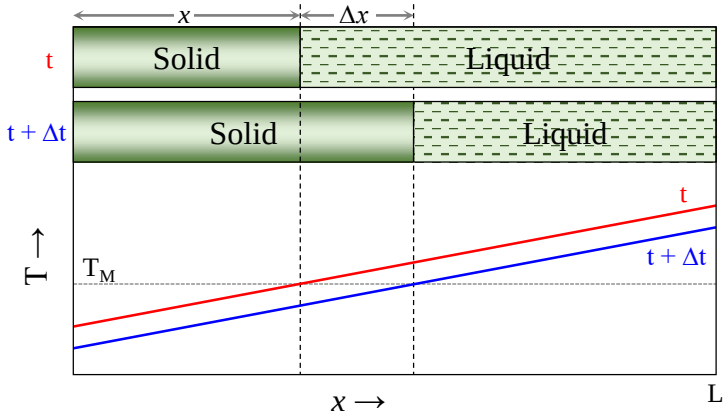

Figure 5.7: Schematic representations of a directional solidification process. T_M refers to the melting/freezing temperature. The solid lines in the graph show temperature profile along the axis of the furnace at time t and $t + \Delta t$.

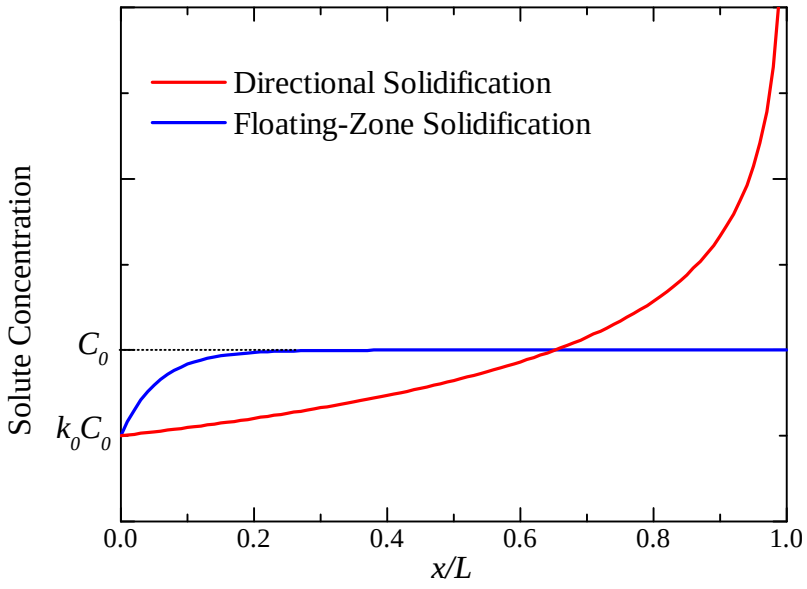

Figure 5.8: Solute concentration distribution for the directional solidification and floating zone solidification.

liquid, and to limit the process to grow only a small crystal length. However, there will still be finite, though small, concentration gradient within the grown crystal. Also, such an approach will result in a loss of a large amount of material.

In a floating zone growth, however, due to localized melting this issue can be addressed efficiently. Let us consider a growth from a rod of length L with homogeneous solute concentration (C_0) and assume that during growth there is a constant zone volume (l) and constant distribution coefficient ($k_0 < 1$) throughout the total growth length. At the beginning of the growth the melt will have the composition of the feed rod i.e., C_0. So the growth will start with solute concentration, $C_S = k_0 C_0$. Let $C_L(x)$ be the solute concentration of the floating-zone at a length x from the beginning of the growth. Now, a further growth by an amount dx will solidify an amount of solute $\propto k_0 C_L(x)dx$ from the zone, and at the same time dx amount of feed will melt into the zone which will also incorporate an amount of solute in the zone $\propto C_0 dx$. Thus the change in the amount of solute (dC_L) in the zone over the length dx of the growth can be expressed as:

$$dC_L = (C_0 - k_0.C_L(x))dx \tag{5.5}$$

Considering the initial condition $C_L(x = 0) = C_0$, the expression for the solute concentration $[C_S(x)]$ in the grown crystal during a floating zone growth can be obtained by integrating equation 5.5 over the entire growth length, and, we get [158]:

$$C_S(x) = C_0 \left[1 - (1 - k_0)\, e^{-k_0 x/l}\right] \tag{5.6}$$

The variation of solute concentration in the grown crystal for $k_0 < 1$ is shown in figure 5.8. In contrast to the directional solidification process, given by equation 5.4, the floating zone method reaches a stable state for sufficiently large x, where the composition of crystal approaches that of the feed rod:

$$i.e., \lim_{x\to\infty} C_s(x) = C_0 \tag{5.7}$$

The zone concentration stabilizes at $C_L = C_0/k_0$. In real experiment, where $k \lesssim 1$, a stable solute concentration can be attained within a few centimetre from the starting

point of the growth experiment.

5.2 Single crystal growth of Sr_2CuO_3 and $SrCuO_2$

In reality, the success of the travelling-solvent-floating zone process depends on several practical aspects that cannot easily be casted in the form of rules. Often the conditions are material specific and require careful optimization through repeated trials. Here, in this section we will describe some of the general practical aspects concerning the difficulties encountered at different stages in the crystal growth of the compounds Sr_2CuO_3 and $SrCuO_2$ and their doped variants. This section also includes various characterisations of the grown crystals, to ensure that they are of sufficiently high quality to warrent advanced studies of their physical properties using inelastic neutron scattering and bulk magnetisation and transport experiments.

5.2.1 SrO-CuO binary phase diagram

We have seen earlier in this chapter that the melting behaviour of a compound plays a decisive role in choosing the crystal growth technique. In the case of SrO-CuO ambient pressure binary system, three stable incongruently melting compounds having compositions Sr_2CuO_3, $SrCuO_2$ and $Sr_{14}Cu_{24}O_{41}$ are reported [159–162]. A schematic view of the SrO-CuO binary phase diagram is presented in figure 5.9. As shown in the figure, upon heating, all the three compounds shows an incongruent melting behaviour. That is, upon heating, they do not transform from the solid phase to a homogeneous melt at a particular temperature (the melting point). On the contrary, they rather decompose into a solid and a liquid phase of different compositions. As an example, the compound $SrCuO_2$, upon heating up to a temperature of peritectic decomposition ($T_P \approx 1085 \pm 5°C$), decomposes according to the following equation:

$$SrCuO_2 \xrightarrow{T_P} Sr_2CuO_3(\text{Solid}) + \gamma_2(\text{Liquid}) \tag{5.8}$$

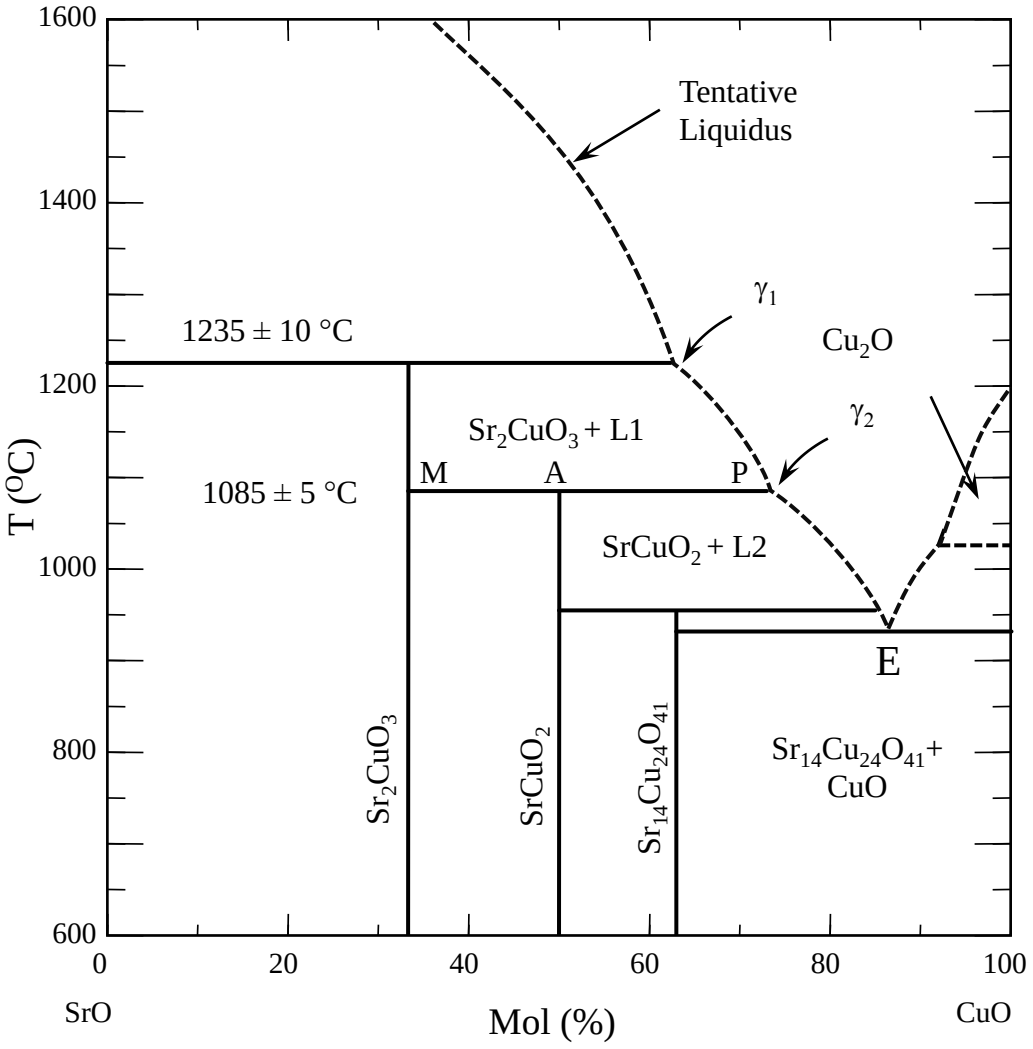

Figure 5.9: (a) Schematics of the phase diagram of the binary SrO–CuO system adapted from references [159] and [160].

where γ_2 is the liquid corresponding to the peritectic point (labelled P) in figure 5.9. At the peritectic temperature, γ_2 exists in equilibrium with the solid phase Sr_2CuO_3 and their relative molar percentages is given by the *Lever rule*; i.e., m(S)/m(L) = MA/AP, where m is the number of moles and MA and PA are the intercepts (see figure 5.9). A very similar peritectic decomposition is shown by the compound Sr_2CuO_3 at temperature $T_P \approx 1250 \pm 25°C$ which can be expressed using the following equation:

$$Sr_2CuO_3 \xrightarrow{T_P} SrO(Solid) + \gamma_1(Liquid) \tag{5.9}$$

Due to their incongruently melting behaviour, Sr_2CuO_3 and $SrCuO_2$ cannot be grown as single crystals using the conventional melt growth techniques, including the conventional floating zone method, where a single crystal is grown directly from the corresponding stoichiometric melt. Method of flux growth, using CuO as the self-flux, was previously reported [163, 164] in context of the compound $SrCuO_2$. However, the single crystals grown by this technique are not suitable in the present case in view of their smaller size, and also because the flux or the crucible material can easily be incorporated in the crystals during the growth experiment which may cause ambiguities while interpreting the data of the doped crystals. Moreover, the crystals grown by the flux method are typically small, not optimal for experiments requiring large sample mass such as the inelastic neutron scattering experiments. Therefore, the crystals were grown using the travelling-solvent-floating-zone (TSFZ) method.

5.2.2 Synthesis of the feed rod

For the crystal growth experiments, polycrystalline feed rods of the compounds Sr_2CuO_3, $SrCuO_2$ and their doped variant were prepared using the standard solid state reaction route (details of the synthesis process has been given in table 5.2). Fine Powders (< 10 μm) of $SrCO_3$, CuO, ZnO, NiO, MnO and Co_3O_4 were used as the starting precursors. $SrCO_3$ was preheated and dried over night at 900°C before weighing. The powders of the starting precursors were mixed thoroughly in a stoichiometric ratio using a mortar and pestle and then calcined in an alumina crucible at 850°C. In the subsequent steps, the mixtures were reground and heat treated for 12-24 hours under atmospheric air, with a sequential increase in temperature by 25 to 30°C at each step, and with a final heat treatment at 1025°C for the compound Sr_2CuO_3 and 975°C in the case of $SrCuO_2$ (including their doped variants). The phase formation was confirmed using powder x-ray diffraction (Bruker D8 Advance). The recorded patterns were matched with the standard data to confirm the phase purity. After the synthesis of a single phase compound, the powders obtained were filled in rubber tubes and cold-pressed under 700 bar

Table 5.2: Details of compound synthesis

Compounds	Precursor Purity		Heat Treatment		Final Phase
	$SrCO_3$	CuO	Temp(°C)	Hours	
Sr_2CuO_3	99.99% (A)	99.995% (A)	900-1025	192	single phase
$Sr_2Cu_{0.99}Zn_{0.01}O_3$	99.99% (A)	99.995% (A)	900-1025	168	single phase
$Sr_2Cu_{0.9975}Co_{0.0025}O_3$	99.9% (A)	99.995% (A)	850-1000	192	single phase
$Sr_2Cu_{0.995}Co_{0.005}O_3$	99.9% (A)	99.995% (A)	850-1000	192	single phase
$Sr_2Cu_{0.99}Co_{0.01}O_3$	99.99% (A)	99.995% (A)	900-1025	192	single phase
$Sr_2Cu_{0.975}Co_{0.025}O_3$	99.9% (A)	99.995% (A)	900-1025	192	single phase
$Sr_2Cu_{0.99}Ni_{0.01}O_3$	99.99% (A)	99.995% (A)	900-1025	168	single phase
$Sr_2Cu_{0.95}Ni_{0.05}O_3$	99.9% (A)	99.995% (A)	900-1040	168	single phase
$Sr_2Cu_{0.9}Ni_{0.1}O_3$	99.9% (A)	99.995% (A)	900-1040	168	single phase
$Sr_2Cu_{0.9975}Mn_{0.0025}O_3$	99.9% (A)	99.995% (A)	900-1025	192	single phase
$Sr_2Cu_{0.99}Mn_{0.01}O_3$	99.9% (A)	99.995% (A)	900-1025	192	single phase
$SrCuO_2$-I	99.9% (S)	99% (S)	800-985	120	small extra phase*
$SrCuO_2$-II	99.9% (S)	99.99% (S)	900-980	145	single-phase
$SrCu_{0.995}Zn_{0.005}O_2$	99.99% (A)	99% (S)	825-960	400	single-phase
$SrCu_{0.99}Zn_{0.01}O_2$	99.9% (S)	99.995% (A)	800-975	150	single-phase
$SrCu_{0.98}Zn_{0.02}O_2$	99.9% (S)	99.995% (A)	800-975	180	single-phase
$SrCu_{0.9975}Co_{0.0025}O_2$	99.9% (S)	99.995% (A)	800-975	190	small extra phase*
$SrCu_{0.995}Co_{0.005}O_2$	99.99% (A)	99.995% (A)	850-975	275	small extra phase*
$SrCu_{0.99}Co_{0.01}O_2$-I	99.9% (S)	99% (S)	900-990	120	single-phase
$SrCu_{0.99}Co_{0.01}O_2$-II	99.9% (S)	99.995% (A)	850-975	210	single-phase
$SrCu_{0.975}Co_{0.025}O_2$	99.9% (S)	99.995% (A)	800-975	240	small unidentified extra phase

S:Sigma-Aldrich; A:Alfa-Aesar; * $Sr_{14}Cu_{24}O_{41}$.

isostatic pressure to obtain uniform rods measuring about 5 mm in diameter and 80-100 mm in length. The rods were then sintered at temperatures around 1050°C for the compound Sr_2CuO_3 and around 990°C for $SrCuO_2$ to obtain very dense, homogeneous rods, which is a necessary condition to ensure uniform melting behaviour during the growth process. About 20 mm long sections, cut from these rods, were used as seeds in the first growth experiments. Table 5.2 provide a summary of the synthesis conditions, including the purity of the starting precursors, total number of sintering hours and the results of phase analysis of the final products.

5.2.3 Choice of the solvent composition

As we explained in the previous section composition of the solvent disk is a key factor in stabilizing the growth process. A steady-state can be reached right in the beginning of a growth experiment by choosing a solvent disk of right size and composition. The knowledge of the correct composition of the solvent disk is therefore crucial. However, in the particular case of compounds Sr_2CuO_3 and $SrCuO_2$, at least four different phase diagrams were previously reported [159–162]. While these phase diagrams are in qualitative agreement with each other; they do not agree about the position of the peritectic point associated with the decomposition of either of the compounds Sr_2CuO_3 or $SrCuO_2$. For instance, the phase diagrams due to Liang et al.[161] and Wong et al.[162] show the composition corresponding to the peritectic point for compound Sr_2CuO_3 to be SrO : CuO = 1 : 1 (henceforth, unless mentioned otherwise, the ratio in the context of the solvent composition stands for molar ratio SrO : CuO) whereas, Solbodin et al.[159] and Hwang et al.[160] reported the composition to be 14 : 24. In the case of the compound $SrCuO_2$, the composition at the peritectic point were reported to be 14 : 24 and 3 : 7 in the respective reports. It is worth pointing out here that while the liquidus lines in the phase diagrams due to Wong et al. and Liang et al. appear to be tentative, both, Solbodin et al. and Hwang et al. mark the liquidus and the positions of the peritectic points with more certainty using the data points obtained from the phase analysis by x-ray powder diffraction of samples quenched from temperatures as high as

1500°C.

In previous works dealing with the TSFZ growth of these compounds, use of three different solvent compositions have been reported. Ohashi et al.[165] reported relatively small size crystals of the compound $SrCuO_2$, measuring 1 cm in length, using the solvent composition 3 : 7. They also reported floating-zone instabilities for growth speeds exceeding 0.5 mm/h. Revcolevschi et al. [152, 153], on the other hand, reported several cm long crystals of both the compounds Sr_2CuO_3 and $SrCuO_2$, using growth speed of 1 mm/h and solvent compositions based on the SrO-CuO phase diagrams due to both Hwang et al.[160] and Liang et al. [161]. However, the details of their growth experiments are not reported. Finally, the use of CuO as solvent disk for the compound $SrCuO_2$ is reported in reference [166] . The authors pointed out excessive bubbling due to the CuO phase transforming to $Cu_2O + \frac{1}{2}O_2$ during melting of the solvent disk; producing an excess of copper in the floating zone. The other problem using CuO is that the growth should be monitored continuously for about 12 hours or more, during which the temperature-composition variations should closely follow the liquidus until the steady state growth condition is reached. Clearly, the use of a CuO pellet as the starting solvent is not only labour intensive but also hazardous to the quartz enclosure as splintered CuO drops fuse with quartz damaging it permanently. In reference [167], where the growth of the compound $SrCuO_2$ is initiated using a CuO disk, the authors also determined the steady state floating zone composition using energy dispersive x-ray analysis of the quenched floating zone at the end of a stable growth. Their analysis revealed that under steady state condition the floating zone has a composition of 3 : 7.

Following the more definitive phase diagrams published in references [159, 160] and the results due to reference [167] , in the present work we used the solvent composition 14 : 24 for the growth of compound Sr_2CuO_3 and 3 : 7 in the case of $SrCuO_2$. In the growth of doped compounds, the corresponding amount of dopant was added to the solvent disk so that the doping level in the growing crystal remains equal to that in the feed rod. For example, in the growth of $SrCu_{0.99}Co_{0.01}O_2$, the composition of the solvent used was SrO : CuO : CoO = 3 : 6.93 : 0.07. Moreover, to confirm that these are indeed the right choices to reach the steady state soon after the floating zone

is formed, we also tried a growth experiment of $SrCuO_2$ with both compositions for $SrCuO_2$, i.e., 14 : 24 and 3 : 7 . We found that it is possible to reach a steady state condition directly using the solvent composition 3: 7 but not with the composition 14 : 24. Representative pictures of some of the grown crystals are shown in figure 5.11. Values of various growth parameters involved in a TSFZ process are summarized in Table 5.3.

5.2.4 Growth protocol

The growth experiment in each case was initiated using the corresponding solvent taken in the form of a disk prepared as a pellet of thickness 3 mm. The crystals were grown under O_2 flow at P = 1 bar. To improve temperature and compositional homogeneity of the float-zone, the upper and lower shafts of the furnace were rotated in opposite directions with rotation speeds ranging from 10 to 20 rpm. The growth rate employed in most of the experiments was around 1 mm/h. Often the upper shaft was translated at a speed slower than the lower shaft by 0.1 to 0.2 mm/h in order to control the size of the grown crystal and that of the steady-state floating-zone (see table 5.3).

Having the right solvent composition, therefore, aids in reaching the steady state condition quickly. However, there is another important consideration, whose non-compliance may result in the interruption of the growth process or may introduce large delays in reaching the steady state in spite of starting with the right solvent composition. This concerns the melting behaviour of the solvent pellet. For example, in the TSFZ growth of pristine Sr_2CuO_3, a sintered solvent pellet of composition 14 : 24, upon heating, will undergo successive phase transformations according to the following equation:

$$Sr_{14}Cu_{24}O_{41}(S) \xrightarrow{950^{\circ}C} SrCuO_2(S) + L_2 \xrightarrow{1085^{\circ}C} Sr_2CuO_3(S) + L_1 \xrightarrow{1235^{\circ}C} \gamma_1$$

where γ_1, L_1 and L_2 are the liquids represented in the phase diagram (see figure 5.9)

From the sequence of transformations that the solvent disk exhibits upon heating, it is evident that unless melted completely the resulting floating zone will neither have the desired composition nor the volume for a sustainable TSFZ process. Very often, in

Table 5.3: Growth parameters during the TSFZ experiments reported here (see text for details)

Sample		Growth rate		Rotation Rate		Growth length (mm)	Results
		v_f(mm/h)	v_g(mm/h)	ω_f(rpm)	ω_g(rpm)		
Sr_2CuO_3	I†	0.82	1.00	25	25	103	Stable Growth
	II	0.75	1.05	25	25	135	Stable growth
$Sr_2Cu_{0.99}Zn_{0.01}O_3$	I	0.80	1.00	31	16	125	Stable Growth
	II	0.80	1.00	30	16	134	Stable Growth
$Sr_2Cu_{0.99}Ni_{0.01}O_3$	I	0.75	1.10	20	8	33	Liquid absorbed by feed
	II	0.75	1.05	25	8	119	Stable Growth
	III	0.80	1.00	30	20	68	Stable Growth
$Sr_2Cu_{0.9}Ni_{0.1}O_3$	I	0.80	1.10	15	10	128	Stable Growth
	II	0.90	1.00	15	20	85	Stable Growth
$Sr_2Cu_{0.9975}Co_{0.0025}O_3$		0.80	1.00	30	30	104.5	Stable Growth
$Sr_2Cu_{0.995}Co_{0.005}O_3$		1.00	1.10	15	15	104.5	Stable Growth
$Sr_2Cu_{0.99}Co_{0.01}O_3$	I	0.70	1.00	20	14	7	Liquid absorbed by feed
	II	0.75	1.05	20	15	22	Liquid absorbed by feed
	III	0.75	1.00	25	10	69	Stable Growth
	IV	0.80	1.00	25	13	93	Stable Growth
$Sr_2Cu_{0.975}Co_{0.025}O_3$	I	0.70	1.10	5	5	37	Liquid flowed down
	II	1.00	1.00	10	1	0	Liquid flowed down
$Sr_2Cu_{0.99}Mn_{0.01}O_3$	I	0.90	1.05	10	10	56	Stable Growth
	II	0.90	1.10	15	9	110	Stable Growth
$Sr_2Cu_{0.99}Mn_{0.01}O_3$		0.95	1.05	25	20	79.8	Stable Growth
$SrCuO_2$	I	0.92	1.00	14	15	79.5	Stable Float Zone (FZ)
	II	0.80	1.10	45	29	82.2	FZ broke due to off-axis growth
$SrCu_{0.995}Zn_{0.005}O_2$		0.80	1.00	20	10	71.4	Unstable FZ due to non-uniform feed diameter
$SrCu_{0.99}Zn_{0.01}O_2$		0.85	1.00	18	11	81.8	Stable FZ
$SrCu_{0.98}Zn_{0.02}O_2$		0.82	1.00	15	10	93.5	Stable FZ
$SrCu_{0.9975}Co_{0.0025}O_2$		0.92	1.00	6	8	115	Stable FZ
$SrCu_{0.995}Co_{0.005}O_2$		0.92	1.00	25	19	80.1	Stable FZ
$SrCu_{0.99}Co_{0.01}O_2$	I	0.85	1.05	10	10	81.3	Stable FZ
	II	0.80	1.05	15	12	125	Stable FZ
$SrCu_{0.975}Co_{0.025}O_2$		0.80	1.00	12	10	80.0	Unstable FZ due to extra phase

$v_f \rightarrow$ feeding rate; $v_g \rightarrow$ growth rate; $\omega_f \rightarrow$ rotation rate of the feed; $\omega_g \rightarrow$ rotation rate of the crystal; † → Growth number.

the actual experiments, once the decomposition of the solvent disk starts the liquid thus produced tends to flow downward under gravity, which prompts the crystal grower to establish a floating zone by lowering the feed and allowing it to come in contact with a liquid which is more copper rich than desired.

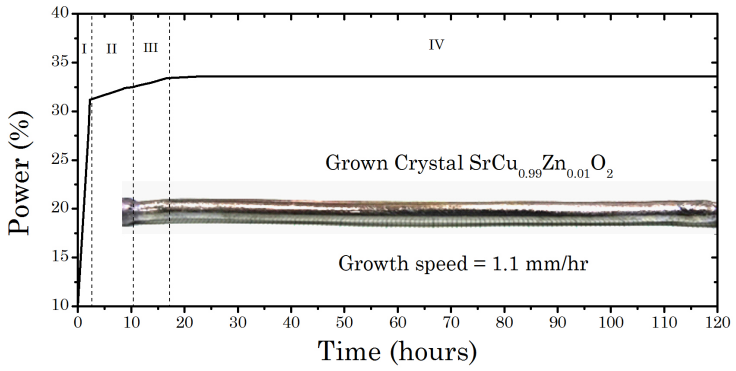

Figure 5.10: Plot of furnace power against time in the TSFZ growth experiment of $SrCu_{0.99}Zn_{0.01}O_2$. Region I: Power increased fast to reach a temperature close to the peritectic temperature. Region II: The solvent disk is partially melted and its temperature is gradually raised to enrich the liquid with Strontium. Region III: Fine tuning of the furnace power to reach the steady state. Region IV: The steady state region. See text for details.

In the present work, we overcome this difficulty using a two step process. In the first step, the solvent disk is fused to the lower end of the feed rod. This is achieved by first fixing the feed to the lower shaft, placing the disk on top of it and increasing the furnace power slowly to reach the temperature where the disk, majority of whose volume remains outside the hot region, starts decomposing to produce a thin liquid layer at the interface. Upon quickly cooling by decreasing fast the furnace power, the liquid layer freezes bonding the disk temporarily to the feed rod. In the second step, the feed, with the fused disk at its lower end, and the seed are loaded in the furnace in the conventional way. After flushing the growth chamber with O_2 gas for 12 hours the power is increased in 3-4 hrs to a value close to the power at which the pellet was fused in the previous step. From here onward, a slow automated heating process is started to melt the pellet completely which is then used to form a floating-zone. Because the process temperature cannot be measured directly in an image furnace of the type used in the present work, some uncertainty may remain in the floating-zone composition

which may require further fine tuning to reach the steady state. To illustrate this point further, we show in figure 5.10 a plot of furnace power vs. time (halogen lamps of power 500 W each were used) during the growth experiment of $SrCu_{0.99}Zn_{0.1}O_2$. In the graph, the various stages of the TSFZ process are indicated. Region IV corresponds to the steady-state condition, during this phase no power adjustment was required. In the region III, the furnace power was increased from 32.5% to 33.6% to fine tune the temperature-composition of the floating-zone. Regions II and I correspond to initial phases, i.e., prior to floating zone formation. During stage I, the power was quickly increased from 0 to 28% in 2-3 hrs and in stage II (slow-heating regime) the power was increased gradually from 28% to 32.5%. With some experience, one can eliminate completely or minimize the stage III as is evident from the slopes of the heating curves in the two regions.

Apart from the solvent composition and its melting behaviour, there are other considerations to keep in mind to allow a TSFZ process to proceed uninterruptedly. The density and diameter of the feed rod should be uniform throughout its length, because changes in the zone-volume due to non-uniform melting of the feed rod may eventually lead to a failure of the growth process (e.g., growth $SrCu_{0.0995}Zn_{0.005}O_2$, table 5.3). Another complication that can prove detrimental to the stability of the floating zone concerns the off-axis growth, that is, the crystal prefers to grow away from the axis of the furnace as seen in the case of $SrCuO_2$-II in Table 5.3. Typically, slower rotation speed helps in keeping the growing crystal along the furnace axis, but too slow a rotation speed may result in temperature-compositional inhomogeneity within the floating zone. In the present work we typically used a rotation speed of 15 rpm, however, in few cases, where a slight tendency towards off-axis growth was noticed, rotation speeds as low as 6 rpm were used.

5.2.5 Results and characterization

Figure 5.11 summarizes the results of several growth experiments. The diameters of all the grown crystals range between 4 and 4.5 mm, and their length between 70 and 100

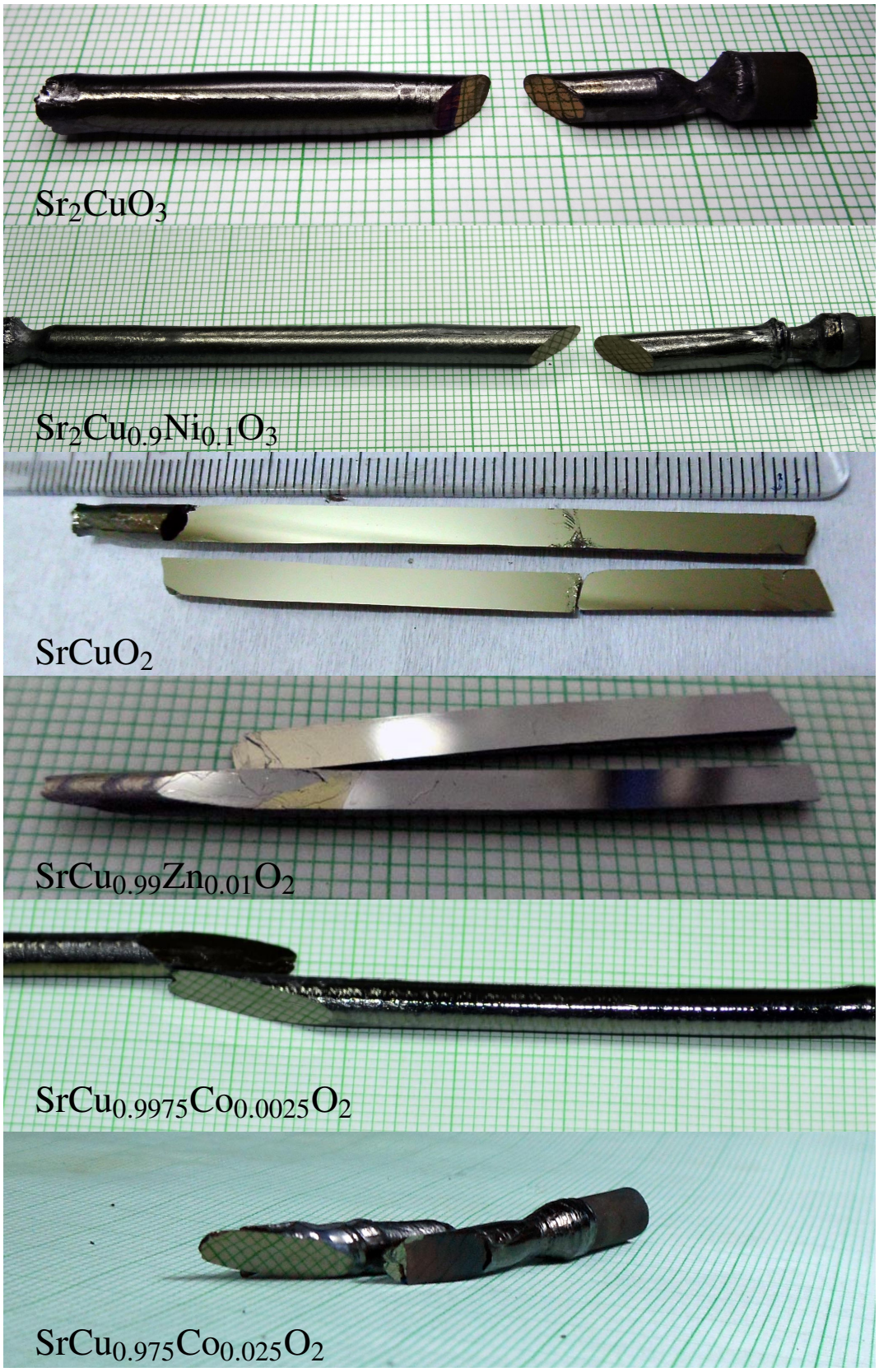

Figure 5.11: Representative images of the as-grown crystals.

mm. The crystals were found to cleave rather easily with large mirror finished surface whose orientation was later confirmed to be perpendicular to the planes containing the Cu-O chains i.e., the crystallographic *a*-axis for the compound Sr_2CuO_3 and the crystallographic *b*-axis for the compound $SrCuO_2$ [see figure 3.1 in chapter 1]. In some cases, where the chain containing plane of the crystal happens to be oriented along the growth axis, the length of the cleavage section extended over the entire length of the grown crystal boule. The relative ease with which these crystals cleave can be attributed to a weaker inter-planar bonding compared to the in-plane bonding. Within the planes, the magnetic Cu-O-Cu exchange interaction along the chain direction is about ~2000 K, which is far too high compared to the temperature at which their TSFZ growth occurs (~1370 K). It might, therefore, be possible that their growth behaviour is governed by the in-plane magnetic bonding.

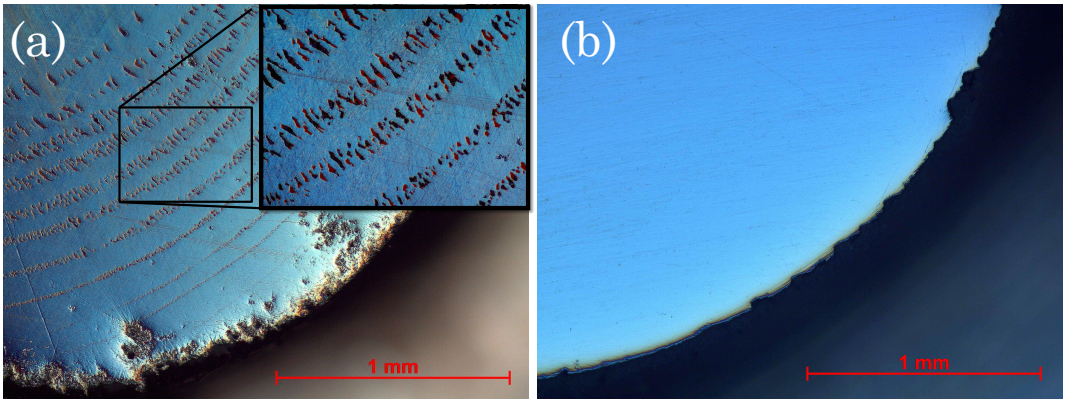

Figure 5.12: Representative optical images under polarized light of the polished cross-sections at different lengths of the grown crystal ($SrCu_{0.99}Co_{0.01}O_2$-III) (a) at 44 mm and (b) at 78 mm from the beginning of the growth.

Due to their tendency to cleave rather easily along the growth direction, cutting perpendicular sections from the grown crystal boules presented some difficulties. We employed a 30 μm thickness diamond saw at very slow speeds and without the use of any coolant, to cut perpendicular sections at different places from one of the grown crystal boules ($SrCu_{0.99}Co_{0.01}O_2$ -II). These sections were dry polished using silicon-carbide papers of progressively higher grit sizes with final polishing at the grit size 1200 (approx. 15 microns particle size) and were examined under an optical microscope using polarized light. The results of two different sections at 44 mm and 76 mm from the

beginning of a growth experiment, are shown in figure 5.12. The polished section at 44 mm shows segregation of extra phase located along nearly concentric circular arcs. Above 48 mm, these arcs were pushed further out towards the peripheral region of the crystal. The section at 76 mm does not show any signs of segregation. Along the circumference of the crystal, however, smaller regions of inhomogeneity or of differently oriented domains compared to the bulk of the crystal were seen in some of the sections, which is likely the result of large convexity of the melt-growth interface. The x-ray powder diffraction measurements done on several sections indicated the existence of an extra phase of $Sr_{14}Cu_{24}O_{41}$ in almost all the grown crystals. In the best cases, segregation of any secondary phases ($Sr_{14}Cu_{24}O_{41}$ in the crystal grown for the pristine and doped $SrCuO_2$ and $SrCuO_2$ in the crystal grown for the pristine and doped Sr_2CuO_3) disappeared after 10-15 mm of growth and in the worst cases it persisted up to about 50 mm of growth length. These variations are related to the composition of the initial floating zone.

Several freshly cleaved sections from various regions of the grown crystals were rigorously investigated using the SEM. To elucidate the morphology and growth behaviour, some representative secondary electronic images are shown in figure 5.13. The layered morphology of the grown crystals, derived from their anisotropic layered structure, is evident in these pictures due to the appearance of steps and terraces typically seen on the cleaved sections of layered crystals (see panels (a) and (d) of figure 5.13). The examined sections showed a very homogeneous composition. In particular, none of the examined specimens showed any secondary phases or aggregates, suggesting a uniform distribution of the dopants within the crystal bulk. Attempts to determine the actual dopant concentration in our crystals using EDX analysis did not prove very successful because their small concentration is almost at the sensitivity limit of the EDX probe. The lattice parameters shown in Table 5.4 were obtained from powder diffraction patterns (see figure 5.14) using the UNITCELL software. No significant variation of the lattice parameters with Co and Zn doping could be observed, which is expected since the ionic radii differ only slightly in +2 oxidation state and 4-fold coordination [168] for Cu $\simeq$ 58 pm, Co $\simeq$ 57 pm and Zn $\simeq$ 60 pm. The crystallographic orientation

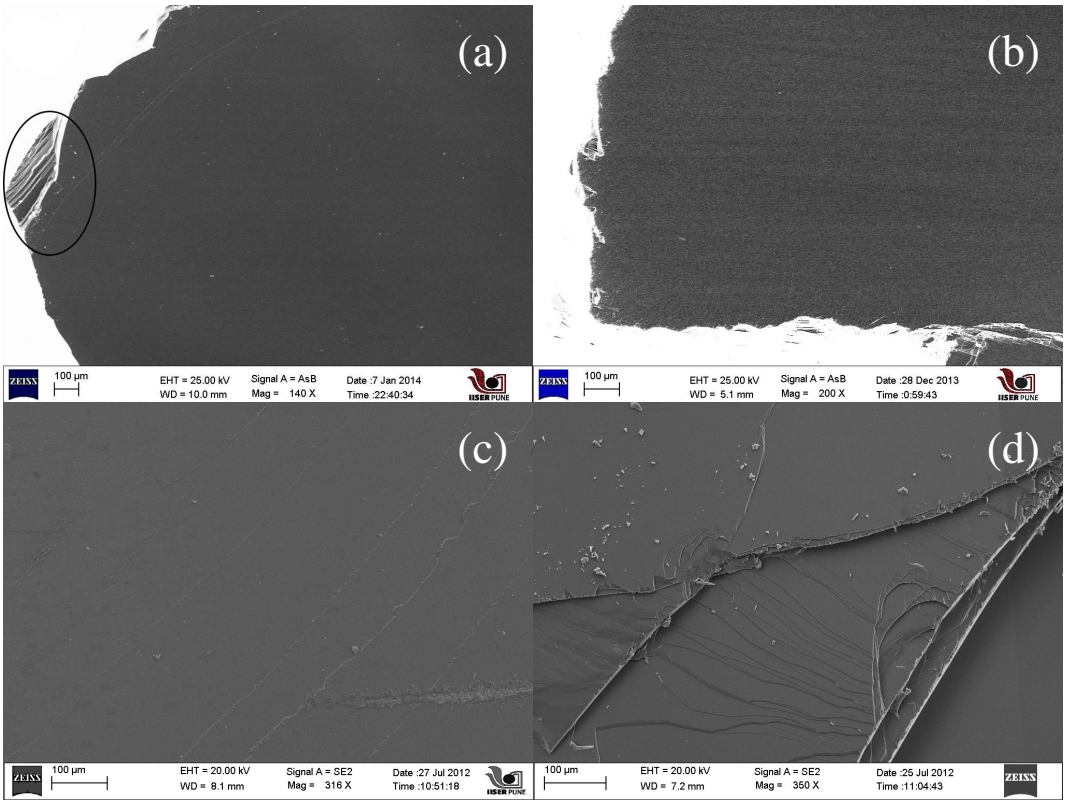

Figure 5.13: Backscattered electron images (inverted mode) of the cleaved surfaces of the (a) Sr_2CuO_3 and (b) 1 % Co doped Sr_2CuO_3 (c) 1 % Zn doped $SrCuO_2$ and (d) 1 % Co doped $SrCuO_2$ crystals. All the images shows the layered morphology of these crystals, which is highlighted using a circle in panel (a).

of the cleaved surfaces is confirmed using Laue diffraction and x-ray diffraction in the Bragg-Brentano geometry [figure 5.15]. Sharp Laue spots are indicative of high crystal quality and the symmetry of the Laue spots confirms that the cleaved face is the plane containing the Cu-O chains. x-ray diffraction from the cleaved faces exhibit sharp lines having indices h00 for Sr_2CuO_3 (see panel (a) of figure 5.15) and 0k0 for $SrCuO_2$ (see panel (c) of figure 5.15), where h and k are even. The absence of diffraction lines other than these indices also confirm that the crystals are free from any secondary phase(s). Since x-ray diffraction is essentially a surface sensitive technique,1.5-2 cm long single crystal pieces cut from the as-grown boule of pure and 1% Co doped $SrCuO_2$ crystal were also investigated using the neutron diffraction technique to assess the crystalline quality of the bulk. The experiments were performed by fixing the detector at the corresponding Bragg angle and rocking the crystals about their *b* axes. The crystals were

fully illuminated by the neutron beam during these experiments. The full-width at half-maximum (FWHM) of the diffraction peak at 001 is found to be around 0.5° for both pure and 1 % Co-doped crystals which again points to a very good crystalline quality (figure 5.16).

Table 5.4: Lattice parameter (Å) for the grown crystals

Sample	a	b	c	Cell volume
$SrCuO_2$ Standard[163]	3.577	16.342	3.918	229.028
$SrCuO_2$	3.5741 (4)	16.332 (1)	3.9112 (3)	228.31 (3)
$SrCu_{0.995}Zn_{0.005}O_2$	3.5722 (5)	16.328 (1)	3.9101 (4)	228.06 (4)
$SrCu_{0.99}Zn_{0.01}O_2$	3.5723 (5)	16.333 (1)	3.9098 (4)	228.13 (4)
$SrCu_{0.9975}Co_{0.0025}O_2$	3.5749 (5)	16.337 (1)	3.9117 (4)	228.45 (4)
$SrCu_{0.995}Co_{0.005}O_2$	3.5710 (4)	16.322 (1)	3.9089 (3)	227.83 (3)
$SrCu_{0.99}Co_{0.01}O_2$	3.5734 (4)	16.331 (1)	3.9118 (3)	228.28 (3)
$SrCu_{0.975}Co_{0.025}O_2$	3.5741 (5)	16.335 (1)	3.9106 (4)	228.29 (3)
Sr_2CuO_3 Standard	12.7024	3.9114	3.4986	173.82
Sr_2CuO_3	12.7090 (9)	3.9138 (4)	3.4986 (2)	174.02 (2)
$Sr_2Cu_{0.99}Zn_{0.01}O_3$	12.7078 (9)	3.9129 (3)	3.4987 (2)	173.97 (2)
$Sr_2Cu_{0.99}Co_{0.01}O_3$	12.704 (1)	3.9128 (3)	3.5012 (6)	174.03 (3)
$Sr_2Cu_{0.975}Co_{0.025}O_3$	12.6961 (9)	3.9099 (3)	3.5015 (2)	173.82 (2)
$Sr_2Cu_{0.99}Ni_{0.01}O_3$	12.7109 (9)	3.9053 (3)	3.4982 (2)	173.65 (2)
$Sr_2Cu_{0.9}Ni_{0.1}O_3$	12.6895 (9)	3.9048 (3)	3.5038 (3)	173.61 (2)
$Sr_2Cu_{0.9975}Mn_{0.0025}O_3$	12.7097 (9)	3.9124 (4)	3.4993 (2)	174.00 (2)

5.3 Analysis of the TSFZ process

Though there are several reports on the successful crystal growth of incongruently melting compounds using the TSFZ method, details of the steady state growth mechanism are scarcely reported in the literature. The composition/micro-structure of the frozen-in floating zone and the regions of the feed and crystal adjacent to the floating zone often contain valuable information concerning the TSFZ growth process[169, 170], whose knowledge can help in improving the quality of the grown crystals. In the present work, we examined the quenched floating zone in our growth experiments which provided indispensable information about the FZ composition (in particular, the concentration of dopant in the FZ) and the mechanism of the TSFZ process; i.e., how the partially

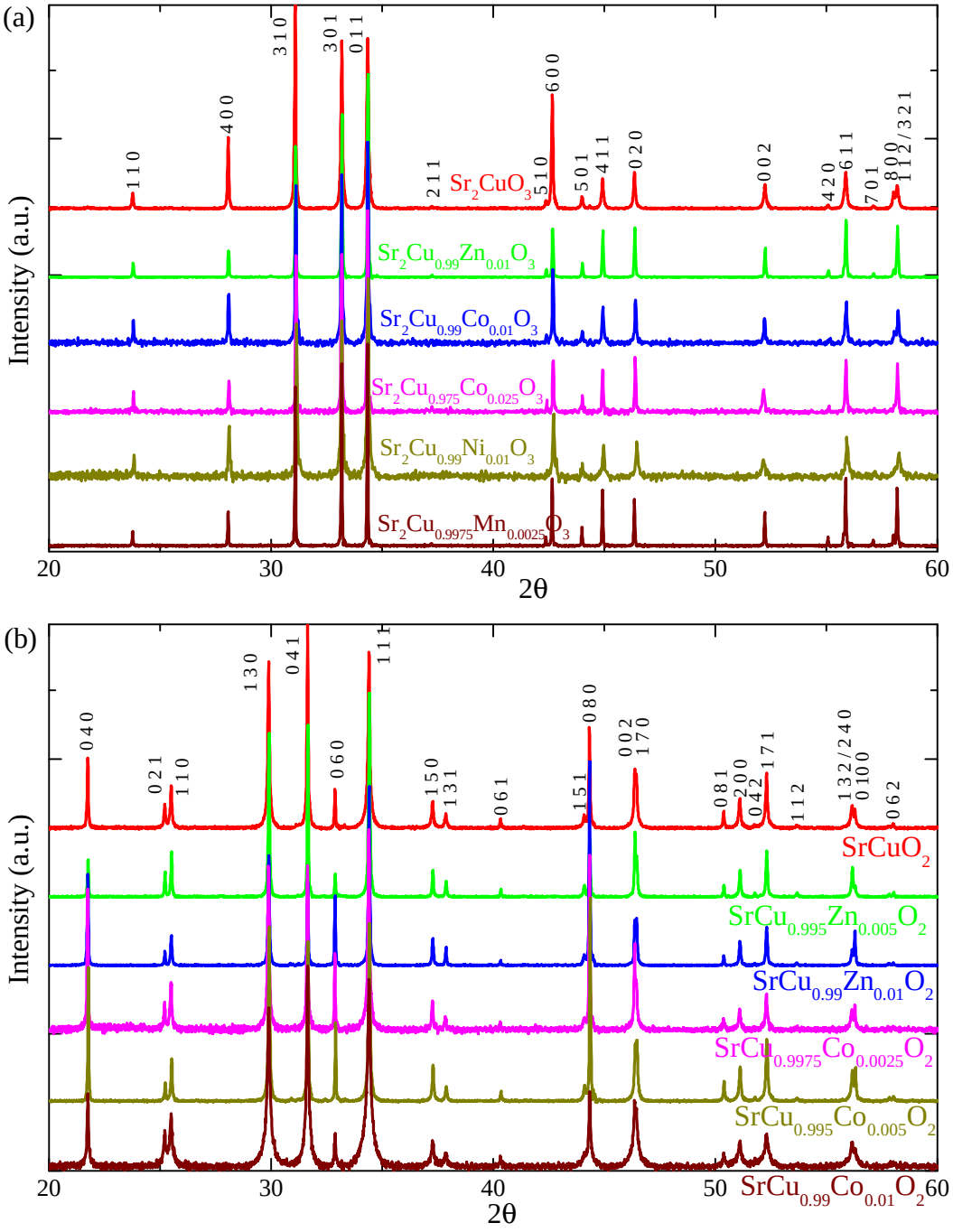

Figure 5.14: Representative powder x-ray diffraction patterns for the pristine and doped Sr_2CuO_3 [in panel (a)] and $SrCuO_2$ [in panel (b)], measured on the powders obtained by crushing small crystal pieces. The *miller hkl* are shown.

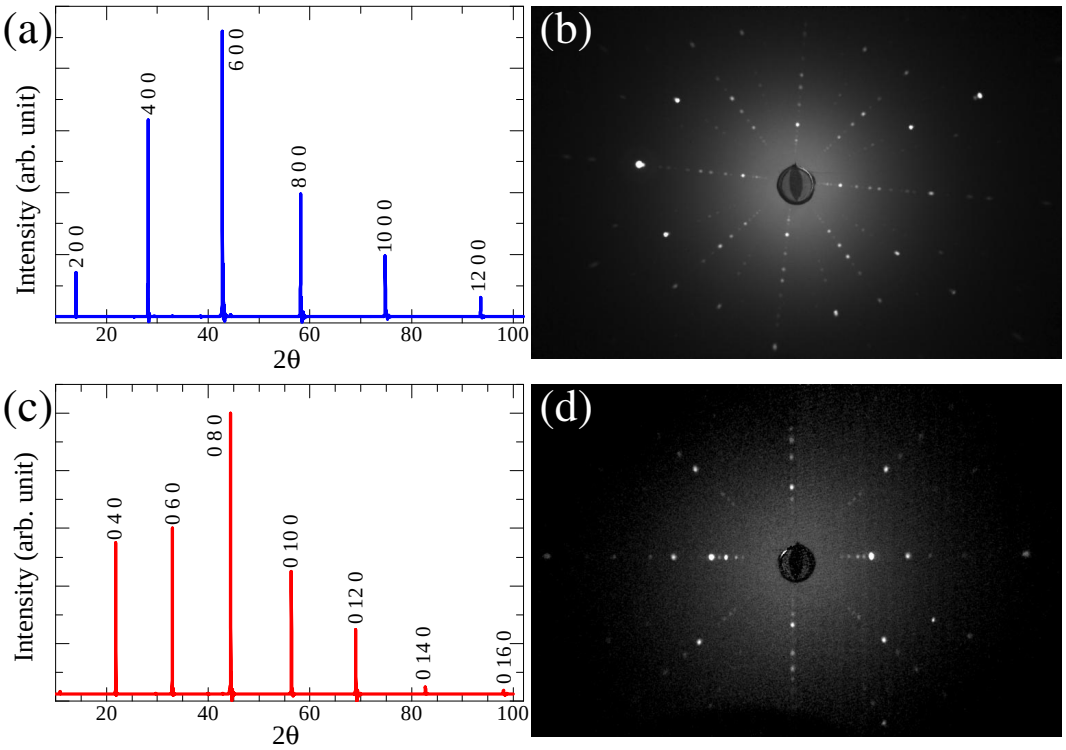

Figure 5.15: Representative x-ray diffraction pattern from a cleaved surface ($\perp$ to the plane containing Cu-O chains) of (a) Sr_2CuO_3 and (c) $SrCuO_2$ using Bragg-Brentano geometry and corresponding Laue diffraction pattern in the panels (b) and (d).

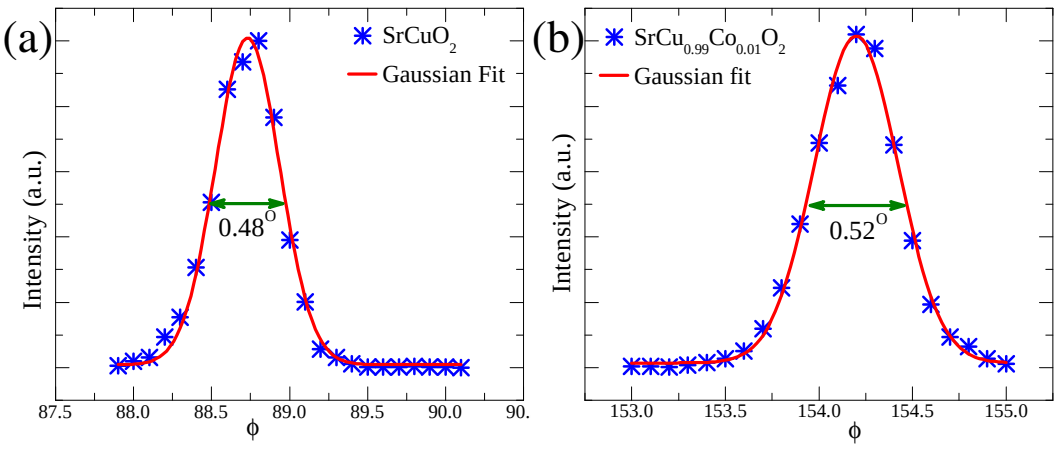

Figure 5.16: Rocking curve of nuclear Bragg reflections measured by neutron diffraction (a) pure (b) Co1% doped single crystals (see text for details). The solid lines are Gaussian fits to the data.

melted portion of the feed between the feed (solid) and FZ(liquid) allows a dynamical equilibrium to establish leading to the steady state growth condition where the FZ volume/composition remains invariant in time.

However, before furnishing the results of our experiment, we first briefly mention here the procedure involved: the FZ analyzed and reported here were from those growth experiments that had ran steadily without interruption or external intervention for several days and were near completion. To quench the floating zone, the furnace power was quickly decreased from its steady-state value to a predetermined value where the FZ is expected to have solidified completely. This value was obtained in a separate experiment where the melting behaviour of the solvent disk was examined in the image furnace under 1 bar oxygen flow [171]. From these initial experiments we estimated the furnace cooling rate during the quenching process to be around 40-60 °C/s. After the FZ is solidified, the furnace is allowed to cool down to the room temperature in 2-3 hrs. The frozen-in FZ was sectioned longitudinally in air using a low-speed diamond saw without coolant. The sectioned surfaces were dry polished using silicon carbide papers of progressively higher grit size. The final polishing was done using the grit size 1200 ($\sim 15\mu$m roughness). Immediately after the final polishing, the samples were stored in an Ar-filled glove box because of their strong tendency to decompose in the presence of moisture [172].

5.3.1 Lamp power dependence of the TSFZ process

The outcome of a TSFZ growth experiment depends significantly on the temperature profile of the image furnace, which in turn depends primarily on the shape/size and power of the lamp filaments employed. Typically, lamps of smaller power and flat filament geometry create a sharper temperature gradient along the vertical furnace axis.

The first set of growth experiments were carried out using two different sets of lamps: (i) one, with a power rating of 300 W, and (ii) another with that of 150 W. The images of the frozen-in FZs, obtained using an optical microscope under the polarized light, are shown in Figure 5.17 for the two cases. From these images it is evident that

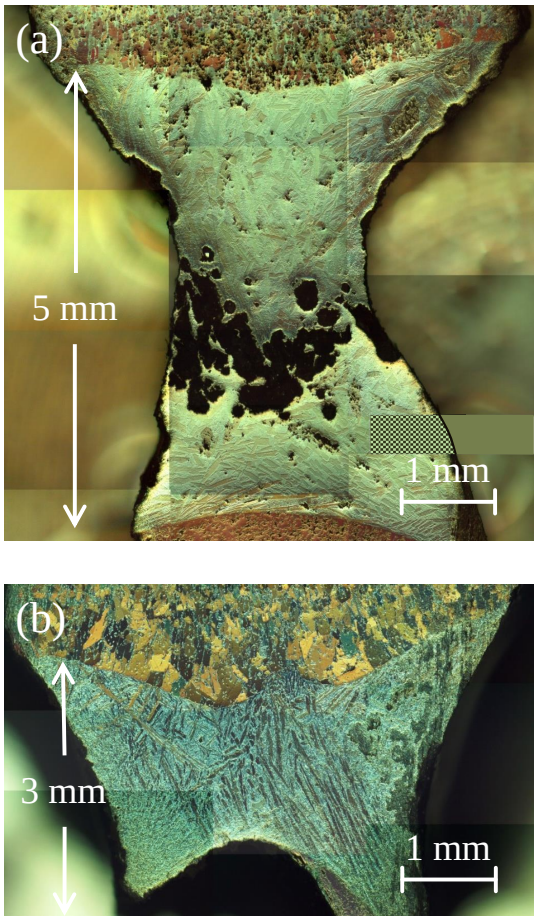

Figure 5.17: Optical images of the longitudinal section of the frozen-in floating zone during the steady state growth of Sr_2CuO_3 using lamps of power rating (a) 300 W and (b) 150 W

the aspect ratio of the resulting FZ varies considerably depending on the power-rating of the lamps used. Using the 300 W lamps, the FZ is considerably longer and thinner in the middle. On the other hand, the zone length using the 150 Watt lamps was found to be smaller and the zone thickness wider enough to provide the necessary stability to the FZ. In the subsequent growth experiments and for the growth of all the doped single crystals, therefore, we used lamps with power rating 150 W.

5.3.2 Solid-liquid interfaces

The interface shape has been argued to be one of the important factors that governs the quality and diameter of a crystal grown using the floating-zone method. Although lamps

of lower power help create a smaller liquid zone and thus easier to control, its shaper temperature gradient introduces a convexity to the solid liquid interface (see figures 5.17 and 5.18), which is considered unfavorable as it tends to enhance the concentration of defects along the core of the growing crystal[154]. On the other hand a slightly convex melt-growth interface is considered desirable (as in the case of 300 W lamps) with the least number of defects reported [173]. In our case, the shape of the interface is convex, however, the convexity appears to be enhanced, which suggests a relatively large temperature gradient at the interface of the growing crystal and the possibility of defects and disorientation in the peripheral regions. Typically, the absorption of infrared radiation at the surface of the melt results in a small temperature gradient in the radial direction which may be further augmented due to anisotropic thermal conductivity of the growing crystal. Low relative thermal conductivity in the transverse direction of the growing crystal may result in a temperature gradient within the floating zone, with a slightly cooler core region. One can apply faster rotation speeds to counteract the gradient and thus lamps with lower power can also be used.

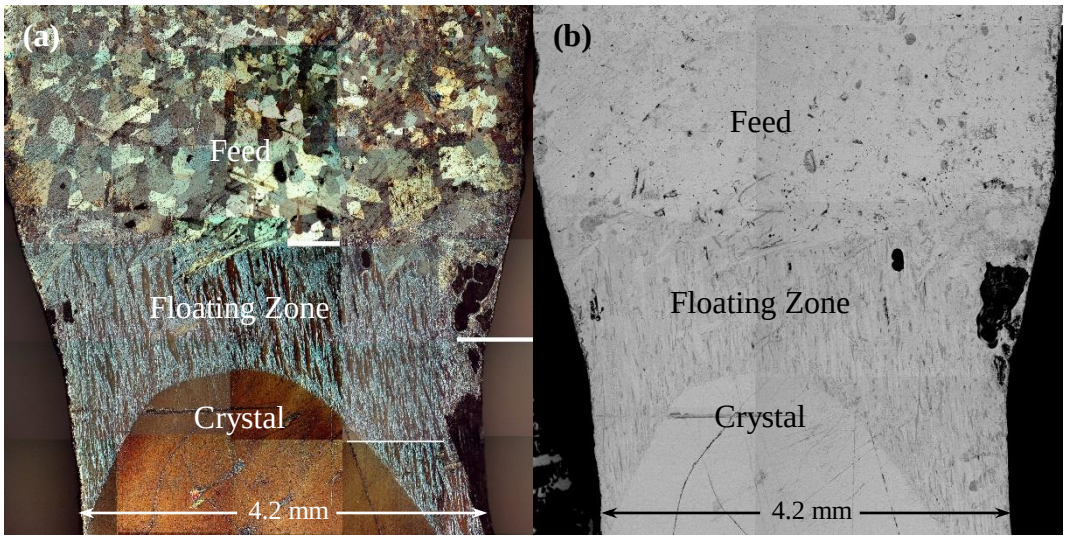

Figure 5.18: (a) Optical image under polarized light of the frozen-in steady state floating zone and (b) the corresponding image obtained using SEM (normal mode).

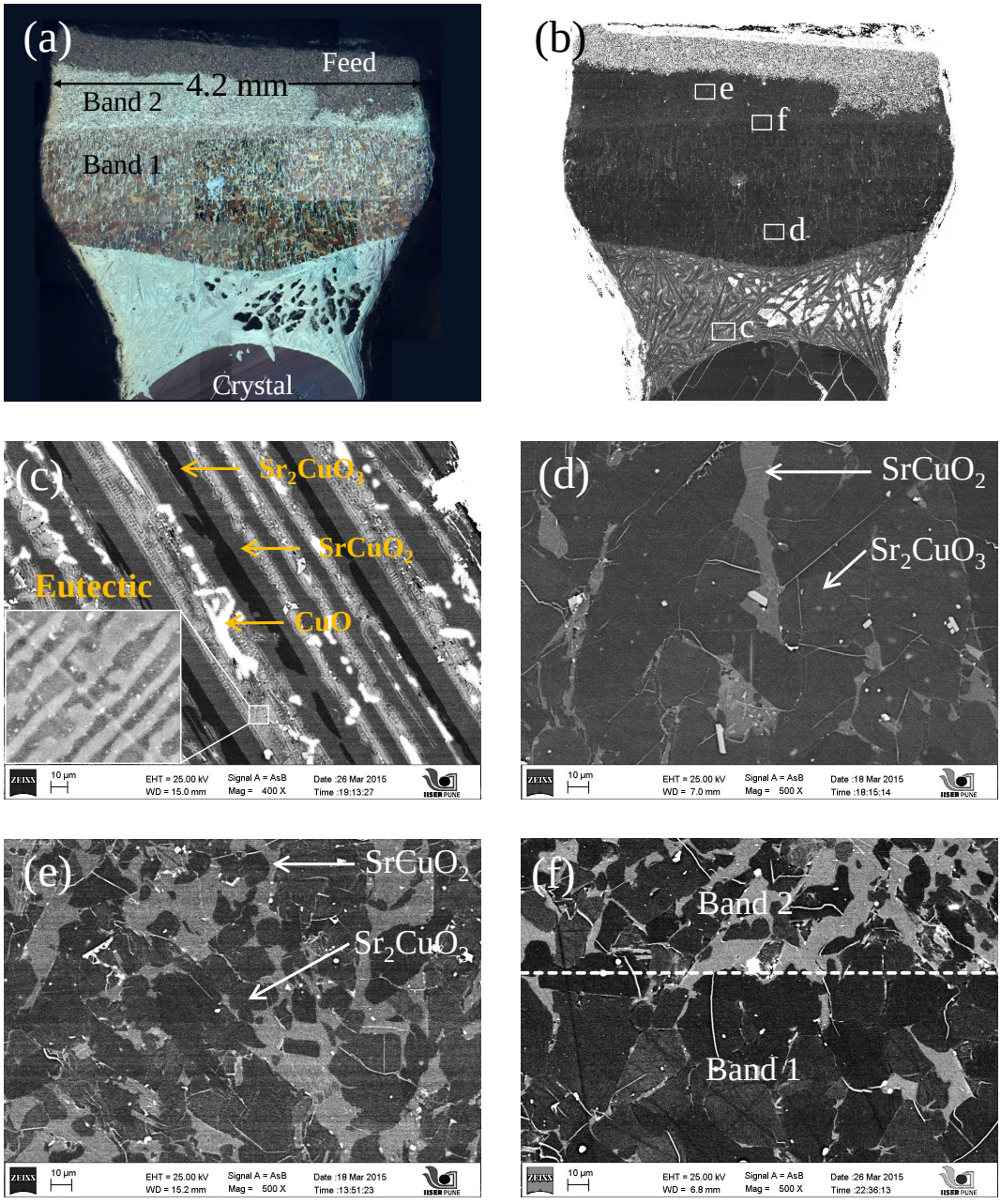

Figure 5.19: Representative (a) optical and (b) BSE images of the quenched floating zone during the growth experiment of 0.25 % Mn doped Sr_2CuO_3. The regions labelled c, d, e and f in panel (b) are shown magnified in the respective panels (c), (d), (e) and (f). In panel (c), the black stripes represent the phase Sr_2CuO_3, the grey ones represent $SrCuO_2$ and the white grains represent CuO_x. The region marked eutectic is exaggerated in the inset of panel (c). The images were captured in the inverted mode (see text for details).

5.3.3 Voids in the solidified TSFZ

Figure 5.19 shows representative images of the longitudinal sections of the solidified FZ from the growth experiments labelled Mn 0.25 % I in Table 5.3. The Presence of voids in the solidified FZ can be readily seen. Such voids were seen in all the cases that we analyzed using optical/scanning electron microscopy. During the steady-state growth conditions, we did not observe the presence of bubbles in the FZ. Post growth analysis also did not reveal any signs of voids in our grown crystals. These voids likely appear during quenching and their occurrence is probably related to the dissolved oxygen gas in the melt. Note that the temperature of TSFZ operation during steady state ($\sim 1250^{\circ}$C) is higher than the temperature at which CuO dissociates into Cu_2O (liquid) and O_2 (gas)[160] (see Figure 5.9). Under an oxygen-rich growth atmosphere, the O_2 gas liberated upon decomposition of CuO is expected to remain dissolved in the melt. Upon sudden cooling, not all the Cu_2O present in the melt will have sufficient time to transform back to CuO; hence, an equivalent amount of gaseous O_2 will be liberated during this process resulting in the formation of voids. This hypothesis is supported by the presence of large CuO_x grains in the SEM images of the frozen-in-zone(see, panel (c) of Figure 5.19).

5.3.4 TSFZ composition

Panel (c) of Figure 5.19 shows typical FZ microstructure. In good agreement with the SrO–CuO phase diagram (Figure 5.9), the average FZ composition obtained using the energy dispersive x-ray analysis of the frozen in zone was found to be $\sim 14:24$ for the compound Sr_2CuO_3 and $\sim 3:7$ for the case of $SrCuO_2$, which reinforce our choice of the solvent composition. The microstructure of the FZ for the growth of 0.25 % Mn doped Sr_2CuO_3 shows the presence of phases: Sr_2CuO_3, $SrCuO_2$ and a eutectic mixture consisting of phases $Sr_{14}Cu_{24}O_{41}$ and CuO. Additionally, we also found the presence of CuO_x grains whose origin has been discussed in the previous section. The growth-melt interfaces in each case were found to be moderately convex shaped, which is preferred as it prevents the concentration of defects along the core of the growing crystal[173].

Table 5.5: Float zone dopant concentrations

Sample	Nominal (%)	Actual (%)
$Sr_2Cu_{0.99}Zn_{0.01}O_3$	1.00	11.13
$Sr_2Cu_{0.99}Co_{0.01}O_3$	1.00	7.50
$Sr_2Cu_{0.975}Co_{0.025}O_3$	2.50	17.71
$Sr_2Cu_{0.99}Ni_{0.01}O_3$	1.00	1.10
$Sr_2Cu_{0.9}Ni_{0.1}O_3$	10.0	7.30
$Sr_2Cu_{0.9975}Mn_{0.0025}O_3$	0.25	0.22

In the doped crystals, the compositional analysis of the solidified FZ is found to be particularly revealing. As mentioned before, in the growth of doped crystal we added to the solvent disk proportionate amount of dopant: for example, in the growth of 1 % Zn-doped crystal, the solvent disk composition was taken as 37% of SrO and 63 % of $Cu_{0.99}Zn_{0.01}O$. In Table 5.5 we show the dopant concentration in the solidified TSFZs. In the case of Co and Zn doping, the concentration of the dopant atoms in FZ was found to be around 8 and 11 %, respectively. These numbers are significantly higher than the 1 % composition of their starting solvent disks. On the other hand, in the case of Mn and Ni doping the agreement is fairly good even for the crystal growth experiment consisting of 10 % Ni doping. From these observations it is easy to conclude that the actual doping in our Co and Zn crystals differ considerably from their nominal values. Since EDX will not be accurate in deciphering such small dopant concentrations in the grown crystal as were used here, an indirect proof of their concentration in the crystal comes from the magnetic susceptibility experiments. Recently, we analyzed the susceptibility of Zn doped Sr_2CuO_3 using the finite-size corrections based on an expression for the susceptibility obtained using the quantum field theory [105] and found that the actual Zn concentration to be roughly half of the nominal value after taking into account the intrinsic defects due to small oxygen off-stoichiometry (see chapter 4). In the 10 % Ni doped crystal where EDX tool can be successfully employed; we found that the concentration of Ni in the grown crystals is indeed close to 10 %, which corroborate the results of the solidified FZ. The growth attempts with Co-concentration 2.5 % did not prove successful which is probably related to a gradual build of Co-concentration in the FZ leading to growth instabilities.

5.3.5 Behaviour of feed in the vicinity of the TSFZ

Another observation common to all the growth experiments of Sr_2CuO_3 and its doped variants, pertains to the region of the feed near the upper interface of the floating zone. As shown in representative images of Figure 5.19, while the lower crystal-melt interface is rather sharp, same is not true for the upper interface. The section of the feed close to the upper interface shows the existence of an intermediate, partially melted, region between the feed and the melt. The micro-structure of this region, which is distinctly different from that of the feed rod, revealed two types of crystalline phases: Sr_2CuO_3 (dark grey) and $SrCuO_2$ (light grey). Upon progressing upwards along the length of the feed, the phase $SrCuO_2$ gradually increases at the expense of the primary phase Sr_2CuO_3 (Compare panel (d) and (e) in Figure 5.19). This trend is also reflected in the composition variation (Cu/Sr) along the length. Figure 5.20 shows the average composition at various distances from the bottom (grown crystal) to the top (feed rod) of the image. Composition of the regions labelled "crystal" and "feed" agrees with the expected Cu/Sr = 0.5. The composition of the FZ is found to be Cu/Sr = 1.70 (or SrO : CuO = 14 : 24) which agrees with the composition of the peritectic point associated with the incongruent decomposition of Sr_2CuO_3 upon heating. In the intermediate region between the FZ and the feed, the Cu/Sr ratio progressively increases from 0.66 to 0.83.

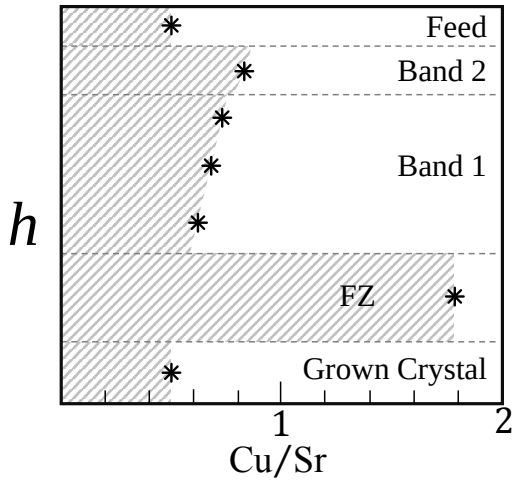

Figure 5.20: Composition Cu/Sr variation shown as a function of distance measured from bottom to top for the floating zone of Figure 5.19.

The feed-melt interface will be sharp provided the feed rod has the desired stoichiometry and its density is near 100 % of the theoretical density. However, the feed rods employed in actual experiments are always porous to some extent which allows the melt from the FZ to creep-up into the feed by the capillary action. As the liquid creeps up, it also experiences a large temperature gradient that causes the liquid composition to change as it move up, in accordance with the liquidus line of the SrO–CuO phase diagram (see Figure 5.9), which explains the observed increase of Cu/Sr ratio in the intermediate region.

A closer investigation of the intermediate region also revealed the existence of a boundary across which the micro-structure changes sharply (see panel (f) of Figure 5.19). Below this boundary (region labelled "Band 1" in panel (a)), the predominant phase is Sr_2CuO_3 (dark grey region) and above it (the region labelled "Band 2" in panel (a)), both, $SrCuO_2$ and Sr_2CuO_3 are present roughly in equal proportion. In accordance with the phase diagram of Figure 5.9, "Band 1" corresponds to the region of the SrO–CuO phase diagram where the liquid L1 co-exists with the solid Sr_2CuO_3. This naturally explains the predominance of the phase Sr_2CuO_3 in band 1. The light grey phase ($SrCuO_2$) in band 1 appears when the liquid L1 is quenched. Similarly, the "Band 2", consists of the solid $SrCuO_2$ (obtained from Sr_2CuO_3 by its reaction with the Cu-rich melt) and the liquid L2 that coexists with it; along with solid Sr_2CuO_3 which is the unreacted feed. In principle, upon quenching, there should also have appeared the phase $Sr_{14}Cu_{24}O_{41}$ and the eutectic mixture corresponding to the point E shown in Figure 5.9 in both the bands. However, given the fact that the quantity of liquid in the partially melted region of the feed is rather small; the corresponding amounts of phase $Sr_{14}Cu_{24}O_{41}$ and of the eutectic mixture will be even smaller, which is probably the reason why these phases were not detected.

5.4 Summary

In summary, we gave a very detailed description of the TSFZ growth process applied to the spin chain compounds Sr_2CuO_3 and $SrCuO_2$, and their doped variants, consisting

Zn, Ni, Co and Mn doped at the Cu-site. We discussed that the knowledge of the melting behaviour of a compound is useful in deciding the appropriate growth technique. In particular, we argue that for incongruently melting solids, the TSFZ technique is appropriate for obtaining large and high-quality single crystals. We showed that a stable floating-zone that can work for days without interruption can be established right at the beginning of the growth experiment by choosing the composition of solvent disk to be the same as that of the associated peritectic point. We argue that for uninterrupted TSFZ growth one should also pay due considerations to the melting behaviour of the solvent disk. The high-quality of the grown crystals was ascertained using several complimentary techniques including scanning electron microscopy, x-ray diffraction and often the rocking curves measured by neutron diffraction on cm-size crystals.

We also carried out a very detailed investigation of the TSFZ process by carefully analyzing the micro-structure and composition of the steady state floating zones which lead to a better understanding of the crystal growth process. Determination of the influence of lamp power on the TSFZ process, and the porosity of the feed rod in the growth experiments were discussed. The dopant composition in the final FZ is determined using EDX. While the concentration of Ni and Mn in the final FZ remains the same as in the starting solvent disk, the same is not true for Zn and Co. In both these cases, we find a strong tendency of the dopant to accumulate in the FZ. This tendency was found to be more pronounced with Zn than Co doping. The experiments suggested that the distribution coefficient of Co and Zn is considerably smaller than 1; while that of Ni and Mn appears to be close to 1.

Chapter 6

Bulk Magnetic Behaviour in the Presence of Dilute Disorder

In chapter 2 we discussed the effects of scalar impurities ($S = 0$) on the bulk magnetic properties of the spin $1/2$ HAF chain. The $S = 0$ disorder can arise due to an intrinsic defect (missing of a spin from its regular site) or an extrinsic non-magnetic impurity at the spin site. Irrespective of its origin, the spin 0 disorder effectively breaks an infinitely long chain into finite-length segments. Due to chain-breaks, the staggered moment at the boundaries of these segments alters the bulk magnetic responses of the chain to an external stimuli, for an example, magnetic field. As mentioned in chapter 2, the problem of finite-size chains was addressed in several papers using the field theoretical calculations (see for example, [105–107, 123]). Theory predicts that the scalar impurity tends to disrupt the local antiferromagnetic correlations, liberating additional, low-energy spin degrees of freedom, which contribute to the bulk magnetic properties of the spin $1/2$ chain. The bulk magnetic susceptibility, for example, exhibits a discernible 'Curie-tail', with a temperature dependent Curie constant [105]. In the quasi-1D spin $1/2$ HAF chain, scalar impurities result in the suppression of the magnetic ordering temperature [106].

In this chapter we examine the finite-size effects on the bulk magnetic behaviour of a quasi-1D spin $1/2$ HAF chain. The main objective of this work is to verify the field theory result by Sirker et al.[105], which quantifies the effect of boundaries on the susceptibility of a spin chain. We also investigated the effective spin state of Ni^{2+}

doped Sr_2CuO_3. This question is important because the field theory result by Eggert and Affleck [91] predicts that an isolated spin 1 impurity in a spin 1/2 chain may essentially act like a scalar impurity ($S_{eff} = 0$) due to the Kondo-like screening of the Ni^{2+} spin by the antiferromagnetically coupled host spins (subsection 2.2.2).

The plan of this chapter is as follows: In section 6.1, we will first discuss the dc magnetic susceptibility of pristine Sr_2CuO_3 containing intrinsic chain-breaks arising due to oxygen off-stoichiometry, as it presents the simplest case due to its linear chain geometry. The procedure is then extended to analyse the susceptibilities of Zn and Ni doped Sr_2CuO_3 crystals in sections 6.2 and 6.3. In the Zn doped Sr_2CuO_3 crystals, the defect concentration obtained is discussed in light of the crystal growth experimental results. The magnetisation of the Ni-doped crystal is fitted by assuming effective Ni^{2+} spin to be zero. Finally, in section 6.4, we present our inelastic neutron scattering results on Zn, Ni and Co doped crystals, which throw light on the low-energy spin excitation spectrum in the presence of dilute non-magnetic and magnetic impurities.

6.1 Bulk magnetic susceptibility of pristine chains

In figure 6.1 the low-temperature magnetic susceptibilities of the pristine Sr_2CuO_3 crystal is shown. The measurements were carried out under an applied magnetic field of $H = 10$ kOe. The data show good agreement with the previous report on well-annealed single crystals by Motoyama *et al.* [56]. The small temperature-independent anisotropy above $T \approx 20$ K is also in agreement with the previous report and is attributed to the *Van Vleck paramagnetism* [56]. At lower temperatures, the presence of the interchain interaction alters this behaviour considerably. As shown in figure 6.1, a distinct change of slope of $\chi(T)$ is observed upon cooling below $T \approx 5$ K, which coincides with the onset of long-range spin ordering in this compound [57]. Due to interchain interactions, the requirement of good one-dimensionality breaks down at low temperature. Judging from the susceptibility anisotropy, which becomes temperature dependent upon cooling below $T = 20$ K, one may expect the interchain interactions to be important only below this temperature. The interchain interaction is not included in equation 2.3, which

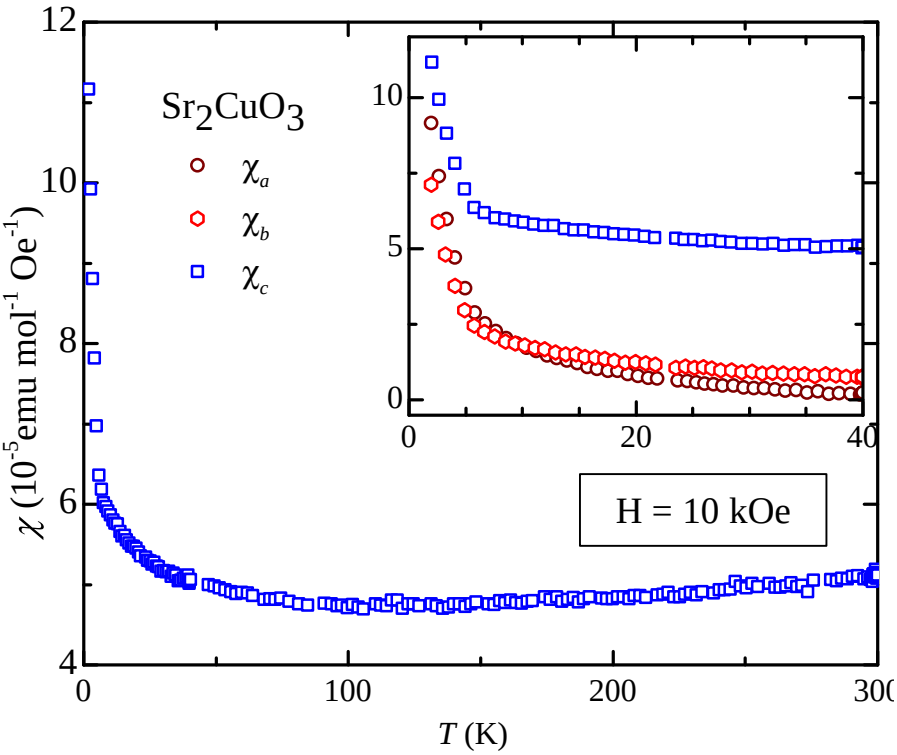

Figure 6.1: Temperature variation of magnetic susceptibility χ of compound Sr_2CuO_3. The data shown are recorded by applying field perpendicular to the CuO_2 plaquettes. Inset: low temperature susceptibilities along crystallographic a, b and c axes.

we shall be using to analyse susceptibility for defect concentration; therefore, we will consider only the data above $T = 20$ K in our analysis.

As seen in the main panel of figure 6.1, upon cooling below room temperature, susceptibility decreases gradually as expected since at room temperature the sample is already cooled far below the temperature $T = 0.675J/k_B$ where $\chi(T)$ is expected to show a broad susceptibility peak [27, 30]. However, in the temperature range below about 100 K or so, the susceptibility shows a significant "Curie-tail" arising primarily from the chain breaks present due to slight oxygen excess in the crystals [54, 56]. In the presence of chain breaks one can decompose the experimentally measured susceptibility as follows: $\chi = \chi_{VV} + \chi_{core} + \chi_{Curie} + \chi_{\text{chain}}$, where χ_{VV} is the Van-Vleck paramagnetic contribution and χ_{core} is the diamagnetic contribution of the ionic cores: both these terms are small and nearly temperature independent. Henceforth, we will use

the symbol χ_0 to represent the algebraic sum of these two terms; χ_{Curie} is the contribution arising due to the chain breaks as discussed above and χ_{chain} is the susceptibility of an uniform endless $S = 1/2$ HAF chain in the absence of defects. Statistically, due to chain-breaks there will be as many odd-length segments as even. To determine the chain break concentration (p), one can assume that at sufficiently low temperatures, the contribution of the even-length segments dies out and that the odd-length segments, having concentration p/2, lock into a spin-doublet ground state ($S_Z = \pm 1/2$) due the nearest neighbour AFM interaction [54]. By fitting the low temperature data using the Curie-Weiss (CW) law one can therefore get the value of p. However, this naive approach leads to a considerable underestimation of the impurity concentration [105]. Moreover, in real systems, a satisfactory fit to the data can only be obtained by including the Curie temperature in the fitting expression. However, the physical significance of the Curie temperature remains ambiguous [54, 126]. As discussed previously in chapter 2, the segmented chains due to the presence of scalar defects behave differently over different temperature ranges. It gives a 1/T contribution to the susceptibility due to odd-length segments at very low temperature; and at high temperatures, apart from the contribution due to bulk of the segments, one should also take into account the boundary contribution arising from the staggered moment at the free ends of a segment which also corresponds to a Curie-like behaviour with logarithmic corrections [107]. Equation 2.3, by *Sirker et al.*, can be used for fitting the experimental susceptibility of a $S = 1/2$ HAF chain in the presence of chain breaks including the boundary corrections [38].

In previous studies, the susceptibility of these compounds is analysed by taking a g value close to 2 [54, 105, 174], since the spin associated with the Cu^{2+} ion behaves like an isotropic Heisenberg spin, which is also reflected in the magnetic susceptibilities that show a nearly temperature-independent anisotropy. Moreover, the electron-spin-resonance (ESR) experiments [175, 176] also suggest that the value of g for these compounds is not significantly different from 2. In view of this, in analysing the susceptibility data using equation (2.3) we have fixed the g value at 2. Slight departures from this value are not expected to change our results significantly.

For χ_{chain} in equation (2.3) we will use the fit function obtained by Johnston *et al.* [reference [40], fit 1, equation (50)]

$$\chi_{\text{chain}} = \frac{1}{4T}\left[\frac{1+\sum_{n=1}^{q}\frac{N_n}{(T/J)^n}}{1+\sum_{n=1}^{r}\frac{D_n}{(T/J)^n}}\right] \tag{6.1}$$

The values of N_n's and D_n's are taken from reference [40]. The expression yields highly accurate values of χ_{chain} in the temperature range 0.01J < T < 5J). Since, J for the compounds under consideration is of the order of 2000 K, this expression is quite appropriate in the temperature range over which the data has been analysed in the present work. It is worth mentioning here that the numerical result for χ_{chain} due to Bonner and Fisher (BF) [27] which is frequently used in the literature to fit the experimental data of spin chains is accurate only at high temperatures $T \geq 0.4J/k_B$ which makes its applicability inappropriate in the present case. This non-applicability of the BF model in fitting the susceptibilities of these compounds has been demonstrated by Motoyama *et al.* [56].

6.1.1 Fitting procedure

In equation 2.3, there are three fitting parameters: (1) the defect concentration p, (2) the intrachain exchange J and (3) the temperature independent contribution to the susceptibility, χ_0 ($\chi_p = \chi - \chi_0$). Fitting the experimental data to equation 2.3 can give rise to arbitrary results if the parameters are not initialized judiciously. This problem is further compounded by the fact that in the temperature range of our measurements the susceptibility values are rather small ($\approx 5 \times 10^{-5}$ emu/mol.Oe). In order to avoid these difficulties, we determined these parameters in steps by selecting suitable temperature ranges where equation 2.3 can be further simplified and the number of parameters reduced.

In the first step, we considered a temperature range over which the measured susceptibility is largely 'p' independent which allowed for the estimation of χ_0 and J. For example, in the high temperature range $250K \leq T \leq 300K$ of our measurements the contribution of the first term ($\approx p/8T$, where $p \leq 0.01$) is negligible. This leaves us

with only the χ_{chain} and the χ_B terms to deal with in equation 2.3. We further note that the relative magnitude of $p\chi_B$ is very small compared to $(1 - p + pJ/T)\chi_{\text{chain}}$. For instance, if one assumes p to have a value of 0.005 and take J to be around 2000 K then near $T = 300$ K the value of the term $p\chi_B \approx 7 \times 10^{-7}$emu/mol.Oe and that of $(1 - p + pJ/T)\chi_{\text{chain}} \approx 9 \times 10^{-5}$emu/mol.Oe, where the value of χ_{chain} itself is $\approx 8.7 \times 10^{-5}$ emu/mol.Oe which is almost 97 % of $(1 - p + pJ/T)\chi_{\text{chain}}$. Therefore, by taking the initial values of J and χ_0 from reference [56], we fitted the measured susceptibility in the above temperature range simply by: $\chi = \chi_0 + \chi_{\text{chain}}$. This gave us a fairly good estimate on the values of χ_0 and J. In the next step, we used these values to fit the data from 20 to 300 K using equation 2.3 by allowing p to vary. In the final step, all three parameters were varied around their values obtained in the previous steps to estimate the size of the error bars.

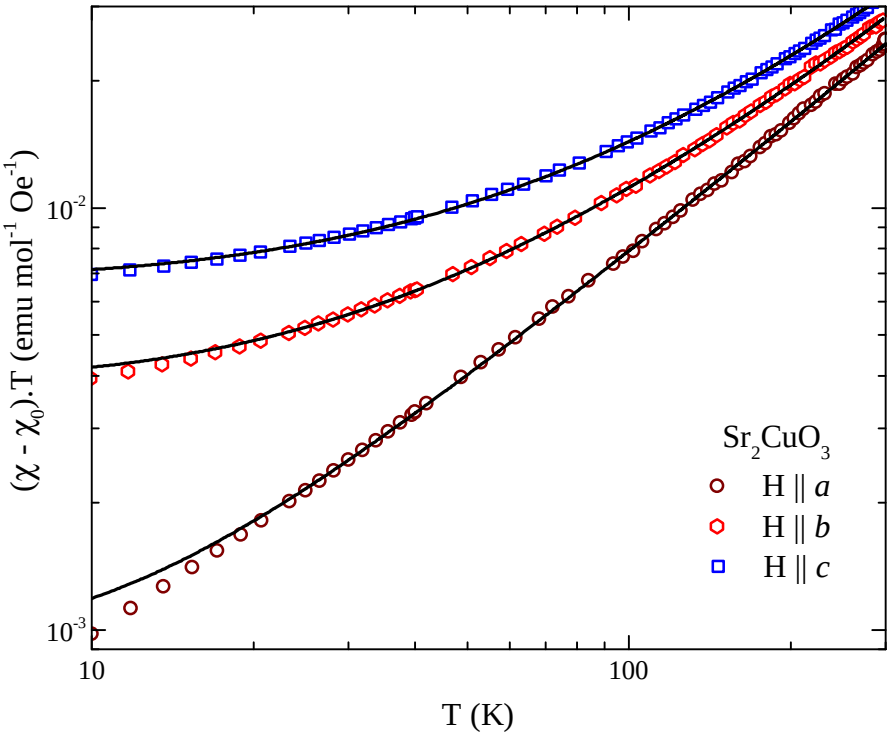

Figure 6.2: Magnetic susceptibility $(\chi - \chi_0)T$ of Sr_2CuO_3. Solid lines represent the theoretical fit using equation (2.3) (see text for details). Data along the *b* and the *c* axes are shifted by multiples of 3 x 10^{-3}.

Table 6.1: Values of intra-chain exchange J, the temperature independent contribution χ_0 and defect concentration p obtained by fitting the experimental susceptibility using equation (2.3). For comparison, the low-temperature data were also fitted to the Curie-Weiss equation. p_{CW} and θ_P are the fitting parameters of this fit (see text for details).

Parameters		J (k_B K)	χ_0 (10^{-5} emu/mol.K)	p (per Cu Site)	p_{CW} (per Cu Site)	θ_p (K)
Sr_2CuO_3	($H \parallel a$)	2100±200	-8.0±0.2	0.0047 (1)	0.001	2.9
	($H \parallel b$)		-7.7±0.2	0.0051 (1)	0.001	-1.5
	($H \parallel c$)		-3.6±0.2	0.0045 (1)	0.001	-4.8
$Sr_2Cu_{0.99}Zn_{0.01}O_3$	($H \parallel c$)		-3.1±0.2	0.011 (1)	0.004	-1.5
$Sr_2Cu_{0.99}Ni_{0.01}O_3$	($H \parallel c$)		-3.5±0.2	0.018 (1)	0.006	7.1

6.1.2 Susceptibility of undoped Sr_2CuO_3

In figure 6.2 we show the temperature variation of quantity $(\chi - \chi_0)T$ along with the fitted curves. The data and the fitted curves are shown on a log-log plot to emphasize the low-temperature behaviour. A satisfactory agreement of the experimental data with the fitted curve is observed over the entire fitting range. However, when extrapolated to lower temperatures the fitted curve tends to saturate to the value $(p/4)[(1-p)/(2-p)] \approx p/8$, whereas the experimental data continue to decrease due to the intrachain exchange not included in our fitting equation. The p values along the three crystallographic axes are listed in table 6.1. The average p value came out to be to be 0.005 per Cu site. This value is consistent with a value of 0.006 per Cu site reported by Sirker *et al.* for their unannealed crystal. An average J value of 2100 ± 200 K and χ_0 values (in the units of 10^{-5} emu/mol.Oe) of $-8.0 \pm 0.2(\chi_0^a)$, $-7.7 \pm 0.2(\chi_0^b)$ and $-3.6 \pm 0.2(\chi_0^c)$, where the superscript on χ_0 denotes the crystal axis along which the external magnetic field is applied are well within the expected range based on the previous studies. For example, Motoyama et al. obtained a value of $J = 2200 \pm 200$ K by analysing the susceptibility data of annealed crystals up to temperatures as high as $T = 800K$ [56]. Here, it should be mentioned that somewhat higher values of J were reported from

the optical absorption ($J = 2850$ K)[58] and the low-temperature specific heat data ($J = 2500$ K) [108], respectively. However, based on a Quantum Monte Carlo study it has been suggested that the value of J estimated from $\chi(T)$ data may be reduced due to phonon induced fluctuations of J not included in fitting the $\chi(T)$ data [177].

In table 6.1 we also list the chain-break concentration obtained by fitting the susceptibility data between $T = 20$ K and 40 K using the CW law. To fit the CW equation, we have subtracted the χ_0 and χ_{chain} contributions from the raw data. χ_{chain} is calculated using the J value listed in Table 6.1. An average chain-break concentration of 0.0012 per Cu site obtained from the CW fit agrees well with that reported previously [56, 126], where a similar method has been used. However, as expected, this value is considerably smaller than that obtained using a more rigorous fitting procedure where the boundary contributions are also taken into account.

As noted earlier, the effective paramagnetic concentration (N_S) in our model is a temperature dependent quantity that shows a non-monotonic behaviour, decreasing rapidly upon increasing the temperature (from a value of $N_S = p/2$ at $T = 0$) before increasing again at high temperatures where it goes as $p/[3ln(2.9J/T)]$. At any intermediate temperature T, N_S can be estimated from $\chi_p(T)$ by subtracting from it the chain susceptibility $\chi_{\text{chain}}(T)$ and then by equating the temperature times this difference to an effective temperature dependent Curie constant $C(T)$ (see equation 7.3 of reference [38]). Using C(T), the value of N_S can be readily calculated (see, for example, reference [10]), using

$$C = (N_s N_A g^2 \mu_B^2 S(S+1))/3k_B. \tag{6.2}$$

In table 6.2, we list the values of N_S for our Sr_2CuO_3 crystals at temperatures $T = 20, 40, 80$ and $300K$. In figure 6.3, we compare the calculated M(H) consisting of a Brillouin term accounting for the $S = 1/2$ paramagnetic impurities (numbering N_S per Cu mol) and the terms linear in H consisting of the contribution due to χ_0 and χ_{chain}. The calculated curves show a good overall agreement with the experimental data at all temperatures and up to the highest applied field. The experimental data, however, show a weak metamagneticlike transition which is evident from a peak in

Table 6.2: Effective paramagnetic impurities in the pristine Sr_2CuO_3.

T (K)	N_S (10^{-4}per Cu site)
20	6.7
40	5.1
80	4.5
300	5.3

the dM/dH plots shown in the insets. The peak position shifts to higher field values with increasing temperature, falling beyond the measurement range of our experimental setup at T = 300 K, where M(H) shows a linear behaviour up to H = 80 kOe, in good agreement with the calculated curve. We shall continue our discussion of this field dependence below. Here, to conclude this subsection, we note that the values of the fitting parameters obtained from our $\chi(T)$ analysis provide a good overall description of the isothermal magnetisation at different temperatures that span a fairly wide range thereby reinforcing confidence in these values. In the future, it will be interesting to investigate how this weak metamagneticlike feature seen in M(H) affects the quality of χ(T) fit at low-temperatures.

6.1.3 Field dependence of magnetisation in Sr_2CuO_3

To probe the observed metamagneticlike behaviour (figure 6.3), we measured the temperature variation of magnetisation under constant applied magnetic fields of increasing strength. The resulting data, plotted as M/H against T, is shown in the panel (e) of figure 6.3. Under low fields (H = 10 kOe), the data show a steep increase below $T = 5K$ which coincides with the magnetic ordering temperature. At higher fields ($H \approx 20$ kOe and higher), a broad maximum above the ordering temperatures is observed, whose position shifts to higher temperatures with increasing field strength. Given that the intrachain coupling is around 2000 K, the observed field dependence of the chain magnetisation under relatively small applied magnetic fields appears surprising. This behaviour was confirmed by performing similar measurements along the other two crystallographic directions (not shown here). While it is difficult to pin down the origin of this behaviour, it is interesting to note that ^{63}Cu NMR spectra recorded on a high-quality crystal of

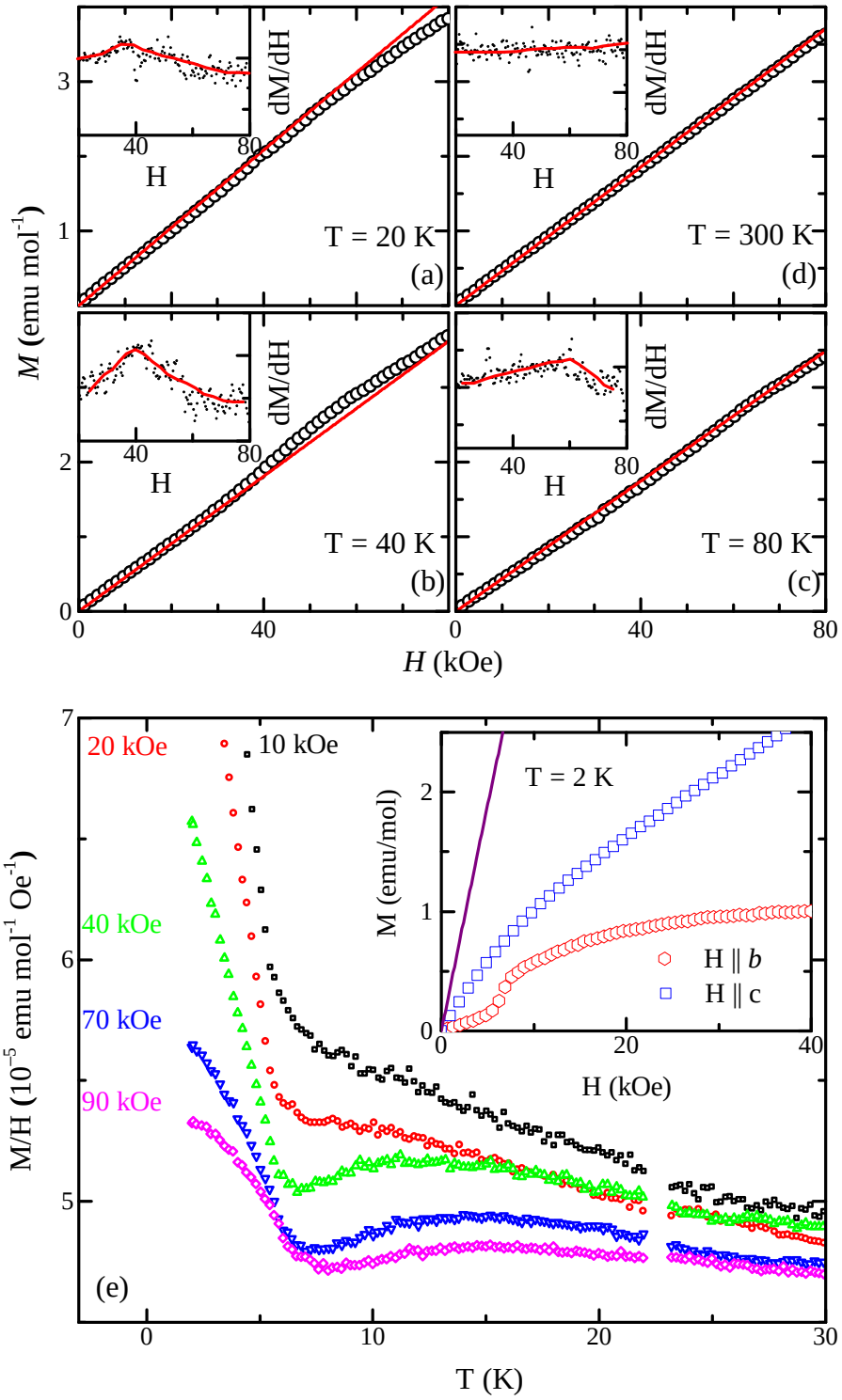

Figure 6.3: (a)–(d) Isothermal magnetisation (M) of Sr_2CuO_3 shown as function of applied magnetic field (H). Solid curves are calculated M(H) (see text for details). Inset: derivative (dM/dH) as a function of H. Lines are guide to the eye; (e) temperature dependence of M/H under various applied fields. In each panel data are shown for field applied perpendicular to the CuO_2 plaquettes

Sr_2CuO_3 also exhibit anomalous features in the same field-temperature range [178]. The field sweep NMR spectra develop a broad background with sharp edges at low temperatures, which was theoretically predicted as arising due to external magnetic field induced local staggered magnetisation near the chain breaks [123]. However, two additional features in the NMR spectra, not expected from the theory of reference [123], were also observed, viz., splitting of the main NMR peak and appearance of shoulders on both sides of the main peak. In one of the theoretical studies, these features were attributed to "mobile bond defects," which can arise due to spin-lattice coupling and result in a "local alternating magnetisation" [179]. In reference [180], however, the role of interchain exchange in giving rise to these additional NMR features has been scrutinized. In the future, it will be interesting to investigate if there is any correspondence between the anomalous NMR line-shape and magnetisation behaviour observed in our experiments.

6.2 Susceptibility of the Zn-doped chain

In order to ascertain the behaviour of scalar disorder in the spin 1/2 chains discussed in the previous subsection we purposefully doped the linear chain compound Sr_2CuO_3 with dilute amount of scalar defect (Zn^{2+}, $S = 0$). As expected the bulk magnetic susceptibility χ shows a enhancement of the Curie contribution (see figure 6.4).

As mentioned in the crystal growth section, by analysing the composition of the frozen-in floating zone we had inferred that the Zn concentration in the grown crystal should be significantly smaller than the nominal value. To test this assertion, we analysed the susceptibility data of the Zn-doped crystals using the same procedure as used for the pristine crystals. The results are shown in figure 6.5. A reasonably good fit to the experimental data is observed down to nearly T = 40 K. The value of the exchange integral did not show any appreciable decrease upon doping, which is not surprising given the dilute levels of doping. Similarly, χ_0 also did not show any significant variation with respect to the pristine compound (Table 6.1). The chain-break concentration was found to be around 0.011(2) per Cu site. Taking a cue from the work of Sirker *et*

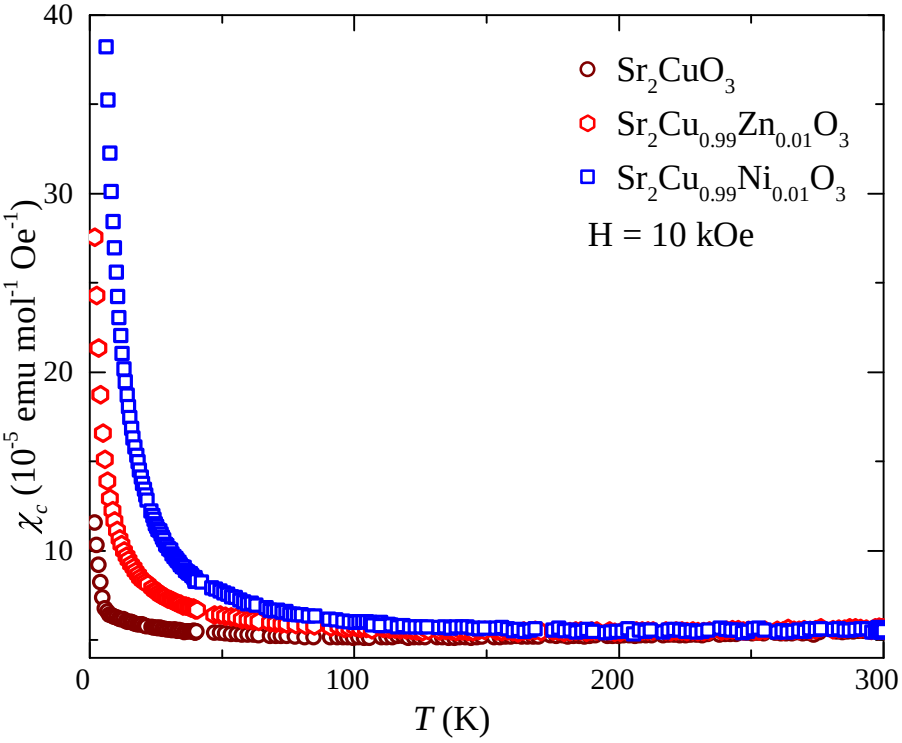

Figure 6.4: dc magnetic susceptibility $\chi(T)$ of the printine, 1% Zn and Ni doped Sr_2CuO_3 in the temprature range 20-300 K.

al., where the chain-break concentration in the doped crystals exceeded the nominal Pd concentration by an amount roughly equal to the concentration of intrinsic chain breaks in their pristine compound, we conclude that the concentration of chain breaks induced by Zn doping in our crystal is around ~ 0.006, the remaining ~ 0.005 being due to the intrinsic defects as inferred from the analysis of the pristine compound. This smaller Zn concentration of 0.6% obtained from the susceptibility analysis is in agreement with the crystal growth results. The smaller value of Zn concentration is further confirmed by the inductively coupled plasma results $*$.

6.3 Ni impurities in spin 1/2 chain

So far, we have seen that the equation 2.3 works well with the spin 1/2 HAF chains in the presence of dilute scalar disorder either due to the intrinsic defects or extrinsic

$*$In collaboration with Prof Christian Hess and his group at IFW, Dresden, Germany

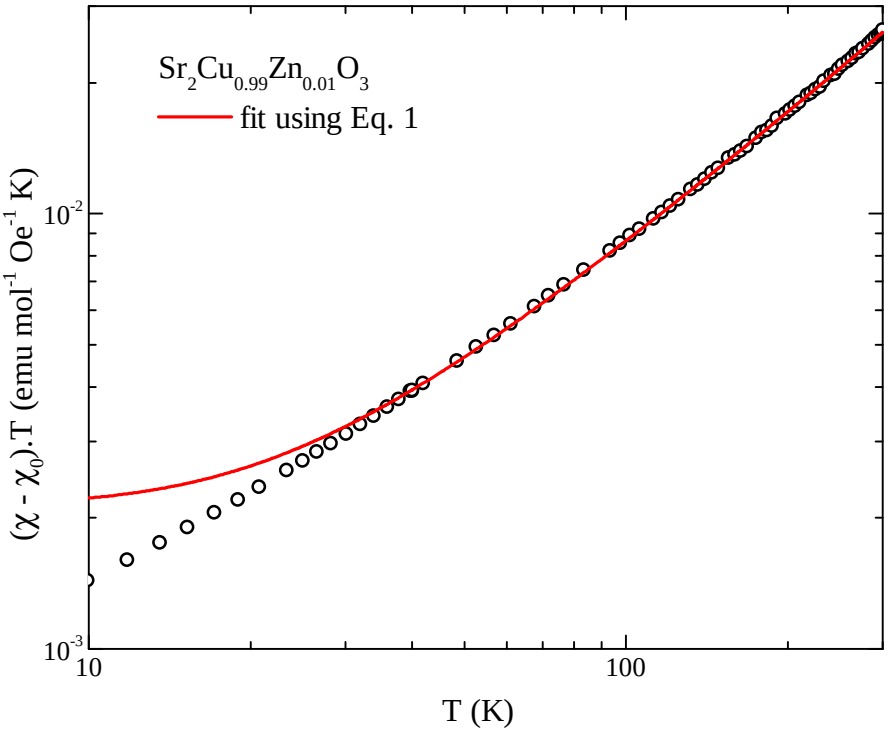

Figure 6.5: Magnetic susceptibility $(\chi - \chi_0)T$ of $Sr_2Cu_{0.99}Zn_{0.01}O_3$. Solid curve in the main panel represents the best theoretical fit using equation (2.3)

scalar impurities. However, a magnetic impurity may also act as a scalar impurity due to the Kondo screening. For the specific case of of dilute Ni impurities in $SrCuO_2$, it was reported that a dramatic change of the low-energy spin excitations takes place upon Ni-doping. Briefly, what had been a gapless two-spinon excitation spectrum for the pristine compound became gapped upon Ni doping [72]. The value of the spin pseudogap was found to be around $\sim$ 8 meV. In our own experiments using inelastic neutron scattering we found a similar gap in Ni-doped Sr_2CuO_3 (shown in the next section). However, no such gap was found in the Zn^{2+} doped crystals [171]. Eggert and Affleck [91] investigated the behaviour of an isolated magnetic impurity substituted in a half-odd-integer-spin HAF chain theoretically. In particular, they considered an isolated $S = 1$ impurity (e.g., Ni^{2+}) in the chain and showed that in the limit of infinite chain length the Ni^{2+} moment either remains decoupled from the chain or is completely screened by the antiferromagnetically coupled neighbouring spins. In the latter case, the screened Ni^{2+} moment essentially breaks the chain at the impurity site.

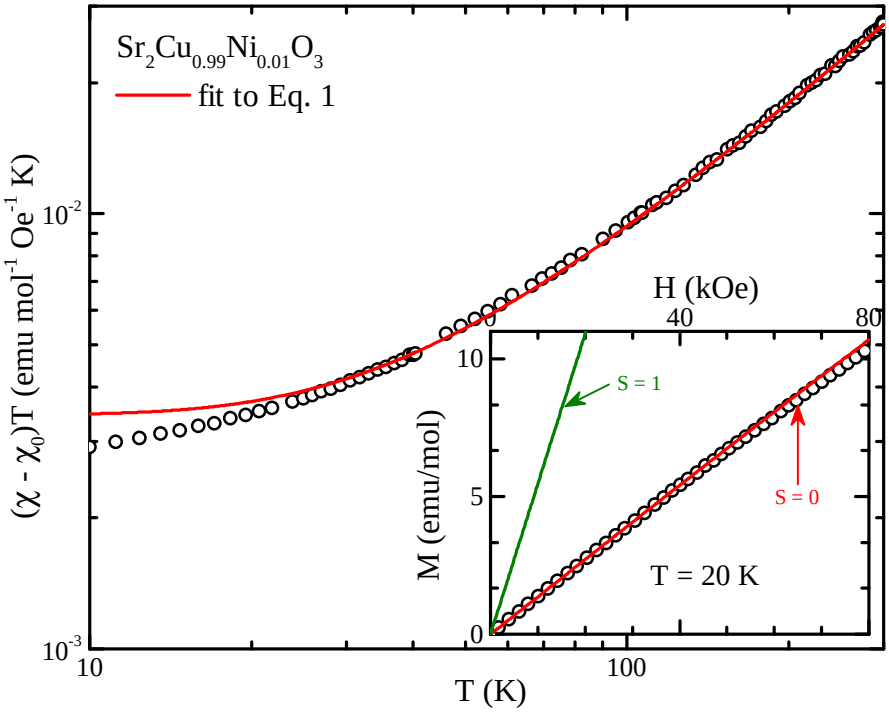

Figure 6.6: Magnetic susceptibility $(\chi - \chi_0)T$ of $Sr_2Cu_{0.99}Ni_{0.01}O_3$. Solid curve in the main panel represents the best theoretical fit using equation (2.3). Inset: isothermal magnetisation at $T = 20$ K. Solid curves are calculated M(H) for S = 0 and S = 1 cases (see text for details).

Therefore, if the spin of Ni^{2+} ion is indeed screened and behaves effectively like a scalar defect, one should be able to find the Ni concentration in our crystal using equation (2.3). In figure 6.4 we show the dc $\chi(T)$ of Ni-doped chains, which also features an enhanced *curie-tail* as was seen in the case of Zn doped samples. The measured susceptibility was analysed using equation (2.3). In figure 6.6, we show the calculated susceptibility for $p = 0.018(1)$ obtained by fitting the experimental data using equation (2.3) as done for the pristine crystal. Within the accuracy of our method, the fitted values of J and χ_0 remains the same as for the pristine crystal (see, table 6.1). The defect concentration estimated here is higher than the nominal value of 0.01. However, if one takes into account the intrinsic defect concentration due to oxygen off-stoichiometry, deduced from the analysis of the pristine compound prepared and annealed under the identical conditions, we get a value of around 0.013(1), which is indeed close to the nominal concentration. We also compared the measured M(H) at

T = 20 K with that calculated for two different spin states: S = 1 and S = 0 for Ni concentration of 1 %. The comparison is shown in the inset of figure 6.6. The calculated magnetisation in the S = 1 case is clearly very large and deviates considerably from the experimental data. On the other hand, in the S = 0 case a close match with the experimental data is observed. There is, therefore, an overall agreement between the experimental data and the calculated curve that proves the point that Ni^{2+} spins are indeed screened. This is also in agreement with the analysis reported in reference [174] on the powder samples of Ni doped Sr_2CuO_3, where it was shown that the Curie tail at low temperatures is considerably smaller than expected from unscreened S = 1 Ni moments.

It should be pointed out that the fit-quality for the Ni-doped case using equation 2.3 is not as good as for the pristine crystal, particularly below T = 100 K. The reason why the fitting equation 2.3 did not work so well is probably related to the fact that the ground state of Ni-doped crystal is gapped which makes the χ_{chain} used in equation(2.3) not suitable at temperatures below which the gap opens. In analogy with $SrCuO_2$, the gap value is expected to be around 8 meV ($\approx$ 80 K) for a similar Ni concentration, which roughly coincides with the temperature below which the fit quality deteriorates. To conclude, our analysis of the magnetisation data supports the screening of the Ni^{2+} moments.

6.4 Magnetic excitations in the weak disorder limit

In pristine form quantum spin chains exhibit several novel properties related to the nature of their low-lying spin excitations. These are known to be *gapless* for chains comprising half-integral spins and gapped for the integral spins [181]. Due to spatial confinement, these excitation are expected to be highly sensitive to the presence of disorder. More specifically, low levels of Ca doping ($\sim$ 10 %) at the Sr site, outside the chain structure, in the spin chain compounds $SrCuO_2$ and Sr_2CuO_3 result in opening of a spin *pseudogap* in their low-lying excitation spectrum [73, 74]. Similarly, merely 1 % Ni doping at the Cu-site in $SrCuO_2$ opens up a sizeable gap ($\sim$ 8 meV), not related to

any structural transition. These observations led Simutis *et al.* to suggest that the spin pseudogap is a generic feature of quantum spin chains with dilute defects [72]. Here, we investigate this point further by considering low ($\leq 1\%$) concentrations of defects characterised by different spin quantum numbers (S).

6.4.1 Spinon energy dispersion in pristine spin 1/2 chains

In figure 6.7 (a) we show the gapless, two-spinon continuum, calculated using the theoretical result by des-Cloizeaux and Pearson. This has been experimentally verified by many reports in the past (for example one may look into the dispersion for $SrCuO_2$, $KCuF_3$ and $KCuGeF_6$ reported in the references [124], [52] and [182], respectively). Since in the compounds $SrCuO_2$ and Sr_2CuO_3, the intra-chain exchange J is about 200 meV [120], the upper boundary of the dispersion curve extends up to $\sim$ 600 meV. In order to investigate the effects of the dilute disorder, we mainly focus on the spinon dispersion for energy transfer $\leq$ 10 meV around the Q point (1/2 0 1/2). In figure 6.7(b) and (c), the low-lying excitations for the undoped $SrCuO_2$ are shown. The intensity maps have been constructed from individual scans measuring the cross section $S(Q, \omega)$ along constant energy transfers. Each individual point was measured for $\sim$ 30 minutes due to the weak scattering signal. In all cases increased intensity can be seen in the middle of the Brillouin zone ($Q = \begin{pmatrix} 1/2 & 0 & 1/2 \end{pmatrix}$ for $SrCuO_2$ and $Q = \begin{pmatrix} 0 & 1/2 & 1/2 \end{pmatrix}$ for Sr_2CuO_3 as measured in our experiments). The vertical dashed lines originating at $Q_L = 0.5$ r.l.u. indicate the des Cloiseaux-Pearson characteristic dispersion of spinon excitations [26], with $J = 230$ meV. The gapless spinon excitation down to instrumental resolution limit $\Delta E = 2$ meV is in a agreement with the theoretical predictions [26].

6.4.2 Effect of dilute disorder on the low-energy excitations

We present our results of the INS experiments in figure 6.8 which summarizes these data for all studied doped crystals. Panels (a) and (b) correspond to Zn and Co doped $SrCuO_2$ respectively and (c) to Ni doped Sr_2CuO_3. Panel (d) shows the normalized Q-integrated intensities as a function of energy transfer (up to 10 meV). The results

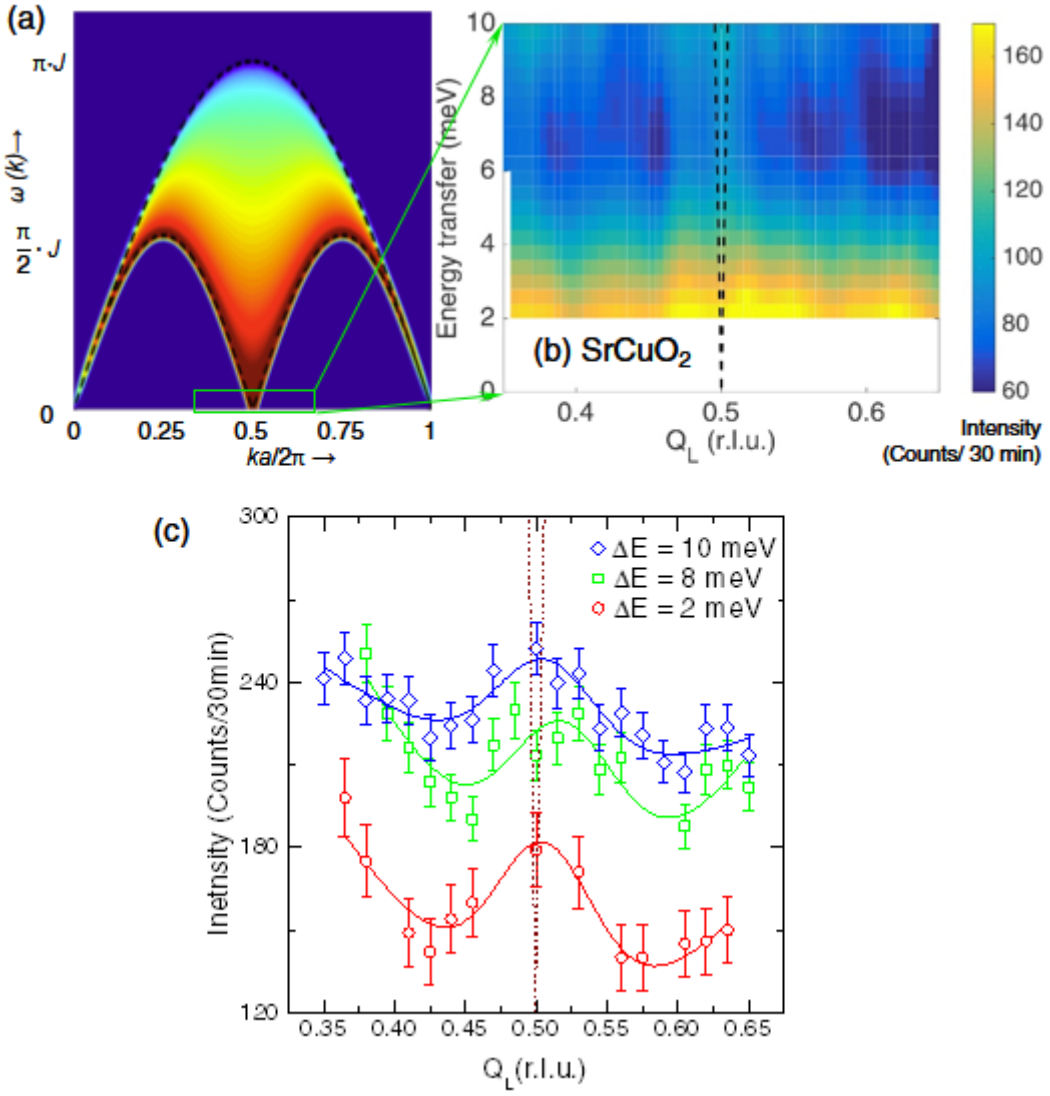

Figure 6.7: (a) Spinon dispersion for an ideal spin 1/2 chain deduced from des-Cloizeaux Peasons results [26]. The green box indicated the energy range investigated here. (b) and (c) 2D and 1D plots of the inelastic neutron scattering data for the undoped $SrCuO_2$, respectively. The solid line indicates a Gaussian fit. The dotted lines indicates the des-Cloizeaux Pearson dispersion.

for the pure $SrCuO_2$ single crystal has been used as a control sample. Surprisingly, all doped samples have average spectral weights that are five-fold stronger as compared to the pure sample. This is by no means expected, especially for the non-magnetic Zn sample. Further, the intensities of the Co- and Zn-doped samples show little variation as a function of energy transfer showing that these samples are gapless down to the instrument's energy resolution of 2 meV. Contrary to this, the Ni-doped sample shows

a gapped behaviour, with considerably reduced intensity below ~ 4meV.

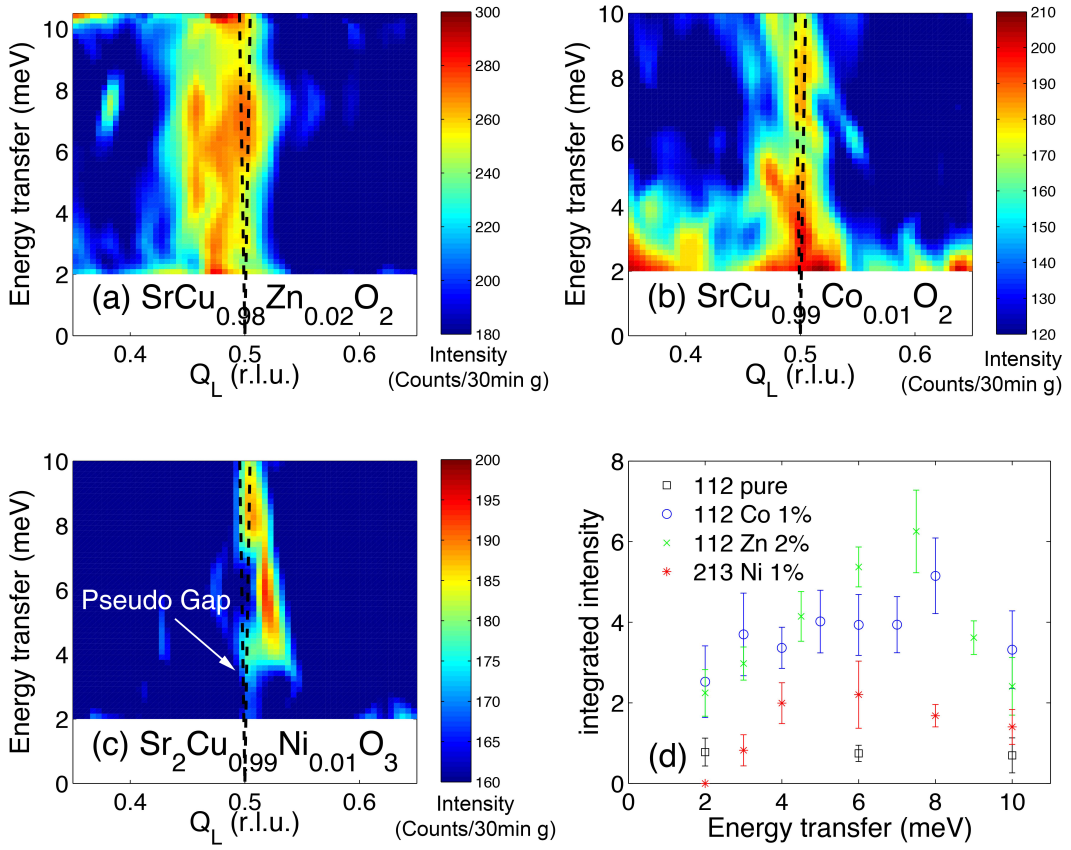

Figure 6.8: Triple-axis neutron spectra constructed by constant energy transfer scans (2-10 meV) with respect to momentum transfer for (a) 2 % Zn doped (b) 1 % Co doped $SrCuO_2$ and (c) 1 % Ni doped Sr_2CuO_3 single crystals. The data have been smoothen by using the matlab built-in delaunay triangulation algorithm. (d) Integrated neutron intensities for the pristine and doped $SrCuO_2$ and Sr_2CuO_3.

It is intriguing as to why Ni doping opens up a gap while the Zn doping apparently does not. An important difference between these two impurity types is that unlike the chain breaks due to the Zn^{2+} impurity, where the spins on the either side of the impurity may still couple weakly through the next-nearest-neighbour interaction (see figure 6.9(b)), the Ni^{2+} impurity results in a spin compensated cloud around the impurity site, which isolates the chain segments (see figure 6.9(a)). In such a scenario, the spinons will be confined over finite-length sections of the chain which should open up a gap in the low-energy spectrum, the gap value should scale inversely with the average segment length ($\overline{L} \sim 1/p$). Another possible reason for not having found a gap in the Zn^{2+} crystals might be related to the fact that Zn^{2+} does not readily replace Cu^{2+} in a crystal

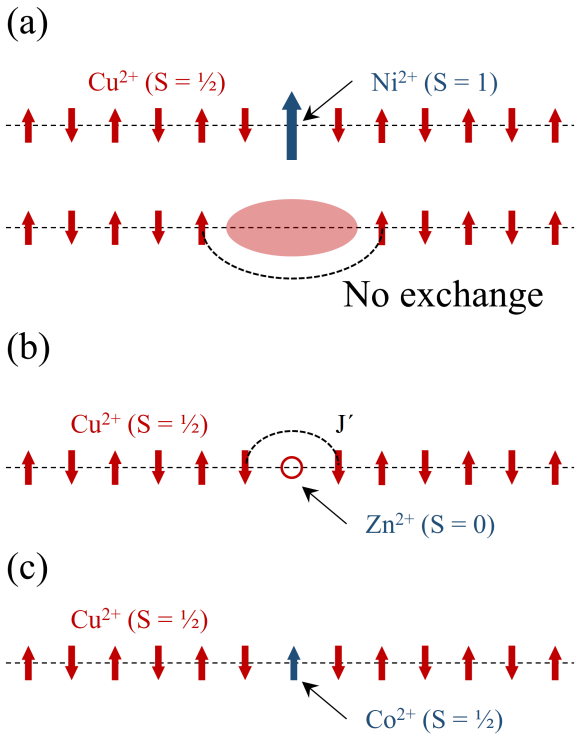

Figure 6.9: Cartoon showing the effect of doped impurity in a spin 1/2 HAF chain. (a) Screening of Ni^{2+} (S = 1) impurity by the neighbouring host spins. (b) Zn^{2+} (S = 0) impurity introduces a scalar defect of size only one atomic site, leaving the chains to be still resulting in a chain break with chain ends coupled via nest-nearest neighbour interactions (J'). (c) Co^{2+} (S = 1/2) impurity which does not severe the chain at impurity site unlike (a) and (b).

grown from the melt; hence the quantity of Zn doped in the chains may not be enough to open up an observable gap. As mentioned earlier, a spin gap has also been reported in the crystals of $Sr_{1.9}Ca_{0.1}CuO_3$ [74] and $Sr_{0.9}Ca_{0.1}CuO_2$ [73]. Since Ca^{2+} replaces Sr^{2+}, the -Cu-O-Cu- chains in these crystals should remain unsegmented. It has been argued that the ionic-size mismatch of Ca^{2+} and Sr^{2+} gives rise to a local bond disorder of the intrachain exchange coupling J which is probably responsible for the observed spingap. The appearance of a spingap is, therefore, not always associated with the segmentation of the chains and substantial bond disorder can also cause the ground state to be gapped. In the light of these recent results, it is fair to admit that the chain break picture is probably too naive. Even the notion of screening, strictly speaking, is valid only at T = 0.

In the case of Co^{2+} ($S = 1/2$) impurities no detectable gap was found in the low-energy excitations. A possible reason for this is probably related to the the "*healing*" of the chain at the defect site discussed in details under section 2.2.2. In the chain, healed at the impurity site the spinon excitation may remain gapless as in the pristine spin-chain.

6.5 Summary

In summary, we have discussed the effects of scalar defects in the spin $S = 1/2$ chains of Sr_2CuO_3. We experimentally verified the field theory results published by Sirker *et al.* [38, 105] describing the finite-size effects on the magnetic susceptibility of a spin 1/2 Heisenberg Antiferromagnetic chain. We also showed that dilute concentration of Ni^{2+}ions in the chain behave like *'scalar'* defects as predicted by the theory of reference [91], which is probably related to gapping of the spinon excitation spectrum upon Ni doping. We also show the inadequacy of equation 2.3 in describing the susceptibility in the cases where the ground state is gapped.

We also carried out neutron scattering experiments on the compounds $SrCuO_2$ (zigzag chains) and Sr_2CuO_3 (linear chains) doped with defects of various spin quantum number. One of the aims of our study was to find out if the low-energy spin excitations show a universal gapping behaviour as proposed in a recent work [72]. We showed that Ni doping in Sr_2CuO_3 results in gapping in agreement with previous report of Ni-doping in $SrCuO_2$. However, it is also shown that upon doping with Zn and Co, the excitations remain gapless, which shows that the quantum spin state of the impurity plays a decisive role in deciding the nature of the low-energy excitations.

Chapter 7

Magnetic Ground State of Sr_2CuO_3 with and without Dilute Doping

In chapter 1 we argued that in 1D there is no static magnetic ordering at any finite temperature [19]. However, the real compounds with quasi-1D magnetic interactions, do show an ordered magnetic ground state due to the residual interchain coupling. Using the field theory approximations, it is estimated that the dimensional crossover from 1D to 3D happens at a temperature of the order of the interchain coupling energy [50]. In disordered chains, the ordering temperature and the nature of the ordered state can be very different depending upon the details of the disorder present in the system. Scalar defects in the spin 1/2 chains are expected to suppress the 3D-ordering [106]. The chain breaks and the associated staggered moments that appear near the ends result in disruption of the local antiferromagnetic correlations which results in a suppression of the ordered state. On the other hand, a spin $1/2$ impurity, antiferromagnetically coupled to the ends of the chain results in a '*healing*' of the chain favouring an ordered state [106]. A spin 1 impurity in the spin $1/2$ chain, on the other hand, behaves effectively as a scalar impurity due to the Kondo-like screening as discussed in the previous chapter. The screening leads to a gapped state which suppresses the magnetic ordering. In this chapter we will investigate the influence of three different kinds of impurities: spin 0 Zn^{2+} ($S = 0$), spin 1 Ni^{2+} and spin $1/2$ Co^{2+}, on the magnetic ground state of Sr_2CuO_3,

The plan of the chapter is as follows: we will first discuss the ordered state in the pristine Sr_2CuO_3 and the influence of applied external field on the magnetic ordering

temperature using the magnetic specific heat. We will then come to the case of Zn^{2+} and Ni^{2+} impurities which show the expected suppression of T_N. Next, we will discuss the case of Co-impurities with the help of bulk magnetisation, specific heat and elastic neutron scattering.

7.1 Magnetic ground state in presence of scalar disorder

7.1.1 Magnetic ordering in pristine Sr_2CuO_3

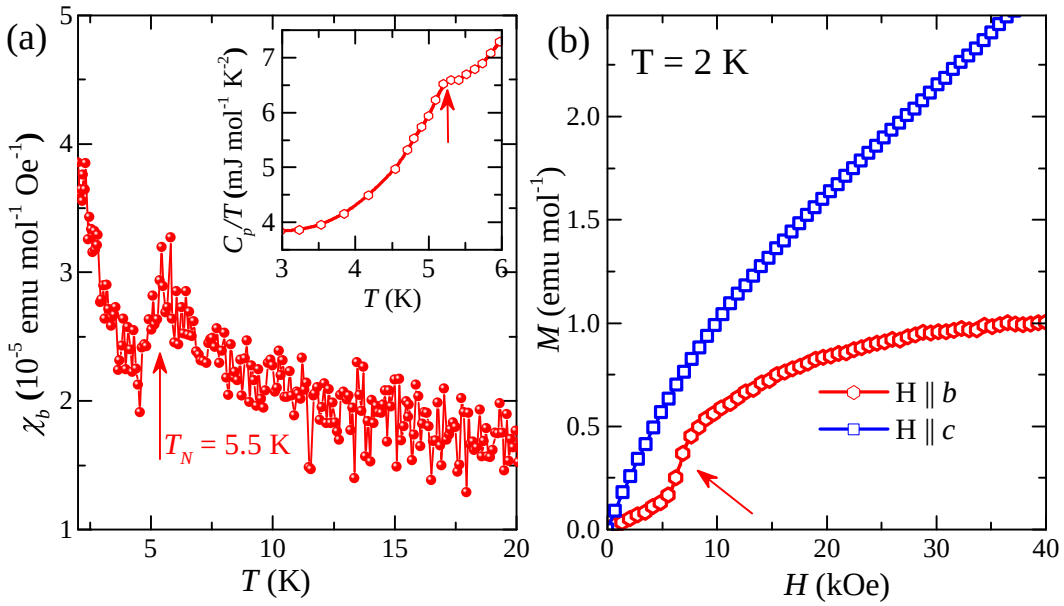

Figure 7.1: (a) Low temperature susceptibilities χ of the pristine Sr_2CuO_3 crystals. Measurements were carried out under an applied field $H = 1$ kOe along the chain direction. Inset: Specific heat C_p/T is shown for the three compounds. The lines are guides to the eye. Arrows show the magnetic transitions. (b) Isothermal magnetisation M(H) of the pristine crystal along crystallographic b and c axes. The arrow indicates the field induced transition in the $H \parallel b$ measurements.

In panel (a) of figure 7.1 we have shown the low-temperature dc magnetic susceptibility by applying an external magnetic field ($H = 1$ kOe) parallel to the chain. A small but clearly discernible peak near $T \approx 5.5$ K in our susceptibility data indicates

a transition to an ordered state. This observation is in agreement with the previous reports where, a weak Néel ordering in Sr_2CuO_3 at $T = 5.4$ K was reported based on the neutron scattering and μSR studies[126]. From neutron studies the ordered Cu moment is reported to be $\lesssim 0.06\mu_B$[126]. The ordering of the Cu^{2+} moments is also reflected in the isothermal magnetisation of the pristine crystal measured at $T = 2$ K for $H \parallel b$ and $H \parallel c$ (i.e., parallel and perpendicular to the chains, respectively), as shown in panel (b) of the figure 7.1. In the ordered ground state, M(H) exhibits a sharp field induced metamagnetic transition near $H = 5$ kOe along the chain direction ($H \parallel b$), while along H $\parallel c$ it shows only a monotonic increase. Since the metamagnetic feature in M(H) appears only for field applied parallel to the chain, it is probably a field induced spin re-orientation.

To confirm the bulk nature of the magnetic transition in $\chi(T)$, specific heat measurements were performed. An anomaly in the specific heat at the same temperatures as the susceptibility as shown in the inset of figure 7.1(a), where molar specific heat divided by temperature (C_P/T) is shown as a function of T, corroborates the bulk nature of magnetic order.

Using the value of the transition temperature $T_N = 5$ K in the mean-field derived expression for T_N, the interchain coupling for the compound Sr_2CuO_3 is estimated to be about 1.4 K [50], which is in a good agreement with the value of 9 K obtained from the neutron scattering studies.

7.1.2 Finite-size effects on the ordered state

In figures 7.2(a) and 7.3, we show the low-T magnetic susceptibility ($\chi(T)$) and specific heat ($c_p(T)$) data for dilutely doped ($\sim 1\%$) crystals consisting of Zn^{2+} and Ni^{2+} as dopants. Data for the undoped compound is also shown for comparison. As shown in the figure, the curves for $\chi(T)$ as well as c_p, for 1 % Zn-doped crystals also features a magnetic anomaly, associated with the onset of a Néel ordered state. However, the ordering temperature, estimated both from $\chi(T)$ and c_p in this case is 4 K, significantly

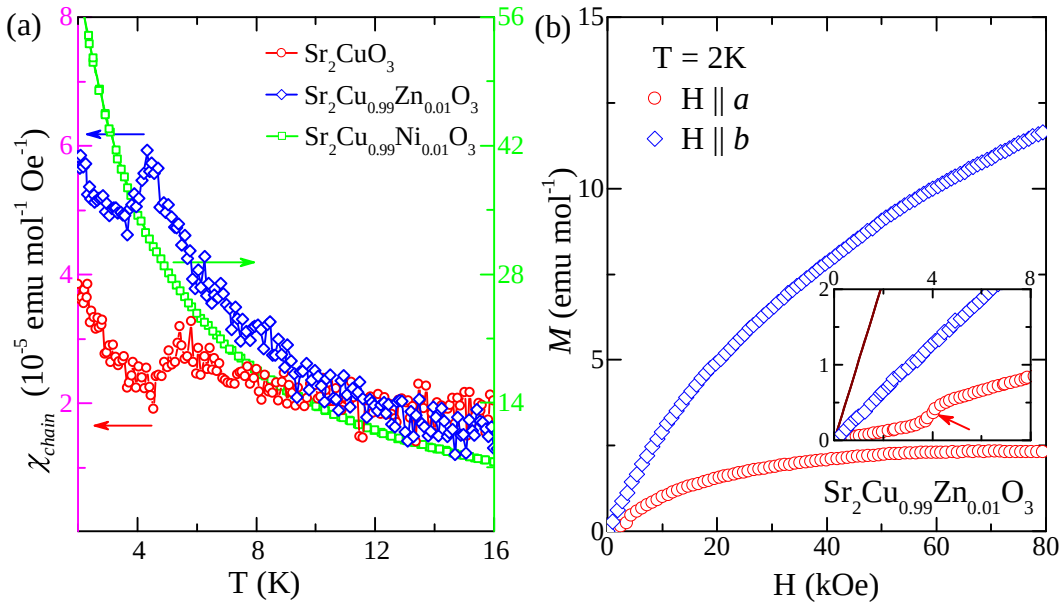

Figure 7.2: (a) Low-temperature magnetic susceptibility ($\chi(T)$) of the pristine, 1% Zn doped and 1% Ni doped crystals, measured by applying magnetic field (H = 1 kOe) along the chain. Arrows indicate respective y-scales. (b) Isothermal magnetisation M(H) for 1% Zn-doped Sr_2CuO_3 at temperature T = 2 K. Inset: zoomed in view of M(H) at low fields. The arrow indicates the field induced transition in the $H \parallel b$ measurements.

lower from its value in the undoped chains. Similar suppression of the ordering temperature was also observed in Pd doped Sr_2CuO_3 in μSR experiments done by *Kojima et al.* [118], in a good agreement with mean-field theoretical calculations by *Eggert et al.* [106]. The staggered moment generated by these scalar defects at the ends of finite-size chain segments, tend to disrupt the antiferromagnetic ordering, lowering the transition temperature. The mean-field approximation with finite length segments and interchain correlations predict a pronounced decrease in the Néel temperature as a function of disorder by as much as a factor of 5. For 1 % of scalar defects, a suppression of about 50 % with respect to the Néel temperature of the pristine crystal is expected (see, figure 2 of ref. [106]). In our case, in the 1% (nominal) Zn doped crystal the drop in T_N is about 30 %. Considering the fact that the real Zn concentration in our crystal is about 60 % of the nominal value, agreement between the experiment and theory is fairly good. In figure 7.2(b), we show the isothermal magnetisation $M(H)$ for 1% Zn doped crystal at temperature T = 2 K. In the Zn doped crystal we observe a sharp field

induced transition near $H = 4$ kOe applied along the chain direction ($H \parallel b$). This transition is analogous to the one observed in the pristine crystal; however, the field at which the spin reorientation occurs has decreased to ~ 4 kOe from its value of ~ 8 kOe.

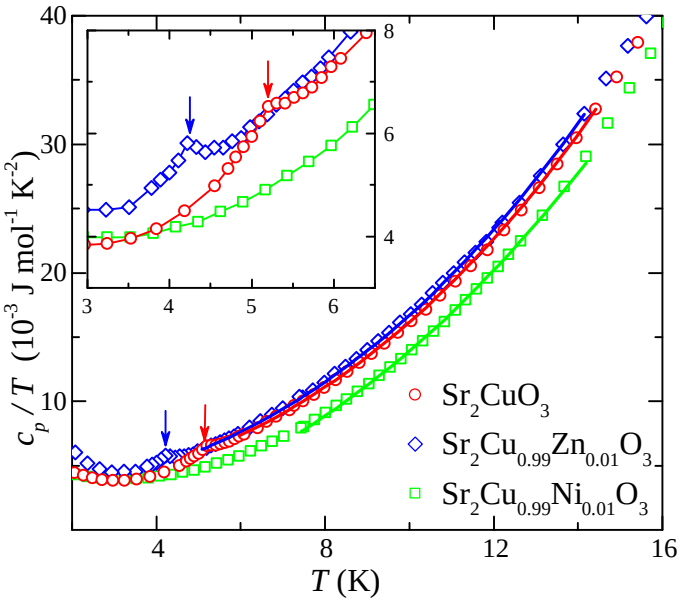

Figure 7.3: Zero-field specific heat c_p/T for pristine, 1% Zn doped and 1% Ni doped crystals. The solid lines are fit to equation 7.3. Inset: an exaggerated view of the specific heat curves. Arrows indicates magnetic anomalies.

In the Ni-doped chains no sign of magnetic ordering has been observed down to $T = 2$ K. As shown in the previous chapter, Ni^{2+} ion in spin 1/2 chains effectively behaves as a scalar defect and, thus, it is expected to suppress the magnetic ordering temperature. However, as shown in figures 7.2, no magnetic ordering could be observed in either magnetic susceptibility or specific heat measurements down to $T = 2$ K. In μSR experiments on the Ni-doped zigzag spin chain compound very recently reported by Simutis et al. roughly 70% suppression of the ordering temperature by about 0.1% Ni-doping is observed. For higher doping levels ($x > 0.5\%$), the ordering temperature is suppressed completely below their lowest measurement temperature of 20 mK [119]. The suppression of the ordering temperature due to Ni-defect is probably analogous to the case of scalar defects discussed earlier. However, the magnitude of suppression is much more pronounced in the case of Ni-doped samples, which might probably be related to the fact that Ni-doping also opens up a sizeable gap in the spinon excitation

spectrum (discussed in chapter 4), which ousts the magnetic ordering completely or at least suppresses it to temperatures far below T = 2 K. It should be noticed that the specific heat of Ni doped crystal at low temperatures is slightly (about 2 – 3 mJ/mol K^2) smaller in magnitude compared to that of the pristine or Zn doped crystal (see figure 7.3). This decrease is likely a manifestation of the spin *pseudogap*. A complete analysis of the specific heat in the absence of a lattice template and without the knowledge of contribution arising from the free spins at the chain ends is difficult at this stage.

Interestingly, an upturn in the specific heat data (c_p/T) was observed for all the samples upon cooling down below $T \approx 4$ K. This features is found to be more pronounced in the doped samples. Though the exact origin of this feature is not understood fully, a probable reason could be that it is high temperature tail of the Schottky anomaly due to the free spins. It should be pointed out that schottky anomaly due to nuclear hyperfine splitting is expected only at much lower temperature. Therefore, the feature in c_p/T at temperatures as high as 4 K cannot have a nuclear origin [183, 184].

Coming back to the temperature range $T > 4$ K, the measured specific heat in this temperature range of the pristine and doped Sr_2CuO_3 have is principle contributions due to the phononic vibrations and magnetic excitations. Being a Mott-insulator, the electronics contribution can be neglected. The phononic contribution can be expressed using the Debye model [10],

$$c_{\text{ph}} = \frac{12}{5} N_A k_B \left(\frac{T}{\Theta_D}\right)^3 \tag{7.1}$$

and the contribution due to magnetic excitations can be expressed as [40],

$$c_{\text{mag}} = \frac{2N_A k_B^2}{3J} T \tag{7.2}$$

Where, N_A and k_B are the Avogadro's number and Boltzmann constant, respectively. Θ_D and J represents the Debye temperature and the intrachain coupling. Thus, the total

Table 7.1: Parameters yielded by fitting the measured c_p by the equation 7.3

Parameters	α (mJ/mol.K^2)	β (mJ/mol.K^4)	J (K)	Θ_D (K)
Sr_2CuO_3	2.75(4)	0.125(1)	2015	250
$Sr_2Cu_{0.99}Zn_{0.01}O_3$	2.84(6)	0.130(1)	1951	246
$Sr_2Cu_{0.99}Ni_{0.01}O_3$	0.16(8)	0.134(1)	3.5×10^4	244

specific heat of Sr_2CuO_3 at low-temperatures can be written as:

$$\begin{aligned} c_p &= \frac{2N_A k_B^2}{3J} T + \frac{12}{5} N_A k_B \left(\frac{T}{\Theta_D}\right)^3 \\ &= \alpha \cdot T + \beta \cdot T^3 \end{aligned} \tag{7.3}$$

where α and β are constants defining the magnetic and phononic contribution of the measured specific heat. In order to extract the values of the intrachain coupling (J) and the Debye temperature (Θ_D), we have fitted the measured specific heat of the pristine and doped crystals using equation 7.3. However, the fitting range is very limited as the model in equation 7.3 represents the measured specific data only over a very limited temperature range. At low-temperatures ($T < 6$ K), equation 7.3 is inadequate due to the magnetic phase transition to the Néel ordered state. At higher temperatures the phononic contribution deviates from the T^3-law which limits the upper fitting range [185].

The solid lines in figure 7.3 are the fitted curve to the data in the temperature range 6 to 14 K yielding parameters listed in table 7.1. As shown in figure 7.3 the measured c_p fits reasonably well to equation 7.3 over the temperature range $6 \sim 14$ K. The values of J and Θ_D, calculated from the values of α and β, are listed in table 7.1. The calculated Debye temperature agrees well with the previous report on $SrCuO_2$, which has a unit cell structure similar to that of Sr_2CuO_3 [166]. The calculated J for the pristine and Zn doped crystals agrees well with the previous reports [54–56] and to our own estimation of J using the bulk magnetic susceptibility (see chapter 4). Here, it should be noticed that the magnetic contribution α, is very small for the Ni-doped sample, which is likely due to the presence of spin pseudogap in the Ni doped crystals.

7.1.3 Variation of the ordering temperature under external magnetic fields

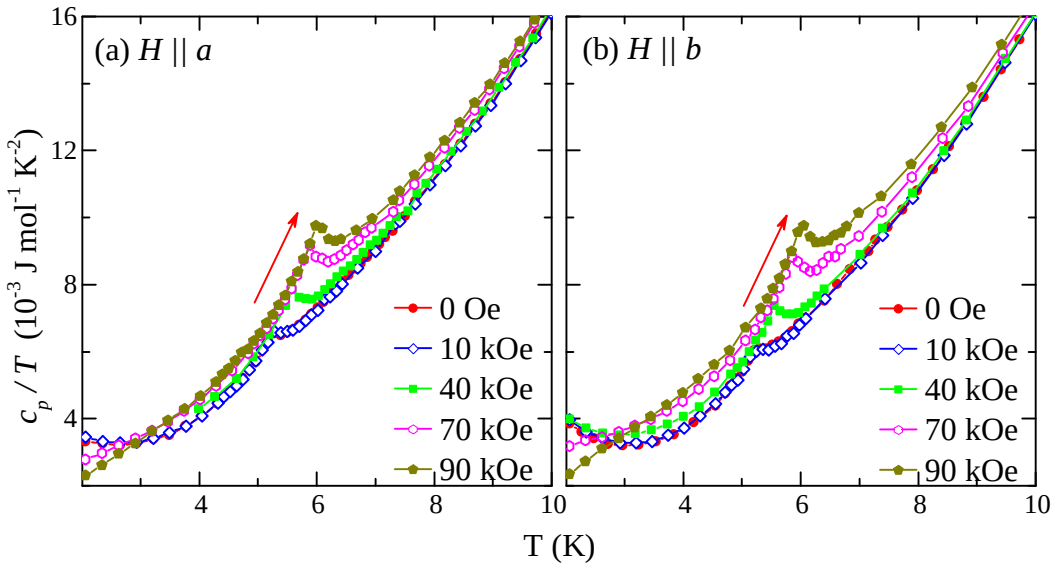

Figure 7.4: Dependence of the specific heat for the pristine Sr_2CuO_3 crystals with the applied magnetic field along (a) perpendicular and (b) parallel to the chain direction. The arrows indicates increase in field applied.

In figures 7.4 we show the temperature dependence of specific heat data of the pristine Sr_2CuO_3 crystal measured under various external magnetic fields parallel and perpendicular to the chains. We found that, although the overall behaviour of the specific heat remains unaltered upon application of the magnetic field, two very distinctive changes result in the c_p/T curves. Firstly, an enhancement of the ordering temperature (T_N) with applied magnetic field and, secondly, a suppression of the low-temperature upturn under applied magnetic field. The low temperature upturn in c_p/T curves may be attributed to a 2-level Schottky anomaly due to a small concentration of spin 1/2 free spins present in the spin chains [186]. Generally, in zero field the Schottky anomaly is not expected, unless the local field due to the ordered magnetic moments at the free spin location triggers it. However, the internal field in an antiferromagnet may not be large enough. In other quantum spin chains, the low-temperature Schottky upturn due to free spins has only been reported under applied magnetic field [186]. Moreover, with increasing applied field, the Schottky anomaly shifts to higher temperatures due

to an increasing Zeeman splitting. The behaviour observed in Sr_2CuO_3 is, however, opposite–i.e., even under zero field there is an upturn, which shifts to lower temperatures with increasing magnetic field. From the behaviour of c_p/T plots under applied magnetic fields, it seems reasonable to conclude that this feature in the low-temperature specific heat cannot be due to the Schottky contribution of the free spins alone. Given that the isothermal magnetisation at $T = 2$ K exhibits a spin reorientation transition near $H = 7$ kOe, it is possible that the low-temperature upturn in the specific heat is precursory to a second phase transition at even lower temperatures.

To extract the Schottky contribution to the heat capacity, we analysed the low-temperature data as follows: In order to minimize the effect of the lattice and spinonic contributions, we analysed the difference, $\Delta c_p = c_p|_{H1} - c_p|_{H2}$ and fitted it with the differential Schottky expression given by,

$$\Delta c_p = n_{f.s.} \left[\left(\frac{\Delta_1}{T}\right)^2 \frac{e^{\Delta_1/T}}{(1+e^{\Delta_1/T})^2} - \left(\frac{\Delta_2}{T}\right)^2 \frac{e^{\Delta_2/T}}{(1+e^{\Delta_2/T})^2} \right] \tag{7.4}$$

where, $n_{f.s.}$ is the density of free spins in the crystal, Δ_i's correspond to the Zeeman energies under external magnetic fields H_i's.

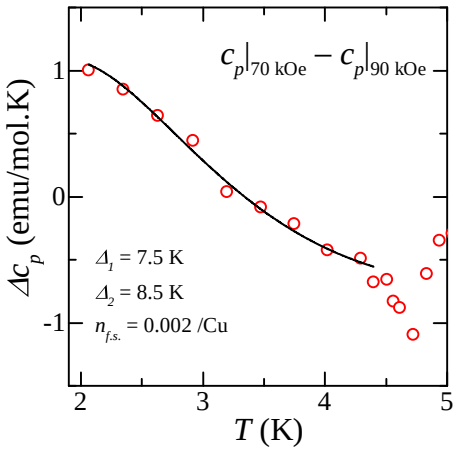

Figure 7.5: Difference in the specific heat measured in different external magnetic fields (H = 90 kOe and H = 70 kOe). The solid lines are the fit to the equation 7.4 using the parameter given.

In figure 7.5, we show the difference specific heat (Δc_p) measured under two different external magnetic fields, 70 kOe and 90 kOe at low-temperatures. The spinon

contribution may have small field dependence, which can be eliminated to a good extend by fitting Δc_p rather than c_p. The main reason for not fitting c_p directly is related to the low-temperature upturn. We argue that the low-temperature upturn is not due to the Schottky contribution of the free-spin alone. In Δc_p, the other contributions will be cancelled out leaving only the difference Schottky contribution which can be fitted to expression 7.4. As shown in figure 7.5, the differential Schottky expression, given by equation 7.4, fits the subtracted data fairly well in the temperature range 2–4.3 K.The parameter yielded are given in the respective panels. The effective density of free spins came out to be 0.2 %, which is very close to the value calculated from our bulk susceptibility analysis ($N_s \sim 1.8 \times 10^{-3}$ /Cu). The values for the Zeeman-energies calculated from the fitting are $\Delta_1 = 7.5$ K and $\Delta_2 = 8.5$ K for external fields 70 kOe and 90 kOe, respectively.

In panel (a) of figure 7.6, we show the specific heat (c_p/T) curves for 1% Zn doped Sr_2CuO_3 crystals under external magnetic field applied perpendicular to the chain. Analogous to the pristine crystal, the Zn-doped crystals also exhibit an increase in the temperature corresponding to the anomaly in the specific heat curve with increasing applied field. A very similar behaviour has also been seen for the field applied parallel to the chains.

In the panel (b) of figure 7.6 we compare the c_p/T Vs T curves for pristine and the Zn-doped crystal under field 90 kOe. In both cases we see a suppression of the low-temperatures upturn due to the external field, and a discernible hump at $T \approx 2.7$ K attributed to previously discussed Schottky anomaly arising due to the spin 1/2 free spins. In the case of the Zn-doped crystal this feature is more prominent. To extract the contribution due to the Schottky anomaly we subtracted the specific heat data of the Zn-doped crystal from that of the pristine crystals, as shown in figure 7.7. Using this approach, the lattice and the spinonic contributions are also expected to be subtracted, leaving the Schottky contribution alone. The subtracted data is then fitted with the Schottky expression for spin $1/2$ free spins, given by:

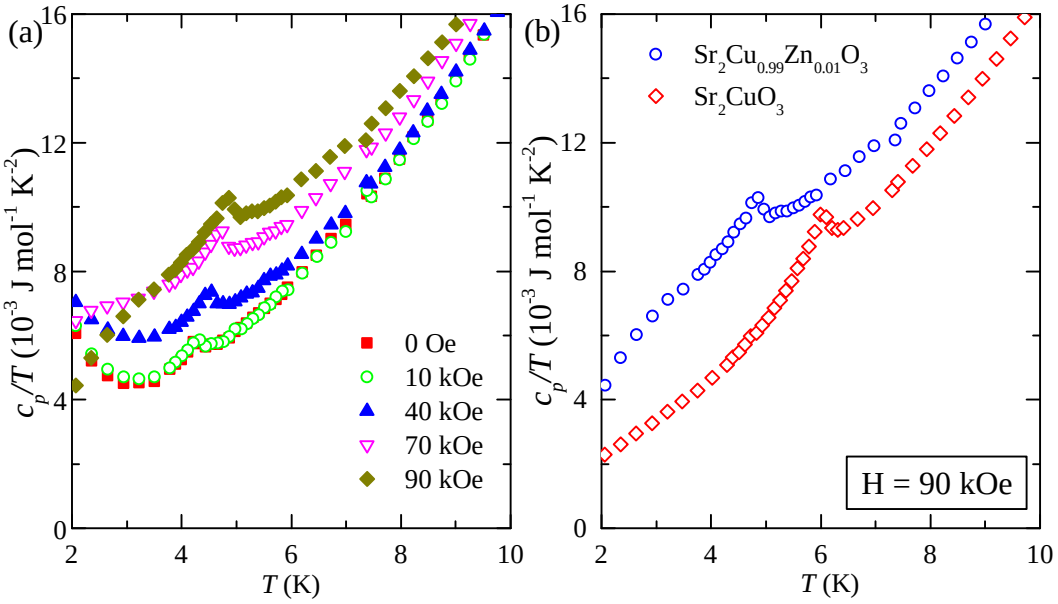

Figure 7.6: (a) Dependence of the specific heat (c_p/T) for the 1% Zn-doped Sr_2CuO_3 crystals with the applied magnetic field perpendicular to the chains. (a) Specific heat c_p/T for pristine, 1% Zn doped crystal under applied field $H = 90$ kOe perpendicular to the chain. The arrows indicates magnetic ordering.

$$\Delta c_p = \Delta n_{f.s.} \left(\frac{\Delta(H)}{T}\right)^2 \frac{e^{\Delta(H)/T}}{\left(1 + e^{\Delta(H)/T}\right)^2} \tag{7.5}$$

where, $\Delta(H)$ correspond to the Zeeman splitting under an external magnetic field H and $\Delta n_{f.s.}$ is the difference in the density of free spins present in the Zn-doped crystal with respect to that of the pristine crystal,

In figure 7.7 we have shown the subtracted data of the specific heat measured for the Zn-doped crystal from that of the pristine crystal. Due to magnetic ordering at temperatures around 4 K in the Zn-doped crystal, subtracted data can be fitted using equation 7.5 in the temperature-range $T < 3.5$ K. The solid lines in figure 7.7 represents the fit to equation 7.5 yielding the values of the parameters included in the figure. The data under lower fields are not analysed, because for low fields, the magnetic ordering of the Zn doped crystal around 4 K is too low to have an appreciable range for fitting the subtracted data. $\Delta n_{f.s.}$ for 1% Zn-doped samples with respected to the pristine compound is found to vary from 0.002 to 0.003 /Cu, which roughly corresponds to the value that we calculated from the bulk susceptibility analysis ($N_s = 0.006$ /Cu),

considering the effective free spin concentration in pristine crystal to be 0.002 /Cu. The values of the Zeeman splitting obtained from the fitting are $\Delta_1 = 8.1$ K and $\Delta_2 = 10.8$ for external fields 70 kOe and 90 kOe, respectively. These values are comparable to the Zeeman splitting in the pristine compound reported in figure 7.5.

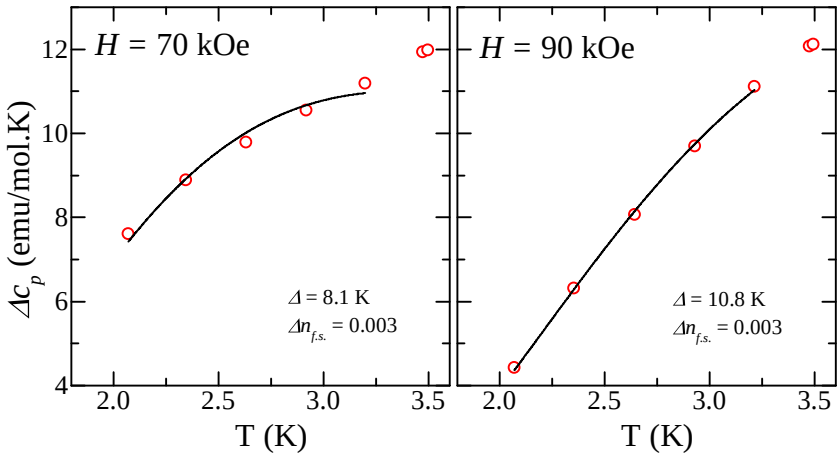

Figure 7.7: (a), (b) Difference in the specific heat $c_p|_{Sr_2Cu_{0.99}Zn_{0.01}O_3} - c_p|_{Sr_2CuO_3}$ measured in different external magnetic fields. The solid lines are the fit to the equation 7.5 using the parameter given.

Coming back to the variation of the ordering temperature with external magnetic field, a field dependent phase diagram for T_N, estimated from the magnetic anomaly in c_p/T curves, is shown in figure 7.8. For the pristine Sr_2CuO_3 crystal, the T_N exhibits an isotropic increase with the applied magnetic field. A similar isotropic increase of T_N with external magnetic field is also observed in the case of Zn doped crystal. In an ideal 3D AFM, the ordering temperature is typically suppressed by the applied field. The increase in the transition temperature with application of field seen here is unusual. A possible explanation of this enhancement of the ordering temperature under the applied field could be related to the enhancement of the transverse staggered correlations. Recall that the suppression of ordering temperature in the spin 1/2 chains with scalar impurities is attributed to the disruption of antiferromagnetic correlation due to the presence of staggered moment in the vicinity of the defect site. In the pristine crystal these are intrinsic defects discussed previously and in the Zn-doped crystal the scalar defect density is even higher.

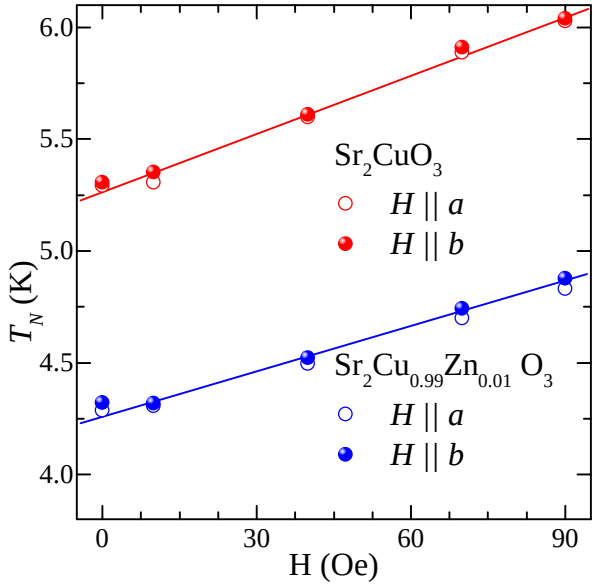

Figure 7.8: Field dependence of the transition temperature of the pristine and 1%-Zn doped Sr_2CuO_3.

7.2 Co-doping in Sr_2CuO_3

As we shall show here, a very different picture arises when spin 1/2 chain is doped with Co^{2+} impurities. We found the ground state of the dilutely Co-doped spin 1/2 chain in Sr_2CuO_3 to be magnetically ordered and anisotropic. The low-energy excitations are found to be gapless as opposed to the gapped excitations in the Ni-doped case. The magnetic ordering temperature shows a large monotonic enhancement with increasing Co-concentration as opposed to the case of scalar doping discussed above where the magnetic ordering temperature is found to be suppressed upon doping. In the following section we discuss the details of the magnetic ground state of the Co-doped Sr_3CuO_3.

7.2.1 Low-field magnetic behaviour

The low-temperature susceptibility of 1 % Co-doped single crystal under an applied magnetic field of $H = 1kOe$ parallel to the chain is shown in panel (a) of figure 7.9. The data for the pristine Sr_2CuO_3 crystal is also shown for comparison. At high temperatures (not shown) a significant increase in the $\chi(T)$ of the Co-doped crystal, over that of the pristine crystal, has been observed below $T = 100$ K. The low-temperature

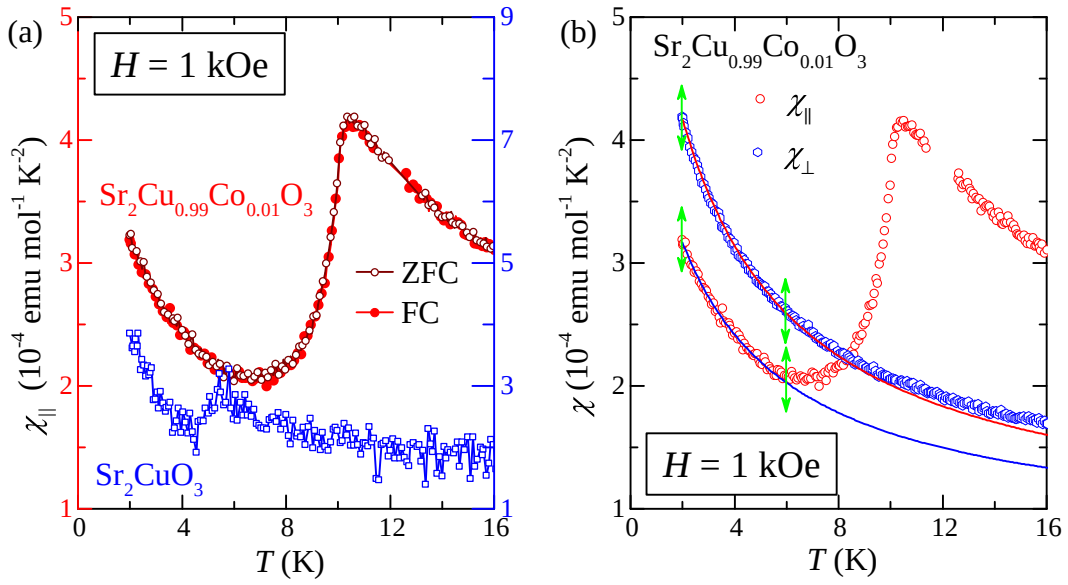

Figure 7.9: (a) Low-temperature magnetic susceptibility of the pristine and 1 % Co-doped Sr_2CuO_3 by applying external magnetic field (H = 1 kOe) parallel ($\chi_{\parallel}$) to the chains length. (b) $\chi_{\parallel}$ and $\chi_{\perp}$ for 1% Co-doped Sr_2CuO_3. The solid lines show Curie–Weiss fitting to the low-temperature ($T \leq 5$ K) susceptibility yielding the parameters given in the text. Double-side arrow indicate the fitting region.

behaviour is marked by a sharp anomaly in χ_b near T = 10.2 K, indicative of a magnetic phase transitions. However, contrary to the case of scalar doping discussed earlier, the transition temperatures of the Co-doped compound is much higher: almost double the value for the pristine crystal. Given that the actual Co-concentration in our crystal is lower than the nominal 1 % value as inferred from the compositional analysis of the frozen-in floating zone (see chapter 5), the observed increase in the magnetic ordering temperature is surprisingly high. This result is quite intriguing and does not fit in the field theory prediction for the scalar impurity. While the gapless nature of the low-energy spin excitations can still be explained within the theoretical framework by Eggert *et al.* [91]. In their model, the $S = 1/2$ of impurity Co may couple with the chain antiferromagnetically and result in a stable periodic chain including the impurity site, which is termed the “healing" of the spin-chain at the impurity site as discussed in chapter 2, [91]. However, the huge increment in the transition temperature with merely 1 % Co-doping is yet to be understood.

The dc susceptibility is also highly anisotropic as no anomaly is observed in the perpendicular susceptibility (panel (b) of figure 7.9). Co^{2+} (d^7) has an unpaired electron in the crystal field split d_{xy} orbital. Since the orbital angular momentum in $Co^{2+}$is not fully quenched, spin-orbit coupling driven single-ion anisotropic behaviour is commonly seen in Co^{2+} containing compounds [187, 188]. Along the same lines, the anisotropic behaviour of the Co-doped Sr_2CuO_3 can be attributed to the single-ion anisotropy of the doped Co-ions.

Below the transition temperature, the susceptibility shows a sharp increase upon cooling the sample below about $T = 4.5$ K. Such an increase of $\chi(T)$ at low-temperatures is typically associated with the presence of paramagnetic impurities (in the present case Cu^{2+} and Co^{2+} ions misplaced from their regular chain sites). We, therefore, attempted a fit to the susceptibility data below $T = 5$ K to the Curie-Weiss law (see panel (b) of figure 7.9): $\chi = \chi_0 + C/(T - \theta_P)$. The values of the fitting parameters thus obtained are as follows (CGS units). For H $\parallel b$: $\chi_0 = 7.5 \times 10^{-5}, C = 1.08 \times 10^{-3}, \theta_P = -2.47$ K and for H $\parallel c$: $\chi_0 = 7.5 \times 10^{-5}, C = 1.59 \times 10^{-3}, \theta_P = -2.65$ K. The C-values correspond to about 0.3 % (H $\parallel$ b) and 0.4 % (H $\parallel c$) of free $S = \frac{1}{2}$ paramagnetic impurities per formula unit. These values are unrealistically inflated given that the actual Co concentration in our crystal is less than 1 % (see section 5.3.4). The sign of χ_0 is also opposite of that in the pristine crystal (see table 6.1). These features of the fitting parameters led us to believe that the upturn in the susceptibility below $T = 5$ K cannot simply be a paramagnetic curie-tail. It is more likely that this upturn is a precursory increase of the susceptibility leading to a spin reorientation transition at even lower temperatures. This assertion can be further supported by the low-temperature isothermal magnetisation data and specific heat measured as a function of field at low temperatures discussed next.

In the dc magnetic susceptibility for the Co-doped crystal, no thermomagnetic irreversibility (ZFC-FC splitting) could be detected down $T = 2$ K (shown in panel (a) of figure 7.9), which gives an indication of the long-range nature of the ordered state. As we shall show in the next chapter, this is the key difference compared to the Co-doped zigzag chains, where the discernible ZFC-FC splitting is observed due to the

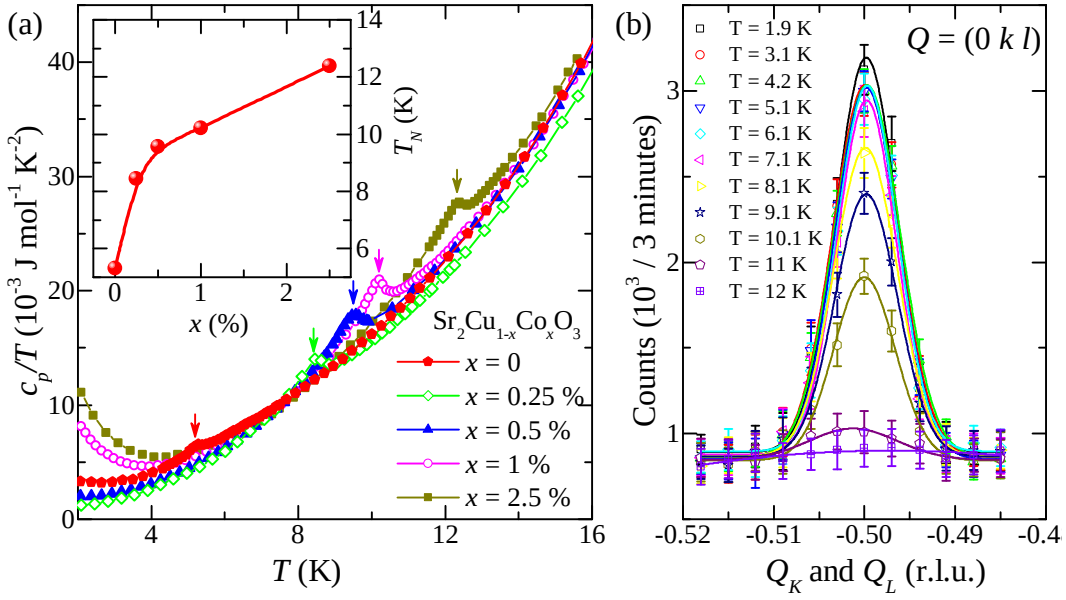

Figure 7.10: (a) Zero-field specific heat of all Co-doped Sr_2CuO_3, where arrows indicated the anomalies due to magnetic transition. Inset a phase diagram of transition temperatures estimated from the specific heat curves. (b) Elastic neutron scattering in 1% Co doped Sr_2CuO_2 crystal around $Q = (0\ \frac{1}{2}\ \frac{1}{2})$. The solid lines show the Gaussian fits to the data.

onset of a quasi-long-range of ordered state. The bulk nature of the magnetic transition was further confirmed using the low-temperature specific heat (c_p) and elastic neutron scattering experiments. In panel (a) of figure 7.10 we summarise the low-temperature specific heat of all the Co-doped crystals of Sr_2CuO_3. For all the compositions, c_p features a magnetic anomaly, which can be attributed to the magnetic phase transition. The transition temperature is found to scale with the Co-concentration. In the inset of figure 7.10(a), we show T_N of Co-doped crystals plotted as a function of the nominal Co-content. A linear rise of T_N is observed above 0.5 % of Co-doping. For initial Co-doping the enhancement of T_N is much more pronounced -changing from 5.4 K for the pristine crystal to about 8.4 K for crystal containing a nominal 0.25 % Co. The scaling of T_N confirms that the majority of the doped Co ions replace the Cu-ions in the crystals. Analogous to the pristine and Zn-doped crystals, c_p/T Vs T curves of the Co-doped crystals also feature a low-temperature upturn ($T < 4$ K). Upon increasing the doping concentration the upturn becomes more pronounced. As pointed out earlier, the low-temperature upturn may be linked to the Schottky anomaly of the free spins. The

field dependence of the low-temperature c_p will be helpful in understanding the origin of this feature.

In panel (b) of figure 7.10 we have shown isothermal elastic neutron scattering (ENS) from Q point around $(0\ \frac{1}{2}\ \frac{1}{2})$. All the curves for $T \leq 10.1$ K feature a sharp magnetic Bragg peak at $Q = (0\ \frac{1}{2}\ \frac{1}{2})$, indicative of the magnetic ordering. The ENS data are fitted with the Gaussian line-shapes, which estimates a narrow FWHM ($\lesssim 0.007$ r.l.u.) i.e., longer correlation lengths ($\xi \gtrsim 140$ unit cells), which confirms the bulk nature of the magnetic order.

7.2.2 Field dependence of the bulk magnetic properties

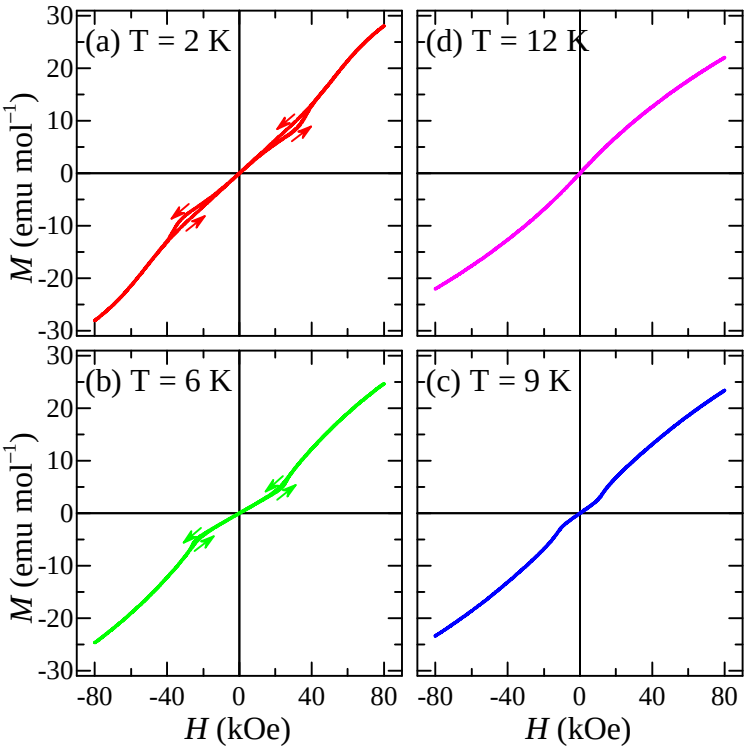

Figure 7.11: Isothermal dc magnetisation of 1% Co doped Sr_2CuO_3 crystal at with respect to external magnetic field applied along the chain length. The arrows indicate the direction of field sweep.

In figure 7.11 we show the magnetic field dependence of dc magnetisation $[M(H)]$ at fixed temperature under magnetic field parallel to the spin chain. As shown in the figure, the isotherms for $T > T_N$, show a paramagnetic behaviour, as was the case

for the pristine and scalar doped chains. However, the isotherms below T_N show a step-like metamagnetic transition, in a field ranging from 10 to 40 kOe depending on the temperature. Also, as the temperature drops the transition gets more pronounced and the transition field increases with a clearly discernible hysteresis between the field increasing and field-decreasing measurements. The presence of hysteresis suggest a first-order nature of the transition. In figure 7.12, we show the elastic neutron intensity scattered at $Q-$point $0\ \frac{1}{2}\ \frac{1}{2}$ measured at $T = 1.9$ K. The data are marked by a pronounced hysteresis in the neutron intensity measured while ramping-up and ramping-down the external magnetic field applied parallel to the chain. The metamagnetic transition is probably due to a spin reorientation under the application of an external magnetic field. We will come back to discuss the metamagnetic transition in last section, after having discussed some other results which are required to throw light on the origin of this transition.

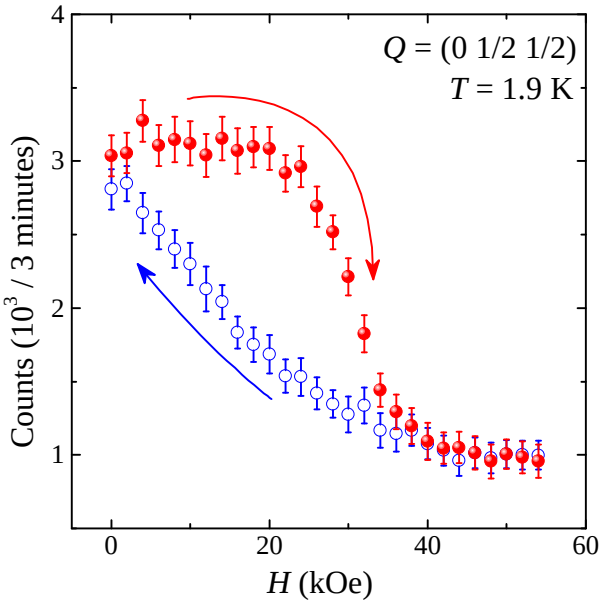

Figure 7.12: Magnetic scattering at $Q = (0\ \frac{1}{2}\ \frac{1}{2})$ in 1% Co doped Sr_2CuO_2 crystal with respect to external magnetic field applied along the chain length. The arrows indicate the direction of field sweep.

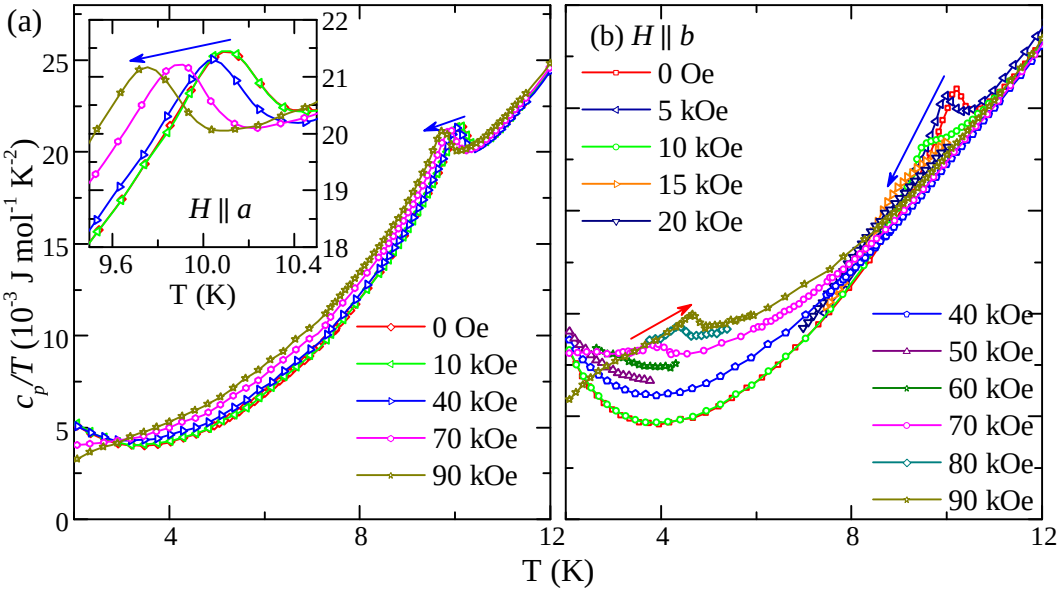

Figure 7.13: Dependence of the specific heat for the 1%-Co doped Sr_2CuO_3 crystals with the Applied magnetic field along (a) perpendicular and (b) parallel to the chain length. The arrows indicates increase in field applied.

7.2.3 Field dependence of the ordering temperature

To investigate the field dependence of the ordering temperature in the Co-doped chains, specific heat measurements were carried out in external magnetic fields applied perpendicular and parallel to the chain length. In figure 7.13 the specific heat (c_p/T) curves are shown for 1 % Co-doped crystals. The peak corresponds to the onset of the ordered state. In the magnetic field applied perpendicular to the spin chain ($H \parallel a$), T_N shows a gradual decrease changing from $T_N = 10.2$ K for $H = 0$ to about 9.7 K for $H = 90$ kOe. However, when the field is applied along the chain, a completely novel scenario emerged. With increasing magnetic field, T_N shows a rapid suppression, dipping below our lowest measurement temperature of 2 K above 30 kOe. The suppression is also accompanied by a considerable broadening of the specific heat anomaly. Curiously, with further increase in the magnetic field, a new anomaly appears, which is seen as a small but sharp and clearly discernible peak in the c_p/T Vs T curves. The position of this new anomaly shifts to higher temperatures with increasing applied magnetic field, reaching upto 5 K under a field of 90 kOe.

The observation are summarised in figure 7.14, where a field-temperature phase

diagram is shown for the pristine and the 1 % Co-doped crystals. The data points are estimated from the specific heat anomaly and derivatives of the dc χ plots. Field dependent ($H||$ chain) elastic neutron data for 1 % Co-doped crystal are also shown in the background as colour plot. Showing the elastic neutron intensity scattered at Q point (0 1/2 1/2).

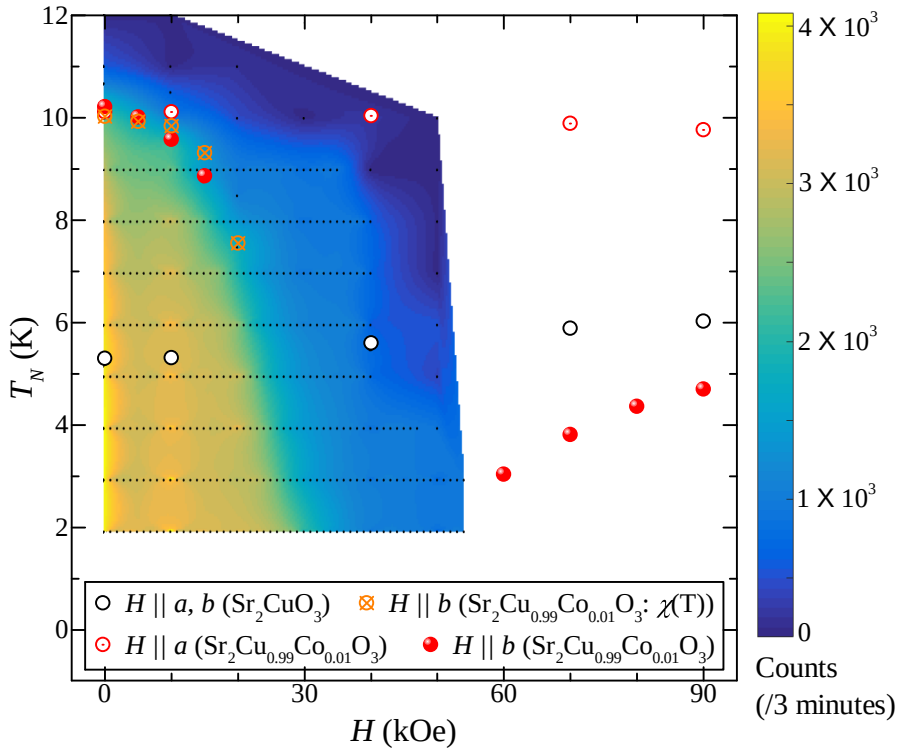

Figure 7.14: Field dependent phase diagram of the transition temperatures for pure and 1% Co doped Sr_2CuO_3. The crosses-circles (⊗) indicated the T_N data obtained for dc magnetic susceptibility. The neutron intensity scattered at Q point (0 $\frac{1}{2}$ $\frac{1}{2}$) has been shown as colour plot in the background.

The observed suppression of T_N is also highly anisotropic. In the field applied perpendicular to the chain, T_N shows only a marginal decrease (see figure 7.13). The anisotropic behaviour of Co-doped Sr_2CuO_3 can be linked to the single-ion-anisotropy of the doped Co^{2+} ions, discussed earlier in this section. However, to understand the behaviour of ordering temperature in the intermediate fields parallel to the chain (20−60 kOe) more data points are needed in the phase diagram. As the anomaly in the specific heat data becomes more flat (see figure 7.13) in the measurement under these fields, the extraction of transition temperature is difficult from the c_p/T Vs T curves.

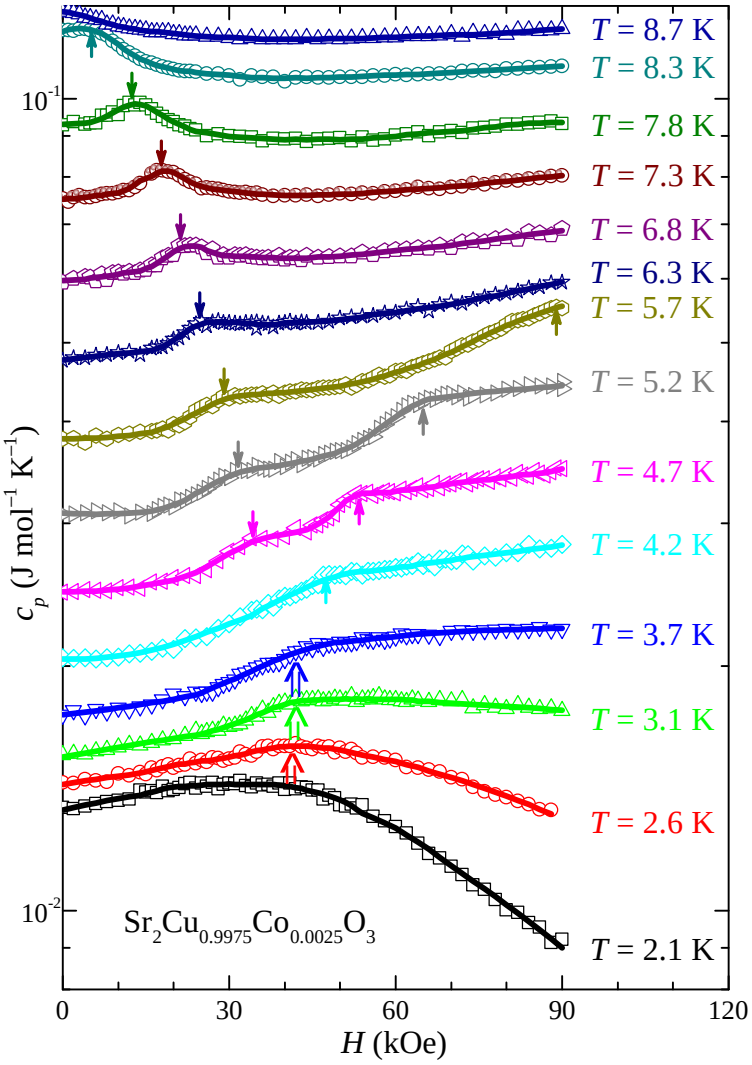

Figure 7.15: (a) Field-dependent specific heat ($c_p(H)$) isotherms for 0.25%-Co doped Sr_2CuO_3. The arrow indicates the transition fields. Solid lines are guides to eyes. The field is applied parallel to the chain.

In order to investigate further the intermediate field range, specific heat of 0.25% Co-doped crystal was measured as a function of applied external field, at constant temperatures ranging from ranging from 2 K to ≈ 9 K. As shown in figure 7.15, the $c_p(H)$ at $T = 8.32$ K, and down to $T = 5.76$ K, shows a weak but clearly discernible anomaly whose position is marked using a down facing arrow. However, the isotherms measured at $T \leq 5.76$ K show the emergence of a new anomaly (shown with an up-facing arrow) at higher fields corresponding to a second field-induced phase transition. At $T = 4.2$ K, the two anomalies seems to have merged, giving rise to a broad step-like feature in

the c_p vs H curve. Which is shown using a double arrow ($\Uparrow$). With further lowering of the temperature, the qualitative features of the c_p vs H curves remain unchanges down to $T = 3.1$ K. At $T = 2.6$ K and 2.1 K, with increasing field the specific heat first increases, passes through a broad maximum and eventually decreases as the magnetic field is increased beyond $40 - 50$ kOe. The rate of decrease of c_p at $T = 2.1$ K being steeper than in the $T = 2.6$ K data. We did these measurements in, both, increasing and decreasing magnetic field, however, no hysteresis could be detected.

In figure 7.16, we show the $H - T$ phase diagram estimated from the specific heat measurements for 0.25% Co-doped crystals. Here, we have also included c_p Vs T data for 0.25 % Co-doped crystal (not shown). The shaded region of the phase diagram corresponds to the isotherms measured at $T < 3.1$ K in figure 7.15, where the position of the anomaly is not well resolved.

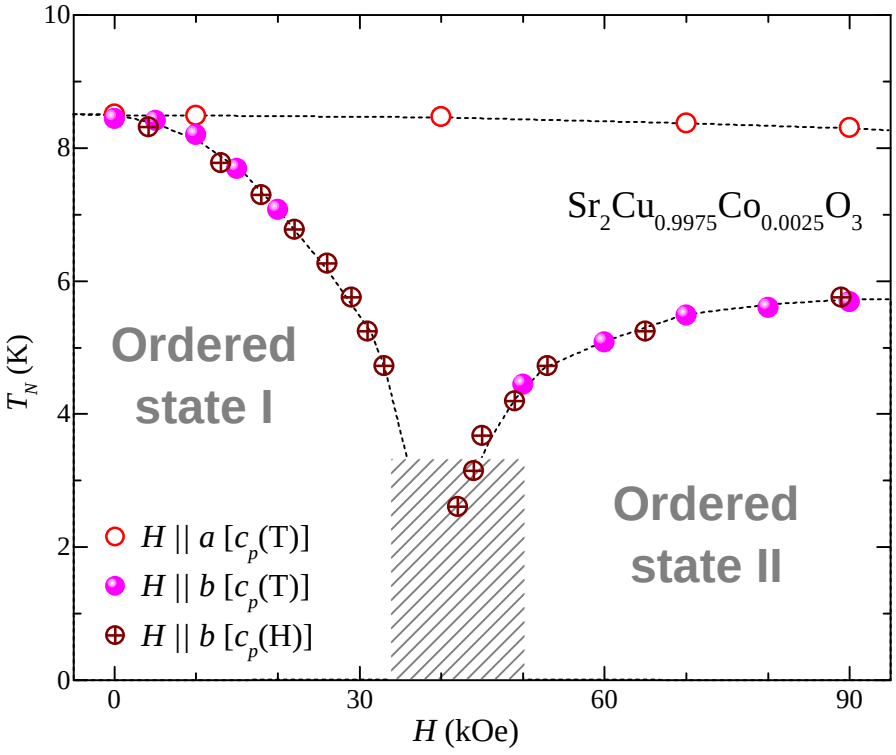

Figure 7.16: Field dependent phase diagram showing the transition temperature estimated from the temperature dependent specific heat ($c_p(T)$), and from field depedent specific heat ($c_p(H)$). The shaded region in the field range 35 - 50 kOe and in the temperature range $T \lesssim 3$ K is the region of the phase diagram which requires further investigations for an accurate mapping.

Discussion

The field dependence of the ordering temperature (T_N) of the Co-doped Sr_2CuO_3 is highly complex. The large anisotropy seen in the bulk magnetisation and the anisotropic field dependence of T_N indicates a clear deviation from the Heisenberg nature of the spin-system. Since, the undoped crystal exhibits an isotropic behaviour except near and below T_N, we are inclined to think that the observed anisotropy is due to the spin-orbit driven single-ion-anisotropy of the doped Co-ions. As mentioned earlier, in a square-planner coordination, the unquenched residual orbital angular momentum imparts an appreciable single-ion anisotropy to the Co^{2+} ion. Effective spin 1/2 magnetic moment and an Ising-like anisotropy is not uncommon to the Co^{2+} based compounds (see for example [187, 188]). What is curious, however, is that the Ising-like anisotropy of the doped Co^{2+} spins in Sr_2CuO_3 appears to have transmitted to the entire chain even at low Co-doping. At first sight, it may appear surprising; however, given that the spin correlations in the quantum spin 1/2 chain show a power law decay, one cannot rule out spin-spin correlations at larger separations. In such a scenario, Co spins can interact with each other via the intervening Cu spins.

The suppression of the ordering temperature with increasing applied magnetic field is also surprising in a different ways: recall that the T_N of pristine and Zn-doped crystals exhibits a slow and isotropic shift to higher temperatures with the increasing external magnetic field. Clearly, the effects of field on the properties of the spin 1/2 Heisenberg chain doped with dilute impurities depend strongly on the quantum state of the impurity.

The field dependence of the ordered phase of our Co-doped crystal bears resemblances to the behaviour of the Ising-like spin 1/2 antiferromagnetic chain under an applied field which shows a transition from the Néel ordered state to a spin liquid phase under external magnetic field applied along the Ising axis.

The Hamiltonian for the spin 1/2 XXZ model in the presence of magnetic field is given by:

$$\mathcal{H} = J \sum_i \left\{ S_i^z S_{i+1}^z + \varepsilon \left(S_i^x S_{i+1}^x + S_i^x S_{i+1}^x \right) \right\} - \gamma \mu_B \sum_i S_i^z H \tag{7.6}$$

where, H is the applied magnetic field and the other symbols have the same meaning

as in equation 1.5, ε being Δ^{-1}. Using the *Bethe ansatz* calculation, the H-ε phase diagram for the ground state of the model is shown in 7.17.

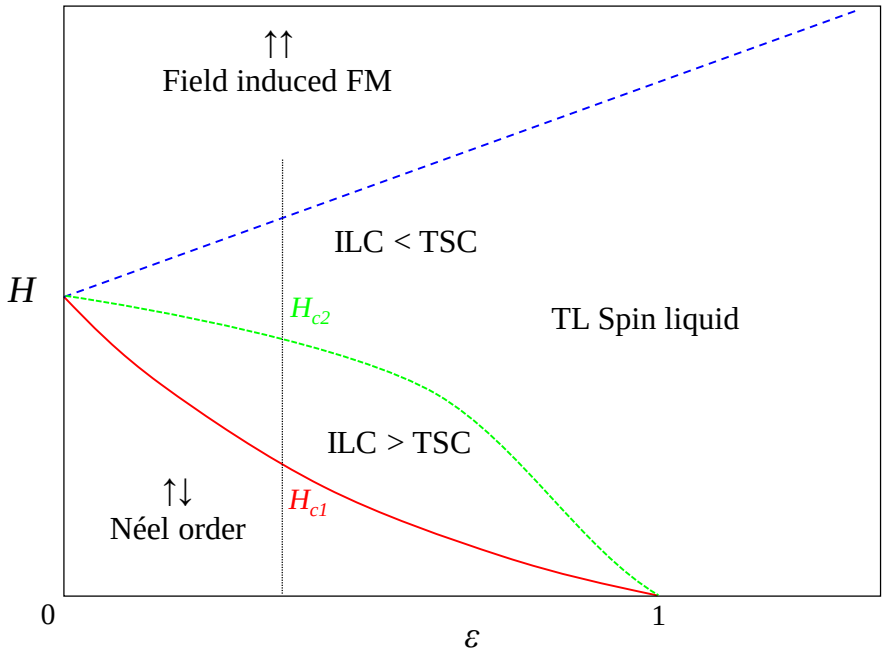

Figure 7.17: Cartoon showing $\varepsilon - H$ phase diagram for the model Hamiltonian 7.6 ($J > 0$). The point $\varepsilon = 1$ corresponds to the isotropic Heisenberg chain, and the region ($0 < \varepsilon < 1$) to an Ising-like chain. The ground state for ($0 \leq \varepsilon < 1$) is Néel ordered. Under an applied magnetic, the long-range ordered is destroyed at H_{c1} (black line), giving way to the *Tomonaga Luttinger* (TL) spin-liquid state ground state. ILC and TSC refer to incommensurate longitudinal and transverse staggered spin correlations. Above H_{c2}, transverse staggered correlations dominate, giving ride to transverse antiferromagnetic phase. Field induced ferromagnetic transition is induced above the dashed line. Due to a finite interchain coupling, the region between H_{c1} and H_{c2}, the spin structure is described as incommensurate longitudinal spin density wave phase. The figure is adapted from [183].

The ground state of the Hamiltonian 7.6 for an Ising-like chain is Néel ordered. If we neglect the interchain coupling, then under external magnetic field the system exhibits a first-order transition above a certain critical field H_{c1} to a quantum critical spin-liquid state -the *Tomonaga Luttinger liquid* (TLL) [183].

TLL is of course not long-range ordered (the ground state is analogous to that of the spin 1/2 HAF chain), however, due to a finite interchain exchange, an incommensurate spin density wave ordering appears in the intermediate fields, and upon further

increasing the field another transition H_{c2}, to a transverse staggered phase (TAP) is expected before the field becomes large enough to induced a ferromagnetic like saturation [189]. The intermediate transitions, at H_{c1}, arises due to a finite interchain interaction. To understand the origin of TAP, one should consider the spin correlations in the TLL phase of the spin 1/2 XXZ chain. These are incommensurate for the longitudinal spin component and staggered for the transverse spin component.

The exponents characterizing the decay of these correlation functions are $\eta_x = \eta$ and $\eta_z = 1/\eta$ for the transverse and longitudinal components, respectively. In the Heisenberg chain (XXX), the transverse staggered correlation is always dominant. In an Ising-like chain, however, above H_c the longitudinal component dominates, unless the field exceeds some critical value (shown by the green dotted line in the phase diagram of figure 7.17), where upon, the transverse correlation wins over. In the TAP phase, therefore, one expects the T_N to increase with the increasing magnetic field (as is the case with spin 1/2 HAF chain).

It is, therefore, anticipated that in the $H-T$ phase diagram of the Co-doped Sr_2CuO_3 (figure 7.16), the ordered phase marked as I, where the ordering temperature decreases rapidly with increasing magnetic field is the Néel ordered phase; and the ordered phase II, where the ordering temperature shows a gradual increase is the TAP. The metamagnetic transition in the isothermal plots (figure 7.11) corresponds to H_{c1}. The first-order nature of transition at H_{c1} can be inferred from the recorded hysteresis. The quasi-linear increase of $M(H)$ below and above H_{c1} with roughly the same slope suggest that this background increase is related to the van Vleck term and the free spins. The first order nature of the transition is more clearly evident in the neutron scattering data shown in figure 7.12. The shaded region in the $H-T$ phase diagram probably corresponds to the TL spin liquid phase. The exact nature of TL phase (i.e., if there is any incommensurate longitudinal spin wave ordering or not) is not clear. However, as shown in figure 7.4, the specific heat measured as a function of external magnetic field at temperatures below $T = 2.6$ K shows only a pronounced hump centred between 30 – 40 kOe. Had there been a field-induced ordered state at low-temperature, we should have seen a distinct anomaly, which we do not see. We rather see a broad maximum which could be a

signature of the emergence of a spin liquid state. The shaded region, therefore, seems to corresponds to the TL region between H_{c1} and H_{c2} but with a long-range ordering.

We should point out that our experimental results are rather similar to the spin chain compound $BaCo_2V_2O_8$ where the Ising-like Co^{2+} spins are reported to undergo a Néel type ordering below $T = 5.5$ K in zero field [190]. In a field applied parallel to the chain, the ordering temperature decreases sharply and the system exhibits a cascade of field induced phase transitions at 39 and 86 kOe once the Néel ordered state is suppressed below 1.8 K (see figure 7.18) [183, 191–193].

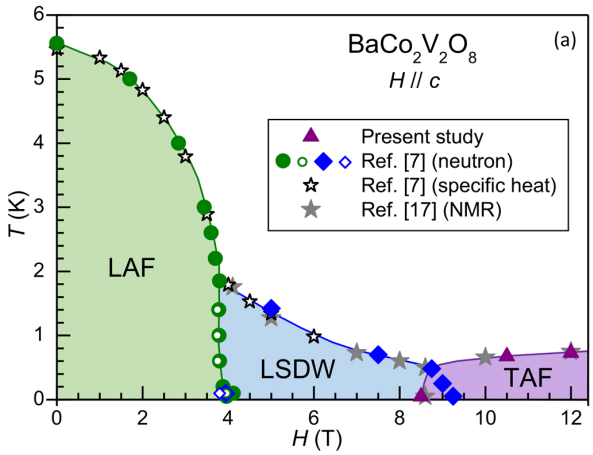

Figure 7.18: H-T phase diagram of $BaCo_2V_2O_8$ taken from reference [191]. Here, LAF is the Néel ordered longitudinal antiferromagnetic phase; LSDW is the incommensurate longitudinal spin density wave phase which arises in the TLL phase due to a finite interchain coupling. TAF is the transverse antiferromagnetic phase which corresponds to spin-flop of the LAF structure as expected in the TLL picture.

7.3 Summary

In summary, we have investigated the magnetic ordering in the spin-chain compound Sr_2CuO_3 in the presence of dilute disorder with different spin quantum states. The bulk dc magnetisation and specific heat measurements suggest a Néel ordered state below $T_N = 5.4$ K in the pristine crystal, which is in good agreement with the previous reports based on neutron and μSR experiments [126]. The specific heat of all the crystals show a low-temperature upturn, partly due to 2-level Schottky anomaly of the free spins present in the system. The Schottky contribution is estimated and analysed

for the free-spin concentrations, which agrees fairly well with those obtained using the susceptibility analysis. The T_N is found to suppress in the presence of scalar disorder due to staggered moment at the open ends at the segment boundaries. The isotropic enhancement of the T_N in presence of external magnetic field indicates the Heisenberg nature of the Cu spins. The enhancement of T_N can be attributed to the enhancement of transverse staggered corrections in an external field.

In the case of Co-doped chains, a highly complex magnetic behaviour is observed. In contrast with the case of scalar impurities, the T_N increases with doping Co impurities. An unprecedented 100 % increment in the T_N is recorded for merely 1% of Co-doping in the spin chain. The ordered state of the Co-doped chains show a complex field dependence. In the field applied along the chain length, the sample exhibits a field induced magnetic phase transition. This behaviour bears a close resemblance with the Ising chain system $BaCo_2V_2O_8$ [183, 190–193] and seems to conform to the spin 1/2 XXZ model.

Chapter 8

Spin Frustration in the Spin $1/2$ Zigzag Heisenberg Chain

In the preceding two chapters we analysed and discussed the effects of dilute disorder in the spin $1/2$ linear chain. Here, we will investigate the physical properties of the spin $1/2$ zigzag chain compound $SrCuO_2$ in the presence of dilute disorder. In chapter 3 we presented the crystal structure of the compound $SrCuO_2$. Here, we recall that the zigzag chain in $SrCuO_2$ comprises edge-sharing CuO_2 plaquettes, running along the crystallographic $c-$axis (figure 8.1). The 180° antiferromagnetic (AFM) superexchange in the zigzag chain has a strength, $J/k_B \approx 2100 \pm 200$ K [56]. Additionally, the edge-sharing chains interact through 90° Cu - O - Cu bond, which is relatively weaker and ferromagnetic (FM) in nature. The FM interaction (J') is estimated to be roughly one-tenth of the AFM superexchange (J) [121].

The zigzag chain has been a subject of several theoretical studies in the past (see for example [194–198]). The case $J \gg |J'|$, in particular, was independently investigated by *White* and *Affleck* [194] and *Allen* and *Senichal* [198]. *White* and *Affleck* used density matrix renormalisation group and a Bosonization approach to show that the zigzag chain exhibits a gapless spin excitation spectrum for weak ferromagnetic J'. However, if J' happens to be antiferromagnetic, the spin excitations become gapless. The gapless phase either exhibits a weak spontaneous dimerization or a finite range incommensurate magnetic order with broken translation symmetry. Since $J \gg |J'|$, at high temperatures ($T \gg J'/k_B$), the zigzag chain effectively behaves like a pair of decoupled chains. From

the structural information in the preceding paragraph, it is obvious that the low-energy excitations in the compound $SrCuO_2$ are expected to be gapless ($J \gg |J'|$), which was confirmed experimentally by *Zaliznyak et al.* [124]

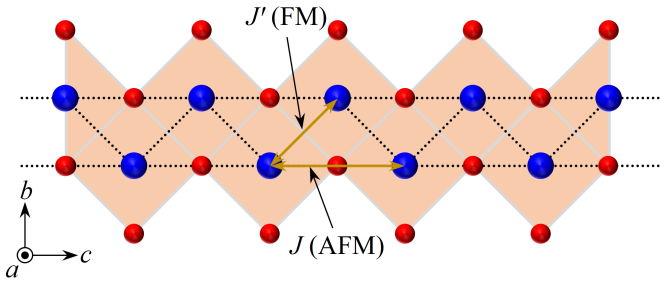

Figure 8.1: The zigzag chains of compound $SrCuO_2$ along the crystallographic $c-$axis

Here, in this chapter we will focus on the effects of magnetic frustration on the magnetic ground state and spin excitations of the frustrated chain in the presence of dilute magnetic and non-magnetic disorder. We show that disorder tends to magnify further the effect of frustration.

8.1 Bulk Magnetic Susceptibility of undoped $SrCuO_2$

In figure 8.2 we show the bulk magnetic susceptibility (χ) of $SrCuO_2$ measured along the three principal crystallographic axes. The susceptibility exhibits a behaviour similar to that of the linear chain compound Sr_2CuO_3 (see figure 6.1) with a gradual decrease upon cooling below room temperature, followed by a sharp increase at low temperatures. This low-temperature "*Curie-tail*", arises due to the inevitable presence of disorder/defect in the crystal as discussed in chapter 6. The difference here, however, is that the upturn in χ starts at relatively higher temperature ($T \approx 100$ K).

8.1.1 Analysis of the Susceptibility data

In analysing the magnetic susceptibility of $SrCuO_2$ we used the equation 2.3. In figure 8.3, we show the fitted curves, obtained using equation 2.3 for the pristine $SrCuO_2$ crystal. A satisfactory fit to the data is obtained down to nearly $T = 30$ K. An average

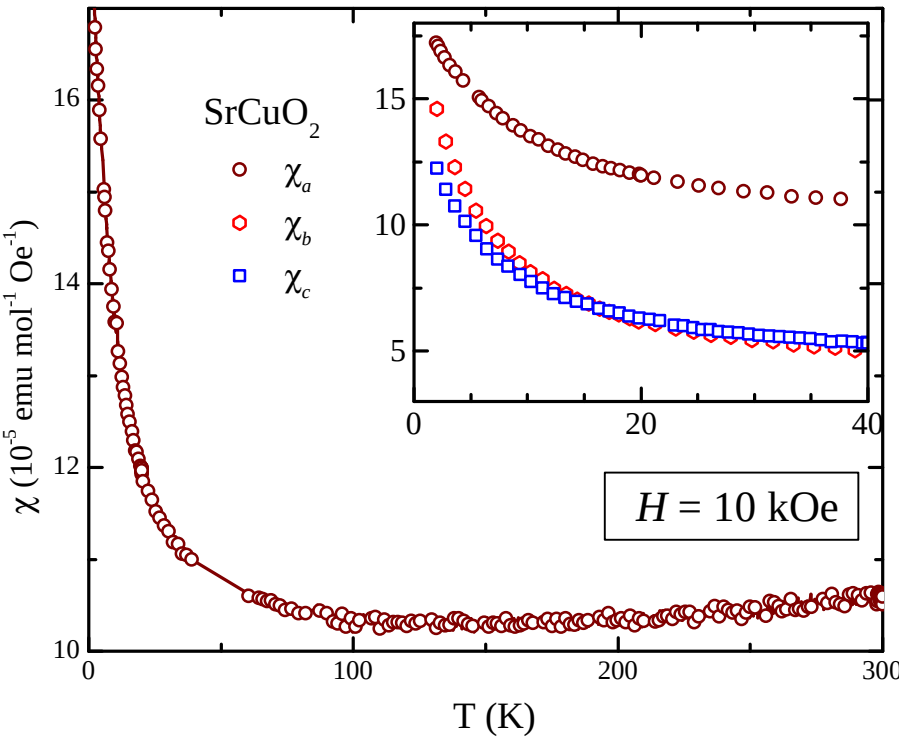

Figure 8.2: Temperature variation of magnetic susceptibility χ of compound $SrCuO_2$. The data shown are recorded by applying field perpendicular to the CuO_2 plaquettes. Inset: low temperature susceptibilities along crystallographic a, b and c axes.

Table 8.1: Values of intra-chain exchange J, the temperature independent contribution χ_0 and defect concentration p obtained by fitting the experimental susceptibility using equation (2.3). For comparison, the low-temperature data were also fitted to the Curie-Weiss equation. p_{CW} and θ_P are the fitting parameters of this fit (see text for details).

Parameters		J (k_B K)	χ_0 (10^{-5} emu/mol.K)	p (per Cu Site)	p_{CW} (per Cu Site)	θ_p (K)
$SrCuO_2$	($H \parallel a$)	1930±200	1.3±0.2	0.0075 (1)	0.003	-2.7
	($H \parallel b$)		-4.3±0.2	0.0077 (1)	0.003	-0.7
	($H \parallel c$)		-4.3±0.2	0.0080 (1)	0.003	-3.5
$SrCu_{0.99}Zn_{0.01}O_2$	($H \parallel a$)		1.3±0.2	0.014 (1)	0.002	-3.3

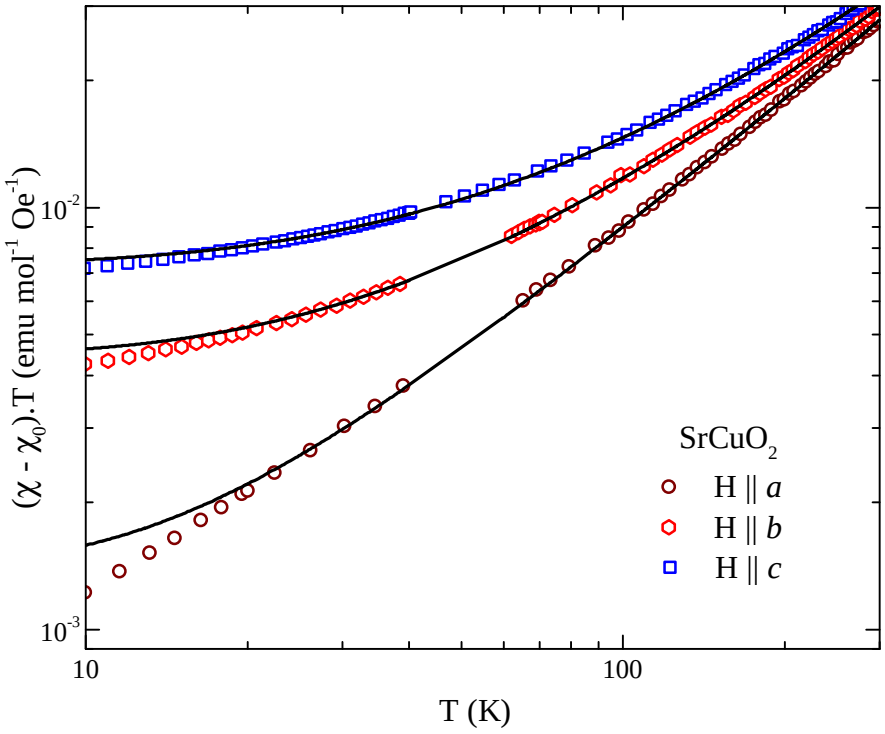

Figure 8.3: Magnetic susceptibility $(\chi - \chi_0)T$ of $SrCuO_2$. Solid lines represent the theoretical fit using equation 2.3 (see text for details). Data along b and c axes are shifted by multiples of 3 x 10^{-3}

J value of $1930^{+200}_{-200}K$ and $\chi_0 = 1.3 \pm 0.2(\chi_0^a), -4.3 \pm 0.2(\chi_0^b), -4.3 \pm 0.2(\chi_0^c)$ (in the units of 10^{-5} emu/mol.Oe) obtained from the fitting analysis are in good agreement with Motoyama et al.[56]. The average defect concentration turned out to be 0.008 per Cu site, which is higher than the corresponding value of 0.005 /Cu for the linear chain compound Sr_2CuO_3. The value of p for the zigzag chain might be slightly overestimated because of the weak zigzag coupling (J') not included in equation 2.3.

In figure 8.4 we compare the susceptibilities of the two compounds by plotting $(\chi - \chi_0)J$ against T/J where the values of χ_0 and J for the two compounds are used from tables 6.1 and 8.1. In this representation, the susceptibility is J-independent. On the same plot, we also show the variation of $\chi_{\text{chain}}J$ [37]. Near room temperature the two data sets collapse on the calculated χ_{chain} as one would have expected. However, upon lowering the temperature below $T \approx 0.1J$ the measured susceptibilities start to deviate from the ideal chain behavior: increasing with decreasing temperature due to

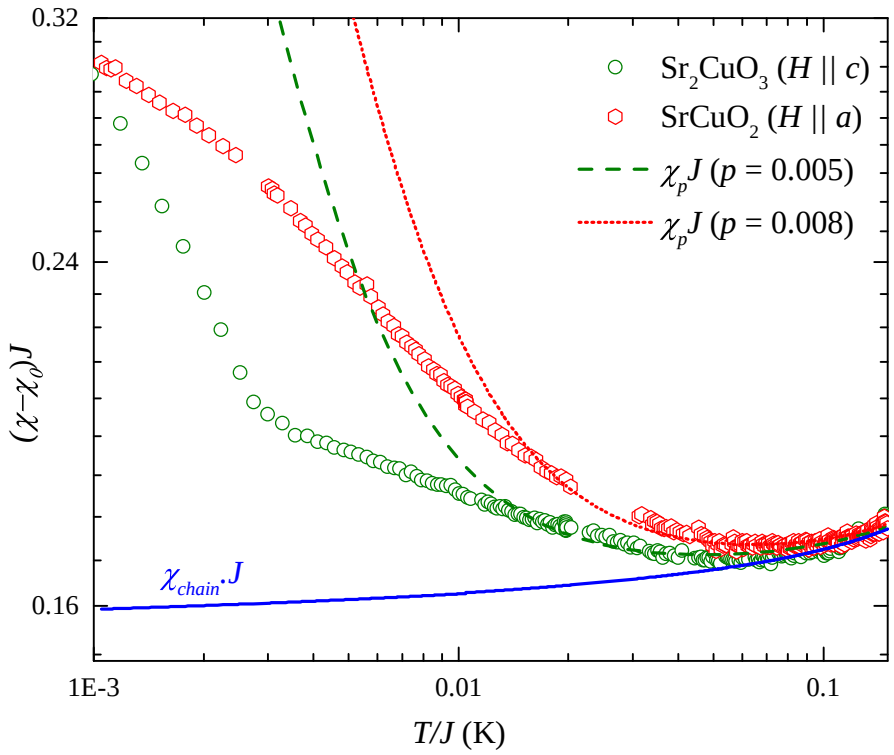

Figure 8.4: Normalized susceptibilities of Sr_2CuO_3 and $SrCuO_2$. In both cases data shown are for field applied along the longest crystallographic axis. The calculated chain susceptibility $\chi_{\rm chain}J$ is also shown (solid line). The dashed lines represent calculated $\chi_p J$ for p = 0.005 and 0.008 per Cu site (see text for details).

chain breaks. This increase is more pronounced in $SrCuO_2$ than in Sr_2CuO_3, in agreement with the higher p value for the former. As mentioned earlier, the double chains of $SrCuO_2$ have an additional ferromagnetic frustrated exchange J' which is estimated to about $0.1J$ [199]. While the dominant antiferromagnetic exchange (J) tends to lower the chain susceptibility upon lowering the temperature, J' has just the opposite effect as it tends to disrupt any tendency towards antiferromagnetic ordering. Therefore, the susceptibility of $SrCuO_2$ is expected to deviate from an ideal chain behaviour at temperatures higher than for the linear chain compound. Moreover, the presence of coupling J' in the double chains itself implies that a defect cannot be considered as a chain break at low temperatures. Therefore, at temperatures below the rung coupling J', equation 2.3 has only a limited validity. It is for this reason, we believe, that the p value obtained here for undoped $SrCuO_2$ is, possibly slightly overestimated. A more direct manifestation of J' evidently is to suppress the onset of long-range spin ordering due to geometrical

frustration discussed later in more details. It is worth mentioning here that though the next-nearest neighbor interaction J_{nnn} along the chain length is estimated to be around 140 K[120], equation 2.3 is shown to be applicable as long as $T \gg p^2 J_{nnn}$ [38]. Thus J_{nnn} is not expected to have any significant influence either on the susceptibility or on the determination of p.

8.1.2 Zinc ($S = 0$) impurities in $SrCuO_2$

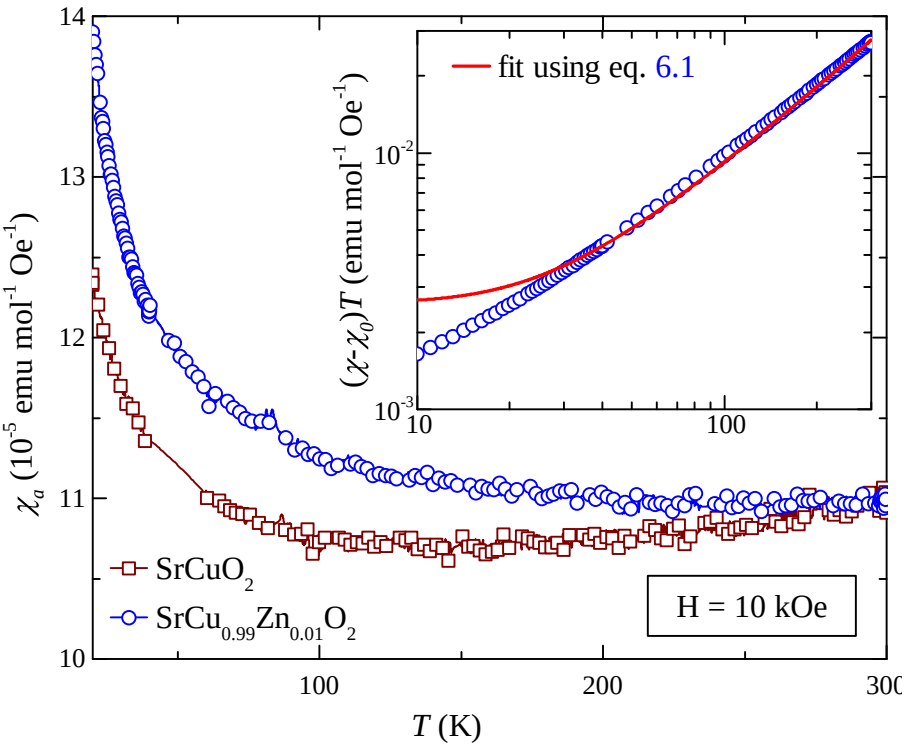

Figure 8.5: dc magnetic susceptibility $\chi(T)$ for the printine and 1% Zn doped $SrCuO_2$ in the temprature range 20-300 K. Inset: Magnetic susceptibility $(\chi - \chi_0)T$ of $SrCu_{0.99}Zn_{0.01}O_2$. Solid curve represent the best theoretical fit using equation 2.3

The bulk magnetic susceptibility of zigzag chains doped with scalar impurities (Zn^{2+}, $S = 0$) exhibits an enhancement of the Curie contribution as shown in figure 8.5. The susceptibility data were fitted using equation 2.3 to get a rough estimate of the defect concentration in the crystal. The fit results are shown in the inset of figure 8.5 and the fitted parameters are presented in table 8.1. The fitting procedure used here is same as described in the previous chapter in the context of the compound Sr_2CuO_3. If

one considers a defect concentration of 0.08% in the pristine crystals of Sr_2CuO_3, the defect concentration in the crystal doped with nominal 1% impurities was found to be 0.14%, implying that the effective Zn concentration in our crystal is about 0.06% which is significantly lower than the nominal value. But from our crystal growth experiments, we had expected Zn concentration in the grown crystals to be significantly smaller than 1%, since the segregation coefficient of Zn was inferred to be smaller than 1 (see section 5.3.4). The fitted curve deviates from the experimental data at low temperatures ($T < 100$ K) due to the presence of frustrated coupling, not included in equation 2.3.

8.2 Magnetic Ground State of the Spin 1/2 Zigzag Chain

As discussed in chapter 1 due to the finite interchain coupling the spin 1/2 linear chain compound undergo a dimensional crossover from 1D to 3D at low-temperatures and enters a magnetic long-range ordered state. The transition temperature is almost linearly dependent on the inter- to intra-chain coupling (see equation 1.15). Accordingly, the compound Sr_2CuO_3 exhibits a magnetically ordered state at temperatures below $T = 5.4$ K, indicated as a peak in the dc susceptibility shown in figure 8.6 for comparison. However, despite having similar intra- and inter chain couplings, the zigzag chain compound $SrCuO_2$ does not exhibits any magnetic anomaly down to $T = 2$K (see figure 8.6). The absence of long-range ordered state in $SrCuO_2$ is further supported by the muon spin rotation (μSR) results, where a static ordering can only be seen below $T = 2$ K [127]. Corresponding elastic neutron scattering experiments indicate the zigzag chains to have a spin frozen ground state with much shorter and anisotropic magnetic correlations. The measured correlation lengths along the three crystallaphic axes were $\xi_a = 60(25)a$, $\xi_b = 2.2(3)b$ and $\xi_c = 200c$ in the units of unit cell dimensions along the three respective axes [122]. The deviation from the long-range ordering seen in the linear chains, can be attributed to the magnetic frustration inbuilt in the zigzag chain.

Similarly, the absence of any magnetic anomaly in low-field dc χ for Zn-doped crystals indicate no magnetic ordering down to $T = 2$ K (see figure 8.6). As we have

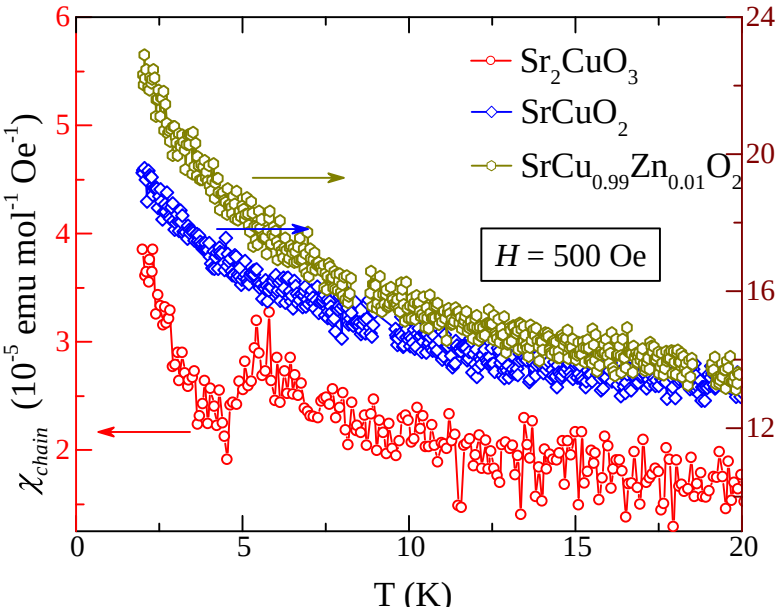

Figure 8.6: Low-temperature dc magnetic susceptibility [$\chi(T)$] of the pristine, 1% Zn doped $SrCuO_2$ and pristine Sr_2CuO_3 crystal in low-field ($H = 500Oe$). Arrows indicated the y-scale.

seen in previous chapter in context of linear chains, scalar defects (Zn^{2+}) are suppose to segment the chain into finite length sections, which disrupts any ordered state due to the staggered moment at the of these chain segments. Following the same mechanism, Zn ions in the zigzag chain may further suppress the short-range ordering in the pristine crystal.

8.2.1 Co-impurities in the Zigzag Chain

In panel (a) of figure 8.7 the temperature dependence of the dc magnetic susceptibility (χ) of 1% Co-doped $SrCuO_2$ is shown. The measurements were carried out in an external magnetic field $H = 500$ Oe applied parallel the chain. For comparison, data for the pristine crystal is also shown. In comparison with the pristine compound, the Co-doped crystal shows a steep rise in the low-temperature susceptibility followed by a clearly discernible magnetic anomaly at temperature $T \approx 6$ K. In the inset of figure 8.7 (a) the variation of T_N is plotted as a function of nominal Co-content of the crystals. An almost linear dependence of T_N with Co concentration is observed, which suggests that up to the highest doping level studied here, the doped Co-atoms are incorporated

in the structure. However, as in the pristine crystal, the magnetically ordered state in the Co-doped crystal also appears to be quasi-long-range due to geometrical frustration of the spins in the zigzag lattice. The quasi-long-range nature of the ordered state is inferred from bulk magnetisation and elastic neutron scattering experiments.

In the dc magnetic susceptibility, the zero-field cooled (ZFC) and field-cooled (FC) measurements were carried out. In panel (a) of figure 8.7, the dc magnetisation in ZFC and FC mode are shown. Below, the peak in χ_c, the ZFC and FC susceptibilities exhibit different temperature dependences. While, the ZFC curve continue to show a decrease with decreasing temperature, the FC curve tends to be nearly temperature independent manner. For comparison, χ of 1% Co-doped Sr_2CuO_3 is also measured parallel to the chain as shown in panel (b) of figure 8.7. The data exhibit a sharp peak near $T = 11$ K, which marks the onset of a magnetic long-range-ordering phase (confirmed using specific heat measurements shown in the preceding chapter). No thermomagnetic irreversibility in the susceptibility could be detected down to the lowest measurement temperature of 2 K in our experiments, which is a crucial difference compared to the zigzag chains under identical doping conditions.

The first indication of the ground state being quasi-long-range ordered come from the ZFC and FC splitting of the chain susceptibility shown in the panel (a) of figure 8.7. To further characterise the magnetic ground state we carried out *ac* magnetisation measurements and also estimated the correlation lengths using elastic neutron scattering (ENS). Muon spin relaxation (μSR) experiments were also carried out at low-temperature to infer the nature of the ordered state∗.

Panel (a) of figure 8.8 shows the temperature dependence of the real part (χ'_{ac}) of the ac magnetic susceptibility, measured by applying an alternating field $H_{ac} = 5$ Oe with frequency (f) ranging from 100 Hz to 10 kHz. χ'_{ac} signals at frequencies smaller than 100 Hz were extremely weak, and the imaginary part χ''_{ac} was even weaker with poor signal-to-noise ratio over the entire frequency range. χ'_{ac} also exhibits a peak in correspondence with the peak observed in χ_c. The peak position shifts towards higher temperatures with increasing f, as is commonly observed in glassy systems [200]. The

∗in collaboration with Dr. Giacomo Prando, IFW-Dresden, Germany

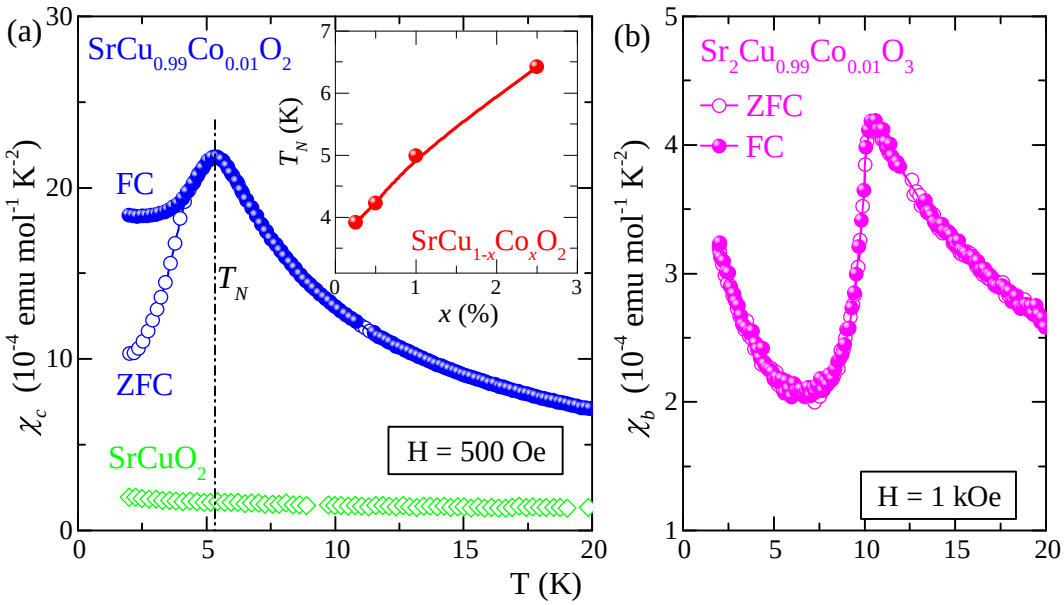

Figure 8.7: (a)Temperature dependent magnetic susceptibility along the chain length for the pristine and Co-doped zigzag chains compound $SrCuO_2$. Inset: Estimated T_N with respect to Co-content in the crystal. (b) Low-temperature susceptibility along the chain length for Co-doped linear chain compound Sr_2CuO_3 for comparison

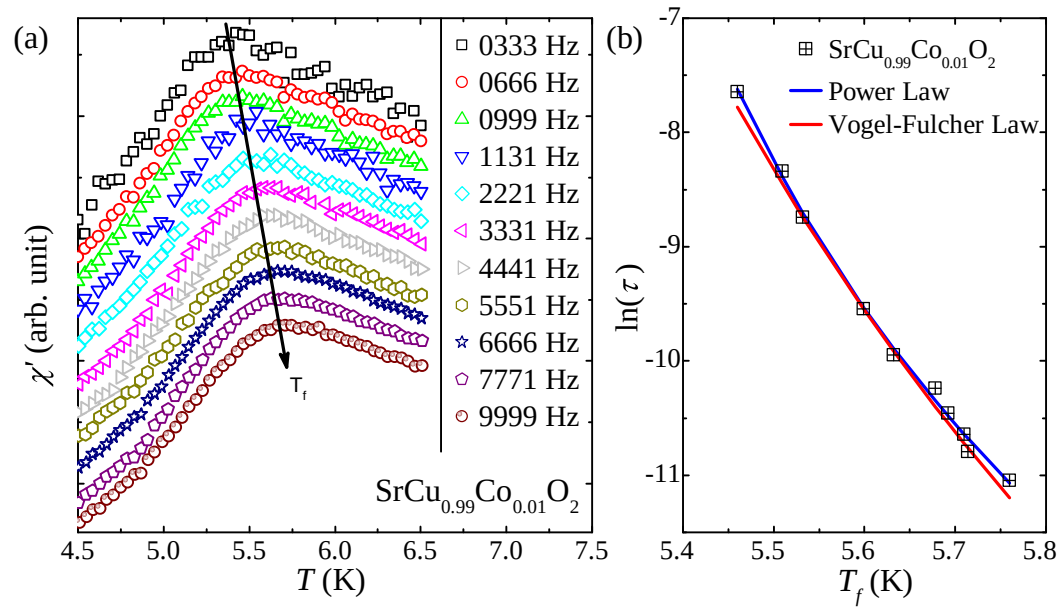

Figure 8.8: (c) Temperature dependence of the real part of ac magnetic susceptibility (χ'). (d) Relaxation time (τ) with respect to the peak temperatures. The solid lines are fit to the data (see text for details). The curves in panel (c) are down shifted for clarity.

corresponding ratio $\Delta T_f/T_f$ was found to be around 0.04 per ω decade ($\omega = 2\pi f$). This value is higher when compared to the atomic spin glasses but smaller than the corresponding values reported for superparamagnets [201]. A more quantitative analysis can be performed by plotting $ln(\tau)$, where $\tau = (2\pi f)^{-1}$ is the relaxation time, against the inverse of the freezing temperature (T_f) for various ac excitation frequencies (panel (b) of figure 8.8). The data points were fitted using the theory of dynamical scaling near a phase transition [202]: $\tau = \tau_0 \left(\frac{T_f}{T_g} - 1\right)^{-z\nu}$, where τ_0 represents a microscopic characteristic time, T_g is the spin glass temperature in the limit $f \to 0$ and $z\nu$ denotes the critical dynamical exponent. From the fitting, we get a value of $\tau_0 \sim 10^{-10\pm1}$ s, $z\nu \sim 4 \pm 1$, and $T_g = 5.2 \pm 0.1$ K. The value of T_g is in good agreement with the position of the peak in the dc magnetic susceptibility. For atomic spin-glasses, the values of τ_0 and of $z\nu$ typically lie in the range $10^{-13\pm1}$ s and 8 ± 1, respectively [202]. The values obtained here fall in the range that is more frequently reported for systems with inhomogeneous or short-range ordering [203–207]. An analogous analysis can be performed using the Vogel-Fulcher law $\tau = \tau_0 \exp\left(\frac{E_a/k_B}{T-T_0}\right)$, which is typically used for glassy systems comprising short-range order, yielded a reasonably good fit by fixing the Vogel temperature $T_0 (< T_g)$ and by varying τ_0 and the energy barrier (E_a) as fitting parameters. For $T_0 = 4.2$ K, the values obtained for τ_0 and E_a are respectively $10^{-10\pm1}$ s and 20 ± 2 K. The value of the former parameter is in good agreement with the dynamical scaling approach.

ENS data for $Sr_{0.99}Co_{0.01}CuO_2$ are presented in figure 8.9, where the magnetic scattering around $(1/2, 0, 1/2)$ at $T = 1.5$ K is displayed. For each data point the scattering signal have been collected for about 10 minutes. Measurements were also performed at $T = 20$ K, allowing us to subtract a weak, higher-order wavelength contamination. Panels (a) and (b) show the background-subtracted pure magnetic scattering along the Q_H and Q_L reciprocal lattice vectors, respectively. These peaks are broadened in both directions uncharacteristic of a purely LRO magnetic phase, which is characterised by instrumental-resolution-limited peak widths. The corresponding correlation lengths obtained are $\xi_a = 44$ Å ($\sim 12\,a$) and $\xi_c = 155$ Å ($\sim 40\,c$). Finally, panel (c) shows the temperature dependence of the magnetic Bragg peak, with a power-law fit yielding

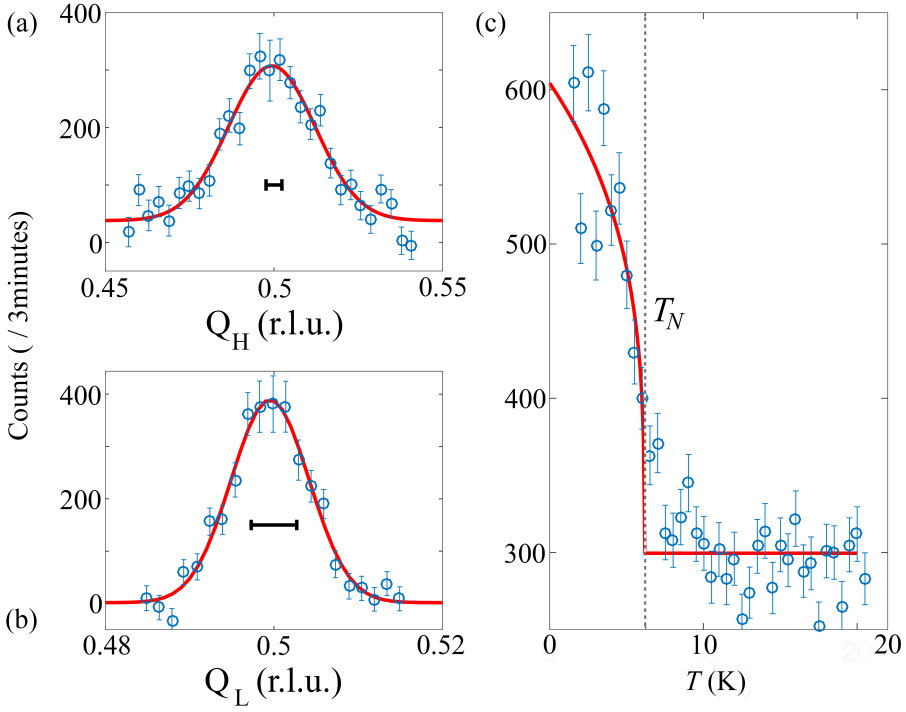

Figure 8.9: (a) and (b) Magnetic scattering in $SrCu_{0.99}Co_{0.01}O_2$ crystal around $(1/2, 0, 1/2)$ at $T = 1.5$ K. The solid lines show the Gaussian fits to the data. The horizontal bars refer to the instrumental resolution/broadening. (c) Temperature dependence of the magnetic scattering at $(1/2, 0, 1/2)$. The solid line indicates the power law fit yielding a magnetic transition at $T = 6.1(3)$ K.

$T_N = 6.1(3)$ K. Accordingly, our ENS results suggest that $SrCu_{0.99}Co_{0.01}O_2$ crystals exhibit an anisotropic and quasi-LRO magnetic phase below $T \approx 6$ K.

In order to understand the spin dynamic in the ordered state muon-spin spectroscopy (μ^+SR) were performed at SμS (PSI) on the GPS spectrometer (πM3 beamline) in the temperature region 1.6 K $< T <$ 20 K, in conditions of zero-magnetic field (ZF$-\mu^+$SR). In ZF-μ^+SR [209, 210], the spin (de)polarization function $P_z(t)$ of implanted μ^+ is measured as a function of time (t). In our measurements [208], the samples were aligned in order to have the z direction parallel to the crystallographic b axis, but with an arbitrary orientation of the a-c plane. Experimental $P_z(t)$ curves for $Sr_{0.99}Co_{0.01}CuO_2$ are reported at representative T values in figure 8.10. Curves were fitted using the function,

$$P_z(t) = \sum_i a_{T_i} \cos(\gamma B_i t)\, e^{\left(-\frac{\sigma_{T_i}^2 t^2}{2}\right)} + a_L \exp(-\lambda_L t)\,, \tag{8.1}$$

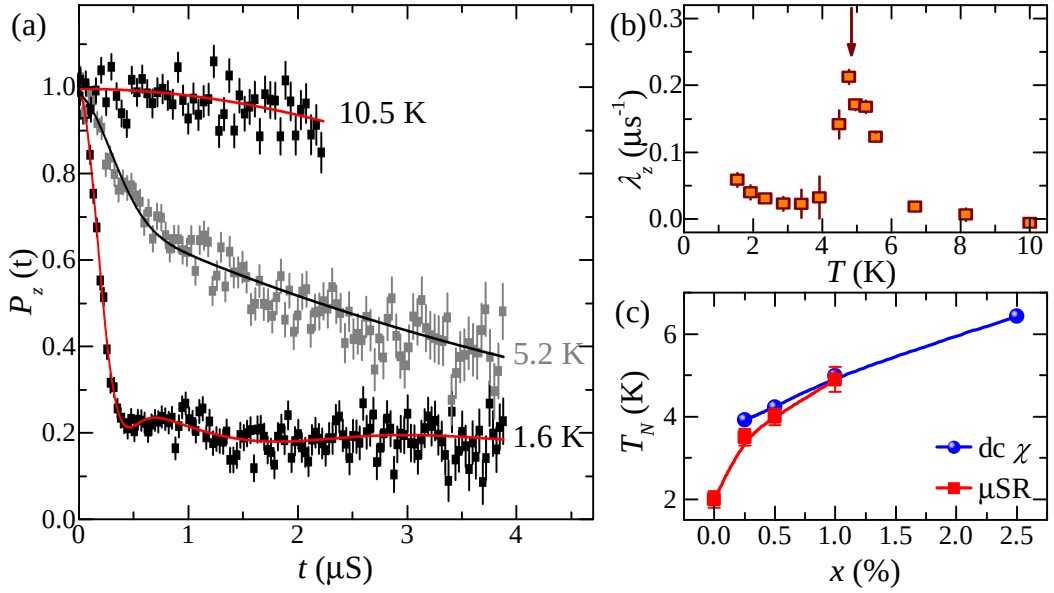

Figure 8.10: Results of μ^+SR measurements for $Sr_{0.99}Co_{0.01}CuO_2$. t-depolarization curves at representative T values are shown in ZF conditions. Continuous lines are best-fits to the experimental data according to equation 8.1. (b) T dependence of the longitudinal relaxation rate. The arrow indicates the estimated T_N value. (c) Estimated T_N from dc χ and μSR data with respect to Co-content in the crystal [208].

which is typically used for materials with long-range magnetically ordered ground state[211]. Here, λ_L is the longitudinal spin-lattice relaxation rate. Its T dependence is shown in the inset of figure 8.10, displaying a narrow critical peak around the magnetic transition. At the same time, the development of two ($i = 1, 2$) highly damped, though visible, oscillations in the transversal fraction at low T denote a local homogeneous magnetic environment for the μ^+ whose distribution's second moment $\sim \sigma_T$ is still smaller than the average value B. All these local evidences further corroborate the interpretation of the ground state of the system as a quasi-LRO phase. Finally, in agreement with bulk magnetisation and ENS data, orienting z along the a-c plane results in an anisotropic behaviour of $P_z(t)$ †.

†private communication with Dr Giacomo Prando, IFW-Dresden, Germany

8.3 Summary

The magnetic frustration in the zigzag chain of compound $SrCuO_2$ seems to play an important role in its magnetic proprieties. For example, despite comparable values of intra- and inter- chain couplings, the linear chain compound undergoes a long-range ordered state below 5.4 K, but the zigzag chain compound shows no sign of magnetic long-range-ordering down to $T = 2$ K. These differences in the behaviour of linear and zigzag chain compounds appeared more striking in the lightly doped crystals.

The effect of scalar doping in the zigzag chains can be approximately described using the field-theory expression for the susceptibility of a linear chain in the presence of a scalar impurities. The susceptibility data of 1% Zn doped $SrCuO_2$, when fitted using this expression yields a reasonable value of the impurity concentration and intra-chain coupling, however, the quality of the fit showed considerable deviation from the measured $\chi(T)$ below about 100 K or so; which also happens to be the strength of the frustrated interaction J' in the zigzag chain not included in the fitting expression. To get a better agreement with the experimental data, it is therefore necessary to improve the field-theory results so that it can be applied to a zigzag chain.

Co-doping appears to favour a magnetically ordered ground state albeit with an enhanced T_N and highly anisotropic magnetisation, which is presumably related to the Ising-like spin of Co^{2+} ions [187, 188]. In Sr_2CuO_3, for example, the T_N is increased from 5.4 K in the pristine sample to 11 K in the sample doped with 1 % Co. The behaviour of $SrCuO_2$ upon Co-doping is analogous, but with the exception that the ordering temperature is slightly lower ($T_N \approx 6$ K) and the ordered phase is not truly LRO. This lack of LRO is related to the zigzag geometry of its spin-chains. Though interchain interactions favour LRO of the spins (as in Sr_2CuO_3), frustrated interactions in the zigzag chain tends to suppress the LRO [127, 212]. If, however, spin disorder is also included, a glassy phase will be favoured [122]. It is interesting that similar levels of Co^{2+} defects in the linear and zigzag chains of comparable intra- and interchain exchange interactions exhibit different behaviours, which underpins the role played by the spin frustration in a chain with a zigzag geometry.

Chapter 9

Summary and Outlook

In this thesis work our main focus had been to investigate the effects of dilute disorder on the magnetic properties of the spin 1/2 Heisenberg antiferromagnetic chain. For this purpose, we chose Sr_2CuO_3 and $SrCuO_2$, as the host compounds to which foreign ions (impurities) were doped to realize various types of disorders. These compounds are known to be the best realizations of the 1D spin 1/2 Heisenberg antiferromagnetic model, comprising quasi-1D spin 1/2 -O-Cu-O- chains. We verified important theoretical results pertaining to the finite-size effects arising due to disorder, and explored new phenomena in the dilute disorder limit. We also investigated spin frustrated chain realized in the compound $SrCuO_2$.

To investigate the effects of dilute disorder, it is necessary to perform experiments on high-quality single crystals doped with controlled level of a given impurity. A part of the experimental work, carried out under this thesis, therefore, involves single-crystal growth of the compounds Sr_2CuO_3 and $SrCuO_2$ with dilute disorder. The disorder was introduced by doping directly in the chains with 1% or less of an impurity, M = Zn, Co, Ni and Mn. The non-congruent melting behaviour of these compounds, and the low distribution coefficient ($k < 1$) of the doped impurities in the crystal are some of the factors that make the crystal growth experiments of these compounds a challenging prospect. We adopted, and further developed, the specialized crystal growth technique, namely, the travelling-solvent-floating-zone technique associated with an optical floating-zone-furnace for the single crystal growth experiments. We optimized parameters associated with the TSFZ growth process, which led to a comprehensive understanding of the mechanism of this technique.

With the access to home-grown high-quality crystals, we measured the physical properties of the pristine and the doped compounds using various complementary techniques. Our study of the dc magnetic susceptibility of Sr_2CuO_3 confirmed the validity of the field theory results for the susceptibility of a spin $1/2$ segmented chain. Extension of this analysis to doped spin chains enabled an accurate determination of the defect density in the crystal. Our analysis of the magnetic susceptibility of the Ni-doped Sr_2CuO_3 crystal reveals that the Ni^{2+}ion in the spin $1/2$ HAF chain behave as a *'scalar'* impurity, in accordance with the field-theoretical calculations that predicted a Kondo-like screening of the Ni spin ($S = 1$) by the neighbouring host spins in the chain. Our inelastic neutron scattering experiments also support this scenario. We show that the expression for calculating the susceptibility of a segmented chain is, however, inadequate for the Ni-doped chain at low-temperatures ($T < 100$ K) due to opening of a spin-gap in the magnetic excitations. In short, the theoretical model for calculating the susceptibility of the Heisenberg spin $1/2$ chain comprising chain breaks is successfully used in fitting the susceptibility of the pristine Sr_2CuO_3 consisting of intrinsic chain breaks due to oxygen off-stoichiometry, and the Zn-doped Sr_2CuO_3 consisting of additional chain breaks due to doped Zn.

We also investigated the low-energy excitations (spinons) of the spin $1/2$ chains comprising dilute impurities with different spin quantum numbers using the inelastic neutron scattering. We emphasize on the importance of the defect's spin quantum state in determining the nature of the low-energy excitations. We showed that Ni^{2+} defects in Sr_2CuO_3 results in gapping of the excitation spectrum, which remains gapless for Zn^{2+} and Co^{2+} impurities. However, for all the doped crystals we observed an enhancement of the spectral density of the scattered neutron. Such an enrichment is unexpected and could not be addressed within the existing theoretical models. Further studies are needed to explain this observation.

We show that scalar or non-magnetic impurities in the spin chain suppress the ordered state in agreement with the theoretical calculations. Interestingly, the transition temperature of the pristine and non-magnetic impurity doped chains is found to increase with the application of an external magnetic field. One possible reason could be that

the transverse staggered correlations are enhanced under an external magnetic field and thus an ordered state is favoured. However, a clear understanding of the observed increases of T_N with increasing magnetic field is not yet available, further investigations are necessary to explain the observed behaviour.

The case of chains doped with Co-ions is found to be particularly interesting. The magnetic ordering temperature upon Co-doping exhibits a significant enhancement: roughly twice the value in the pristine crystal for less than 1% of Co-doping. The magnetic behaviour of the Co-doped chains also shows high anisotropy. The anisotropy is argued to be a single-ion-anisotropy of the Co^{2+} ion. The change of magnetic behaviour with slightest (even < 0.25 %) inclusion of Co in the chains is found to be remarkable, and invite further attention.

Very interestingly, for fields applied along the chain, the magnetic ordering temperature decreases with increasing magnetic field, disappearing below the lowest measurement temperature of 2 K in our experiments for applied fields higher than 30 kOe. And, as the field is increased further above 40 kOe (for 1% Co-doped sample), a new ordered phase emerges. The ordering temperature in the new phase increases with increasing applied magnetic field. These observations indicate a possible field-induced quantum phase transition in the Co-doped Sr_2CuO_3 crystal. Our preliminary neutron scattering experiments corroborate the specific heat and magnetisation data, however, further investigations are necessary to elaborate on the nature of the two ordered phases.

We showed that the magnetic susceptibility of $SrCuO_2$ cannot be fully described using the field-theory results, applicable to the linear chain, however, this result could still be used to get a good estimate of the defect concentration and also the experimental data above $T = J'/k_B$. In order to calculate susceptibility of a zigzag chain, at the lower temperatures proper theoretical modelling, by including the frustrated spin coupling J', should be done.

Due to the magnetic frustration the magnetic ground state of $SrCuO_2$ also differ significantly from that of the linear chain compound Sr_2CuO_3. Despite of having almost equal intra- and inter-chain magnetic exchanges, the zigzag chain compound do not show any long-range magnetic ordering. It rather goes into a short-range spin-frozen

magnetic ground state at $T < 5$ K. In the Co-doped crystals, we observed an enhancement of the effect of the magnetic frustration. We also rigorously characterised the nature of the spin excitations of the zigzag chain. This work should be extended further for other impurity types.

In future, specific heat measurements on the pristine and doped Sr_2CuO_3 crystals under external magnetic field should be extended down to further low-temperatures (< 2 K) in order to understand the origin of the low-temperature upturn in c_p/T Vs T curve. In fact, as mentioned in chapter 7, a second magnetic transition is expected at temperatures below 2 K, which motivetaes low-temperature specific heat experiments. Similarly, it will be useful to carry out low-temperature measurement of the susceptibility. Since $\chi(T)$ plots also indicated a possible low-temperature phase transition.

Analogous to the Ising-like $BaCo_2V_2O_8$, where NMR investigation played an important role in revealing the field-induced transitions, it will be interesting to perform NMR experiments on Co-doped Sr_2CuO_3, whose behaviour appears to conform closely to the spin 1/2 antiferromagnetic XXZ model. Neutron diffraction experiments in external magnetic field will be very helpful to understand the spin structure in the ordered states and thus the origin to the field induced quantum phase transition.

In short, we investigated the effects of dilute disorder on the magnetic properties of the spin 1/2 HAF chains, and compared the results to theoretical calculations. Our investigations show that disorder in 1D spin chain results in rich physical phenomena. Several new features were discovered that raised new questions related to the anisotropic defects and magnetic frustration which should motivate further research.

Bibliography

[1] H.-J. Mikeska and A. K. Kolezhuk, in *Quantum magnetism*, Vol. 3, edited by U. Schollwöck et al. (Springer, Berlin, Heidelberg, 2004) Chap. One-Dimensional Magnets, pp. 1–83.

[2] M. T. Hutchings et al., Phys. Rev. B **5**, 1999 (1972).

[3] U. Schollwöck et al., eds., *Quatum Magnetism* (Springer, Berlin, Heidelberg, 2004).

[4] H. Tasaki, Journal of Physics: Condensed Matter **10**, 4353 (1998).

[5] P. Fazekas, *Lecture notes on electron correlation and magnetism* (1999) Chap. 1, pp. 1–16.

[6] F. H. L. Essler et al., *The one-dimensional hubbard model*, Cambridge Books Online (Cambridge University Press, 2005).

[7] J. Hubbard, Proceedings of the Royal Society of London A: Mathematical, Physical and Engineering Sciences **276**, 238 (1963).

[8] M. C. Gutzwiller, Physical Review **134**, 3–6 (1964).

[9] J. Kanamori, Progress of Theoretical Physics **30**, 275 (1963).

[10] N. Ashcroft and N. Mermin, *Solid State Physics* (Harcourt Brace College Publishers, 1976).

[11] C. P. P. Jr. et al., in *Superconductivity (second edition)*, edited by C. P. Poole et al., Second Edition (Academic Press, Amsterdam, 2007), p. 275.

[12] M. Imada et al., Reviews of Modern Physics **70**, 1039 (1998).

[13] A. Fujimori et al., Physical Review B **29**, 5225–5227 (1984).

[14] A. Fujimori and F. Minami, Physical Review B **30**, 957–971 (1984).

[15] a. Bocquet et al., Physical Review B **53**, 1161 (1996).

[16] A. E. Bocquet et al., Physical Review B **46**, 3771 (1992).

[17] P. A. Lee et al., Rev. Mod. Phys. **78**, 17 (2006).

[18] F. C. Zhang and T. M. Rice, Physical Review B **37**, 3759 (1988).

[19] N. D. Mermin and H. Wagner, Phys. Rev. Lett. **17**, 1133 (1966).

[20] L. de Jongh, ed., *Magnetic Properties of Layered Transition Metal Compounds* (Springer Netherlands, 1990).

[21] F. Boersma et al., Phys. Rev. B **23**, 186 (1981).

[22] L. D. Landau and E. M. j. a. Lifshitz, *Statistical Physics*, Translation of Statisticheskiy fizika (London Pergamon Press, 1958).

[23] I. Affleck, Journal of Physics A: Mathematical and General **31**, 4573 (1998).

[24] T. Giamarchi, *Quantum Physics in One Dimension*, International Series of Monographs on Physics (Clarendon Press, Oxford, 2003).

[25] L. Faddeev and L. Takhtajan, Physics Letters A **85**, 375 (1981).

[26] J. des Cloizeaux and J. J. Pearson, Phys. Rev. **128**, 2131 (1962).

[27] J. C. Bonner and M. E. Fisher, Physical Review **135**, A640 (1964).

[28] W. E. Estes et al., Inorganic Chemistry **17**, 1415–1421 (1978).

[29] L. Balents, Nature **464**, 199 (2010).

[30] R. B. Griffiths, Phys. Rev. **133**, A768–A775 (1964).

[31] M. Takahashi, Progress of Theoretical Physics **46**, 401 (1971).

[32] M. Gaudin, Phys. Rev. Lett. **26**, 1301–1304 (1971).

[33] M. Takahashi and M. Suzuki, Progress of Theoretical Physics **48**, 2187 (1972).

[34] T. Koma, Progress of Theoretical Physics **81**, 783 (1989).

[35] M. Takahashi, Phys. Rev. B **43**, 5788 (1991).

[36] S. Eggert et al., Physical Review Letters **73**, 332 (1994).

[37] S. Lukyanov, Nuclear Physics B **522**, 20 (1997).

[38] J. Sirker et al., Journal of Statistical Mechanics: Theory and Experiment **02015**, 30 (2008).

[39] A. Klümper and D. C. Johnston, arXiv:cond-mat/0002140 **84**, 4701 (2000).

[40] D. C. Johnston et al., Physical Review B **61**, 9558 (2000).

[41] E. H. Lieb and F. Y. Wu, Physical Review Letters **20**, 1445 (1968).

[42] B. J. Kim et al., Nature Physics **2**, 397 (2006).

[43] J. Schlappa et al., Nature **485**, 82 (2012).

[44] C. Kim et al., Phys. Rev. Lett. **77**, 4054 (1996).

[45] C. Kim et al., Phys. Rev. B **56**, 15589 (1997).

[46] R. Neudert et al., Phys. Rev. Lett. **81**, 657 (1998).

[47] V. Lante and A. Parola, Phys. Rev. B **80**, 195113 (2009).

[48] D. J. Scalapino et al., Physical Review B **11**, 2042 (1975).

[49] H. J. Schulz and C. Bourbonnais, Physical Review B **27**, 5856 (1983).

[50] H. J. Schulz, Phys. Rev. Lett. **77**, 12 (1996).

[51] O. A. Starykh et al., Physical Review B **55**, 953 (1997).

[52] D. A. Tennant et al., Physical Review Letters **70**, 4003 (1993).

[53] S. K. Satija et al., Physical Review B **21**, 2001 (1980).

[54] T. Ami et al., Physical Review B **51**, 5994 (1995).

[55] S. Eggert, Physical Review B **53**, 5116 (1996).

[56] N. Motoyama et al., Phys. Rev. Lett. **76**, 3212 (1996).

[57] A. Keren et al., Phys. Rev. B **48**, 12926 (1993).

[58] H. Suzuura et al., Physical Review Letters **76**, 2579 (1996).

[59] L. Regnault and J. Renard, EPL (Europhysics ... **82**, 597 (1995).

[60] V. N. Muthukumar et al., Phys. Rev. B **54**, R9635 (1996).

[61] M. Hase et al., Journal of the Physical Society of Japan **65**, 1392 (1996).

[62] M. D. Johannes et al., Phys. Rev. B **74**, 174435 (2006).

[63] A. A. Belik et al., Journal of Solid State Chemistry **178**, 3461 (2005).

[64] R. Nath et al., Phys. Rev. B **77**, 134451 (2008).

[65] O. Janson et al., New Journal of Physics **11** (2009) 10.1088/1367-2630/11/11/113034.

[66] O. Janson et al., Phys. Rev. B **76**, 115119 (2007).

[67] G. Petrakovskii et al., Journal of Magnetism and Magnetic Materials **140-144, Part 3**, International Conference on Magnetism, 1991 (1995).

[68] J. P. Pouget, Comptes Rendus Physique **17**, 332 (2016).

[69] S. Blundell, *Magnetism in Condensed Matter*, Oxford Master Series in Condensed Matter Physics 4 (OUP Oxford, 2001).

[70] M. Hase et al., Physical Review Letters **70**, 3651 (1993).

[71] I. S. Jacobs et al., Phys. Rev. B **14**, 3036 (1976).

[72] G. Simutis et al., Phys. Rev. Lett. **111**, 067204 (2013).

[73] F. Hammerath et al., Phys. Rev. Lett. **107**, 017203 (2011).

[74] F. Hammerath et al., Phys. Rev. B: Condens. Matter Mater. Phys. **89**, 184410 (2014).

[75] I. Tsukada et al., Physical Review B **60**, 6601–6607 (1999).

[76] T. Shiroka et al., Physical Review Letters **106**, 137202 (2011).

[77] M. Thede et al., Physical Review B - Condensed Matter and Materials Physics **86**, 180407 (2012).

[78] A. Furusaki et al., Phys. Rev. B **52**, 15930–15942 (1995).

[79] T. N. Nguyen et al., Chemistry of Materials **6**, 1642 (1994).

[80] J. E. Hirsch and J. V. José, Physical Review B **22**, 5339 (1980).

[81] C. Dasgupta, Physical Review B **22**, 1305 (1980).

[82] S. K. Ma et al., Physical Review Letters **43**, 1434 (1979).

[83] D. S. Fisher, Physical Review B **50**, 3799 (1994).

[84] C. A. Doty and D. S. Fisher, Physical Review B **45**, 2167 (1992).

[85] G. Refael and E. Altman, Comptes Rendus Physique **14**, 725 (2013).

[86] T. Vojta, Journal of Physics A: Mathematical and General **39**, R143 (2006).

[87] J. Kokalj et al., Physical Review B - Condensed Matter and Materials Physics **91**, 155147 (2015).

[88] F. Iglói and C. Monthus, Physics Reports **412**, 277 (2005).

[89] C. Monthus et al., Phys. Rev. B **58**, 805 (1998).

[90] H. Alloul et al., Rev. Mod. Phys. **81**, 45 (2009).

[91] S. Eggert and I. Affleck, Phys. Rev. B: Condens. Matter Mater. Phys. **46**, 10866 (1992).

[92] J. Igarashi et al., Phys. Rev. B **51**, 5814 (1995).

[93] W Zhang et al., Physical review. B, Condensed matter **54**, 15171 (1996).

[94] W. Zhang et al., Phys. Rev. B **56**, 654 (1997).

[95] S. Rommer and S. Eggert, Physical Review B **59**, 6301 (1999).

[96] a. Furusaki and T. Hikihara, Physical Review B **58**, 5529–5538 (1998).

[97] W. Zhang et al., Journal of the Physical Society of Japan **66**, 1912 (1997).

[98] Y. Wang, Phys. Rev. B **56**, 14045 (1997).

[99] T. J. G. Apollaro et al., Physical Review A - Atomic, Molecular, and Optical Physics **88**, 052336 (2013).

[100] S. Eggert and S. Rommer, Doktorsavhandlingar vid Chalmers Tekniska Hogskola **81**, 1690 (1998).

[101] D. G. Clarke et al., Physical Review B **48**, 7070 (1993).

[102] S. Eggert et al., Physical Review Letters **86**, 516 (2001).

[103] S. Wessel and S. Haas, Physical Review B **61**, 15262 (2000).

[104] B. Schmidt et al., European Physical Journal B **32**, 43 (2003).

[105] J. Sirker et al., Phys. Rev. Lett. **98**, 137205 (2007).

[106] S. Eggert et al., Physical Review Letters **89**, 047202 (2002).

[107] S. Fujimoto and S. Eggert, Physical review letters **92**, 037206 (2004).

[108] A. V. Sologubenko et al., Physical Review B - Condensed Matter and Materials Physics **62**, R6108 (2000).

[109] A. V. Sologubenko et al., Physical Review B **64**, 0544112 (2001).

[110] C. Hess, Eur. Phys. J. Special Topics **151**, 73 (2007).

[111] N. Hlubek et al., Physical Review B - Condensed Matter and Materials Physics **81**, 20405 (2010).

[112] N Hlubek et al., Journal of Statistical Mechanics: Theory and Experiment **2012**, P03006 (2012).

[113] X. Zotos et al., Phys. Rev. B **55**, 11029 (1997).

[114] X. Zotos, Phys. Rev. Lett. **82**, 1764 (1999).

[115] T. Kawamata et al., Journal of Physics: Conference Series **200**, cited By (since 1996) 2 (2010).

[116] T. Masuda et al., Phys. Rev. Lett. **80**, 4566 (1998).

[117] M. Azuma et al., Physical Review B **55**, R8658 (1997).

[118] K. M. Kojima et al., Physical Review B - Condensed Matter and Materials Physics **70**, 094402 (2004).

[119] G. Simutis et al., arXiv:cond-mat **1603**, 04090v1 (2016).

[120] H. Rosner et al., Physical Review B **56**, 23 (1997).

[121] M. Matsuda and K. Katsumata, Journal of Magnetism and Magnetic Materials **140-144**, 1671 (1995).

[122] I. A. Zaliznyak et al., Phys. Rev. Lett. **83**, 5370 (1998).

[123] S. Eggert and I. Affleck, Phys. Rev. Lett. **75**, 934 (1995).

[124] I. A. Zaliznyak et al., Phys. Rev. Lett. **93**, 087202 (2004).

[125] A. C. Walters et al., Nature Physics **5**, 867 (2009).

[126] K. M. Kojima et al., Phys. Rev. Lett. **78**, 1787 (1997).

[127] M. Matsuda et al., Physical Review B **55**, R11953 (1997).

[128] Y. Utz et al., Physical Review B **92**, 060405 (2015).

[129] B. Hafner, *Scanning Electron Microscopy Primer*, tech. rep. (Characterization Facility, University of Minnesota, Twin Cities, 2007), pp. 1–29.

[130] W. H. Bragg and W. L. Bragg, Proceedings of the Royal Society of London A: Mathematical, Physical and Engineering Sciences **88**, 428 (1913).

[131] *Heat Capacity Option User's Manual*, Physical Properties Measurement System,Quantum Design ().

[132] J. S. Hwang et al., Review of Scientific Instruments **68**, 94 (1997).

[133] C. G. Shull et al., Phys. Rev. **83**, 333–345 (1951).

[134] G. Shirane et al., *Neutron Scattering with a Triple-Axis Spectrometer: Basic Techniques* (Cambridge Univeristy Press, 2002).

[135] W Marshall and R. D. Lowde, Reports on Progress in Physics **31**, 705 (1968).

[136] *Spallation - in focus*, (NA) `http://www.brodeck.de/ess/pages/spallation.htm`.

[137] A. Furrer et al., *Neutron Scattering in Condensed Matter Physics* (World Scientific, 2010).

[138] M. J. Cooper and R. Nathans, Acta Crystallographica **23**, 357 (1967).

[139] B. Dorner, Acta Crystallographica Section A **28**, 319 (1972).

[140] R. Cortenraad et al., Journal of Crystal Growth **222**, 154 (2001).

[141] S. I. Bozhko et al., Journal of Crystal Growth **311**, 1 (2008).

[142] W. D. Lawson and S Nielsen, *Preparation of single crystals*, English (Butterworths Scientific Publications, London, 1958).

[143] D. Hurle, ed., *Czochralski growth. In: Handbook of Crystal Growth*, English, Vol. 2a (North Holland, Amsterdam 1994, 1994) Chap. 3, p. 99.

[144] W. Pfann, Journal of Metals **4**, 747 (1952).

[145] H. Theuerer, US Patent 3,060,123 (1962).

[146] P. H. Keck and M. J. E. Golay, Phys. Rev. **89**, 1297 (1953).

[147] G. Behr et al., pat. (Germany) (2006).

[148] G. Behr et al., pat. (Germany) (2007).

[149] T. Fujii et al., Journal of Crystal Growth **223**, 175–180 (2001).

[150] A Cröll et al., Journal of Crystal Growth **166**, 239 (1996).

[151] S. Koohpayeh et al., Progress in Crystal Growth and Characterization of Materials **54**, 121 (2008).

[152] A. Revcolevschi et al., Physica C (Amsterdum, Neth.) **282-287**, 493 (1997).

[153] A Revcolevschi et al., Journal of Crystal Growth **198-199, Part 1**, 593 (1999).

[154] K. Kitamura et al., Journal of Crystal Growth **57**, 475 (1982).

[155] R. S. Feigelson, MRS Bulletin **13**, 47 (1988).

[156] D Gazit and R. S. Feigelson, Journal of Crystal Growth **91**, 318–330 (1988).

[157] B. R. Pamplin, *Crystal Growth* (Pergamon Press Oxford, 1975).

[158] J. Shah, *Crystal Growth*, Chapter 4, pages 113 (Pergamon Press, 1975).

[159] B. V. Slobodin et al., Sverkhprovodimost: Fiz. Khim. Tekh **3**, 523–526 (1990).

[160] N. M. Hwang et al., Journal of the American Ceramic Society **73**, 2531 (1990).

[161] J. K. Liang et al., *Phase Diagram of SrO-CaO-CuO Ternary System*, ISTC-Technical Report TR-92017 (Institute of Scientific and Technical Information of China; Beijing, China, 1992), pp. 1–9.

[162] W. Wong-Ng et al., Physica C: Superconductivity **299**, 9 (1998).

[163] Y. Matsushita et al., Journal of Solid State Chemistry **114**, 289 (1995).

[164] C. Lin et al., Journal of Crystal Growth **140**, 72 (1994).

[165] N. Ohashi et al., Journal of Crystal Growth **186**, 128 (1998).

[166] P. M. R. Ribeiro, "One-Dimensional Quantum Magnets in Cuprates: Single Crystal Growth and Magnetic Heat Transport Studies", PhD thesis (der Fakultät Mathematik und Naturwissenschaften der Technischen Universität Dresden, 2007).

[167] P. M. R. Ribeiro, "Einkristallherstellung und magnetischer Wärmetransport von niedrigdimensionalen Kupraten", MA thesis (Diploma Thesis, RWTH-Aachen, 2003).

[168] R. D. Shannon, Acta Crystallographica Section A **32**, 751 (1976).

[169] T.-C. Mao et al., J. Cryst. Growth **282**, 143 (2005).

[170] N. Wizent et al., J. Cryst. Growth **401**, 596 (2013).

[171] K. Karmakar et al., Cryst. Growth Des. **14**, 1184 (2014).

[172] J. M. Hill et al., Phys. Rev. B: Condens. Matter Mater. Phys. **65**, 10 (2001).

[173] K Kimura, S. and. Kitamura and I. Shindo, Journal of Crystal Growth **65**, 543 (1983).

[174] a. Mahajan and N. Venkataramani, Physical Review B **64**, 92410 (2001).

[175] H. Ohta et al., Journal of Physical Society of Japan **61**, 3370 (1992).

[176] H. Asakawa et al., Physical Review B **57**, 8285 (1998).

[177] a. W. Sandvik et al., Phys. Rev. B **56**, 23 (1997).

[178] M. Takigawa et al., Physical Review B **55**, 14129 (1997).

[179] J. P. Boucher and M. Takigawa, Phys. Rev. B **62**, 367 (2000).

[180] J. Sirker and N. Laflorencie, EPL (Europhysics Letters) **86**, 57004 (2009).

[181] F. D. M. Haldane, Physical Review Letters **50**, 1153–1156 (1983).

[182] I. Umegaki et al., Physical Review B **92**, 174412 (2015).

[183] S. Kimura et al., Phys. Rev. Lett. **100**, 057202 (2008).

[184] A. K. Pathak et al., Phys. Rev. Lett. **110**, 186405 (2013).

[185] A. Tari, *The Specific Heat of Matter at Low Temperatures* (Imperial College Press, 2003).

[186] K. A. Moler et al., Physical Review Letters **73**, 2744 (1994).

[187] J. C. Slonczewski, Journal of Applied Physics **32**, S253 (1961).

[188] A. K. Bera et al., Phys. Rev. B: Condens. Matter Mater. Phys. **89**, 094402 (2014).

[189] K. Okunishi and T. Suzuki, Physical Review B - Condensed Matter and Materials Physics **76**, 224411 (2007).

[190] Z. He et al., Physical Review B - Condensed Matter and Materials Physics **72**, 172403 (2005).

[191] B. Grenier et al., Physical Review B - Condensed Matter and Materials Physics **92**, 1–7 (2015).

[192] S. Kimura et al., Phys. Rev. Lett. **101**, 207201 (2008).

[193] S. K. Niesen et al., Phys. Rev. B **87**, 224413 (2013).

[194] S. R. White and I. Affleck, **54**, 9862 (1996).

[195] B Normand et al., Physical Review B **56**, R5736 (1997).

[196] F. D. M. Haldane, Physical Review B **25**, 4925–4928 (1982).

[197] M. Kumar et al., Phys. Rev. B **81**, 104406 (2010).

[198] D Allen and D. Sénéchal, Phys. Rev. B **55**, 299 (1997).

[199] T. M. Rice et al., EPL (Europhysics Letters) **23**, 445 (1993).

[200] M. Charilaou et al., Phys. Rev. B **83**, 224414 (2011).

[201] J. A. Mydosh, *Spin Glasses: An Experimental Introduction* (Taylor & Francis, 1993).

[202] R. Mathieu et al., Physical Review Letters **93**, 227202 (2004).

[203] Z. Śniadecki et al., Journal of Applied Physics **109**, 123921 (2011).

[204] N. Hanasaki et al., Phys. Rev. Lett. **99**, 086401 (2007).

[205] C. Lu et al., Journal of Magnetism and Magnetic Materials **322**, 2845 (2010).

[206] F. Wang et al., Physical Review B **80**, 024419 (2009).

[207] K De et al., Journal of Physics D: Applied Physics **40**, 7614 (2007).

[208] G. Prando and K. Karmakar et al., to be published, 2016.

[209] S. J. Blundell, Contemporary Physics **40**, 175 (1999).

[210] A. Yaouanc and P. Dalmas de Réotier, *Muon spin rotation, relaxation, and resonance: applications to condensed matter* (Oxford University Press, Oxford, 2011).

[211] G. Prando et al., Phys. Rev. B **87**, 174519 (2013).

[212] F. D. M. Haldane, Physical Review Letters **61**, 1029 (1988).